===== **REVIEW** =====

Theory of Threshold Characteristics of Semiconductor Quantum Dot Lasers

L. V. Asryan[1, 2^] and R. A. Suris[1^^]

[1]*Ioffe Physicotechnical Institute, Russian Academy of Sciences, St. Petersburg, 194021 Russia*
[2]*Department of Electrical and Computer Engineering, State University of New York, Stony Brook, NY 11794-2350, USA*
^*e-mail: asryan@theory.ioffe.rssi.ru*
^^*e-mail: suris@theory.ioffe.rssi.ru*
Submitted March 6, 2003; accepted for publication April 30, 2003

Abstract—A comprehensive theory of threshold characteristics of quantum dot (QD) lasers, which provides a basis for optimization of their design, is reviewed. The dependences of the gain, transparency current, threshold current, characteristic temperature, and multimode generation threshold on the parameters of the QD ensemble (surface density and size dispersion of QDs), cavity (stripe length and thickness of the waveguide region), heterocontacts (band offsets), and temperature are considered in detail. The limiting characteristics of the laser (optimum structure parameters, minimum threshold current density, and characteristic temperature of the optimized structure) are discussed at length. The results of the analysis may serve as direct recommendations for the development of QD lasers that significantly outperform the semiconductor lasers currently in use. © *2004 MAIK "Nauka/Interperiodica".*

1. INTRODUCTION

Heterostructures and devices based on them constitute one of the most important objects of the modern physics of semiconductors and semiconductor electronics [1, 2]. Presently, advances in the field of micro- and optoelectronics are largely made possible by the use of low-dimensional heterostructures. In quantum dots (QDs), heterostructures with spatial confinement of carriers in three dimensions, we have the limiting case of quantum confinement, and the energy spectrum is discrete. The extraordinary interest in QDs, from both the fundamental and practical point of view, is primarily due to the dramatic difference between the carrier spectra in them and in heterostructures based on bulk crystals, quantum wells (QWs),[1] and quantum wires (QWRs),[2] in which the spectrum is continuous within the bands or subbands of allowed states.

As they are similar to transitions between exactly discrete levels of a single atom, transitions between levels in a QD composed of several thousands or tens of thousands of atoms seem to be ideal for lasing.

With decreasing dimensionality of the active region of an injection laser, the density of states and gain spectra become narrower (Fig. 1), which leads to a decrease in the number of states to be filled to make the active region transparent (zero population inversion and zero gain) and to achieve lasing (gain equal to loss). Consequently, the transparency current (or inversion current, i.e., the injection current at which the population inversion is zero) and the threshold current (injection current at which the gain is equal to the loss and lasing begins) decrease and their temperature dependences become weaker. The decrease in the threshold current and increase in its temperature stability reflect one of the main areas of development and improvement of injection lasers (see, e.g., [3–8] for the evolution of the threshold current densities of QW lasers). Owing to the continuous nature of the carrier spectrum within the allowed subbands, the use of QWs [9–12] or QWRs [12] as active medium for optical transitions can only quantitatively improve the parameters of devices based on them compared with devices with a bulk active region [9, 13]. It can be seen from Fig. 1 that a fundamental change in the density of states and gain spectra is only achieved in a zero-dimensional active region. Consequently, a fundamental decrease in the threshold current and weakening of its temperature dependence can only be achieved by using QDs. The use of QDs as active medium in injection lasers is the most topical application of nanotechnology to the development of devices that present great commercial interest. Thus, semiconductor (diode) QD lasers are the most promising generation of injection lasers with fundamentally improved operating characteristics [14, 15]. Among the advantages of QD lasers over the presently used QW lasers are their narrower gain spectra, much lower threshold currents, and ultrahigh temperature stability, as well as the wider possibilities for controlling their lasing wavelength.

---

[1] A QW is an ultrathin layer in which carriers are spatially confined in a single (transverse) direction and move freely in the other two directions (in the well plane).

[2] In QWRs, carriers are spatially confined in two (transverse) directions and move freely in the third (longitudinal) direction (along the wire).
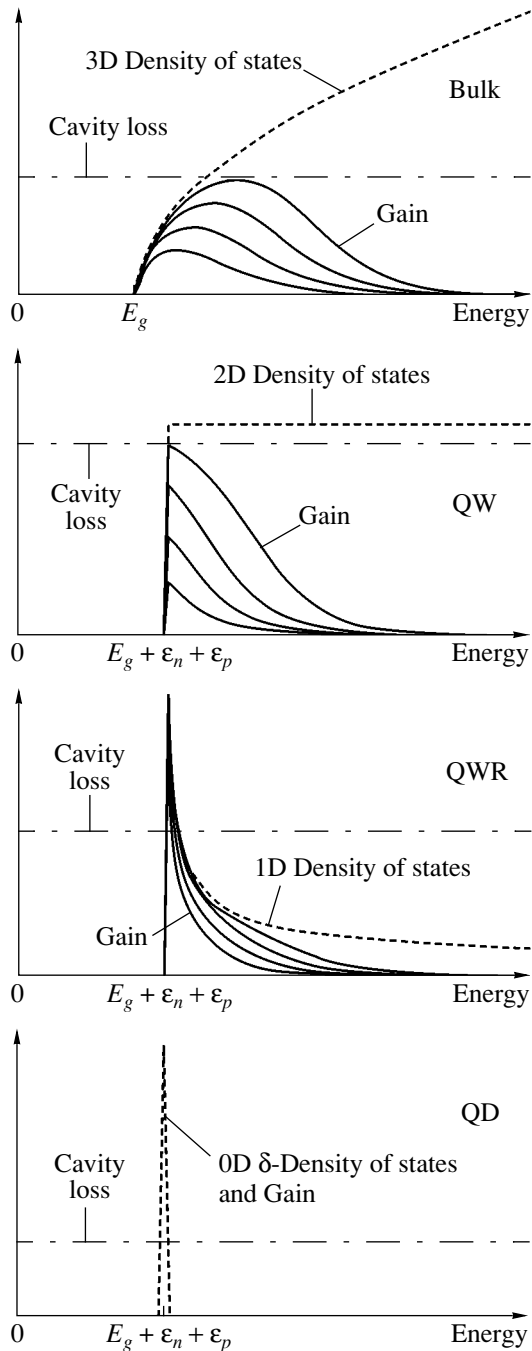
Fig. 1. Modification of the density of states and the shape of the gain spectrum with decreasing dimensionality of the active region.

Lasing from QDs (first with optical pumping [19] and then with current injection [20]) was made possible by the fabrication of dot arrays that satisfy rather stringent requirements for the uniformity of dot size and shape. The commercial prospects of QD lasers are stimulating research in this field. By now, much has been achieved in the development of QD lasers [21]. A number of research groups have reported successful fabrication of QD lasers [19–43]. The record-breakingly low, for all kinds of injection lasers, threshold current density $j_{th} = 19$ A/cm^2 at room temperature in the CW mode has been demonstrated [28].

Experimental advances in the design of QD lasers have made it practically relevant to develop a comprehensive theory of their operating characteristics, which could give practical recommendations for realizing their potential advantages over the lasers currently in use. Such a theory must include analysis of the basic processes (generation–recombination, capture into QDs and thermal escape therefrom, diffusion in the waveguide region), take into account inhomogeneous line broadening, and make it possible to determine the limiting parameters of the lasers and to optimize their design. This paper reviews a detailed theory of threshold characteristics of interband (bipolar) semiconductor QD lasers based on original studies by the authors [44–57]. The development of such a theory assumed that the following basic problems, which determine the structure of the paper, are to be solved. It is necessary

—to determine how the inhomogeneous line broadening caused by dispersion of QD parameters affects the threshold characteristics (Sections 2–6);

—to reveal the influence of parasitic recombination (recombination outside QDs) on the threshold characteristics (Sections 2–6);

—to determine how charge neutrality violation in QDs affects the threshold characteristics (Sections 3 and 4);

—to study the temperature dependence of the threshold current j_{th} and calculate the characteristic temperature T_0 of the laser (Section 4);

—to determine the influence of optical transitions from excited states in QDs on the threshold characteristics (Section 5);

—to study the effect of spatial hole burning (SHB) and the phenomenon of multimode generation (Section 6);

—to find ways of optimizing the QD laser structures in order to minimize j_{th} and raise T_0 and the threshold of multimode generation; to calculate the best possible characteristics of the laser (Sections 2–4, 6).

2. INHOMOGENEOUS LINE BROADENING AND THE THRESHOLD CURRENT DENSITY

The advantages of QD lasers over the QW lasers currently in use are due to the delta-function-like density of states in QDs. In the ideal case of identical QDs,

Achieving each of these advantages was the aim of research in the field of semiconductor lasers from the very beginning. For example, lasing in various spectral ranges in a continuous-wave (CW) mode at high temperature was one of the reasons for using heterostructure lasers instead of homojunction devices [16]. It should be noted that the low threshold currents of heterostructure lasers compared with homojunction devices were demonstrated at an early stage [17, 18].

the gain spectrum would also be a delta function. In real structures, there occurs inhomogeneous line broadening caused by the inevitable scatter of parameters (primarily, size) of QDs.[3] In structures with QDs fabricated by electron-beam lithography [29], this scatter is due to the "noise" of the lithographic process. Such fluctuations are also characteristic of QD ensembles formed via self-assembling in molecular-beam epitaxy [58] and metal-organic chemical vapor deposition. Inhomogeneous line broadening is a key factor limiting the characteristics of a QD laser. The dispersion of QD parameters and deviation of the gain spectrum from the ideal case adversely affect these characteristics by lowering the maximum gain, raising the threshold current, and making its temperature dependence more pronounced.[4] The advantages of QD structures can only be realized in the case of QDs that are sufficiently uniform in size and shape. Theoretical studies of QD lasers have been reported previously [59–61].[5] However, the question of how the threshold characteristics of a laser depend on QD size fluctuations, i.e., on the perfection of the laser structure, remained unanswered. This section is concerned with the effect of inhomogeneous broadening on the gain and threshold current density j_{th}. The effect of inhomogeneous broadening on the temperature dependence of j_{th} (i.e., on the characteristic temperature T_0 of a laser) and on the multimode generation threshold is considered, among other issues, in Sections 4 and 6, respectively.

2.1. Description of Structure and Main Processes. Lasing Threshold Condition

A separate confinement double heterojunction laser structure is considered (Fig. 2). The optical confinement layer (OCL) is created in the field region of the p–n junction. The active region, which is one or several QD layers, is created in the central part of the OCL along the longitudinal (wave propagation direction) and lateral directions in a planar cavity. Carriers are injected from wide-bandgap regions (claddings), which are the p- and n-regions of structure, in the transverse direction (direction perpendicular to the QD layer).

Together with the main process of band-to-band radiative recombination of electrons and holes in QDs, recombination in the OCL and capture of carriers into QDs and their thermal escape therefrom are consid-
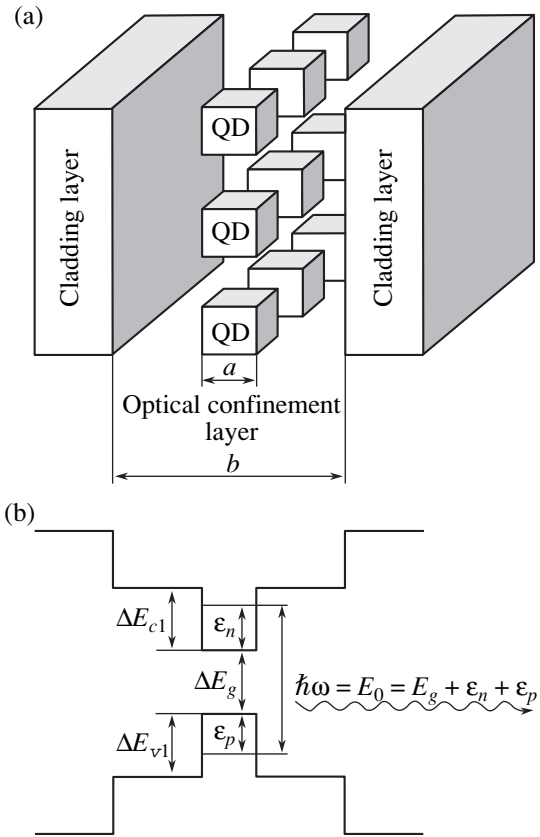

Fig. 2. (a) Schematic and (b) energy band diagram of a QD laser.

ered.[6] In studying the effect of SHB (Section 6), diffusion of free carriers in the OCL is also considered.

At and below the lasing threshold, the injection current goes into spontaneous recombination in QDs and the OCL. The lasing threshold is given by

$$g^m = \beta, \qquad (1)$$

where g^m is the peak value of the modal gain spectrum $g(E)$ which is the effective gain of the active layer with QDs, and β is the total loss in the system. The minimum injection current at which the lasing condition is satisfied is, by definition, the threshold current of a laser.

2.2. Gain and Current of Spontaneous Radiative Recombination

The general expressions for $g(E)$ and current density j of spontaneous recombination were given in [46].

Depending on temperature and carrier localization energies, two fundamentally different modes of QD fill-

---

[3] In this sense, QD lasers differ from solid-state lasers, in which the line broadening is due to inhomogeneities of the matrix in which emitting atoms are embedded, rather than to fluctuations in the spectra of these atoms.

[4] Homogeneous broadening, which occurs in QD lasers to the same extent as in any other type of semiconductor laser, is beyond the scope of this review.

[5] In [59], the gain and threshold current of a QD laser were analyzed without taking into account fluctuations in QD size. In [60], the gain was analyzed for a Gaussian size distribution of spherical QDs without relating it to the problem of threshold current. In [61], the threshold current was calculated for a single linewidth.

[6] In [46, 53], the photoexcitation of carriers from QD levels into the continuum states in the course of lasing is also considered. This photoexcitation is an analogue of light absorption by free carriers in the bulk material. It is shown that taking into account the light absorption in photoexcitation is only necessary at an extremely low loss ($\beta < 1$ cm^{-1}), e.g., in the case of long cavities.

ing with carriers, nonequilibrium and equilibrium, are possible.

2.2.1. Equilibrium QD filling (relatively high temperatures and/or shallow potential wells). If the characteristic times of thermal escape of carriers from QDs are shorter than the time of radiative recombination in QDs, $\tau_{n,p}^{esc} \ll \tau_{QD}$, carriers will be redistributed among QDs and a quasi-equilibrium distribution common to all the QDs will be established. The degrees (probabilities) of levels' filling in QDs will be specified by the Fermi–Dirac distribution function with electron and hole quasi-Fermi levels corresponding to a given current. By analogy with the Sah–Noyce–Shockley–Read carrier capture centers [62, 63]

$$\tau_n^{esc} = \frac{1}{\sigma_n v_n n_1}, \quad \tau_p^{esc} = \frac{1}{\sigma_p v_p p_1}, \quad (2)$$

where $\sigma_{n,p}$ are cross sections of electron and hole capture into QD levels, $v_{n,p}$ are thermal velocities, and n_1 and p_1 are given by

$$n_1 = N_c \exp\left(-\frac{\Delta E_{c1} - \varepsilon_n}{T}\right),$$
$$p_1 = N_v \exp\left(-\frac{\Delta E_{v1} - \varepsilon_p}{T}\right), \quad (3)$$

where $N_{c,v}$ are the effective densities of states in the conduction and valence bands; $\Delta E_{c1,v1}$, the band offsets at the QD–OCL interface; $\varepsilon_{n,p}$, the electron and hole energy levels in a mean-sized QD; and T, the temperature measured in energy units.

The condition for equilibrium filling of QDs has the form $T > T_g$, where

$$T_g = \max\left[\frac{\Delta E_{c1} - \varepsilon_n}{\ln(\sigma_n v_n N_c \tau_{QD})}, \frac{\Delta E_{v1} - \varepsilon_p}{\ln(\sigma_p v_p N_v \tau_{QD})}\right] \quad (4)$$

is the temperature boundary between the equilibrium and nonequilibrium QD filling modes. The temperature T_g becomes higher with increasing energies of carrier localization in QDs, $\Delta E_{c1,v1} - \varepsilon_{n,p}$, i.e., with wider bandgap material used as the OCL.

The temperature T_g depends on the QD size. This dependence is primarily due to the dependences of the energies of electron and hole levels, $\varepsilon_{n,p}$, on QD size. The processes of carrier capture/escape (and the corresponding capture cross sections $\sigma_{n,p}$) and carrier relaxation effects are also size dependent in low-dimensional systems.[7] Since, however, $\sigma_{n,p}$ appear in expression (4) for T_g as an argument of a logarithmic function,

___

[7] For example, LA-phonon-mediated relaxation of electrons may become ineffective with decreasing QD size [64, 65]. At the same time, Auger relaxation (associated with carrier–carrier interaction) may be rather effective and become the main mechanism in small QDs [66]. As first demonstrated in [67], relaxation processes in QDs are effectively rather fast, and the so-called bottleneck problem in QDs, mentioned in [64], is not too important.

their dependences on QD size will affect T_g to a lesser extent than do the dependences of $\varepsilon_{n,p}$.

The free carrier densities in the OCL are expressed in terms of the electron and hole level occupancies $f_{n,p}$ in a mean-sized QD as

$$n = n_1 \frac{f_n}{1 - f_n}, \quad p = p_1 \frac{f_p}{1 - f_p}. \quad (5)$$

In the case of a narrow QD size distribution $(\Delta\varepsilon)_{inhom} < T$ [$(\Delta\varepsilon)_{inhom}$ is the inhomogeneous line broadening] the current density and gain are given by

$$j = Z_L \frac{eN_S}{\tau_{QD}} f_n f_p + ebBn_1 p_1 \frac{f_n f_p}{(1 - f_n)(1 - f_p)}, \quad (6)$$

$$g(E) = g^{max}(f_n + f_p - 1)$$
$$\times \frac{w[(E_0 - E)/(q_n\varepsilon_n + q_p\varepsilon_p)]}{w(0)}, \quad (7)$$

where Z_L is the number of QD layers; N_S, the surface density of QDs in a layer; b, the OCL thickness; B, the radiative constant in the OCL (see expression (10) in [46]); E, the photon energy; w, the probability density of relative QD size fluctuations; $E_0 = E_g + \varepsilon_n + \varepsilon_p$, the transition energy in a QD of mean size a (Fig. 2); E_g, the bandgap of the QD material; and $q_{n,p} = -\partial\ln\varepsilon_{n,p}/\partial\ln a$, numerical constants.

The gain spectrum reproduces the curve for $w[(E_0 - E)/(q_n\varepsilon_n + q_p\varepsilon_p)]$ (Fig. 3a) scaled along the vertical axis with the factor $(f_n + f_p - 1)$, which is the population inversion in a mean-sized QD.

For the reciprocal of the spontaneous radiative recombination time for transitions from the electron energy level to the hole energy level in a QD, the following expression is obtained

$$\frac{1}{\tau_{QD}} = \frac{8}{3}\alpha\sqrt{\epsilon}\frac{E_0}{\hbar}\left(\frac{P}{\hbar c}\right)^2 I, \quad (8)$$

where $\alpha = e^2/\hbar c$ is the fine structure constant; ϵ, the dielectric constant of the material of the OCL; P, Kane's parameter[8] [68]; and I, the overlap integral of the electron and hole wave functions. For the structure considered in Section 2.3.2.3, $\tau_{QD} = 0.71$ ns.

The peak modal gain appearing in the lasing condition, which is reached at $E = E_0$, is given by

$$g^m = g^{max}(f_n + f_p - 1). \quad (9)$$

The quantity g^{max} is the maximum possible ("saturated") value of the peak modal gain. This value is reached when $f_{n,p}$ simultaneously take their maximum values, i.e., unity. The equation for g^{max} is as follows:

$$g^{max} = \frac{\xi}{4}\left(\frac{\lambda_0}{\sqrt{\epsilon}}\right)^2 \frac{1}{\tau_{QD}}\frac{\hbar}{(\Delta\varepsilon)_{inhom}}\frac{\Gamma}{a}Z_L N_S, \quad (10)$$

___

[8] This parameter can be conveniently used because of its weak dependence on the particular type of the material (see, e.g., [69]).

where ξ is a numerical constant (equal to $1/\pi$ and $1/\sqrt{2\pi}$ for Lorentzian and Gaussian QD size distributions, respectively); $\lambda_0 = 2\pi\hbar c/E_0$, the lasing wavelength; and Γ, the optical confinement factor in the transverse direction per QD layer [see Eq. (22) for Γ below].

The inhomogeneous line broadening appearing in (10) is given by

$$(\Delta\varepsilon)_{\text{inhom}} = (q_n\varepsilon_n + q_p\varepsilon_p)\delta, \qquad (11)$$

where δ is the root-mean-square (RMS) of relative QD size fluctuations.

The finite value of g^{max} is responsible for the experimentally observed gain saturation in a QD laser. Since $g^{\text{max}} \propto 1/(\Delta\varepsilon)_{\text{inhom}}$, controlling the uniformity of QD size is of fundamental importance for raising the gain.

In the case of a broad QD size distribution $[(\Delta\varepsilon)_{\text{inhom}} > T]$, the $g(E)$ spectrum gradually "fills" the $w[(E_0 - E)/(q_n\varepsilon_n + q_p\varepsilon_p)]$ curve as the pumping level increases (Fig. 3b).

The maximum cross section of stimulated emission in a QD, averaged over the line width, is given by

$$\sigma_{\text{QD}}^{\text{max}} = \frac{\xi}{4}\frac{\hbar}{(\Delta\varepsilon)_{\text{inhom}}}\frac{1}{\tau_{\text{QD}}}\left(\frac{\lambda_0}{\sqrt{\epsilon}}\right)^2. \qquad (12)$$

This expression passes exactly into the expression for the cross section of stimulated emission for an atom in a gas laser (see, e.g., [70]) if by $(\Delta\varepsilon)_{\text{inhom}}$ and τ_{QD} are understood, respectively, the Doppler line broadening and the intrinsic radiative lifetime for a transition in an atom.

The use of electron and hole level occupancies averaged over the QD ensemble assumes that the analysis is made in the mean field approximation. For the case of separate capture of electrons and holes into QDs with many levels (but provided that the numbers of electron and hole levels are equal), the approach regarding the capture and recombination of carriers as random processes [71] leads to a minor increase (by a factor of 5/4) in the recombination current in QDs, j_{QD}, given by the first term in (6). For the case of simultaneous capture of electrons and holes (i.e., electron–hole pairs), in which QDs are considered to be neutral, j_{QD} increases by a factor of 2 [71]. Such modifications of j_{QD} can be readily accounted for by including the above factors in Eq. (8) for the time of spontaneous recombination in QDs. In this case, the equation for j_{QD} remains unchanged.

2.2.2. Nonequilibrium QD filling (relatively low temperatures and/or deep potential wells). At $T < T_g$, in which case $\tau_{n,p}^{\text{esc}} \gg \tau_{\text{QD}}$, carriers recombine in those QDs into which they have been injected (having no time to move to other QDs). The mode of QD filling is nonequilibrium. Since equal numbers of carriers are injected into each QD initially, the level occupancies in
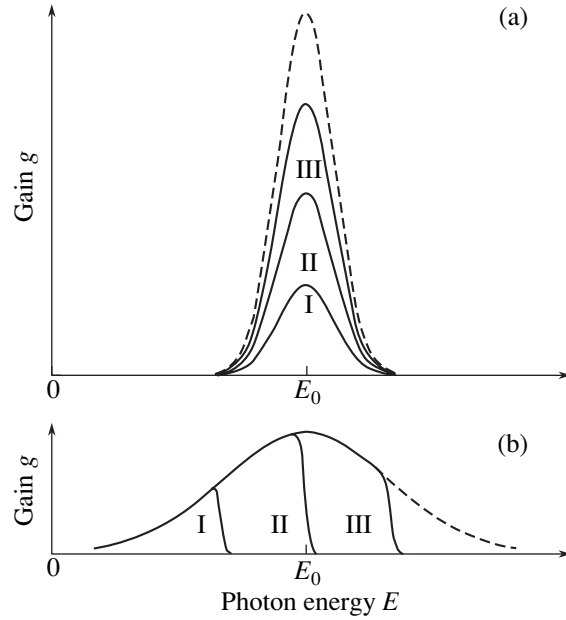
Fig. 3. Gain spectra: (a) equilibrium mode (small QD size dispersion) and nonequilibrium mode and (b) equilibrium mode (large QD size dispersion). The curves are numbered in order of increasing population inversion in QDs. Dashed lines correspond to inversion equal to unity. $E_0 = E_g + \varepsilon_n + \varepsilon_p$.

all the QDs will be the same.[9] As in the case of equilibrium QD filling and narrow QD size distribution, the $g(E)$ spectrum exactly reproduces the shape of this distribution (Fig. 3a), and the amplitude of this spectrum is proportional to the population inversion ($f_n + f_p - 1$). The contributions of all the QDs to lasing are the same; $g(E)$ and g^m are still given by expressions (7) and (9); the only difference is that the level occupancies for a mean-sized QD appear in the expressions in the equilibrium case, while the level occupancies are the same for all the QDs in the nonequilibrium case.

The free carrier densities in the OCL are given by

$$n = \frac{1}{\sigma_n v_n \tau_{\text{QD}}}\frac{f_n f_p}{1 - f_n}, \quad p = \frac{1}{\sigma_p v_p \tau_{\text{QD}}}\frac{f_n f_p}{1 - f_p}. \quad (13)$$

The current density of spontaneous radiative recombination is

$$j = Z_L\frac{eN_S}{\tau_{\text{QD}}}f_n f_p + \frac{ebB}{\sigma_n\sigma_p v_n v_p \tau_{\text{QD}}^2}\frac{f_n^2 f_p^2}{(1 - f_n)(1 - f_p)}. (14)$$

In the equilibrium mode, n and p are controlled by thermal escape from QDs and depend on T exponentially [see (5) and (3)]. In the nonequilibrium mode,

---

[9] The dependence of $\sigma_{n,p}$ on QD size leads to a similar dependence of $f_{n,p}$ in the nonequilibrium mode. However, this dependence is much weaker than that in the equilibrium mode; in the latter case, the QD size enters into the exponents of the Fermi filling factors [via the $\varepsilon_{n,p}(a)$ dependence].
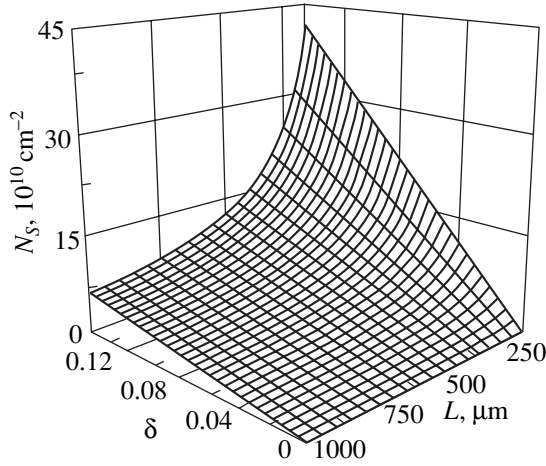
Fig. 4. Range of tolerable values of the surface density of QDs N_S, RMS of relative QD size fluctuations δ, and cavity length L (region above the surface).

n and p are controlled by capture into QDs. The temperature dependences of n and p are determined in this case by temperature dependences of capture cross sections $\sigma_{n,p}$ and thermal velocities $v_{n,p}$ and are weak compared with the exponential dependence in the equilibrium case.

The situation with an ensemble of QDs characterized by scatter in size and, consequently, in energy resembles that in heavily doped or amorphous semiconductors. The possibility that there is no quasi-equilibrium in the spatial distribution of carriers in semiconductors of this type was discussed in [72, 73]. In [74, 75], criteria for quasi-equilibrium and nonequilibrium carrier distribution in semiconductors with a large-scale potential profile associated with inhomogeneities were formulated (in relation to characteristic amplitude and period of the potential, drift length in the characteristic field of inhomogeneities, and temperature). Specifically, the conditions for uniform (strongly nonequilibrium) carrier distribution throughout a sample, which is an analogue of the uniform (strongly nonequilibrium) carrier distribution among QDs, were formulated.

2.3. Threshold Current Density and Laser Optimization

The dependence of the amplitude g^m of the gain spectrum on level occupancies in QDs should be used to determine the occupancies satisfying lasing condition (1). Substitution of these $f_{n,p}$ into the expression for j yields j_{th}.

2.3.1. Critical tolerable parameters. Lasing in QD structures is only possible in a certain range of tolerable parameters. This range is specified by the inequality $g^{max} \geq \beta$ (Fig. 4). The boundary of this region (the $g^{max} = \beta$ surface in Fig. 4) determines the critical tolerable parameters of the structure: the minimum surface

density of QDs N_S^{min}; the maximum RMS of relative QD size fluctuation δ^{max}; the minimum cavity length L^{min} (minimum and maximum OCL thicknesses also exist; see Section 2.3.2.2). The expressions for N_S^{min}, δ^{max}, and L^{min} are as follows:[10]

$$N_S^{min} = \frac{4}{\xi}\left(\frac{\sqrt{\epsilon}}{\lambda_0}\right)^2 \tau_{QD}\frac{(\Delta\epsilon)_{inhom}}{\hbar}\beta\frac{a}{\Gamma}\frac{1}{Z_L}, \qquad (15)$$

$$\delta^{max} = \frac{\xi}{4}\left(\frac{\lambda_0}{\sqrt{\epsilon}}\right)^2\frac{1}{\tau_{QD}}\frac{\Gamma}{a}\frac{\hbar}{(q_n\epsilon_n + q_p\epsilon_p)}\left(\ln\frac{1}{R}\right)^{-1}LZ_LN_S, (16)$$

$$L^{min} = \frac{4}{\xi}\left(\frac{\sqrt{\epsilon}}{\lambda_0}\right)^2 \tau_{QD}\frac{a}{\Gamma}\frac{(\Delta\epsilon)_{inhom}}{\hbar}\frac{1}{Z_L}\frac{1}{N_S}\ln\frac{1}{R}, \qquad (17)$$

where L is the cavity length, and R is the energy reflectivity of the mirrors (the role of mirrors in the conventional, stripe geometry of edge-emitting semiconductor lasers is played by cleaved edge facets of crystals). The more perfect the structure [i.e., the lower $(\Delta\epsilon)_{inhom}$] or the lower the loss, the smaller N_S^{min}. The denser the ensemble of QDs (i.e., the greater N_S) or the longer the cavity, the higher δ^{max}. The more perfect the structure or the denser the ensemble of QDs, the shorter L^{min}. For the structure considered in Section 2.3.2.3, in which $N_S = 6.1 \times 10^{10}$ cm^{-2}, $\delta = 0.025$ (5% fluctuations), $L = 500$ μm, and $R \approx 0.33$ (the so-called as-cleaved facets), the critical parameters have the following values: $N_S^{min} = 2.1 \times 10^{10}$ cm^{-2}, $\delta^{max} = 0.074$ (14.8% maximum tolerable fluctuations), and $L^{min} = 170$ μm.

With the use of the critical parameters, the lasing threshold condition can be represented as

$$f_n + f_p - 1 = \frac{\delta}{\delta^{max}}. \qquad (18)$$

Equation (18) yields the population inversion in a mean-sized QD, which is necessary for lasing at a given value of δ.

It can be seen from (18) that, with the parameter approaching its critical value, f_n and f_p simultaneously tend to unity; i.e., the electron and hole levels become fully occupied. Such a QD filling requires infinitely high free carrier densities in the OCL [see (5) and (13)] and, consequently, an infinitely high driving current (threshold current) j_{th} [see (6) and (14) and Fig. 5]. As shown in Section 6.3, the relative multimode generation threshold tends to zero (see Fig. 5, insets), which means that the number of simultaneously generated cavity modes grows infinitely.

Determining the level occupancies in QDs and the threshold current requires, in addition to (18), one more equation. Sections 2.3.2 and 2.3.3 consider the case of a symmetric structure in which this equation is the

---

[10]Below, the internal loss is disregarded in comparison with the mirror loss, and, accordingly, it is assumed that $\beta = (1/L)\ln(1/R)$.

charge neutrality condition in a QD: $f_n = f_p$. Combined with Eq. (18), this gives

$$f_{n,p} = \frac{1}{2}\left(1 + \frac{\delta}{\delta^{max}}\right). \qquad (19)$$

In Eqs. (18) and (19), δ/δ^{max} can be equivalently replaced with N_S^{min}/N_S or L^{min}/L.

The possibility of lasing at a finite level of threshold pumping (threshold current in the case of injection lasers) in only a limited range of structure parameters is a property common to all types of lasers. The particular practical relevance of this issue for QD lasers is due to the strong sensitivity of their characteristics to structure parameters and the need to adjust these parameters accurately.

2.3.2. Equilibrium filling of QDs and narrow QD size distribution.

2.3.2.1. Dependence of threshold current density on the surface density and size dispersion of QDs and on cavity length. The threshold current density as a function of δ is given by[11]

$$j_{th}(\delta) = \frac{1}{4}\frac{eN_S}{\tau_{QD}}(1 + \delta/\delta^{max})^2 + ebBn_1p_1\frac{(1 + \delta/\delta^{max})^2}{(1 - \delta/\delta^{max})^2}. \qquad (20)$$

Equation (20) represents j_{th} as a function of N_S (or L) if δ/δ^{max} is replaced with N_S^{min}/N_S (or L^{min}/L).

The dependence of j_{th} on N_S is nonmonotonic (Fig. 5a). At $N_S \longrightarrow N_S^{min}$, the recombination current in the OCL $j_{OCL} \longrightarrow \infty$ [second term in (6) and (20)]. If, however, $N_S \longrightarrow \infty$, then the recombination current in QDs j_{QD} tends to infinity [first term in (6) and (20)]. This is because, at $N_S \longrightarrow \infty$, $f_{n,p}$ tends to a finite, rather than zero, value equal to 1/2 [see (19)]; thus, on average one electron and one hole must be present in each QD in order to provide lasing, which requires an infinitely high pumping level.

As $\delta \longrightarrow 0$ or $L \longrightarrow \infty$ (Figs. 5b, 5c), j_{th} decreases and tends to the transparency current (inversion current, i.e., current at $f_n + f_p - 1 = 0$) density:

$$j_{tr} = \frac{1}{4}\frac{eN_S}{\tau_{QD}} + ebBn_1p_1. \qquad (21)$$

At $\delta \longrightarrow \delta^{max}$ or $L \longrightarrow L^{min}$, $j_{th} \longrightarrow \infty$ (Figs. 5b, 5c). An indefinite rise in j_{th} as QD size dispersion increases and reaches a certain value (Fig. 5b) has been observed experimentally [25].

2.3.2.2. Optical confinement factor and dependence of threshold current density on OCL thickness.

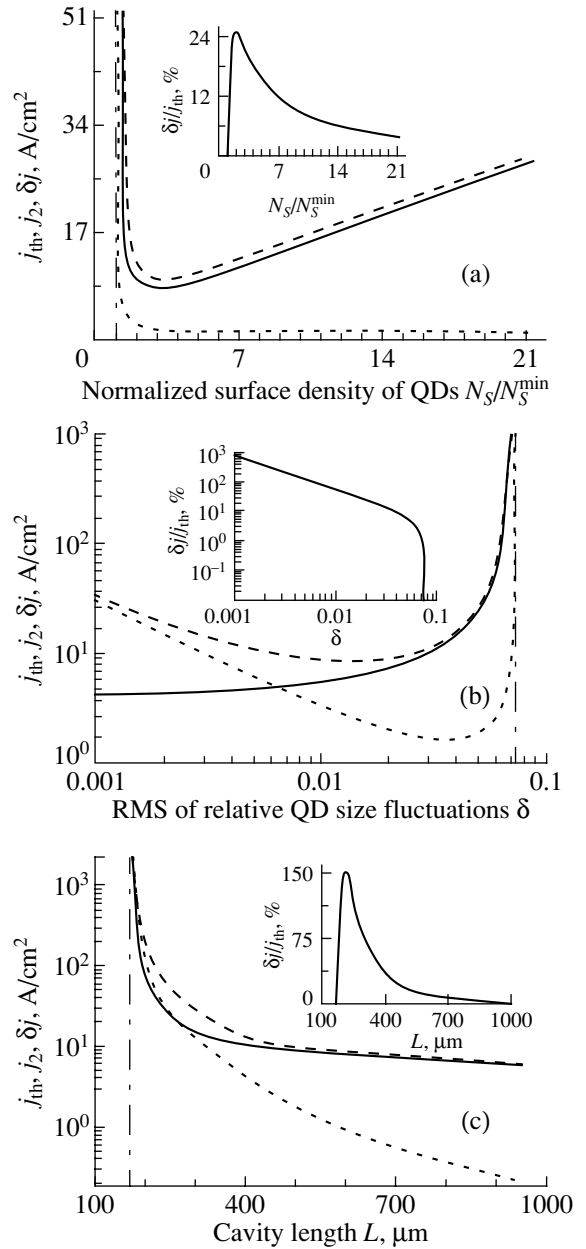[11]Henceforth, only a structure with a single layer of QDs ($Z_L = 1$) is considered.

Fig. 5. Threshold current densities j_{th} for the main mode (solid line) and j_2 for the next mode (dashed line), and the multimode generation threshold δj (dotted line) vs. (a) surface density of QDs, (b) RMS of relative QD size fluctuations, and (c) cavity length. Insets: similar dependences for the relative multimode generation threshold $\delta j/j_{th}$.

The optical confinement factor in the active layer of thickness a (in the QD layer) is given by [46]

$$\Gamma = \frac{a}{b/2 + 1/\gamma}, \qquad (22)$$

where $\gamma = \sqrt{K^2 - \epsilon' E_0^2/\hbar^2 c^2}$; ϵ' is the dielectric constant of the material of the claddings; and K is the propagation constant found from the dispersion equation
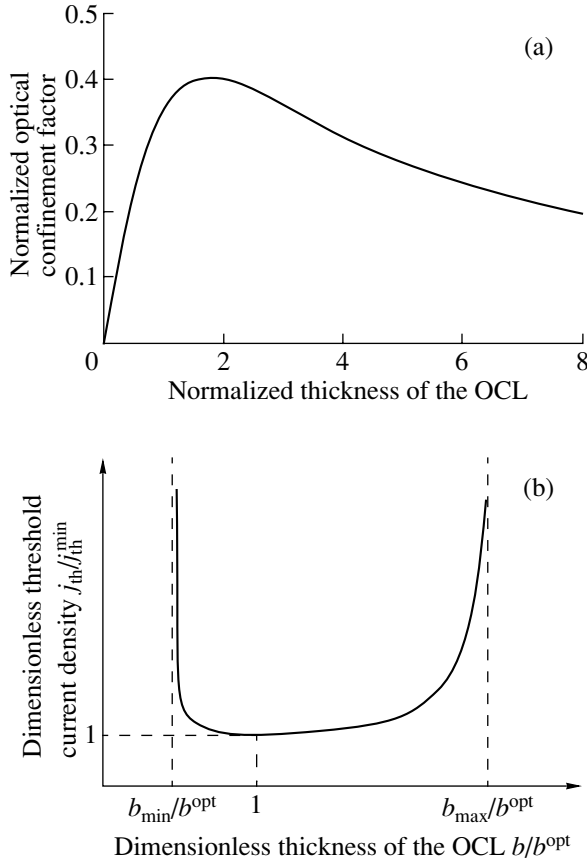
Fig. 6. (a) Universal dependence of the normalized optical confinement factor on normalized OCL thickness and (b) dependence of dimensionless threshold current density on dimensionless OCL thickness.

$\tan(\chi b/2) = \gamma/\chi$, in which $\chi = \sqrt{\epsilon E_0^2/\hbar^2 c^2 - K^2}$. The values of K, χ, and γ depend on b.

Figure 6a presents in a universal form the dependence of the normalized optical confinement factor $\Gamma/(a/b_0)$ on the normalized OCL thickness b/b_0. The characteristic thickness b_0, to which the OCL thickness is normalized, is

$$b_0 = \frac{\lambda_0}{2\pi\sqrt{\epsilon - \epsilon'}}. \qquad (23)$$

The dependence of Γ on b has a maximum, $\Gamma/(a/b_0) \approx 0.406$, at $b/b_0 \approx 1.739$ (for more detail, see [46]).

In addition to the explicit dependence on b in expression (20), the dependence of j_{th} on b is also determined by the dependence $\Gamma(b)$ appearing in this expression via Eq. (16) for $\delta^{\max}$. In view of the nonmonotonic dependence of Γ on b, the dependence of j_{th} on b, as well as on N_S, exhibits nonmonotonic behavior (Fig. 6b). The quantities $b_{\min}$ and $b_{\max}$ are the minimum and maximum tolerable OCL thicknesses, which determine the bounds for the range of b within which lasing is possible.

In the general case of $f_n \ne f_p$ (Sections 3 and 4), the run of the dependence of j_{th} on structure parameters is close to that for a symmetric structure.

2.3.2.3. Laser optimization. It can be seen from Figs. 5a and 6b that there exist optimum values of N_S and b for which j_{th} is at a minimum. It was shown in [46, 47] that for any device design, i.e., an arbitrary relationship between f_n and f_p, the minimum threshold current density $j_{\mathrm{th}}^{\min} = j_{\mathrm{th}}(N_S^{\mathrm{opt}}, b^{\mathrm{opt}})$ is given in a universal form by the equation

$$j_{\mathrm{th}}^{\min} = eb^{\mathrm{opt}} B n_1 p_1 \left[1 + \sqrt{\frac{a}{b^{\mathrm{opt}}\Gamma(b^{\mathrm{opt}})} s} \right]^2, \qquad (24)$$

where the dimensionless parameter s is determined by the ratio of the rate of stimulated transitions in a QD at the lasing threshold to that of spontaneous transitions in the OCL at the transparency threshold

$$s = \frac{(4/\xi)(\sqrt{\epsilon}/\lambda_0)^2 [(\Delta\epsilon)_{\mathrm{inhom}}/\hbar]\beta}{B n_1 p_1}. \qquad (25)$$

The optimum OCL thickness b^{opt} appearing in (24) is also a universal function of s and can be found from the equation

$$\left(\frac{\gamma^{\mathrm{opt}} b^{\mathrm{opt}}}{1 + \gamma^{\mathrm{opt}} b^{\mathrm{opt}}/2} \right)^{1/2} \left[\frac{(\chi^{\mathrm{opt}}/\gamma^{\mathrm{opt}})^2}{1 + \gamma^{\mathrm{opt}} b^{\mathrm{opt}}/2} - 1 \right] = \frac{2}{\sqrt{s}}, \qquad (26)$$

where $\gamma^{\mathrm{opt}} = \gamma(b^{\mathrm{opt}})$, $\chi^{\mathrm{opt}} = \chi(b^{\mathrm{opt}})$.

In contrast to $j_{\mathrm{th}}^{\min}$ and b^{opt}, the optimum surface density of QDs depends on the design of the device. In the case of a symmetric structure [see (19)], N_S^{opt} is also a function of s:

$$N_S^{\mathrm{opt}} = N_S^{\min}(b^{\mathrm{opt}}) \left\{ 1 + 2\sqrt{\frac{b^{\mathrm{opt}}\Gamma(b^{\mathrm{opt}})}{a}\frac{1}{s}} \right. $$
$$\left. + \sqrt{\left[1 + 2\sqrt{\frac{b^{\mathrm{opt}}\Gamma(b^{\mathrm{opt}})}{a}\frac{1}{s}} \right]^2 - 1} \right\}. \qquad (27)$$

Figure 7 shows universal dependences of the following normalized quantities on the parameter s: the optimum OCL thickness b^{opt}/b_0, optical confinement factor $\Gamma(b^{\mathrm{opt}})/(a/b_0)$, optimum surface density of QDs $(N_S^{\mathrm{opt}}/\tau_{\mathrm{QD}})/(b_0 B n_1 p_1)$, and minimum threshold current density $(j_{\mathrm{th}}^{\min}/e)/(b_0 B n_1 p_1)$ [the characteristic thickness b_0 is given by Eq. (23)].
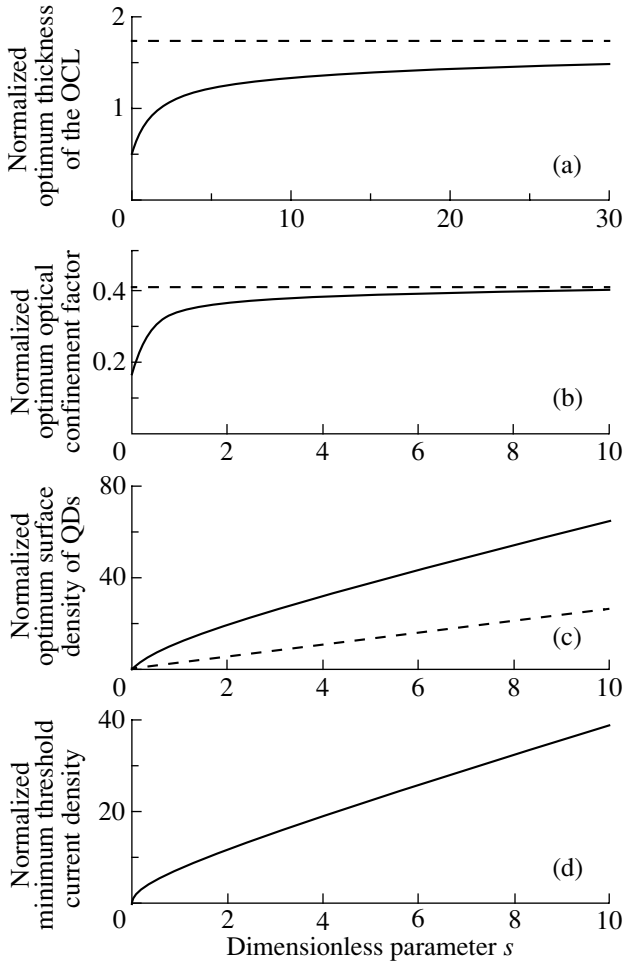
Fig. 7. Normalized quantities as universal functions of dimensionless parameter s. (a) Optimum OCL thickness; the dashed horizontal line represents the asymptote at $s \longrightarrow \infty$. (b) Optical confinement factor (at $b = b^{\mathrm{opt}}$); the dashed horizontal line is the asymptote at $s \longrightarrow \infty$. (c) Optimum surface density of QDs; the dashed line is the minimum surface density of QDs (at $b = b^{\mathrm{opt}}$). (d) Minimum threshold current density.
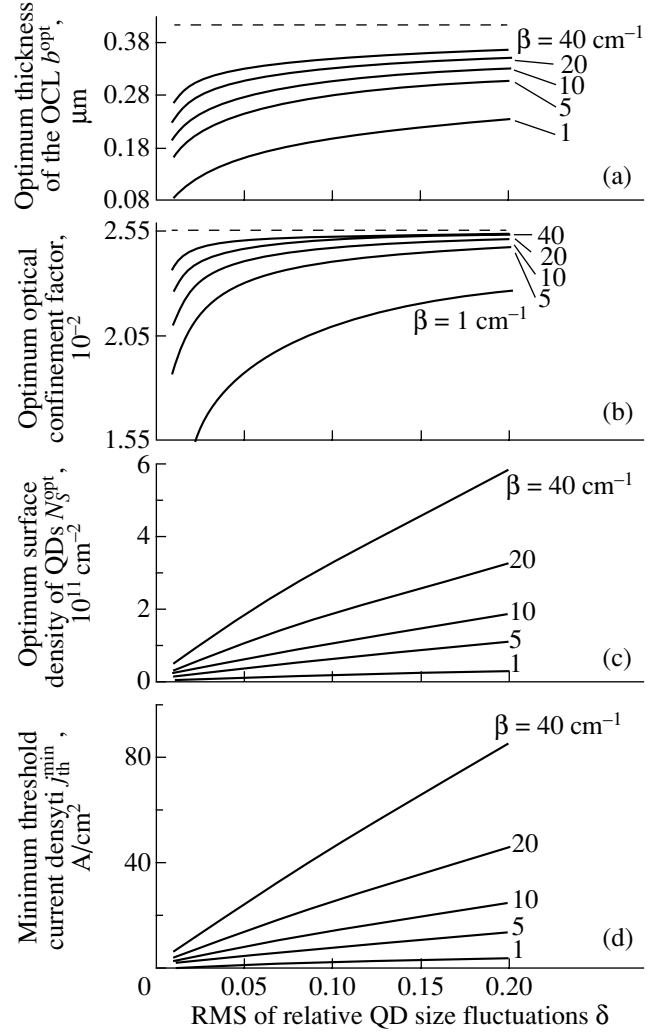

Fig. 8. (a) Optimum OCL thickness, (b) optical confinement factor at $b = b^{\mathrm{opt}}$, (c) optimum surface density of QDs, and (d) minimum threshold current density vs. RMS of relative QD size fluctuations at different loss β for a $\mathrm{Ga}_x\mathrm{In}_{1-x}\mathrm{As}_y\mathrm{P}_{1-y}/\mathrm{InP}$ heterostructure lasing at about 1.55 μm. Dashed lines: (a, b) asymptotes of b^{opt} and $\Gamma(b^{\mathrm{opt}})$ at $\beta \longrightarrow \infty$.

At relatively large fluctuations in QD size and/or high loss ($s \gg 1$), $j_{\mathrm{th}}^{\mathrm{min}}$ is determined by the rate of stimulated transitions in QDs at the lasing threshold:

$$j_{\mathrm{th}}^{\mathrm{min}} \approx 1.569 \frac{1}{\xi} e \frac{\epsilon}{\sqrt{\epsilon - \epsilon'}} \frac{\beta}{\lambda_0} \frac{(\Delta\epsilon)_{\mathrm{inhom}}}{\hbar}. \qquad (28)$$

At relatively narrow scatter of QD sizes and/or low loss ($s \ll 1$), $j_{\mathrm{th}}^{\mathrm{min}}$ is determined by the geometric mean of the rate of stimulated transitions in QDs at the lasing threshold and that of spontaneous transitions in the OCL at the transparency threshold:

$$j_{\mathrm{th}}^{\mathrm{min}} = 4\sqrt{2} \frac{1}{\pi} e \left[\frac{1}{\xi} \frac{\epsilon}{\epsilon - \epsilon'} B n_1 p_1 \beta \frac{(\Delta\epsilon)_{\mathrm{inhom}}}{\hbar} \right]^{1/2}. \qquad (29)$$

It can be seen from (28) and (29) that, with decreasing $(\Delta\epsilon)_{\mathrm{inhom}}$ or β, the dependence of $j_{\mathrm{th}}^{\mathrm{min}}$ on these parameters changes from linear to square root (Figs. 7, 8).

Using the universal dependences of the normalized quantities on the parameter s (Fig. 7), it is easy to pass to dependences of the corresponding dimensional quantities on each of the factors determining this parameter. The results obtained in the analysis and in comparison with commercial QW lasers are illustrated using a structure based on a $\mathrm{Ga}_x\mathrm{In}_{1-x}\mathrm{As}_y\mathrm{P}_{1-y}/\mathrm{InP}$ heterojunction that emits near 1.55 μm (one of the most important wavelengths for telecommunications). InP, $\mathrm{Ga}_{0.21}\mathrm{In}_{0.79}\mathrm{As}_{0.46}\mathrm{P}_{0.54}$, and $\mathrm{Ga}_{0.47}\mathrm{In}_{0.53}\mathrm{As}$ are the materials of the claddings, OCL, and QDs, respectively. The corresponding dependences are shown in Fig. 8. At room temperature, cavity loss $\beta = 10$ cm^{-1}, and 10%

QD size fluctuations ($\delta = 0.05$) (such a size scatter is typical; see, e.g., [58, 76, 77]),

$$N_S^{\text{opt}} \approx 6.2 \times 10^{10} \text{ cm}^{-2}, \quad j_{\text{th}}^{\text{min}} \approx 8.3 \text{ A/cm}^2. \quad (30)$$

This value of $j_{\text{th}}^{\text{min}}$ is more than an order of magnitude lower than that in QW lasers with the same loss.

Taking into account nonradiative processes in the OCL leads to a certain increase in j_{th}. It is clear that the correction due to Auger processes should be small at low j_{th}. Using the method for estimating the lifetime of carriers in the OCL in relation to their density described in [61] (this method takes into account all the possible nonradiative recombination processes) will lead to a slight increase in j_{th} (from 8.3 to 9.5 A/cm² for the structure under consideration).

2.3.3. Nonequilibrium filling of QDs. In this case, the $f_{n,p}$ required for lasing are still determined by expression (19). Substitution of (19) into (14) yields j_{th} as a function of δ:

$$j_{\text{th}}(\delta) = \frac{1}{4} \frac{e N_S}{\tau_{\text{QD}}} \left(1 + \frac{\delta}{\delta^{\text{max}}} \right)^2$$
$$+ \frac{1}{4} \frac{ebB}{\sigma_n \sigma_p v_n v_p \tau_{\text{QD}}^2} \frac{(1 + \delta/\delta^{\text{max}})^4}{(1 - \delta/\delta^{\text{max}})^2}. \quad (31)$$

All that has been said above about how j_{th} depends on N_S, δ, L, and b (Figs. 5, 6) remains valid in this case, too. In the limit of large δ and/or β, $j_{\text{th}}^{\text{min}}$ is still given by Eq. (28).

At small δ and/or β, the minimum threshold current density

$$j_{\text{th}}^{\text{min}} \approx 6.505 \frac{1}{2\pi} \frac{e}{\tau_{\text{QD}}} \left[\frac{1}{\xi} \frac{\epsilon}{\epsilon - \epsilon'} \frac{B}{\sigma_n \sigma_p v_n v_p} \beta \frac{(\Delta\varepsilon)_{\text{inhom}}}{\hbar} \right]^{1/2} (32)$$

and depends on temperature only slightly (via the dependences of $\sigma_{n,p}$ and $v_{n,p}$ on T). Thus, in going from the equilibrium QD filling to the nonequilibrium case with decreasing temperature, $j_{\text{th}}^{\text{min}}$ falls more slowly than would follow from (29) and tends to a constant value. The true value of $j_{\text{th}}^{\text{min}}$ at low T [Eq. (32)] considerably exceeds the value yielded by Eq. (29) for the same temperature [the latter value is, as can be seen from (29) and expressions (3) for n_1 and p_1, exponentially small at low T].

3. VIOLATION OF CHARGE NEUTRALITY IN QDs

Local charge neutrality holds in the QWs of QW laser structures [78, 79]. QD structures differ fundamentally in this regard from QW structures. This difference is due to the low effective capacitance of the QD layer compared with the QW. Neutrality violation in QWs is suppressed by the high well capacitance. The capacitance of a QD layer, limited by the surface density of QDs, whose typical values are one and a half to two orders of magnitude lower than the 2D density of carriers in the QW, is much lower than the QW capacitance. Because of this circumstance, the electric field arising in the case of neutrality violation in QDs is low. It was shown in [47] that the electron and hole level occupancies in QDs are different; i.e., the QDs are, indeed, charged. The neutrality violation strongly affects the magnitude and the temperature dependence of j_{th}.

A second [in addition to (18)] equation relating f_n and f_p, which is required to calculate the recombination current density, can be written as

$$f_p - f_n = \Delta. \quad (33)$$

The particular form of the function Δ depends on the design of the device, i.e., on the spatial distribution of donor and acceptor impurities, conduction and valence band offsets, and the position of the QD layer in the OCL. Using (18) and (33), the occupancies can be written as

$$f_n = \frac{1}{2} + \frac{1}{2} \frac{N_S^{\text{min}}}{N_S} \text{sgn}(g^m) - \frac{1}{2}\Delta,$$
$$f_p = \frac{1}{2} + \frac{1}{2} \frac{N_S^{\text{min}}}{N_S} \text{sgn}(g^m) + \frac{1}{2}\Delta, \quad (34)$$

where N_S^{min} is yielded by Eq. (15) in which β is replaced with $|g^m|$. With the aim of studying the dependence of the gain on the injection current (Section 3.4), both positive (above the transparency threshold) and negative (below the transparency threshold) values of g^m are considered here.

In the general case, $\Delta = 0$ both at $N_S = N_S^{\text{min}}$ and at $N_S \longrightarrow \infty$. The first condition is apparent from the following considerations: at $N_S = N_S^{\text{min}}$, $f_n = f_p = 1$ at $g^m > 0$ and $f_n = f_p = 0$ at $g^m < 0$. The second condition corresponds to a transition from a QD layer to a QW in which the local neutrality holds.

3.1. QD Layer in p–i–n Heterojunction

A self-consistent problem concerning the distribution of the electrostatic potential is solved. The OCL is the i-region of the structure. The step in the field strength at the QD layer is controlled by its surface charge. It has been found for Δ [47] that

$$\Delta = \frac{v + \aleph_{\text{as}}}{\alpha}, \quad (35)$$

where v is a root of the equation

$$-v - \aleph_{\text{as}} = \alpha \frac{\sinh v}{\cosh[(V - E_0)/2T] + \cosh v}. \quad (36)$$
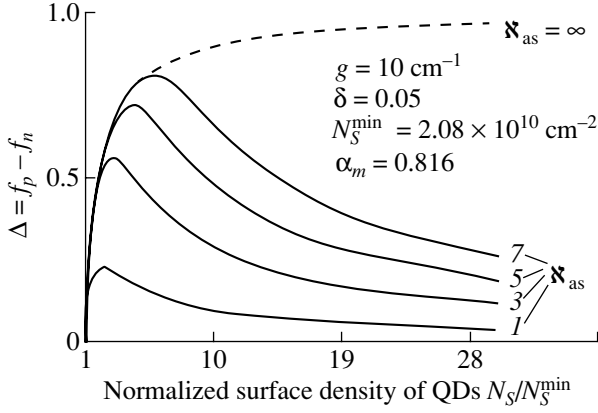
Fig. 9. Difference between hole and electron level occupancies in QD vs. normalized surface density of QDs at different values of the asymmetry parameter $\aleph_{as}$.

Fig. 10. Threshold current density vs. normalized surface density of QDs. The inclined line represents the transparency current density at $N_S \longrightarrow \infty$. Inset: relative difference of true N_S^{opt} and that calculated on the assumption of charge neutrality [see (27)] vs. $\aleph_{as}$.

The dimensionless asymmetry parameter $\aleph_{as}$ and the parameter α, which control $\Delta = f_p - f_n$, i.e., the QD charge, are given by

$$\aleph_{as} = \frac{(\Delta E_v - \varepsilon_p + F_p) - (\Delta E_c - \varepsilon_n + F_n)}{2T},$$

$$\alpha = \frac{e^2 N_S / 4T}{\epsilon_s / 4\pi b}, \tag{37}$$

where V is the voltage (in energy units) applied to the structure; $\Delta E_{c,v} = \Delta E_{c,v,1} + \Delta E_{c,v,2}$; $\Delta E_{c,v,1}$ and $\Delta E_{c,v,2}$ are the band offsets at the QD–OCL and OCL–cladding heterointerfaces, respectively; $F_{n,p}$, the quasi-Fermi levels in the n- and p-claddings, respectively, far from the heterointerfaces with the OCL (reckoned from the band edges in the cladding layers); and ϵ_s, the static dielectric constant.

The parameter $\aleph_{as}$ is determined by the difference (asymmetry) between the electron and hole parameters of the structure. The greater $\aleph_{as}$, the higher Δ (Fig. 9).

There exists a certain value of N_S at which Δ is at a maximum (Fig. 9). It can be seen from the figure how strong the neutrality violation is: $\Delta = f_p - f_n$ is comparable with f_n and f_p themselves.

The neutrality criterion in QDs is $\aleph_{as} = 0$. Because of the temperature dependence of $F_{n,p}$, the neutrality criterion depends on T. This means that (at given parameters) the QDs can be neutral only at a single temperature.

The parameter α_m (value of α at $N_S = N_S^{min}$) determines the ratio of the differential capacitance of a QD layer to the capacitance of the OCL [47]. The smaller α_m, the greater Δ; i.e., Δ grows with decreasing capacitance of the QD layer. It is the value of the capacitance that gives rise to the strong difference between the QD layer and the QW as regards the charge neutrality.
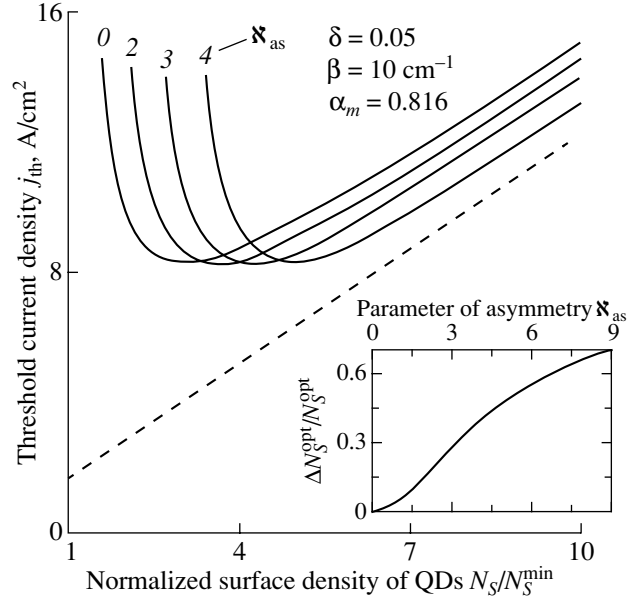
The minimum threshold current density is given by the universal equation (24) and is independent of the QD charge, whereas the neutrality violation strongly affects the optimum surface density of QDs at which j_{th} is at a minimum: N_S^{opt} grows as the neutrality violation becomes more pronounced (Fig. 10).

3.2. Transparency Current Density

The injection current at which the population inversion in the active region is zero ($f_n + f_p - 1 = 0$) and, accordingly, the gain is zero ($g^m = 0$) is, by definition, the inversion or transparency current.

From (34) for the level occupancies at the transparency threshold we have

$$f_n = \frac{1}{2} - \frac{\Delta}{2}, \quad f_p = \frac{1}{2} + \frac{\Delta}{2}, \tag{38}$$

where Δ is found from Eqs. (35) and (36) at voltage $V = E_0 = E_g + \varepsilon_n + \varepsilon_p$ corresponding to the transparency threshold. Substituting (38) into (6) yields for the transparency current density

$$j_{tr} = \frac{1}{4} \frac{eN_S}{\tau_{QD}} [1 - \Delta^2(N_S)] + ebBn_1 p_1. \tag{39}$$
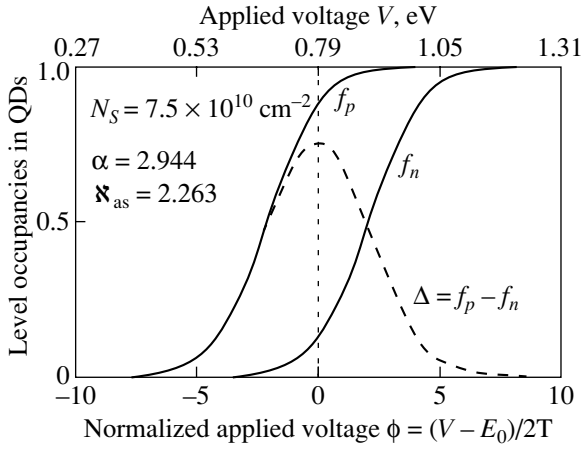
Fig. 11. Electron and hole level occupancies in QDs (solid lines) and difference of the occupancies (dashed line) vs. applied voltage. Vertical dotted line represents the transparency threshold.

Fig. 12. I–V characteristic. Inset: current density associated with recombination–generation in QDs.

Comparing (39) with expression (21) for neutral QDs ($\Delta = 0$) shows that neutrality violation leads to a decrease in j_{tr}.

3.3. Current–Voltage (I–V) Characteristic

The dependences of $f_{n,p}$ and Δ on applied voltage V are shown in Fig. 11. At the transparency threshold ($V = E_0$), Δ reaches its maximum value; this occurs because the differential capacitance of the QD layer is at a minimum at the transparency threshold [47]. Using the dependences of $f_{n,p}$ on V, the I–V characteristic of a laser can be calculated (Fig. 12):

$$j = \frac{eN_S}{\tau_{QD}}(f_n f_p - f_n f_p|_{V=0}) + ebBn_i^2\left[\exp\left(\frac{V}{T}\right) - 1\right], \tag{40}$$

where n_i is the intrinsic carrier density in the OCL. The type of voltage dependence of the second term in (40), which is the recombination–generation current density in the OCL, is typical of bimolecular (quadratic in carrier density) recombination.

3.4. Level Occupancies in a QD and Gain as Functions of Injection Current Density

Figure 13 shows dependences of $f_{n,p}$ on the injection current density. These curves for QD lasers are analogues of curves describing the dependence of the carrier density in the active region on current density for QW lasers or bulk lasers.

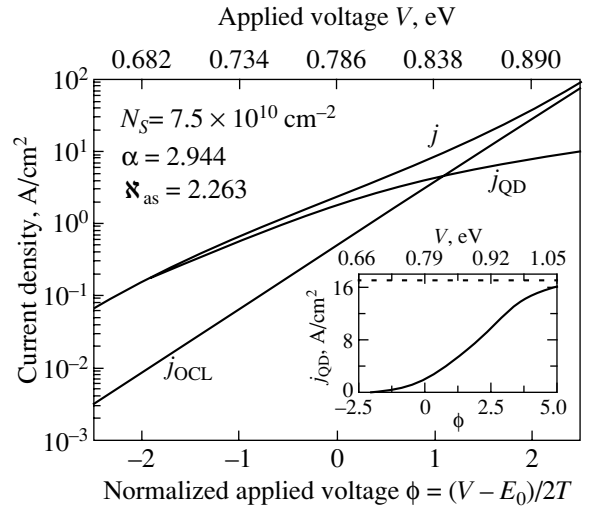One more important characteristic of a semiconductor laser is the dependence of the peak modal gain g^m on

the injection current density j. For a QD laser, this dependence (Fig. 14) is found from the equation

$$j(g^m) = \frac{1}{4}\frac{eN_S}{\tau_{QD}}\left[\left(1 + \frac{g^m}{g^{max}}\right)^2 - \Delta^2\left(\frac{g^m}{g^{max}}\right)\right]$$
$$+ ebBn_1p_1\frac{(1 + g^m/g^{max})^2 - \Delta^2(g^m/g^{max})}{(1 - g^m/g^{max})^2 - \Delta^2(g^m/g^{max})}, \tag{41}$$

where g^{max} is given by Eq. (10). At $g^m = \beta$, Eq. (41) yields j_{th} as a function of loss. As noted in Section 3.3, the function $\Delta(g^m/g^{max})$ has a maximum at the transparency threshold $g^m = 0$. With increasing j, g^m tends to a constant value (saturates). Nevertheless, the injection currents necessary to reach values of g^m equal to typical loss β (up to several tens of cm^{-1}) are much lower than those for a laser with a single or multiple QWs.
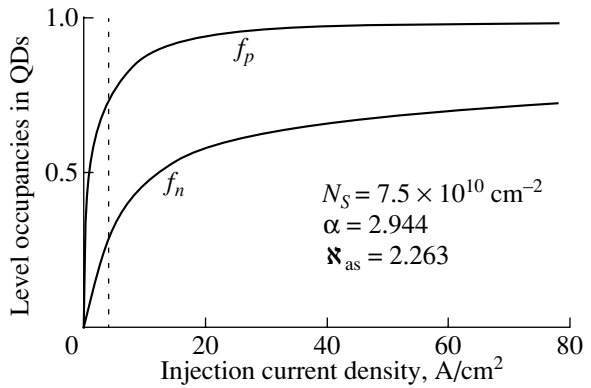

Fig. 13. Electron and hole level occupancies in QDs vs. injection current density. Vertical dotted line represents the transparency threshold, at which the difference $f_p - f_n$ is at a maximum.

4. TEMPERATURE DEPENDENCE
OF THRESHOLD CURRENT

Commercial QW lasers based on the InGaAsP/InP system, which are presently used in telecommunications, have threshold currents with poor temperature stability [79–81] (the characteristic temperature T_0 of lasers of this kind does not exceed 90 K). A highly important advantage that can be achieved in QD lasers is the extremely weak temperature dependence of the threshold current. In the ideal case, j_{th} of a QD laser would be temperature independent and, consequently, T_0 would be infinitely high [15]. This would occur if the whole injection current went into recombination in the QDs and neutrality in the QDs held. In reality, in all diode laser designs QDs are embedded in a conducting material (OCL or barrier regions) into which carriers are injected from the contact regions and then find their way into QDs.[12] Carrier recombination in the OCL gives rise to an additional component of j_{th}. This component (j_{OCL}), which is associated with thermal escape of carriers from QDs, depends on T exponentially. It is this component that is responsible for the temperature dependence of j_{th} in a QD laser at relatively high T. This was confirmed in the first injection QD laser to be developed [20]. As technology reaches a level that allows structures with perfect QD ensembles to be grown and thereby makes it possible to control to a considerable extent inhomogeneous line broadening, it is the thermal escape of carriers from QDs that may become the main problem of laser design.

It can be seen from condition (18) that the population inversion is independent of T at the lasing threshold. Assuming neutrality in a QD ($f_n = f_p$), we would immediately obtain temperature-independent $f_{n,p}$ [see, (19)]. In this case, the threshold current density component associated with recombination in QDs, j_{QD}, would be temperature independent. One important manifestation of charge neutrality violation is the temperature dependence of the electron and hole level occupancies in QDs and, consequently, the temperature dependence of j_{QD}. Thus, even if recombination outside QDs is completely suppressed, a temperature dependence of j_{th} exists caused by neutrality violation in QDs. It is this effect that leads to a finite value of T_0, observed at relatively low T [20], at which the thermal escape of carriers from QDs and recombination outside QDs are virtually completely suppressed.

Thus, the temperature dependence of the components associated with recombination in the OCL and QDs means that the threshold current in a real QD laser is temperature dependent, especially at high T. Consequently, the characteristic temperature T_0 is finite. This was first observed experimentally in [20].

Fig. 14. Peak modal gain vs. injection current density at different N_S.

As discussed above (Section 2), the modes of QD filling with carriers may be equilibrium or nonequilibrium, depending on temperature and carrier localization energies. At $T < T_g$ (nonequilibrium filling), where T_g is given by Eq. (4), there is no temperature dependence of the free carrier density in the OCL,[13] and, consequently, j_{th} is temperature independent. At $T > T_g$ (equilibrium filling), j_{th} depends on T. Thus, the temperature dependence of the threshold current in QD lasers fundamentally differs from that for lasers with a bulk active region and QW lasers. Such a temperature dependence was observed experimentally in the first injection QD laser [20]: j_{th} remained virtually unchanged (80 A/cm^2) as the temperature increased to 180 K; the characteristic temperature for this temperature range was very high ($T_0 = 380$ K). As T increased above 180 K, j_{th} demonstrated thermally activated growth, with the activation energy in good agreement with the estimates of carrier localization energies in QDs, which confirmed that the rise in the threshold current is, indeed, associated with the thermal escape of carriers from QDs.

In this section, a detailed quantitative analysis of the temperature dependence of j_{th} is presented and the characteristic temperature T_0 in the equilibrium mode is calculated.

4.1. Threshold Current Components

The components of the threshold current density are given by

$$j_{QD} = \frac{eN_S}{\tau_{QD}} f_n f_p, \qquad (42)$$

---

[12]The use of QDs in insulating (e.g., glass) matrices is promising only for creating devices with optical pumping because of the impossibility in principle of current injection in this case.
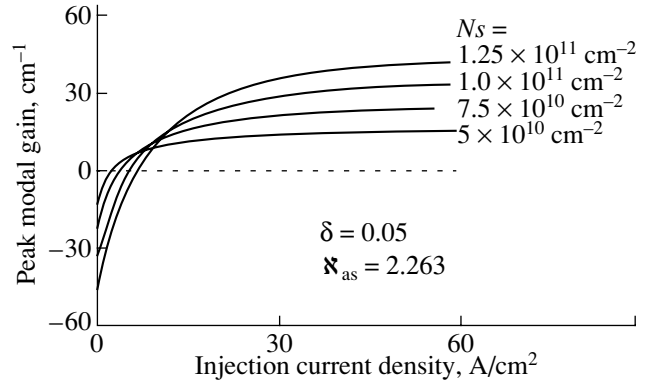
[13]To be more precise, there is a weak temperature dependence of n and p, which is due to the similar dependences of the cross sections of carrier capture into QDs ($\sigma_{n,p}$) and thermal velocities ($v_{n,p}$) [see (13)].
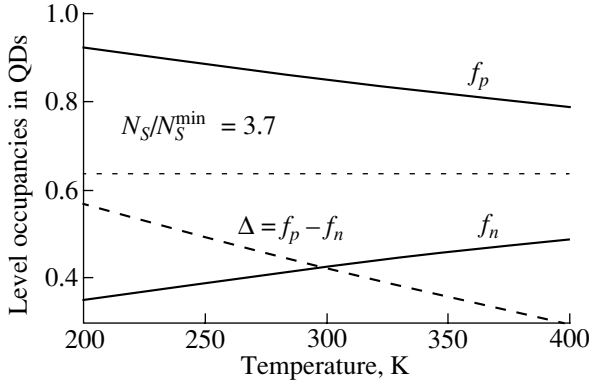
Fig. 15. Electron and hole level occupancies in QDs and their difference vs. temperature. The horizontal dotted line represents $f_{n,p}$ calculated on the assumption of neutrality in QD. $\beta = 10$ cm^{-1}, $\delta = 0.05$; $N_S^{\min} = 2.1 \times 10^{10}$ cm^{-2}. Optimum N_S and b at $T = 300$K are taken: $N_S = 3.7 N_S^{\min} = 7.7 \times 10^{10}$ cm^{-2}, $b = 0.28$ μm.
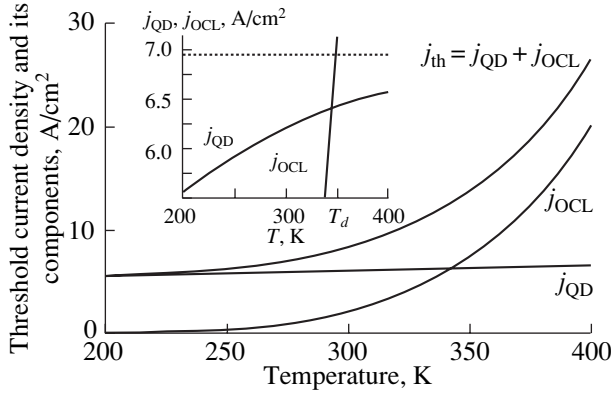

Fig. 16. Threshold current density and its components vs. temperature. Inset: j_{QD} and j_{OCL} on enlarged (along the vertical axis) scale; at $T = T_d = 344$ K, $j_{OCL} = j_{QD}$; the dotted line represents the current density j_{QD} calculated on the assumption of neutrality in QDs.

$$j_{OCL} = ebBnp = ebBn_1 p_1 \frac{f_n f_p}{(1 - f_n)(1 - f_p)}. \quad (43)$$

Assuming QD neutrality, the temperature dependence of j_{OCL} can be represented as

$$j_{OCL}(T) \equiv j_{OCL, \text{neutral}}(T) \propto Bn_1 p_1$$

$$\propto T^{3/2} \exp\left(-\frac{\Delta E_{g1} - \varepsilon_n - \varepsilon_p}{T}\right), \quad (44)$$

where $\Delta E_{g1} = \Delta E_{c1} + \Delta E_{v1}$ is the difference between the bandgaps of the materials of the OCL and QDs.

As $\Delta E_{g1} - \varepsilon_n - \varepsilon_p = (\Delta E_{c1} - \varepsilon_n) + (\Delta E_{v1} - \varepsilon_p)$ increases, the free carrier densities in the OCL and, consequently, the parasitic recombination current

become lower, which leads to a decrease in j_{th} and a weakening of its temperature dependence. In [76] a material with a wider bandgap, AlGaAs, was used instead of GaAs as the material of the OCL in order to raise the height of the barriers for carriers in QDs and thereby suppress the thermal escape. As a result, j_{th} was substantially reduced.

It can be seen from (35)–(37) that Δ (i.e., the QD charge) and, consequently, $f_{n,p}$ [see (34)] depend on T. Thus, neutrality violation in QDs leads to a temperature dependence of the recombination current density, j_{QD}, in QDs. With increasing T, the neutrality violation is suppressed: Δ falls gradually and the values of f_n and f_p approach each other (Fig. 15).

The temperature dependence of j_{QD} is much weaker than that of j_{OCL} (Fig. 16). Nevertheless, the conclusion that j_{QD} depends on T is extremely important. The point is that the recombination channels in the OCL (i.e., leakage currents) must be suppressed in properly optimized structures. However, even in this case, the threshold current determined exclusively by recombination in the QDs will depend on T.

The recombination current density in the OCL, j_{OCL}, grows exponentially with T and has activation energy $\Delta E_{g1} - \varepsilon_n - \varepsilon_p$ [see (44) and Fig. 16]. That is why, in order to describe the temperature dependence of $j_{th} = j_{QD} + j_{OCL}$, it is convenient to introduce the temperature T_d at which j_{OCL} becomes equal to j_{QD}. When T is significantly lower than T_d, $j_{OCL} \ll j_{QD}$ and there is only a very weak dependence of j_{th} on T. Conversely, when T exceeds T_d to a sufficient extent, $j_{OCL} \gg j_{QD}$ and j_{th} strongly depends on T (Fig. 16). There is a certain analogy between the thus defined T_d and the depletion (ionization) temperature of impurity centers. An equation for T_d was presented in [49]; T_d grows with increasing ΔE_{g1} or N_S and decreasing δ or β [49]. Using T_d, the j_{OCL} to j_{QD} ratio can be represented as

$$\frac{j_{OCL}(T)}{j_{QD}(T)} = \frac{j_{QD}(T_d) - eN_S^{\min}/\tau_{QD}}{j_{QD}(T) - eN_S^{\min}/\tau_{QD}}\left(\frac{T}{T_d}\right)^{3/2}$$

$$\times \exp\left(\frac{\Delta E_{g1} - \varepsilon_n - \varepsilon_p}{T_d} - \frac{\Delta E_{g1} - \varepsilon_n - \varepsilon_p}{T}\right). \quad (45)$$

4.2. Characteristic Temperature T_0

The characteristic temperature is an extremely important parameter that describes empirically the temperature dependence of j_{th} for a semiconductor laser [82]:

$$T_0 = \left(\frac{\partial \ln j_{th}}{\partial T}\right)^{-1}. \quad (46)$$

Despite the fact that the dependence of j_{th} on T is never an exponential dependence of the type $\exp(T/T_0)$ [as it might seem from (46)], the parameter T_0 adequately describes the temperature dependence of j_{th}, provided that it is itself a function of temperature: $T_0 = T_0(T)$.

T_0 of a QD laser can be represented as

$$\frac{1}{T_0} = \frac{j_{QD}}{j_{QD} + j_{OCL}}\frac{1}{T_0^{QD}} + \frac{j_{OCL}}{j_{QD} + j_{OCL}}\frac{1}{T_0^{OCL}}, \qquad (47)$$

where T_0^{QD} and T_0^{OCL} are defined in the same way as T_0, but for the functions $j_{QD}(T)$ and $j_{OCL}(T)$, respectively.

The equations for T_0^{QD} and T_0^{OCL} are as follows:

$$\frac{1}{T_0^{QD}} = -\frac{1}{4}\frac{1}{f_n f_p}\frac{\partial \Delta^2}{\partial T}, \qquad (48)$$

$$\frac{1}{T_0^{OCL}} = \frac{3}{2}\frac{1}{T} + \frac{\Delta E_{g1} - \varepsilon_n - \varepsilon_p}{T^2}$$

$$\qquad\qquad (49)$$

$$- \frac{e N_S^{min}/\tau_{QD}}{j_{QD} - e N_S^{min}/\tau_{QD}}\frac{1}{T_0^{QD}}.$$

Since the absolute value of Δ decreases with increasing T (Fig. 15), T_0^{QD} is positive.

If one assumes that the QDs are neutral [i.e., $\Delta = 0$, $f_{n,p} = (1 + N_S^{min}/N_S)/2$, and, consequently, $T_0^{QD} = \infty$], the following expression is obtained for the characteristic temperature:

$$T_{0, neutral} = \left[1 + \frac{1}{4\tau_{QD}}\frac{N_S}{}\left(1 - \frac{N_S^{min}}{N_S}\right)^2 \Big/ bB n_1 p_1\right]$$

$$\times \left(\frac{3}{2}\frac{1}{T} + \frac{\Delta E_{g1} - \varepsilon_n - \varepsilon_p}{T^2}\right)^{-1}. \qquad (50)$$

4.2.1. Temperature dependence of T_0. The characteristic temperature falls steeply with increasing T (Fig. 17c). The pronounced (severalfold) decrease in T_0 occurs on passing from temperatures at which j_{th} is controlled by recombination in QDs to those at which j_{th} is controlled by recombination in the OCL (Fig. 17c). Such a dependence of T_0 on T is in agreement with the experiment (see, e.g., [20]).

It should be noted that $T_0^{QD} \gg T_0^{OCL}$. Nevertheless, as can be seen from (47), $1/T_0$ is determined not only by $1/T_0^{QD}$ and $1/T_0^{OCL}$, but also by relative contributions of the threshold current density components, $j_{QD}/(j_{QD} + j_{OCL})$ and $j_{OCL}/(j_{QD} + j_{OCL})$. Therefore, it is important to take into account the first term in the right-hand part of (47) at relatively low temperatures ($T < T_d$), at which j_{th} is controlled by the component j_{QD}. At these temperatures, Eq. (50) gives values of $T_{0, neutral}$ (Fig. 17c, dashed line) that exceed substantially the true T_0 yielded by Eq. (47), which takes into account the neutrality violation in QDs (Fig. 17c, solid line). Thus, it is the neutrality violation at low T that is the main reason for the temperature dependence of j_{th}, and taking this effect into account is necessary for a correct calculation of T_0 to give results in agreement with the experiment.
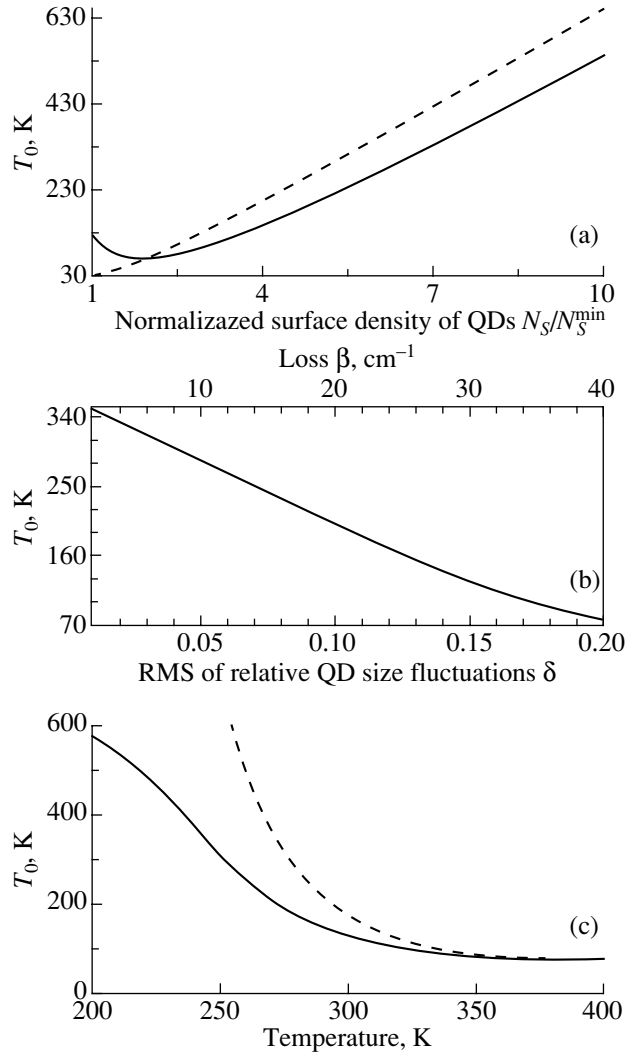
Fig. 17. Characteristic temperature vs. (a) surface density of QDs, (b) RMS of relative QD size fluctuations (at $\beta = 10$ cm^{-1}, lower axis) and loss (at $\delta = 0.05$, upper axis) at $N_S = 1.3 \times 10^{11}$ cm^{-2}, and (c) temperature at $N_S = 7.7 \times 10^{10}$ cm^{-2}. Dashed lines: $T_{0, neutral}$ [see (50)].

4.2.2. Dependence of T_0 on structure parameters.
Sufficiently far away from N_S^{min}, T_0 grows with increasing N_S (Fig. 17a). The reason is that the j_{th} component that is less dependent on T, specifically, j_{QD}, grows with increasing N_S, whereas the more temperature-sensitive component, i.e., j_{OCL}, falls.

The more perfect a structure (i.e., the smaller δ) or the smaller β, the higher T_0 (Fig. 17b). At room temperature, $N_S = 1.3 \times 10^{11}$ cm^{-2}, cavity loss $\beta = 10$ cm^{-1}, and 10% QD size fluctuations ($\delta = 0.05$),

$$T_0 \approx 286 \text{ K}. \qquad (51)$$

This value of T_0 is much (severalfold) greater, at the same loss, than that in QW lasers, in which T_0 does not exceed 90 K.
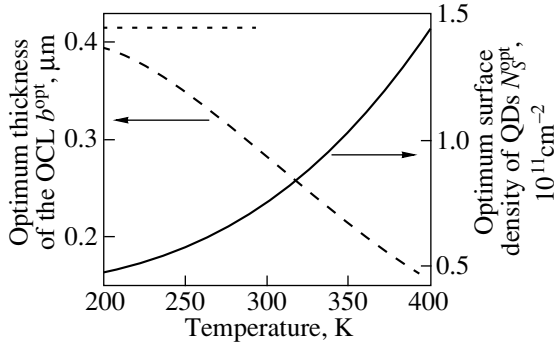
Fig. 18. Optimum surface density of QDs and optimum OCL thickness vs. temperature. The horizontal dotted line shows the OCL thickness at which the optical confinement factor is at a maximum.

4.3. Temperature Dependences for an Optimized Structure

The optimum laser parameters that ensure minimum j_{th} are temperature dependent [49]. Thus, a structure optimized at a given T is not optimized at any other temperature. The optimum OCL thickness decreases, and the optimum surface density of QDs grows, with increasing T (Fig. 18).

The temperature dependences of j_{th}^{min} and T_0^{opt} for an optimized structure were analyzed in detail in [46, 49].

At high T [$s \ll 1$, see (29)], at which recombination in the OCL is important, the temperature dependence of j_{th}^{min} is determined by that of the square root of the rate of spontaneous transitions in the OCL, Bn_1p_1, i.e., is much weaker than that for an unoptimized structure [for which it is determined by the temperature dependence of the rate Bn_1p_1 itself, see (44)]:

$$j_{th}^{min} \propto \sqrt{Bn_1p_1} \propto T^{3/4} \exp\left(-\frac{\Delta E_{g1} - \varepsilon_n - \varepsilon_p}{2T}\right). \quad (52)$$

At low T ($s \gg 1$), at which recombination in the OCL is insignificant, the dependence of j_{th}^{min} on T and ΔE_{g1} vanishes [see (28)].

The characteristic temperature for the function $j_{th}^{min}(T)$ is

$$T_0^{opt} = \left\{ \frac{1}{1 + \{[a/b^{opt}\Gamma(b^{opt})]s\}^{1/2}}\left(1 - \frac{d\ln b^{opt}}{d\ln s}\right)\right.$$

$$\left. + \frac{\{[a/b^{opt}\Gamma(b^{opt})]s\}^{1/2}}{1 + \{[a/b^{opt}\Gamma(b^{opt})]s\}^{1/2}}\frac{d\ln\Gamma(b^{opt})}{d\ln s}\right\}^{-1} \quad (53)$$

$$\times \left(\frac{3}{2}\frac{1}{T} + \frac{\Delta E_{g1} - \varepsilon_n - \varepsilon_p}{T^2}\right)^{-1}.$$

The expression in braces is a universal function of the dimensionless parameter s [see (25) for a definition of s] that can be derived from the dependences of b^{opt} and $\Gamma(b^{opt})$ on s (Fig. 7).

When T exceeds the temperature for which the structure is optimized, T_0 cannot be higher than T_0^{opt} yielded by Eq. (53).

5. EXCITED-STATE OPTICAL TRANSITIONS IN QDs

In the ideal case, for the advantages of QD lasers to be manifested to the maximum possible extent, it is necessary that only a single electron level and a single hole level be present in a QD. For a QD of highly symmetric (e.g., cubic) shape, it is sufficient that a single (ground) level exist only for electrons. Radiative transitions from the ground electron to excited hole levels in QDs of this kind are partly or completely forbidden by selection rules (at least in the first order). In real laser structures containing QDs whose shape is not highly symmetric (e.g., pyramidal), such transitions are not forbidden. In addition, excited electron levels may be present [83]. Transitions from excited states affect the threshold characteristics of a laser [54, 55].

The general expressions for the modal gain spectrum $g(E)$ and spectral density of the flux of spontaneous recombination in QDs, $r_{sp}(E)$, for an arbitrary number of radiative transitions in the dots were given in [54]. Various possible cases of modifying these spectra by changing the injection current were described.

5.1. Universal Relationship between Spectra of Gain and Spontaneous Emission

In the case of quasi-equilibrium QD filling with both electrons and holes, the $r_{sp}(E)$ to $g(E)$ ratio is described for an arbitrary number of transitions in QDs and their arbitrary size distribution by the universal function [54]

$$\frac{r_{sp}(E)}{g(E)} = \frac{a}{\Gamma(E)}\frac{\varepsilon(E)E^2}{\pi^2\hbar^3c^2}$$

$$\times \left\{1 - \exp\left[\frac{E - (E_g^{QD} + \mu_n + \mu_p)}{T}\right]\right\}^{-1}, \quad (54)$$

where $\varepsilon(E)$ and $\Gamma(E)$ are the dielectric constant and the optical confinement factor (both photon-energy-dependent), and $\mu_{n,p}$ are the quasi-Fermi levels for electrons and holes, reckoned from the band edges in the QDs. Since $\Gamma \propto a$ [see (22)], there is no dependence on QD size in (54); a/Γ is the characteristic length of photon localization in the transverse direction in the waveguide.

Equation (54) is a generalization of the well-known relation between $r_{sp}(E)$ and $g(E)$ in semiconductors
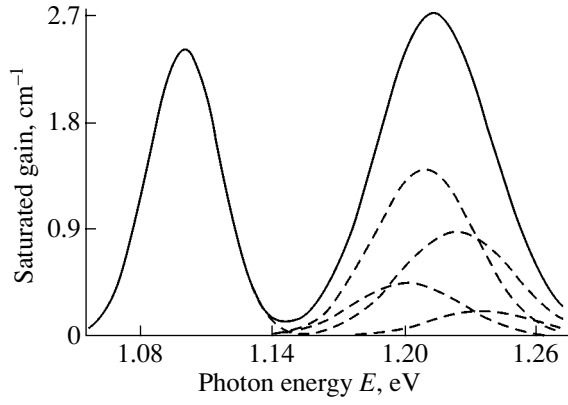
Fig. 19. Saturated gain of a laser with a single layer of self-assembled pyramidal InAs QDs in GaAs. Dashed lines: spectra for each of the transitions. $\delta = 0.05$.
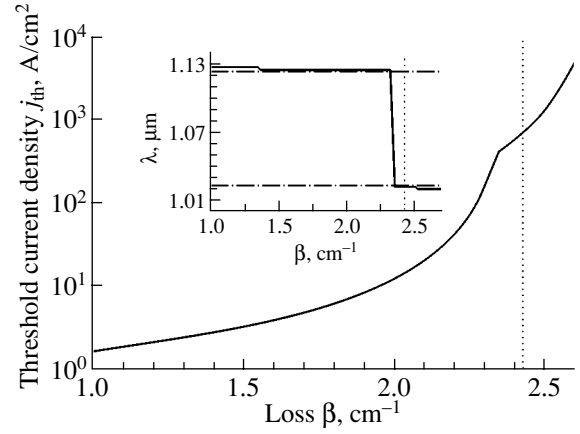

Fig. 20. Threshold current density and (inset) emission wavelength λ vs. loss. Vertical dotted line: g_1^{max}.

[84]. It is highly important for analysis of characteristics of a QD laser. It is the spectrum of photo- or electroluminescence [i.e., $r_{sp}(E)$] that is commonly measured experimentally. Using (54) for the equilibrium filling of QDs, the $g(E)$ spectrum can be readily obtained from the experimental $r_{sp}(E)$ spectrum.

5.2. Microscopic Parameters Controlling the Maximum Gain for a Separate Transition

It was shown in [54] that the lasing wavelength may vary with loss gradually or stepwise, depending on the separation of the transition energies, inhomogeneous broadening, and maximum gain for the transitions.

The key role in determining the emission wavelength, i.e., the peak position of the gain spectrum, is played by the ratio of the maximum (saturated) gains for the transitions. The maximum gain and the time of spontaneous recombination for the transition from an electron level characterized by a set of quantum numbers i to a hole level with a set of numbers j are yielded by expressions (10) and (8), in which the parameters for the transition $i \longrightarrow j$ appear instead of the corresponding values for the ground-state transition. The degeneracy of the transition is additionally introduced into the expression for g_{ij}^{max} ($g_{ij}^{max} \propto d_{ij}$). Thus, g_{ij}^{max} is controlled by the following microscopic parameters: inhomogeneous broadening, degeneracy, and overlap integral. The overlap integral governs the time of spontaneous recombination ($1/\tau_{ij}^{QD} \propto I_{ij}$).

The transition parameters affect g_{ij}^{max} in different ways. The inhomogeneous broadening is always more pronounced for a transition with a higher index. The overlap integral is commonly smaller for a transition with a higher index [83]; thus, τ_{ij}^{QD} is always longer for such a transition. The degeneracy of the ground-state transition is always unity [double spin degeneracy is

taken into account for each of the transitions by (8)]. The higher the transition index, the greater the degeneracy [32, 36]. For pyramidal (with a square base) or cubic QDs, the degeneracy of the transition from the first excited electron state to a similar hole state is 2 or 3, respectively, provided that there are no piezoelectric effects. Thus, the only possible physical reason for which g_{ij}^{max} may be higher for a transition with a higher index is the greater degeneracy. However, QDs actually have an irregular shape. Moreover, even if the QDs were of regular shape, piezoelectric effects would lift the degeneracy of the excited states (see [83] for pyramidal QDs). Thus, g_{ij}^{max} for a separate excited-state transition cannot exceed that for the ground-state transition in real QDs. Nevertheless, a stepwise change (switching) of the emission wavelength may occur in laser structures with QDs of this kind (see Section 5.3).

5.3. Threshold Characteristics of a Laser with Self-Assembled Pyramidal InAs QDs in a GaAs Matrix

As a result of the piezoelectric effect [83], the degeneracy of excited states is completely removed in QDs of this kind. The spectrum of the saturated gain (at injection current $j = \infty$) and the dependences of the emission wavelength and j_{th} on β, calculated in [54, 55], are shown in Figs. 19 and 20. As can be seen from Fig. 19, all the four transitions from the excited states lie within the energy interval T and, consequently, effectively "act" as a single transition. The maximum gain for this combined excited-state transition somewhat exceeds the maximum gain for the ground-state transition g_1^{max} (Fig. 19), which makes stepwise switching of lasing from the ground state possible. The change in the peak position of the gain spectrum $g(E)$ occurs when β approaches g_1^{max}; at $\beta > g_1^{max}$, lasing occurs via the combined excited-state transition. The

1: Radiative recombination in QDs
2: Radiative recombination in the OCL
3: Capture into QDs and thermal escape from QDs
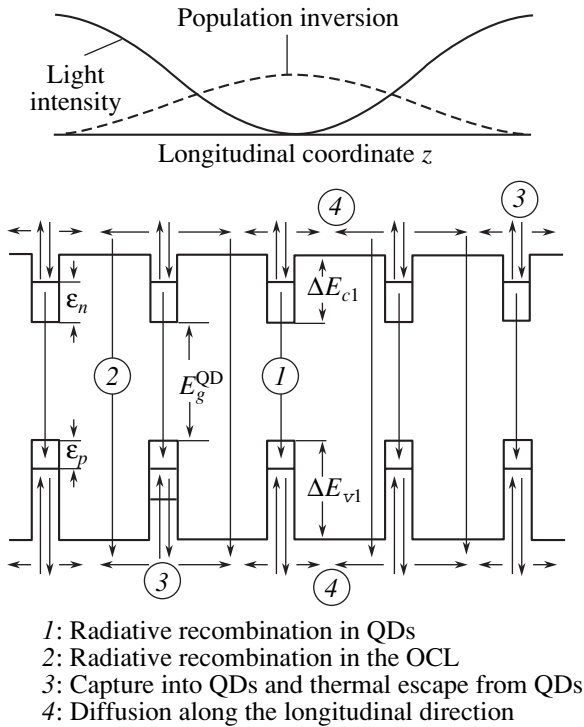**4**: Diffusion along the longitudinal direction

Fig. 21. Schematic of a QD laser in the longitudinal direction and main processes.

discontinuity in $\partial j_{th}/\partial \beta$ at $\beta = g_1^{max}$ (Fig. 20) reflects the abrupt change in the emission wavelength (see [36] and [85] for experimental demonstration of this effect for QD and QW lasers, respectively). The overlap integrals, and, consequently the values of g^{max} too, for the fourth and fifth transitions are much smaller than the corresponding values for the first three transitions. Nevertheless, it is notable that taking into account the fourth and fifth transitions (the so-called forbidden transitions, i.e., transitions with $i \neq j$) is necessary to explain the emission wavelength switching. The point is that the maximum gain for a combined transition composed of the second and third transitions would be lower than g_1^{max}.

Thus, the stepwise change in the lasing wavelength with varying loss in the lasers under consideration is due to a changeover from the ground-state transition to an effective excited-state transition, which is a superposition of several closely lying transitions via excited states. Transitions from excited states in structures of this kind make lasing possible with a loss exceeding the maximum gain for the ground-state transition.

The possibility of electrically controlled switching of the emission wavelength makes QD lasers attractive for "write" and "read" operations, and also for wavelength multiplication and division [32].

6. SPATIAL HOLE BURNING
AND THE MULTIMODE LASING THRESHOLD

SHB in semiconductor lasers [86, 87] (and also in solid-state lasers [88]) is due to the nonuniformity of stimulated recombination and leads to the generation of higher cavity modes in addition to the main mode. The problem of multimode generation is of practical worth from both the fundamental and applied points of view [9]. Studying the physical processes that control the multimode generation threshold is necessary to suppress additional modes and to develop single-mode lasers.

Stimulated emission in a cavity is a standing wave (with several thousand half-wavelengths fitted in the cavity length).[14] In QD lasers, several QDs can be accommodated within a half-wavelength in a medium. Thus, the rate of stimulated recombination is the highest (or lowest) in QDs lying near antinodes (or nodes) of the intensity of emitted light. As a result, SHB occurs in the population inversion: QDs lying close to antinodes are depleted, and those near nodes, overfilled.

In lasers with a bulk active region and QW lasers, diffusion makes the nonuniform carrier distributions even, thereby partly or completely suppressing the SHB effect [86]. The situation in QD lasers is fundamentally different. Since only carriers localized in the QDs contribute to stimulated emission, the leveling of the nonuniform inversion requires that carriers be thermally released from the overfilled QDs, diffuse in the OCL to depleted QDs, and then be captured into these QDs (Fig. 21). Thus, the isolated positions of QDs and the absence of direct carrier exchange between them may hinder leveling of the nonuniform population inversion and lead to a strong SHB effect.

At and somewhat above the lasing threshold, only the main [closest to the peak of the $g(E)$ spectrum] mode is emitted. Because of the SHB effect, the population inversion in a QD, averaged along the longitudinal direction, is higher than its threshold value, which may mean that the lasing condition is satisfied for higher longitudinal cavity modes. Since the main task is to determine ways to suppress the additional modes, the lasing condition for the next, i.e., closest to the main, mode[15] is analyzed in detail, and, accordingly, the injection current densities exceeding the threshold current density for the main mode, j_{th}, and not exceeding the threshold current density for the next mode, j_2, are considered. The multimode generation threshold δj is defined as the excess of the injection current density

[14] Strictly speaking, there are also traveling-wave components in the cavity, which are to be taken into account properly in the general case (especially near the mirrors). However, as shown in [9, 89], these components can be disregarded in the case of sufficiently high mirror reflectivities.
[15] If the gain spectrum is symmetric with respect to its peak, the two modes that lie symmetrically relative to the main mode may be the next modes.

over the threshold current for the main mode, which is necessary for generation of the next cavity mode:

$$\delta j = j_2 - j_{th}. \qquad (55)$$

The analysis is made on the basis of time-independent rate equations for carriers localized in QDs, free carriers, and photons [50–52]. It is shown that the ratio of the flux of thermal escape of holes to the diffusion flux of holes is much smaller than unity; i.e., it is the thermal escape of carriers from QDs, and not diffusion in the OCL, that is the slow process that controls the leveling of the spatially nonuniform population inversion.[16] Because of this circumstance, the general expression for δj can be simplified; below, it is analyzed for the cases of high and low temperatures.

6.1. Relatively High Temperatures

For T leading to equilibrium QD filling at and below the lasing threshold (i.e., $\tau_{QD} \gg \tau_{n,p}^{esc}$; for the structure under consideration, $\tau_{QD} = 0.71$ ns and, at room temperature, $\tau_n^{esc} = 7$ ps, $\tau_p^{esc} = 60$ ps), δj is controlled by the finite times $\tau_{n,p}^{esc}$:

$$\delta j = \left[\hbar \frac{c}{\sqrt{\epsilon}} \frac{\pi}{L} \Big/ (\Delta \epsilon)_{inhom} \right]^2 (f_n + f_p - 1)$$
$$\times \frac{e N_S}{\tau_n^{esc}(1 - f_n) + \tau_p^{esc}(1 - f_p)}. \qquad (56)$$

A similar situation is the case for band-to-impurity lasing transitions [91, 92].

It can be seen from (2) and (56) that δj grows with increasing $\sigma_{n,p}$. Naturally, the greater $\sigma_{n,p}$, the faster the capture and thermal escape and the weaker the SHB effect.

6.2. Relatively Low Temperatures

For T leading to nonequilibrium QD filling at and below the lasing threshold (i.e., $\tau_{QD} \ll \tau_{n,p}^{esc}$), δj is controlled by the time of spontaneous recombination in QDs, τ_{QD}:

$$\delta j = \left[\hbar \frac{c}{\sqrt{\epsilon}} \frac{\pi}{L} \Big/ (\Delta \epsilon)_{inhom} \right]^2 (f_n + f_p - 1)$$
$$\times \frac{f_n + f_p - f_n f_p}{2 - f_n - f_p} \frac{e N_S}{\tau_{QD}}. \qquad (57)$$

The point is that δj is controlled by the fastest process by which carriers leave QDs. At high T, this is the thermal escape from QDs, and, accordingly, the times $\tau_{n,p}^{esc}$

---

[16]Since $D_n \gg D_p$, the diffusion of electrons in the OCL cannot be the limiting factor; for GaInAsP, $D_n = 40$ cm²/s and $D_p = 1.6$ cm²/s [90].

appear in (56). At low T, the faster process is spontaneous recombination, and, accordingly, the time τ_{QD} appears in (57).

6.3. Dependences of Multimode Generation Threshold on Structure Parameters

Here we consider relatively high temperatures.

As one of the structure parameters approaches its critical value ($N_S \longrightarrow N_S^{min}$, or $\delta \longrightarrow \delta^{max}$, or $L \longrightarrow L^{min}$), the threshold current densities of the main and next modes, as well as the multimode generation threshold, grow infinitely [see (56) and Fig. 5]. In this case, the relative multimode generation threshold $\delta j/j_{th}$ tends to zero (Fig. 5, insets), which means an indefinite increase in the number of generated longitudinal cavity modes. To realize the advantages of QD lasers, the structure parameters must be sufficiently far from their critical values.

At $\delta \longrightarrow 0$, δj, $\delta j/j_{th}$, and, consequently, j_2 grow infinitely as δ^{-1} (Fig. 5b).

At $L \longrightarrow \infty$, δj and $\delta j/j_{th}$ decrease as L^{-3} (Fig. 5c), j_2 decreases and tends to j_{th}, and both these quantities approach the transparency current density (Fig. 5c).

It can be seen from Fig. 5a that there exists a certain value of N_S that ensures the maximum $\delta j/j_{th}$. Since $\delta j/j_{th} \longrightarrow 0$ both at $L \longrightarrow L^{min}$ and $L \longrightarrow \infty$, there also exists a value of L at which $\delta j/j_{th}$ is at a maximum (Fig. 5c). Such a behavior of the dependence of $\delta j/j_{th}$ on N_S and L makes it possible to optimize the structure in order to maximize $\delta j/j_{th}$.

For structures optimized to minimize the threshold current density for the main mode, Fig. 22 shows the relative multimode generation threshold and the minimum threshold current density for the main mode as functions of the RMS of relative QD size fluctuations, cavity length, and temperature. For structures optimized for $\delta = 0.025$ (5% scatter) and 0.1 (20% scatter), $\delta j/j_{th} \approx 21$ and 2%, respectively; $j_{th}^{min} \approx 8$ and 25 A/cm², respectively.

6.4. Temperature Dependence of Multimode Generation Threshold

The values of $f_{n,p}$ at the lasing threshold for the main mode appear in (56) and (57). On the condition that neutrality is maintained in QDs, δj would be virtually temperature independent at low T. The neutrality violation (Section 3) leads to a weak temperature dependence of f_n and f_p (Section 4) and, consequently, of δj, too, at these temperatures.

For the structure used as an example (see Section 2.3.2.3), δj increases by approximately a factor of 24 on passing from low to room temperature.

Fig. 23. Threshold current densities for the main mode (solid line) and next mode (dashed line) and multimode generation threshold (dotted line) vs. temperature. Inset: relative multimode generation threshold.
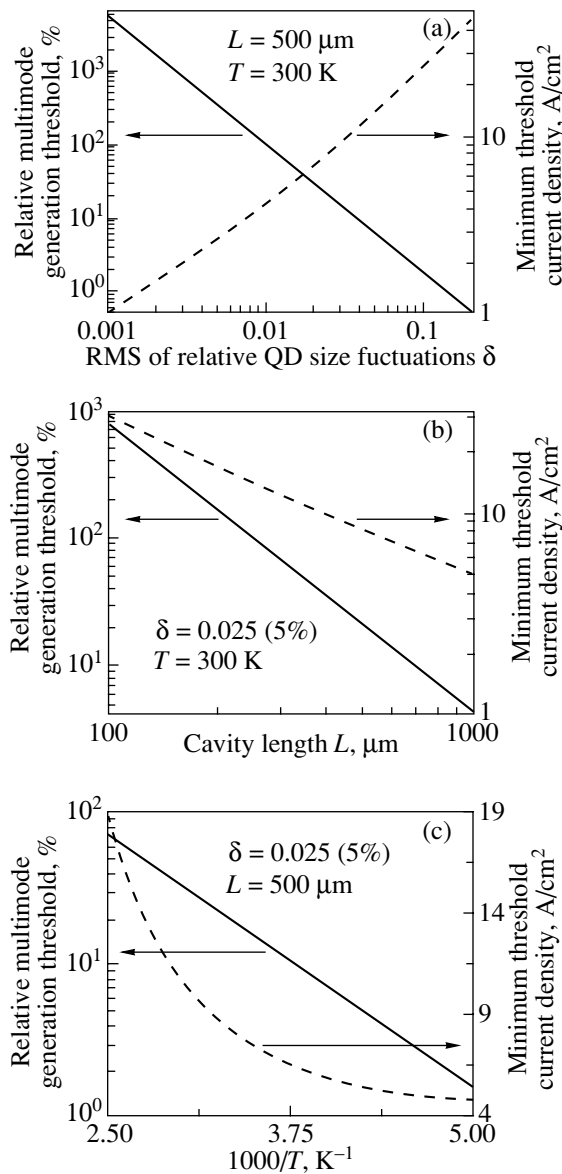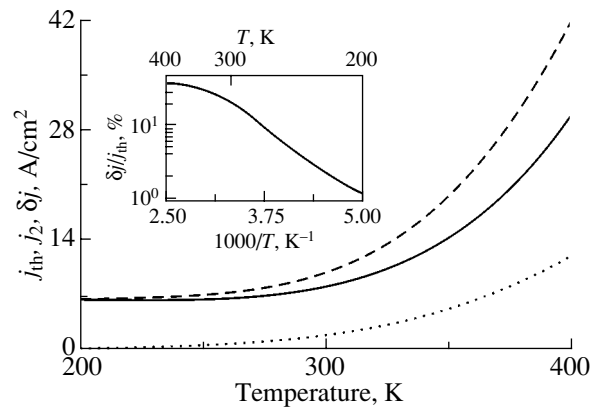
Fig. 22. Relative multimode generation threshold $\delta j/j_{th}$ (solid line) and minimum threshold current density for the main mode (dashed line) vs. (a) RMS of relative QD size fluctuations, (b) cavity length, and (c) temperature. (a–c) Each point in the curves corresponds to a particular structure optimized at a given δ, L, and T, respectively.

The temperature dependence of δj at high T is due to temperature dependences of the times $\tau_{n,p}^{esc}$ [see (2) and (3)]. Simultaneously with an undesirable rise in j_{th} as T increases, j_2, δj, and $\delta j/j_{th}$ grow (Fig. 23). This occurs because the thermal escape of carriers from QDs and, consequently, the leveling of the spatially nonuniform population inversion become more effective at high T.[17] Provided that the SHB effect is the only (or main) rea-

son for multimode generation in a QD laser, the number of emitted modes must decrease with increasing T, and, consequently, the dependence of the output power on the injection current must become more linear. It is this factor that may be one of the reasons for the rise in the differential efficiency of the QD laser with increasing T, which is observed experimentally in [37].

7. CONCLUSION

A comprehensive theory of the threshold characteristics of injection QD lasers was presented in which the following is demonstrated:

(1) There exist critical tolerable parameters of a QD structure, i.e., bounds for the range of parameters in which lasing is possible. When a parameter approaches its critical value, the threshold current grows infinitely.

(2) Depending on temperature and carrier localization energies, two fundamentally different modes of QD filling with carriers, nonequilibrium and equilibrium, are possible. The temperature determining the boundary between these modes becomes higher with increasing localization energies.

(3) The temperature dependence of the threshold current in QD lasers differs fundamentally from that for lasers with a bulk active region and QW lasers: at low temperature (nonequilibrium QD filling), the threshold current is virtually temperature independent; at high temperature (equilibrium filling), the threshold current is controlled by thermal escape from QDs and grows exponentially with temperature. This circumstance accounts for the fast fall of the characteristic temperature T_0 at high temperature.

(4) In contrast to lasers with a bulk active region and QW lasers, the local charge neutrality in the QDs of QD laser structures is violated, which strongly affects the threshold current and its temperature dependence

---

[17]In semiconductor lasers with a bulk active region, the multimode generation threshold also grows with increasing T, which is due to a rise in the diffusion coefficient at high T [86].

(characteristic temperature T_0). The neutrality violation leads to a temperature dependence of the threshold current component associated with recombination in QDs and is the main reason for the temperature dependence of the threshold current at low temperature.

(5) At equilibrium QD filling, there exists a universal relationship between the spectra of gain and spontaneous recombination, which holds for an arbitrary number of radiative transitions in QDs and an arbitrary QD size distribution.

(6) Spatial localization of carriers contributing to stimulated emission may result in a strong SHB effect in QD lasers, which leads to multimode generation.

(7) There exist optimum structure parameters that minimize the threshold current density. The limiting characteristics of a laser (optimum parameters, minimum threshold current density, and characteristic temperature for an optimized structure) depend on QD size dispersion, cavity length, band offsets at the heterointerface with QDs, and temperature. Making the QD size dispersion smaller leads to a lower threshold current, higher characteristic temperature T_0, and higher multimode generation threshold.

(8) At 10% QD size scatter and a loss of 10 cm^{-1}, threshold current densities of less than 10 A/cm^2 can be achieved at room temperature in the CW mode, which is more than an order of magnitude lower than those in QW lasers at the same loss. The corresponding characteristic temperatures may exceed 280 K, which considerably (severalfold) exceeds that in QW lasers.

ACKNOWLEDGMENTS

REFERENCES

1. Zh. I. Alferov, Rev. Mod. Phys. **73**, 767 (2001).
2. H. Kroemer, Rev. Mod. Phys. **73**, 783 (2001).
3. J. P. van der Ziel, R. Dingle, R. C. Miller, *et al.*, Appl. Phys. Lett. **26**, 463 (1975).
4. R. D. Dupuis, P. D. Dapkus, N. Holonyak, *et al.*, Appl. Phys. Lett. **32**, 295 (1978).
5. W. T. Tsang, Appl. Phys. Lett. **40**, 217 (1982).
6. Zh. I. Alferov, A. I. Vasil'ev, S. V. Ivanov, *et al.*, Pis'ma Zh. Tekh. Fiz. **14**, 1803 (1988) [Sov. Tech. Phys. Lett. **14**, 782 (1988)].
7. N. Chand, E. E. Becker, J. P. van der Ziel, *et al.*, Appl. Phys. Lett. **58**, 1704 (1991).
8. G. W. Turner, H. K. Choi, and M. J. Manfra, Appl. Phys. Lett. **72**, 876 (1998).
9. G. P. Agrawal and N. K. Dutta, *Long-Wavelength Semiconductor Lasers* (Van Nostrand Reinhold, New York, 1986).
10. *Quantum Well Lasers*, Ed. by P. S. Zory, Jr. (Academic, Boston, 1993).
11. L. A. Coldren and S. W. Corzine, *Diode Lasers and Photonic Integrated Circuits* (Wiley, New York, 1995).
12. *Semiconductor Lasers*, Ed. by E. Kapon (Academic, San Diego, 1999).
13. P. G. Eliseev, *Introduction to Physics of Injection Lasers* (Nauka, Moscow, 1983).
14. R. Dingle and C. H. Henry, U.S. Patent No. 3982207 (1976).
15. Y. Arakawa and H. Sakaki, Appl. Phys. Lett. **40**, 939 (1982).
16. Zh. I. Alferov and R. F. Kazarinov, Inventor's Certificate No. 181,737 (1963).
17. Zh. I. Alferov, V. M. Andreev, E. L. Portnoǐ, and M. K. Trukan, Fiz. Tekh. Poluprovodn. (Leningrad) **3**, 1328 (1969) [Sov. Phys. Semicond. **3**, 1107 (1970)].
18. I. Hayashi, M. B. Panish, P. W. Foy, and S. Sumski, Appl. Phys. Lett. **17**, 109 (1970).
19. N. N. Ledentsov, V. M. Ustinov, A. Yu. Egorov, *et al.*, Fiz. Tekh. Poluprovodn. (St. Petersburg) **28**, 1483 (1994) [Semiconductors **28**, 832 (1994)].
20. N. Kirstädter, N. N. Ledentsov, M. Grundmann, *et al.*, Electron. Lett. **30**, 1416 (1994).
21. D. Bimberg, M. Grundmann, and N. N. Ledentsov, *Quantum Dot Heterostructures* (Wiley, Chichester, 1999).
22. N. N. Ledentsov, M. Grundmann, F. Heinrichsdorff, *et al.*, IEEE J. Sel. Top. Quantum Electron. **6**, 439 (2000).
23. M. V. Maximov, Yu. M. Shernyakov, A. F. Tsatsul'nikov, *et al.*, J. Appl. Phys. **83**, 5561 (1998).
24. M. V. Maximov, L. V. Asryan, Yu. M. Shernyakov, *et al.*, IEEE J. Quantum Electron. **37**, 676 (2001).
25. V. P. Evtikhiev, I. V. Kudryashov, E. Yu. Kotel'nikov, *et al.*, Fiz. Tekh. Poluprovodn. (St. Petersburg) **32**, 1482 (1998) [Semiconductors **32**, 1323 (1998)].
26. V. P. Evtikhiev, V. E. Tokranov, A. K. Kryganovskii, *et al.*, J. Cryst. Growth **202**, 1154 (1999).
27. G. Park, O. B. Shchekin, S. Csutak, *et al.*, Appl. Phys. Lett. **75**, 3267 (1999).
28. G. Park, O. B. Shchekin, D. L. Huffaker, and D. G. Deppe, IEEE Photonics Technol. Lett. **13**, 230 (2000).
29. H. Hirayama, K. Matsunaga, M. Asada, and Y. Suematsu, Electron. Lett. **30**, 142 (1994).
30. J. Temmyo, E. Kuramochi, M. Sugo, *et al.*, Electron. Lett. **31**, 209 (1995).
31. R. Mirin, A. Gossard, and J. Bowers, Electron. Lett. **32**, 1732 (1996).
32. W. Zhou, O. Qasaimeh, J. Phillips, *et al.*, Appl. Phys. Lett. **74**, 783 (1999).
33. L. Harris, D. J. Mowbray, M. S. Skolnick, *et al.*, Appl. Phys. Lett. **73**, 969 (1998).
34. E. O'Reilly, A. Onishchenko, E. Avrutin, *et al.*, Electron. Lett. **34**, 2035 (1998).
35. P. M. Smowton, E. J. Johnston, S. V. Dewar, *et al.*, Appl. Phys. Lett. **75**, 2169 (1999).
36. H. Shoji, Y. Nakata, K. Mukai, *et al.*, IEEE J. Sel. Top. Quantum Electron. **3**, 188 (1997).
37. M. Sugawara, K. Mukai, and Y. Nakata, Appl. Phys. Lett. **74**, 1561 (1999).
38. T. C. Newell, D. J. Bossert, A. Stintz, *et al.*, IEEE Photonics Technol. Lett. **11**, 1527 (1999).
39. P. G. Eliseev, H. Li, G. T. Liu, *et al.*, IEEE J. Sel. Top. Quantum Electron. **7**, 135 (2001).
40. F. Klopf, R. Krebs, J. P. Reithmaier, and A. Forchel, IEEE Photonics Technol. Lett. **13**, 764 (2001).

41. M. Arzberger, G. Böhm, M. C. Amann, and G. Abstreiter, Phys. Status Solidi B **24**, 827 (2001).

42. N.-T. Yeh, J.-M. Lee, T.-E. Nee, and J.-I. Chyi, IEEE Photonics Technol. Lett. **12**, 1123 (2000).

43. J. K. Kim, R. L. Naone, and L. A. Coldren, IEEE J. Sel. Top. Quantum Electron. **6**, 504 (2000).

44. L. V. Asryan and R. A. Suris, in *Proceedings of International Symposium on Nanostructures: Physics and Technology* (St. Petersburg, 1994), p. 181.

45. R. A. Suris and L. V. Asryan, Proc. SPIE **2399**, 433 (1995).

46. L. V. Asryan and R. A. Suris, Semicond. Sci. Technol. **11**, 554 (1996).

47. L. V. Asryan and R. A. Suris, IEEE J. Sel. Top. Quantum Electron. **3**, 148 (1997).

48. L. V. Asryan and R. A. Suris, Electron. Lett. **33**, 1871 (1997).

49. L. V. Asryan and R. A. Suris, IEEE J. Quantum Electron. **34**, 841 (1998).

50. L. V. Asryan and R. A. Suris, Appl. Phys. Lett. **74**, 1215 (1999).

51. L. V. Asryan and R. A. Suris, Fiz. Tekh. Poluprovodn. (St. Petersburg) **33**, 1076 (1999) [Semiconductors **33**, 981 (1999)].

52. L. V. Asryan and R. A. Suris, IEEE J. Quantum Electron. **36**, 1151 (2000).

53. L. V. Asryan and R. A. Suris, Fiz. Tekh. Poluprovodn. (St. Petersburg) **35**, 357 (2001) [Semiconductors **35**, 343 (2001)].

54. L. V. Asryan, M. Grundmann, N. N. Ledentsov, *et al.*, IEEE J. Quantum Electron. **37**, 418 (2001).

55. L. V. Asryan, M. Grundmann, N. N. Ledentsov, *et al.*, J. Appl. Phys. **90**, 1666 (2001).

56. L. V. Asryan and R. A. Suris, Int. J. High Speed Electron. Syst. **12**, 111 (2002).

57. L. V. Asryan and R. A. Suris, in *Selected Topics in Electronics and Systems*, Vol. 25: *Quantum Dots*, Ed. by E. Borovitskaya and M. S. Shur (World Sci., Singapore, 2002), Chap. 5.

58. D. Leonard, S. Fafard, K. Pond, *et al.*, J. Vac. Sci. Technol. B **12**, 2516 (1994).

59. M. Asada, Y. Miyamoto, and Y. Suematsu, IEEE J. Quantum Electron. **22**, 1915 (1986).

60. K. J. Vahala, IEEE J. Quantum Electron. **24**, 523 (1988).

61. Y. Miyamoto, Y. Miyake, M. Asada, and Y. Suematsu, IEEE J. Quantum Electron. **25**, 2001 (1989).

62. C. T. Sah, R. N. Noyce, and W. Shockley, Proc. IRE **45**, 1228 (1957).

63. S. M. Sze, *Physics of Semiconductor Devices*, 2nd ed. (Wiley, New York, 1981; Mir, Moscow, 1984).

64. H. Benisty, C. M. Sotomayor-Torres, and C. Weisbuch, Phys. Rev. B **44**, 10945 (1991).

65. U. Bockelmann and G. Bastard, Phys. Rev. B **42**, 8947 (1990).

66. U. Bockelmann and T. Egeler, Phys. Rev. B **46**, 15574 (1992).

67. N. N. Ledentsov, M. Grundmann, N. Kirstädter, *et al.*, in *Proceedings of 22nd International Conference on Physics of Semiconductors, Vancouver, Canada, 1994,* Ed. by D. J. Lockwood (World Sci., Singapore, 1994), Vol. 3, p. 1855.

68. E. O. Kane, J. Phys. Chem. Solids **1**, 249 (1957).

69. E. H. Perea, E. E. Mendez, and C. G. Fonstad, Appl. Phys. Lett. **36**, 978 (1980).

70. A. Maitland and M. H. Dunn, *Laser Physics* (North-Holland, Amsterdam, 1969; Nauka, Moscow, 1978).

71. M. Grundmann and D. Bimberg, Phys. Rev. B **55**, 9740 (1997).

72. A. P. Levanyuk and V. V. Osipov, Fiz. Tekh. Poluprovodn. (Leningrad) **7**, 1058 (1973) [Sov. Phys. Semicond. **7**, 721 (1973)].

73. V. V. Osipov, T. I. Soboleva, and M. G. Foĭgel', Zh. Éksp. Teor. Fiz. **75**, 1044 (1978) [Sov. Phys. JETP **48**, 527 (1978)].

74. L. V. Asryan, S. G. Petrosyan, and A. Ya. Shik, Pis'ma Zh. Éksp. Teor. Fiz. **45** (4), 187 (1987) [JETP Lett. **45**, 232 (1987)].

75. L. V. Asryan, S. G. Petrosyan, and A. Ya. Shik, Fiz. Tekh. Poluprovodn. (Leningrad) **21**, 1765 (1987) [Sov. Phys. Semicond. **21**, 1070 (1987)].

76. N. N. Ledentsov, V. A. Shchukin, M. Grundmann, *et al.*, Phys. Rev. B **54**, 8743 (1996).

77. M. Sopanen, M. Taskinen, H. Lipsanen, and J. Ahopelto, in *Proceedings of 23rd International Conference on Physics of Semiconductors* (Berlin, 1996), Vol. 2, p. 1409.

78. E. S.-M. Tsui, P. Blood, and A. I. Kucharska, Semicond. Sci. Technol. **5**, 333 (1990).

79. L. V. Asryan, N. A. Gun'ko, A. S. Polkovnikov, *et al.*, Semicond. Sci. Technol. **15**, 1131 (2000).

80. D. A. Ackerman, G. E. Shtengel, M. S. Hybertsen, *et al.*, IEEE J. Sel. Top. Quantum Electron. **1**, 250 (1995).

81. S. Seki, H. Oohashi, H. Sugiura, *et al.*, IEEE J. Quantum Electron. **32**, 1478 (1996).

82. J. I. Pankove, IEEE J. Quantum Electron. **4**, 119 (1968).

83. O. Stier, M. Grundmann, and D. Bimberg, Phys. Rev. B **59**, 5688 (1999).

84. C. H. Henry, R. A. Logan, and F. R. Merritt, J. Appl. Phys. **51**, 3042 (1980).

85. J. J. Coleman and K. J. Beernink, J. Appl. Phys. **75**, 1879 (1994).

86. H. Statz, C. L. Tang, and J. M. Lavine, J. Appl. Phys. **35**, 2581 (1964).

87. M. A. Alam, IEEE J. Quantum Electron. **33**, 1018 (1997).

88. C. L. Tang, H. Statz, and G. deMars, J. Appl. Phys. **34**, 2289 (1963).

89. K. Y. Lau and A. Yariv, in *Semiconductors and Semimetals*, Ed. by W. T. Tsang (Academic, New York, 1985; Radio i Svyaz', Moscow, 1990), Vol. 22, Part B, Chap. 2.

90. H. Hirayama, J. Yoshida, Y. Miyake, and M. Asada, IEEE J. Quantum Electron. **30**, 54 (1994).

91. R. A. Suris and S. V. Shtofich, Fiz. Tekh. Poluprovodn. (Leningrad) **16**, 1327 (1982) [Sov. Phys. Semicond. **16**, 851 (1982)].

92. R. A. Suris and S. V. Shtofich, Fiz. Tekh. Poluprovodn. (Leningrad) **17**, 1353 (1983) [Sov. Phys. Semicond. **17**, 859 (1983)].

Translated by M. Tagirdzhanov

LOW-DIMENSIONAL SYSTEMS

Formation of Nanocrystalline Silicon Films Using High-Dose H+ Ion Implantation into Silicon-on-Insulator Layers with Subsequent Rapid Thermal Annealing

I. E. Tyschenko*, V. P. Popov, A. B. Talochkin, A. K. Gutakovskiĭ, and K. S. Zhuravlev

Institute of Semiconductor Physics, Siberian Division, Russian Academy of Sciences,
ul. Akademika Lavrent'eva 13, Novosibirsk, 630090 Russia
*e-mail: tys@isp.nsc.ru

Abstract—The formation of nanocrystalline Si films as a result of rapid thermal annealing of silicon-on-insulator structures implanted with high doses of H+ ions is studied. It is ascertained that the process of formation of Si nanocrystals is active even at temperatures of 300–400°C and is controlled by the hydrogen content in the silicon film and by the duration of annealing. It is concluded that the formation of nuclei of the crystalline phase occurs in silicon islands surrounded by microvoids and is caused by the ordering of Si–Si bonds in the course of release of hydrogen from the bound state. It is important that microvoids do not coalesce at temperatures up to ~900°C in conditions of rapid thermal annealing. It is found that synthesized films exhibit luminescence in the green–orange region of the spectrum at room temperature. © 2004 MAIK "Nauka/Interperiodica".

1. INTRODUCTION

Silicon is the most important element in microelectronics and, according to predictions, will retain its leading status over the next 40 years. However, silicon is an indirect-gap semiconductor and, as a result, is an extremely inefficient emitter of light. This circumstance renders silicon unsuitable for applications in optoelectronics. At the same time, progress in communication technologies is imposing increasingly stringent requirements upon optoelectronic components integrated with electronic networks that are produced on the basis of silicon. The discovery of photoluminescence (PL) in porous silicon in the visible region of the spectrum [1] was responsible for the intense initial interest of researchers in this material. However, there are a number of problems related to the complexity of the practical application of porous silicon and caused by the instability of the properties of this material [2, 3]. In turn, this circumstance led to the development of a number of alternative methods for formation of nanocomposite materials that are based on silicon, emit efficiently in the visible region of the spectrum, and are quite compatible with available silicon technology. These methods include recrystallization of amorphous silicon using rapid thermal annealing [4], chemical deposition from the gaseous phase [5], thermal [6] and laser-induced [7] evaporation, high-frequency sputtering [8], deposition using the gas discharge [9], ion-beam synthesis in the SiO_2 host [10, 11], and other methods. Each of these methods has its own advantages and disadvantages. In particular, synthesis of nanocrystals by the vast majority of these methods requires annealing temperatures of ≥ 1000°C. Therefore, the

development of new methods (including those implemented at compatively low temperatures) for the production of nanocomposite materials remains a very urgent challenge. The physical basis of the method we used is the ability of hydrogen incorporated into silicon at high concentrations (amounting to several atomic percent) to stimulate the formation of microvoids and microcracks [12–15] that alternate with Si regions saturated with hydrogen. The size and number of microvoids depend both on the concentration of the incorporated hydrogen and on the temperature and duration of subsequent heat treatment [16]. This observation means that a decrease in the duration of heat treatment to several seconds can give rise to a high density of small voids separated by islands of crystalline silicon; i.e., this decrease can lead to the formation of films of nanoporous–nanocrystalline material and, what is more, at very moderate temperatures. The aim of this paper was to study the formation of nanocrystalline Si films in silicon layers implanted with high doses of hydrogen and subjected to rapid heat treatment. In order to eliminate the effect of the silicon substrate on properties of nanocrystalline films, we formed these films in silicon-on-insulator layers rather than in bulk Si.

2. EXPERIMENTAL

Silicon-on-insulator (SOI) structures were formed on Si (100) substrates. They incorporated a 500-nm-thick top Si layer and a 280-nm-thick buried SiO_2 layer and were implanted with 24-keV H+ ions to doses of 1×10^{17} and 3×10^{17} cm^{-2}; an ion–plasma source was used for implantation. After implantation, the samples
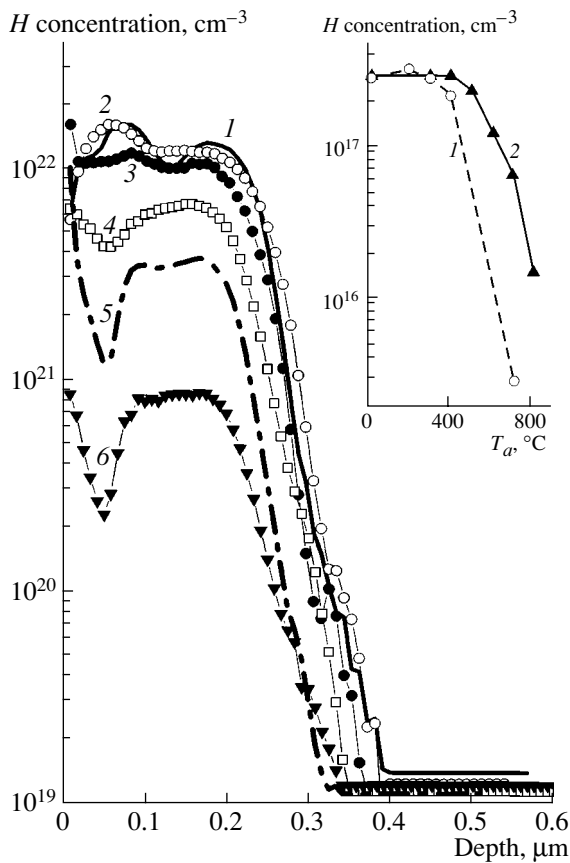
Fig. 1. Hydrogen concentration profiles measured by secondary-ion mass spectroscopy in silicon-on-insulator structures implanted with 24-keV H^+ ions with a dose of 3×10^{17} cm^{-2} (*1*) before annealing and after annealing for 10 s at $T_a =$ (*2*) 400, (*3*) 500, (*4*) 600, (*5*) 700, and (*6*) 800°C. Dependences of integrated hydrogen concentration on the temperature of annealing for (*1*) 1 h and (*2*) 10 s are shown in the inset.

were subjected to rapid thermal annealing for 10 s at temperatures $T_a = 300–900°C$ in ambient atmospheric air. For comparison, heat treatment with a duration of 1 h was also carried out in some cases in a furnace at the same temperatures in a nitrogen flow. The concentration profiles of hydrogen in SOI structures before and after heat treatment were measured using secondary-ion mass spectroscopy (SIMS). O_2^+ ions with an energy of 10 keV were used for sputtering. The structure of the layers was studied using Raman scattering spectroscopy and high-resolution transmission electron microscopy (HRTEM). The Raman spectra were measured in the backscattering configuration employing a DFS-52 spectrometer. The Raman spectra were excited using Ar laser radiation with a wavelength of 488 nm. Two geometric configurations of the sample were used in the excitation of Raman processes: $x(y + z, y + z)\bar{x}$ (the allowed geometry) and $x(y, y)\bar{x}$ (the forbidden geometry), where x, y, and z correspond to orientations (100),

(010), and (001). The use of forbidden geometry made it possible to substantially reduce the intensity of the line at 520 cm^{-1}; this line corresponds to scattering by optical phonons in the Si substrate. All the Raman spectra were measured at room temperature. The HRTEM studies were carried out using a JEM-4000EX microscope with a resolution of 0.2 nm and an accelerating voltage of 250 kV. Photoluminescence (PL) in the wavelength range $\lambda_{em} = 340–850$ nm was excited using the radiation of an N_2 laser with a wavelength $\lambda_{exc} = 337$ nm and a power of ~10 mW at room temperature.

3. RESULTS AND DISCUSSION

In Fig. 1 we show the concentration profiles of implanted H^+ in SOI structures before and after rapid thermal annealing. It can be seen that almost all the implanted hydrogen is initially (curve *1*) uniformly distributed in the layer with a thickness of ~0.3 μm. Subsequent annealing for 10 s at temperatures $T_a = 300–500°C$ did not result in redistribution of hydrogen in the implanted Si layer. A further increase in T_a brought about both changes in the shape of the hydrogen concentration profile and reduction in the hydrogen integrated concentration. An increase in the annealing temperature in the region $T_a > 500°C$ led to accumulation of hydrogen in the surface region; in addition, a dip in the hydrogen concentration at a depth of ~50 nm was observed. The dependence of the integrated hydrogen concentration in silicon on the temperature of postimplantation annealing is shown in the inset in Fig. 1. For comparison, the corresponding data on the results of thermal annealing for 1 h in a conventional furnace are also shown; the data were obtained by integrating the hydrogen concentration profiles reported previously by Tyschenko *et al.* [17]. An analysis of these dependences shows that, in the case of rapid thermal annealing, the integrated hydrogen concentration in the implanted silicon layer at the corresponding temperatures is higher than this concentration in the case of conventional annealing by a factor of 20. This result is consistent with the ratio of root functions for the furnace and the rapid heat treatments used in our experiments.

In Fig. 2 we show the Raman spectra obtained in the allowed geometry for the SOI structures implanted with a 3×10^{17} cm^{-2} dose of H^+ ions; the spectra were measured before and after rapid thermal annealing at temperatures $T_a = 300–700°C$. Two peaks were observed in the Raman spectra immediately after implantation (spectrum *1*). A broad peak located at about 480 cm^{-1} coincides with the spectrum of amorphous Si. The second peak located at 520 cm^{-1} is related to scattering by optical phonons in the Si host. In the course of isochronous annealing, we observe first a decrease in the half-width of the peak related to the amorphous phase ($T_a = 300°C$, spectrum *2*) and then (as T_a increases) a gradual decrease in the intensity of this peak. It is worth noting that we did not observe any shift in the energy position
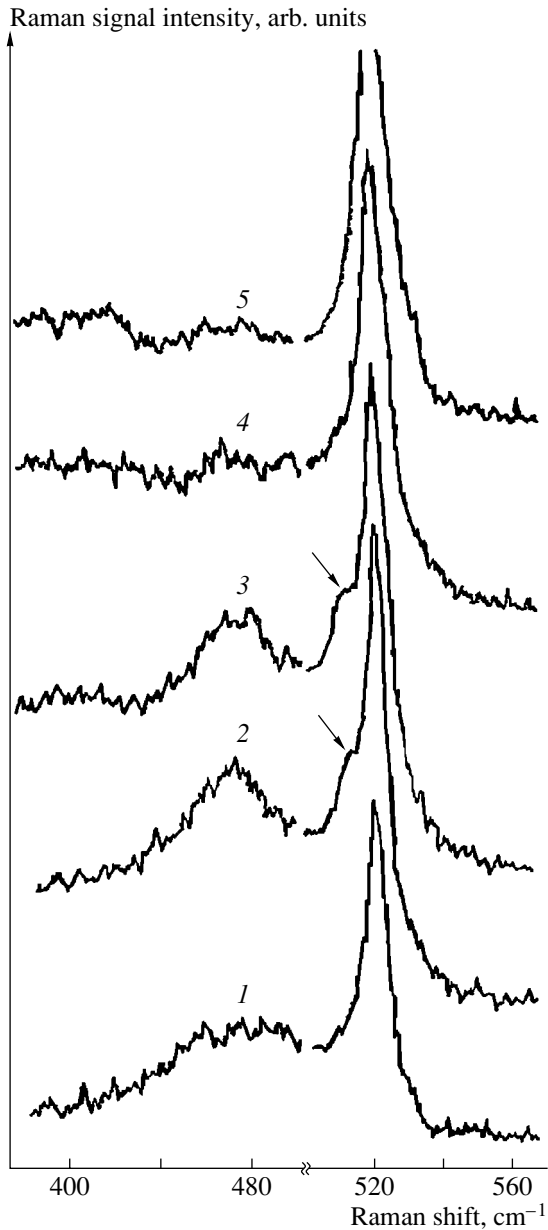
Raman signal intensity, arb. units

Raman signal intensity, arb. units

Fig. 2. Raman spectra measured in the allowed configuration for silicon-on-insulator structures implanted with 24-keV H$^+$ ions with a dose of 3×10^{17} cm^{-2} (*1*) before and after postimplantation annealing for 10 s at $T_a = $ (*2*) 300, (*3*) 400, (*4*) 600, and (*5*) 700°C.

Fig. 3. Raman spectra measured in the forbidden configuration for silicon-on-insulator structures implanted with 24-keV H$^+$ ions with a dose of 3×10^{17} cm^{-2} (*1*) before and after postimplantation annealing for 10 s at $T_a = $ (*2*) 400, (*3*) 600, (*4*) 700, and (*5*) 800°C.

of the peak with increasing annealing temperature. This circumstance can serve as additional evidence that the peak at 480 cm^{-1} corresponds to a broadened spectrum of phonon states in amorphous silicon. In the entire range of annealing temperatures T_a, the intensity of the peak at 520 cm^{-1} increased only slightly. At the same time, a line indicated by an arrow in Fig. 2 appears near the Si peak. We relate this line to silicon nanocrystals that formed in the amorphous host. The shift of the wave number of this line relative to the wave number of
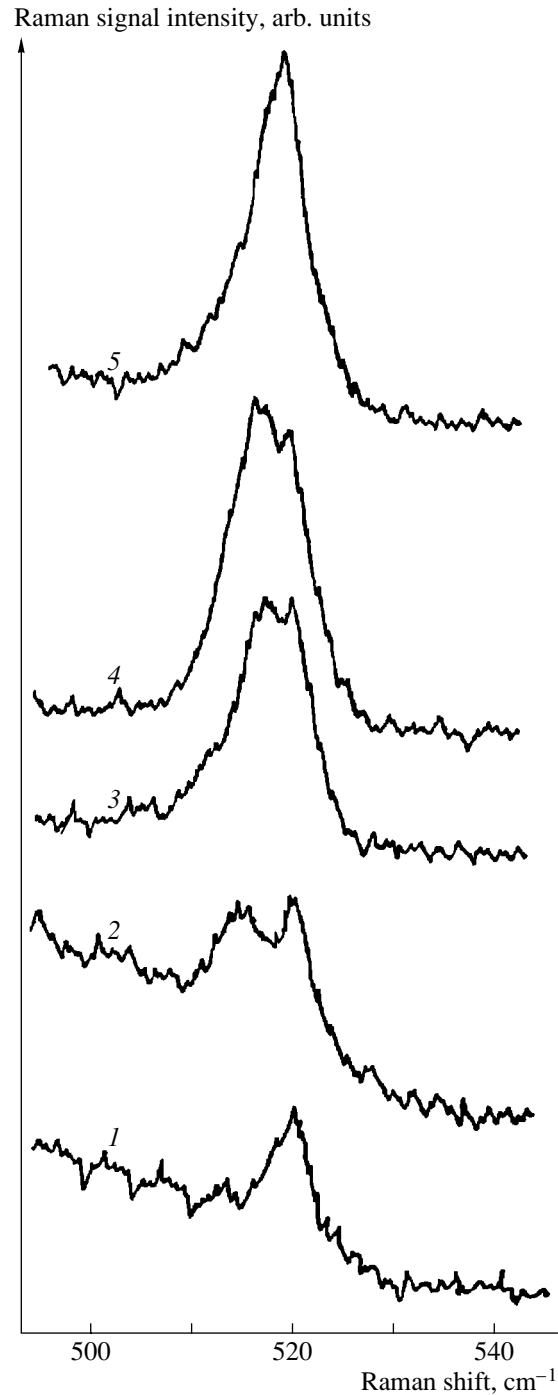
optical phonon in bulk Si (520 cm^{-1}) is caused by quantum-dimensional effects in Si nanocrystals. In Fig. 3 we show the Raman spectra of SOI structures after annealing at various temperatures; the spectra were obtained in the forbidden geometry of scattering. In this geome-
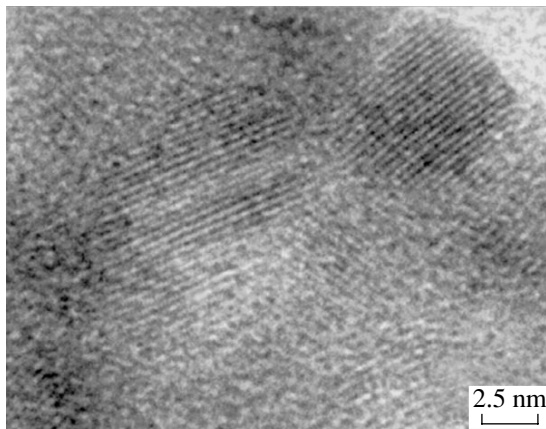
Fig. 4. An HRTEM image of the films obtained by implantation of silicon-on-insulator structures with 24-keV H^+ ions with a dose of 3×10^{17} cm^{-2} after subsequent annealing for 10 s at $T_a = 900°C$.

try, the intensity of the phonon line related to the Si substrate (520 cm^{-1}) is considerably suppressed, which makes it possible to study the behavior of the peak related to Si nanocrystals in more detail. As the annealing temperature increased, we observed a shift of this peak to higher frequencies (from 514 cm^{-1} after annealing at $T_a = 300–400°C$ to 517 cm^{-1} after annealing at $T_a = 600°C$ and 518 cm^{-1} after annealing at $T_a = 700°C$). As can be seen from Figs. 2 and 3, this shift occurs simultaneously with an increase in the intensity of the phonon-related line for Si nanocrystals and a decrease in the intensity of the peak related to optical phonons in the amorphous Si layer. These effects correspond to an increase in the sizes of Si nanocrystals in the course of crystallization of the amorphous phase. The presence of an intense line related to Si clusters and observed in the forbidden geometry indicates that these clusters are completely misoriented in reference to the Si substrate. No peaks related to nanocrystals were observed in the Raman spectra of the samples implanted with hydrogen ions at a dose of 1×10^{17} cm^{-2}.

The HRTEM studies showed also that rapid thermal annealing at $T_a \approx 400°C$ gave rise to Si nanocrystals embedded in the amorphous host. As the annealing temperature was increased in the range $T_a = 400–700°C$, the average dimensions of nanocrystals increased from 4.6 to 7.4 nm. A further increase in the annealing temperature to 900°C did not result in significant changes in the size of the Si nanocrystals. The nanocrystal density remained virtually unchanged in the entire T_a range under consideration and was equal to $\sim10^{12}$ cm^{-2}. In Fig. 4, we show an HRTEM image of nanocrystals formed as a result of annealing at 900°C. Calculations of interplanar spacing in these nanocrystals yield a value of ~0.314 nm. The latter is consistent with the separation between (111) planes in the diamond-like lattice of bulk Si. Figure 5 shows the distribution of nanocrystals in sizes after annealing at $T_a =$
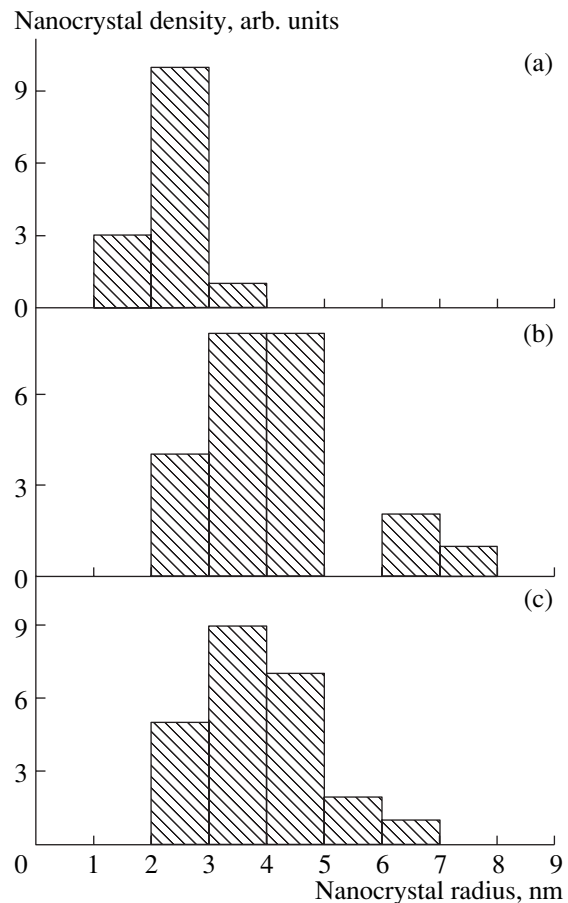

Fig. 5. Distributions of nanocrystals in sizes as obtained by statistical processing of HRTEM data for silicon-on-insulator structures implanted with 24-keV H^+ ions with a dose of 3×10^{17} cm^{-2} after postimplantation annealing for 10 s at $T_a =$ (a) 400, (b) 700, and (c) 900°C.

400, 700, and 900°C. These distributions can be described by Gaussian functions with the full width at half-maximum (FWHM) equal to 1.2 and 2 nm for annealing temperatures of 400 and 700–900°C, respectively.

The PL spectra measured at room temperature for the samples implanted with a high dose of hydrogen ions are shown in Fig. 6. No PL in the visible spectral region was detected in the case of unimplanted samples. A low-intensity broad band in the emission wavelength range from ~400 to ~600 nm was observed in the PL spectrum measured immediately after implantation. As the temperature of rapid thermal annealing T_a increased, the intensity of this PL band increased and attained a maximum at $T_a = 600°C$ (see the inset in Fig. 6). After annealing at this temperature, the FWHM of the PL band was equal to ~1 eV and the intensity was higher than that in unannealed samples by a factor of 3.5. An increase in T_a above 600°C was accompanied by a corresponding decrease in the PL intensity. Annealing at all temperatures T_a under consideration

only brought about a change in the PL intensity. No significant shifts of energy position of the PL band were observed.

In order to gain insight into the mechanism of formation of silicon nanocrystals under the conditions of rapid thermal annealing, let us consider in more detail the processes of structural transitions in silicon layers implanted with high doses of H^+ ions. Implantation of H^+ ions into silicon with concentrations amounting to tens of atomic percent is accompanied by the formation of microvoids separated by silicon regions with a high concentration of implanted hydrogen. In this case, hydrogen completes the dangling bonds and is found in the bound state. The properties of these microvoids are mainly controlled by the concentration of the implanted hydrogen. The exact mechanism of microvoid formation has yet to be clarified. The microvoids can coalesce as a result of postimplantation heat treatment. The process of microvoid coalescence depends on both the temperature and duration of the heat treatment. At the same time, the processes of hydrogen escape from the bound state and formation of H_2 molecules, which then diffuse to microvoids, are activated at annealing temperatures higher than 350°C [18]. As a result, hydrogen gas accumulates in a microvoiod and gas bubbles are formed. As T_a increases and hydrogen buildup in the microvoid increases, pressure in the microvoid increases to a certain critical value P_{cr}; the latter depends on the microvoid size and the distance from the microvoid to the surface [16]. At pressures $P > P_{cr}$, microvoids are destroyed and gas escapes from the implanted layer. In the case of small microvoids, the gas pressure in a microvoid can be lower than P_{cr}. As a result, hydrogen can diffuse to the Si surface as H_2 molecules and microvoids are not destroyed. This situation is apparently realized under conditions of rapid thermal annealing. The microvoids have no time to coalesce in an annealing time of ~10 s. In this case, recrystallization of the film can be considered as a process of recrystallization of silicon regions that are separated by microvoids and contain a high concentration of bound hydrogen. The formation of crystalline-phase nuclei occurs owing to the relocation of Si–Si bonds at the sites where hydrogen escapes from the bound state and to diffusion of hydrogen to microvoids and the silicon surface. This inference is supported by the fact that nanocrystals are formed even at comparatively low temperatures of pulsed (rapid) annealing $T_a \approx$ 300–400°C and that the nanocrystal density is independent of T_a. The density of the nuclei formed should be governed by the density and sizes of microvoids or by the concentration of the implanted hydrogen. Assuming in the simplest case that microvoids and crystalline regions are arranged regularly, we can estimate the average sizes of microvoids. Since the nanocrystal sizes remained virtually unchanged with T_a increasing from 700 to 900°C, we may assume that the silicon regions confined by voids crystallized completely at $T_a =$ 700°C, while the remaining portion of the volume is
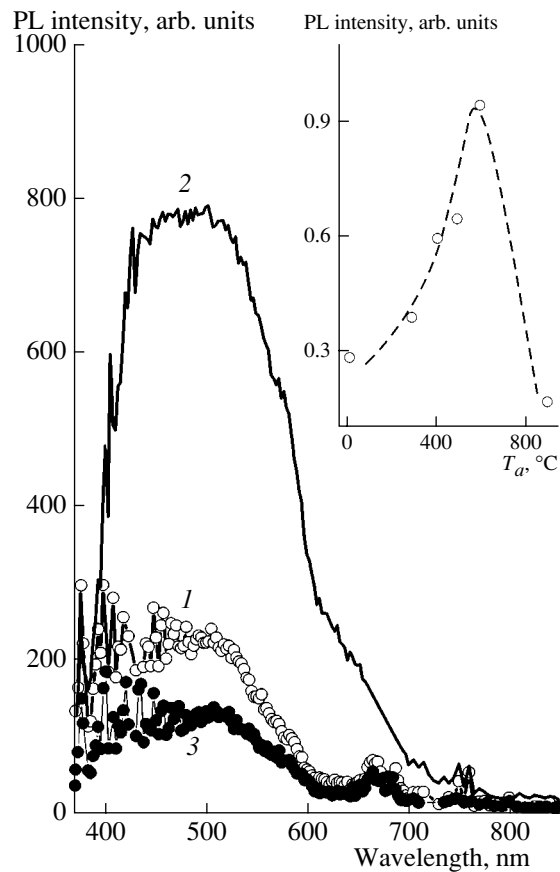

Fig. 6. Photoluminescence (PL) spectra of silicon-on-insulator structures implanted with 24-keV H^+ ions with a dose of 3×10^{17} cm^{-2} (*1*) before and after postimplantation annealing for 10 s at $T_a =$ (*2*) 600 and (*3*) 900°C. The wavelength of excitation radiation was 337 nm. The dependence of integrated intensity of photoluminescence (PL) on the annealing temperature is shown in the inset.

occupied by voids. Estimations show that nanocrystals with average dimensions of ~7.4 nm occupy ~40% of the implanted-layer volume after annealing at $T_a =$ 700°C. This means that the average size of voids located between nanocrystals is equal to ~9 nm. Thus, we are dealing in this case with nanocrystalline–nanovoid material whose properties differ from those of bulk silicon. Indeed, the invariance of the intensity of the Raman peak at 520 cm^{-1} when T_a increases to 900°C indicates that the absorption coefficient of the SOI-structure top layer that forms as a result of rapid thermal annealing remains higher than the absorption coefficient of single-crystal silicon. While annealing for 1 h at 700°C (see Fig. 2) brought about the complete crystallization of the top Si layer, at the same time the absorption coefficient of this layer decreased drastically and became much smaller than that of the uncrystallized layers. As a result, the intensity of the peak at 520 cm^{-1} increased by a factor of 4.5 after annealing at $T_a =$ 700°C.

An analysis of PL spectra shows that a variation in the PL band does not correlate with sizes of Si nanocrystals in the implanted layer of the SOI structure; i.e., the origin of this PL band is not related to direct recombination of quantum-mechanically confined electrons and holes in Si nanocrystals. Such a PL band has been previously observed in PL spectra of hydrogenated amorphous silicon [19]. Some researchers have expressed the opinion that the origin of this band is more probably related to organic contaminants at the surface rather than to bulk states in an amorphous film. However, in our experiments, PL was not observed in the samples implanted with hydrogen at a dose of 1×10^{17} cm^{-2}, which indicates that the PL was not related to surface contaminants. In our experiments, the PL intensity increased as hydrogen escaped from the bound state and attained a maximum at $T_a = 600°C$, when hydrogen should be mainly located in microvoids. The subsequent falloff of the PL intensity correlates with the escape of hydrogen gas from the implanted layer at $T_a > 600°C$. This observation may indicate that the observed PL band is related to the presence of unbound hydrogen atoms in the film; these atoms are located either at the grain boundaries of nanocrystals or in nanovoids.

4. CONCLUSION

We showed that rapid thermal annealing of silicon-on-insulator structures implanted with hydrogen ions brought about the formation of nanocrystalline Si films if the annealing temperatures were higher than about 300°C. It has been established that the formation of Si nanocrystals is controlled by the hydrogen content in the silicon film and proceeds efficiently if the hydrogen content is no lower than ~20 at %. On the basis of the data obtained, it is concluded that the coalescence of microvoids does not occur during rapid thermal annealing if the annealing temperature is no higher than ~900°C. In this case, the formation of the crystalline-phase nuclei takes place in silicon islands confined by microvoids and is caused by the ordering of Si–Si bonds in the course of hydrogen escape from the bound state. Synthesized films exhibit luminescence in the green–orange region of the spectrum at room temperature.

ACKNOWLEDGMENTS

REFERENCES

1. L. T. Canham, Appl. Phys. Lett. **57**, 1046 (1990).
2. L. T. Canham, M. R. Houlton, W. Y. Leong, *et al.*, J. Appl. Phys. **70**, 422 (1991).
3. C. H. Chen, Y. F. Chen, A. Shih, and S. C. Lee, Phys. Rev. B **65**, 195 307 (2002).
4. X. Zhao, O. Schoenfeld, J. Komuro, *et al.*, Phys. Rev. B **50**, 18 654 (1994).
5. M. Ruckschloss, B. Landkammer, and S. Veprek, Appl. Phys. Lett. **63**, 1474 (1993).
6. H. Morisaki, H. Hashimoto, F. W. Ping, *et al.*, J. Appl. Phys. **74**, 2977 (1993).
7. E. Werwa, A. A. Seraphin, L. A. Chiu, *et al.*, Appl. Phys. Lett. **64**, 1821 (1994).
8. Q. Zhang, S. C. Bayliss, and D. A. Hutt, Appl. Phys. Lett. **66**, 1977 (1995).
9. R. E. Hummel, M. H. Ludvig, and S.-S. Chang, Solid State Commun. **93**, 237 (1995).
10. T. Shimizu-Iwajama, S. Nakao, and K. Saitoh, Appl. Phys. Lett. **65**, 1814 (1994).
11. H. A. Atwater, K. V. Shcheglov, S. S. Wong, *et al.*, Mater. Res. Soc. Symp. Proc. **316**, 409 (1994).
12. L. B. Freund, Appl. Phys. Lett. **70**, 3519 (1997).
13. C. M. Varma, Appl. Phys. Lett. **71**, 3519 (1997).
14. M. K. Weldon, V. E. Marsico, Y. J. Cjabal, *et al.*, J. Vac. Sci. Technol. B **15**, 1065 (1997).
15. T. Höchbauer, A. Misra, M. Nastasi, and J. W. Mayer, J. Appl. Phys. **92**, 2335 (2002).
16. W. Han and J. Yu, J. Appl. Phys. **89**, 6551 (2001).
17. I. E. Tyschenko, A. B. Talochkin, B. A. Kolesov, *et al.*, Nucl. Instrum. Methods Phys. Res. B **186**, 329 (2002).
18. V. P. Popov, A. K. Gutakovskii, L. N. Safronov, *et al.*, in *Progress in SOI Structures and Devices Operating at Extreme Conditions*, Ed. by F. Balestra, A. Nazarov, and V. S. Lysenko (Kulwer Academic, Dordrecht, 2002), p. 269.
19. B. A. Wilson, Phys. Rev. B **23**, 3102 (1981).

Translated by A. Spitsyn

AMORPHOUS, VITREOUS, AND POROUS SEMICONDUCTORS

The Effect of a Au Impurity on the Photoluminescence of Porous Si and Photovoltage on Porous-Si Structures

E. F. Venger, S. I. Kirillova, I. M. Kizyak, É. G. Manoĭlov*, and V. E. Primachenko

Institute of Semiconductor Physics, National Academy of Sciences of Ukraine, Kiev, 03028 Ukraine
*e-mail: dept_5@isp.kiev.ua
Submitted February 10, 2003; accepted for publication April 21, 2003

Abstract—The effect of doping with gold on the photoluminescence properties and electronic states of structures consisting of porous Si and single-crystal Si, formed by chemical stain etching, was studied. The time-resolved photoluminescence spectra and the temperature dependences of the capacitor photovoltage were measured. It is shown that the introduction of Au from gold-salt solutions into porous Si somewhat decreases the intensity of photoluminescence and changes its spectral distribution. The parameters of electronic states in porous Si and at the interface between porous Si and single-crystal Si change more significantly, which manifests itself in photovoltage measurements. © 2004 MAIK "Nauka/Interperiodica".

1. INTRODUCTION

Joint analysis of the photoluminescence and the electronic properties of low-dimensional Si structures yields important information on the nature of photoluminescence (PL) in the visible spectral region at room temperature, the mechanisms of recombination of charge carriers and excitons, and the parameters of local electronic states. This information is required to develop structures for silicon optoelectronic devices. Measurements of time-resolved PL spectra and temperature dependences of capacitor photovoltage are effective methods of investigation. Previously (see, for example, [1, 2]), these methods were used to study structures consisting of layers of porous silicon (*por*-Si) on *p*-type single-crystal silicon (*por*-Si–*p*-Si), which were prepared by chemical stain etching. It was shown that, both for these *por*-Si layers and for *por*-Si obtained by anodization, the PL is related to the quantum-confinement effects caused by the limitation of charge carriers and excitons in Si nanocrystals. Local states were found which serve as traps for nonequilibrium electrons at the interface between *por*-Si and p-Si and nonequilibrium holes in the *por*-Si layer. Spectra of boundary electronic states of *p*-Si were also investigated.

In this paper, we report the results of studying the effect of a Au impurity on the properties of structures formed of *por*-Si and *p*-Si using measurements of time-resolved PL and capacitor photovoltage. Deposition of metals on *por*-Si has always received much attention (see, for example, [3]) in view of the potential possibilities of developing device structures. Effective passivation of dangling bonds in Si by gold was revealed in [4], where the electron spin resonance in single-crystal Si doped with gold was studied. Recently, we have demonstrated the significant effect of gold on the photolu-

minescence and electronic properties of nanocrystalline Si (*nc*-Si) films obtained by pulsed laser ablation (gold was introduced into the films during their formation) [5]. However, the effect of metals on *por*-Si has been insufficiently studied, especially their effect on the parameters of electronic states in *por*-Si and at the interface between porous Si and single-crystal Si.

The purpose of this paper is to study the time-resolved PL spectra and the electronic states of *por*-Si–*p*-Si structures obtained by stain etching with subsequent treatment in solutions containing a gold salt.

2. EXPERIMENTAL

Layers of *por*-Si less than 1 μm thick were formed on chemomechanically polished surfaces of KDB-10 silicon (*p*-Si:B, $\tau = 10 \, \Omega$ cm) wafers with (100) orientation, which were treated in a solution HF : HNO$_3$: H$_2$O (1 : 3 : 5) for 10 min [1]. The PL spectra and photovoltage were measured in the initial *por*-Si–*p*-Si structures. Then these structures were doped with a Au impurity from a solution of AuCl$_3$ dissolved either in water or in an aqueous solution of HF(1%) [6]. The dopant concentration in the solutions was 2×10^{-5} M and the time of treating a sample in a solution amounted to 2 min. The measurements of the PL spectra and the photovoltage were performed again with the Au-doped samples.

The PL was excited by pulses of nitrogen-laser radiation with wavelength $\lambda = 377$ nm, pulse width $\tau = 8$ ns, and peak power $P_p = 2$ kW. The sampling measurement of signals was performed in the photon-counting mode. The measurement strobe (during which photons are accumulated) had a width of 250 ns. The PL-decay times shorter than 250 ns were measured by an oscilloscope. Successive spectra were recorded with a delay of
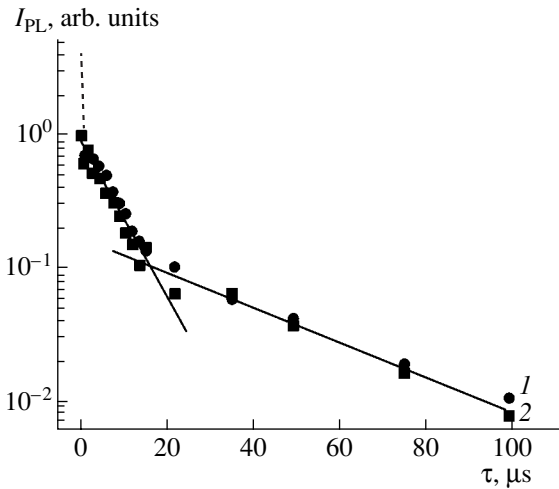
I_{PL}, arb. units

Fig. 1. PL decay for *por*-Si–*p*-Si structures (*1*) before and (*2*) after treatment in an aqueous HF solution (1%) with 2×10^{-5} M of $AuCl_3$.

the measurement strobe with respect to the laser pulse. The delay (equal to an integer number of strobe widths) was increased arbitrarily up to the longest times of relaxation spectra, i.e., to tens of microseconds.

In order to measure the photovoltage across *por*-Si–*p*-Si samples, a capacitor of the sample–mica type with a semitransparent conducting layer of $SnO_2\langle Sb\rangle$ on the back side of the mica was fabricated. The ohmic contacts to *p*-Si were formed by deposition of aluminum onto Si with subsequent alloying by a laser beam. The photovoltage generated in the SnO_2–*por*-Si–*p*-Si–Al capacitor under illumination by light pulses was recorded on a storage oscilloscope. As a source of light pulses, we used an ISSh-100 flash lamp generating pulses of white light with an intensity of $\sim 10^{21}$ photons/(cm^2 s) and a width of 10 µs in single-pulse mode or a train of pulses with a frequency of 1 Hz. The temperature dependences of photovoltage were measured as the temperature was decreased from $T = 300$ to 100 K, after the measuring capacitor was placed in a cryostat with a pressure of residual gases of $\sim 10^{-4}$ Pa.

Pulses of both white and red light were used to measure the photovoltage. In the latter case, a KS-19 light filter was used, which transmits radiation in the wavelength range 700–2700 nm. Under illumination by pulses of red light, which is absorbed mainly in *p*-Si, we measured the photovoltage that was generated in the *p*-type substrate and was equal (with the sign reversed) to the boundary potential of *p*-Si (with regard to the calibration coefficient of the measurement scheme). The light-pulse intensity is sufficient to flatten the energy bands of *p*-Si at the interface with *por*-Si. This circumstance makes it possible to disregard the Dember voltage due to the equalizing of the mobilities of nonequilibrium electrons and holes caused by the electron–hole scattering at large densities of charge carriers [7].

Under illumination by pulses of white light, we measured the total photovoltage, which is generated both in *p*-Si and in *por*-Si (where the short-wavelength part of the radiation is absorbed).

The measurements showed that the photovoltage signal generated by the first light pulse may differ in magnitude from the signals generated by the second or any subsequent pulse in the train. This phenomenon is related to the capture of nonequilibrium charge carriers by traps at the interface between *por*-Si and *p*-Si or in *por*-Si. When we used red light (in this case, the capture of nonequilibrium electrons at the *por*-Si–*p*-Si interface was observed at low temperatures), after each measurement, a sample was heated to make the captured electrons escape from traps and then cooled again to a new temperature for measuring the photovoltage generated by the first and second pulses. It should be noted that the photovoltage signals generated by the second and subsequent pulses of both white and red light could not be distinguished, which indicates the saturation of traps (both in *por*-Si and at the interface between *por*-Si and *p*-Si) by nonequilibrium carriers even during the first light pulse.

3. EXPERIMENTAL RESULTS

The most drastic decrease in the intensity of the PL of initial and Au-doped structures occurs a few hundred nanoseconds after the PL excitation. Then, as can be seen from Fig. 1, the PL decays by the exponential law successively with two characteristic times: $\tau_1 \approx 35$ µs and $\tau_2 \approx 120$ µs. Figures 2a and 2b show the normalized spectral dependences of the PL intensity $I_{PL}(h\nu)$ measured, respectively, during the first strobe (the fast PL with a decay time of 250 ns) and in the range from 250 ns to the time corresponding to the complete decay of PL (the integrated PL). In the case of doping with gold from an aqueous solution of $AuCl_3$, the spectral dependences of the fast and integrated PL $I_{PL}(h\nu)$ changed only slightly: the maximum values of I_{PL} decreased by 10 and 20%, respectively, and the positions of peaks and the shapes of the dependences did not change. The decay times τ_1 and τ_2 also did not change. Such a weak effect of Au in the case of doping from an aqueous solution may be caused by the presence of an amorphous SiO_2 layer on the surface of *por*-Si formed by stain etching [8], which impedes the penetration and deposition of Au^{+3} ions in *por*-Si. Therefore, Figs. 1 and 2 also show the dependences for a sample doped with gold from an aqueous HF solution (1%) with $AuCl_3$. HF dissolves the SiO_2 layer, and as a result the Au impurity has a greater effect on the PL of the structure.

As can be seen from Fig. 1, doping with gold somewhat decreases the times τ_1 and τ_2. After doping, the peaks in the dependences $I_{PL}(h\nu)$ for the fast (Fig. 2a) and integrated (Fig. 2b) PL shift from 2.0 to 2.05 eV and from 1.9 to 1.8 eV, respectively. Notably, the peak intensities of the fast and integrated PL decrease in
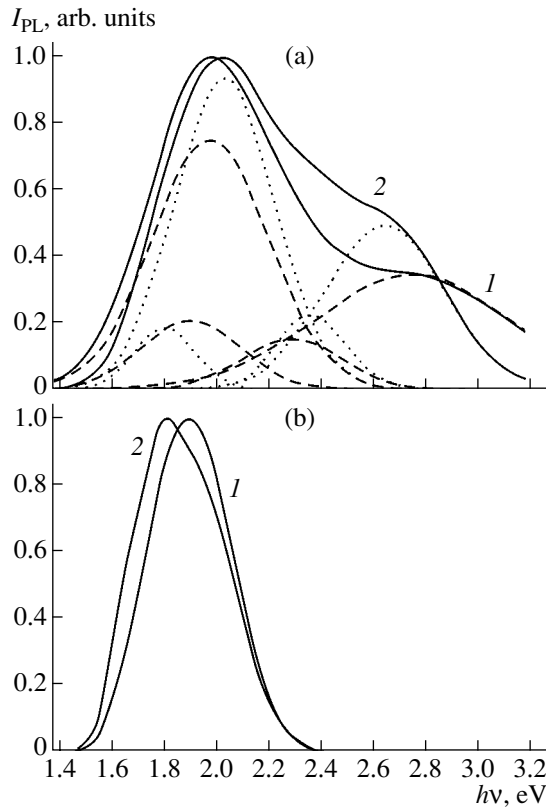
Fig. 2. Normalized spectral dependences of PL (*1*) before and (*2*) after treatment in an aqueous HF solution (1%) with 2×10^{-5} M of $AuCl_3$. (a) Fast PL (<250 ns) with expansion of spectra *1* and *2* in Gaussians (dashed and dotted lines, respectively). (b) Time-integrated PL spectrum.

magnitude by a factor of 3 and 5, respectively. In addition, the spectral distribution of the fast PL (Fig. 2a) changes. Indeed, the spectrum measured before doping can be expanded in four Gaussian functions peaked at energies $h\nu$ = 1.90, 1.98, 2.30, and 2.75 eV, whereas, after doping, the corresponding peaks are located at 1.80, 2.05, 2.35, and 2.65 eV, respectively.

The control experiments aimed at studying the effect of an aqueous HF solution (1%) without gold on *por*-Si showed that it is mainly HF that is responsible for the decrease in the maximum values of $I_{PL}(h\nu)$, the shift of the peak from 1.9 to 1.8 eV (Fig. 2b) in the spectral dependences of the integrated PL, whose shape is close to Gaussian both before and after doping, and the decrease in the values of I_{PL} of the fast PL at $h\nu$ > 2.9 eV. At the same time, the introduction of gold into the structure leads to a decrease in the times τ_1 and τ_2, a shift of the peak in the dependence $I_{PL}(h\nu)$ of the fast PL, and an increase in the normalized value of the fast PL intensity in the range 2.0–2.8 eV.

Figure 3 shows the temperature dependences of the photovoltage for the initial structure and that doped with Au from water (a) and for the structures treated in an aqueous HF solution (1%) and doped with Au from
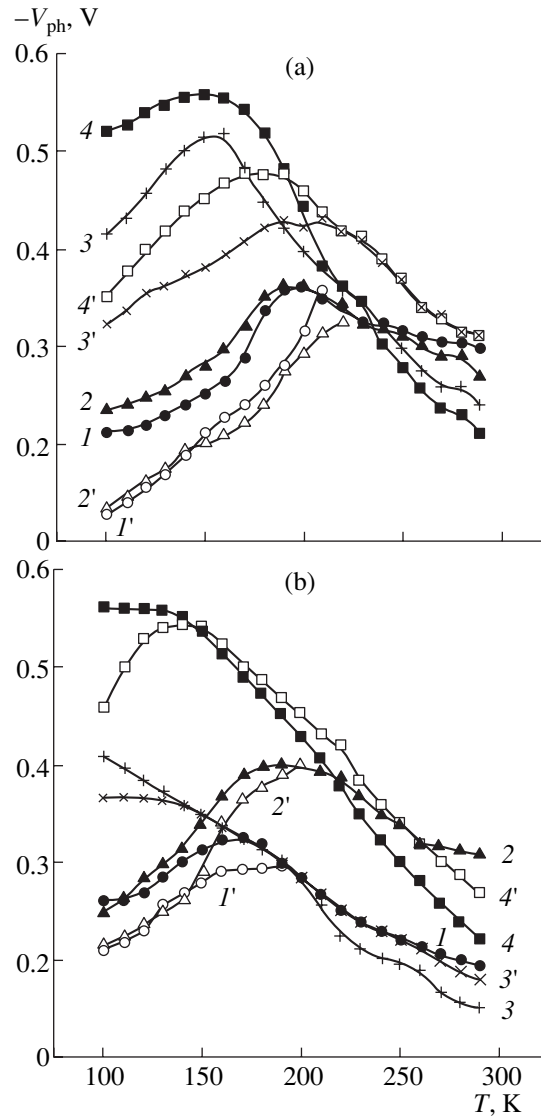

Fig. 3. Temperature dependences of photovoltage in the *por*-Si–*p*-Si structures: (a) initial and doped with Au from water; (b) treated in an HF solution (1%) and doped with Au from an HF solution (1%). The curves were measured (*1*, *1'*, *3*, *3'*) before and (*2*, *2'*, *4*, *4'*) after doping with Au. Curves (*1–4*) correspond to the first pulses of (*1*, *2*) red and (*3*, *4*) white light and curves (*1'–4'*) correspond to the second pulses of (*1'*, *2'*) red and (*3'*, *4'*) white light.

an HF solution (1%) (b). Curves *1*, *1'*, *3*, and *3'* were obtained for undoped structures illuminated by the first (*1*, *3*) and the second (*1'*, *3'*) pulses of red (*1*, *1'*) and white (*3*, *3'*) light of the flash lamp. Curves *2*, *2'*, *4*, and *4'* were measured for Au-doped structures illuminated by the first (*2*, *4*) and the second (*2'*, *4'*) pulses of red (*2*, *2'*) and white (*4*, *4'*) light. The values of the photovoltage V_{ph} were always negative (the negative potential on the $SnO_2\langle Sb\rangle$ electrode). In the case of illumination by red light, the photovoltage is equal to the boundary potential of the *p*-Si substrate $\varphi_s = |V_{ph}|$. At room temperature, the lowest positive potential φ_s = 0.195 V
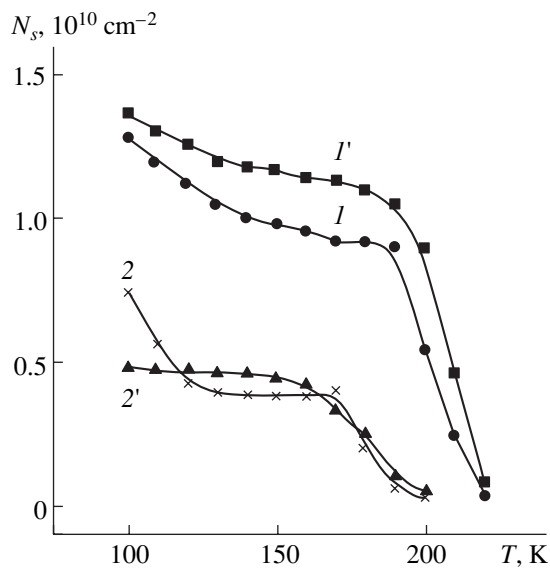
N_s, 10^{10} cm^{-2}

Fig. 4. Temperature dependences of the concentration of nonequilibrium electrons captured by boundary traps in *p*-Si for the following structures: (*1*) initial, (*1'*) doped with Au from water, (*2*) treated in an HF solution (1%), and (*2'*) doped with Au from an HF solution (1%).

(the energy bands at the *p*-Si surface are bent down) is observed after treating the *por*-Si–*p*-Si system in an aqueous HF solution (1%). Doping with gold from an HF solution (1%) leads to an increase in φ_s up to 0.310 V. Doping with gold from water hardly changes the boundary potential of the initial system ($\varphi_s = 0.300$ and 0.270 V before and after doping, respectively).

The portions of curves *1* and *2* in Figs. 3a and 3b, in which $\varphi_s = |V_{ph}|$ increases as temperature decreases, are due to the charging of the boundary electronic states of *p*-Si by holes, which occurs when the Fermi level of the bulk *p*-Si shifts towards the valence band. The density of boundary electronic states in the structures under investigation can be calculated (see, for example, [9]). It was found that, both for the initial structure and that treated in an HF solution (1%), the density of boundary electronic states near the midgap of Si, E_i, amounts to $\sim 2 \times 10^{11}$ cm^{-2} eV^{-1}. Doping with Au from water and an HF solution (1%) increases the density of boundary electronic states near E_i to $\sim 1 \times 10^{12}$ cm^{-2} eV^{-1}, which is consistent with the results obtained previously for the case of a real Si surface doped with Au [6].

Curves *1* and *2* in Figs. 3a and 3b show that, at $T \leq 200$ K, φ_s decreases with decreasing temperature. This phenomenon is due to the reversible reconstruction of the system of boundary electronic states, which is caused by stresses at the interface between *por*-Si and *p*-Si (the latter arise as temperature decreases [2]). In addition, at low temperatures ($T < 180$ and < 200 K for structures untreated and treated in an HF solution (1%), respectively), curves *1* and *2*, measured under illumination by the first pulses of red light, differ from curves *1'* and *2'*, measured under illumination by the second

pulses of red light. This circumstance means that, in the case of illumination by the first pulse, boundary traps in *p*-Si capture nonequilibrium electrons, which, being retained in traps, ensure the photomemory of the surface potential [2, 6]. The difference between the values yielded by curves *1* and *1'*, *2* and *2'* can be used to calculate the number of electrons captured by boundary traps, N_s [10], which is equal to the number of traps since the latter become saturated with electrons even during the first light pulses. Figure 4 shows the obtained dependences $N_s(T)$. The increase in N_s with decreasing temperature is due to the fact that shallower traps (located closer to the bottom of the conduction band of Si) become involved in trapping and conservation of nonequilibrium electrons. It can be seen from Fig. 4 that doping with gold from an aqueous solution somewhat increases the concentration of deeper traps, whereas doping with gold from an HF solution (1%) decreases the concentration of shallow traps. It is noteworthy that the concentration of deep traps decreases significantly when the initial structure is treated in an HF solution (1%).

Let us now analyze the dependences $V_{ph}(T)$ measured with decreasing temperature under illumination of structures by white light, which is absorbed not only in the *p*-Si substrate, but also in the *por*-Si film (Figs. 3a, 3b; curves *3*, *3'*, *4*, *4'*). The important feature of the measured dependences is that, at $T > 150$–180 K, the values of $|V_{ph}|$ obtained under illumination by the first light pulse are smaller than in the case of illumination by the second pulse. This fact means that the capture of nonequilibrium holes by traps located in *por*-Si occurs in this temperature range. The time of confinement of holes at traps in *por*-Si exceeds 10^2 s even at room temperature; furthermore, it increases significantly as temperature decreases. Therefore, when measuring the dependences $V_{ph}(T)$, we did not perform any procedures aimed at releasing holes from traps (delay in time and heating of samples), as was done to release the captured electrons from boundary traps in *p*-Si in the case of illumination with red light. In this context, we did not calculate the temperature dependences for the holes captured in *por*-Si, which accumulate there as the measurement temperature increases. With a decrease in temperature, the accumulation of holes in *por*-Si leads to a significant increase in $|V_{ph}|$ both in undoped and Au-doped structures. It is worth noting that the maximum values of $|V_{ph}|$ for Au-doped structures (curves *4*) exceed the corresponding values for undoped structures (curves *3*). This means that the capture of holes in *por*-Si doped with Au from water (Fig. 3a) and from an HF solution (1%) (Fig. 3b) is more intense. This is confirmed by the differences between curves *3*, *3'* and *4*, *4'* at room temperature for the undoped and Au-doped structures: 0.065 and 0.090 V (doping from water) and 0.035 and 0.045 V (doping from an HF solution (1%)), respectively. The calculations performed for $T = 290$ K (in this case, traps in *por*-

Si do not contain any stored holes before the first and second light pulses) showed that the surface density of holes captured in the layer of *por*-Si in the starting structure and in that treated in an HF solution (1%) is no less than 9.2×10^9 and 5.8×10^9 cm^{-2}, respectively, whereas, after doping with Au, the corresponding values are 13.6×10^9 and 6.6×10^9 cm^{-2}, respectively.

Since in the case of illumination with white light we measure the total photovoltage in *p*-Si and *por*-Si, at $T < 220$–200 K, the above-mentioned capture of electrons by traps in *p*-Si near the interface occurs along with the capture of holes in *por*-Si. In addition, the photovoltage $|V_{ph}|$ in *p*-Si decreases due to the structural reconstruction of the interface between *por*-Si and *p*-Si. Both these factors mean that the total photovoltage $|V_{ph}|$ for the case of illumination with white light, having attained a maximum with decreasing temperature, may then decrease as temperature decreases further. Such behavior was observed experimentally for all the structures under study (Figs. 3a, 3b) except for the one doped with Au from an HF solution (1), when the photovoltage only levels off as temperature decreases.

The difference between the values of photovoltage V_{ph}^w and V_{ph}^r obtained for the first pulses of white and red light, respectively, is equal to the photovoltage arising in *por*-Si: $V_{ph}^{por\text{-}Si} = V_{ph}^w - V_{ph}^r$. Figure 5 shows the dependences of $V_{ph}^{por\text{-}Si}$ for the initial structure (curve *1*) and that treated in an HF solution (1%) (curve *2*) and for the initial structure and that doped with doped with Au (curves *1'* and *2'*, respectively). It can be seen that, at relatively high temperatures, the photovoltage in *por*-Si is positive, in contrast to the photovoltage generated in *p*-Si. The photovoltage may be positive only if there is an initial built-in negative charge in the *por*-Si film, located close to its external boundary.

With a decrease in temperature, the positive photovoltage $V_{ph}^{por\text{-}Si}$ decreases and changes its sign in the temperature range $T = 240$–170 K for different structures, increasing in magnitude with a further decrease in temperature. First of all, the reason for the change of sign is the above-considered capture of holes by traps in *por*-Si. With a decrease in temperature, these holes, captured and retained by traps, give rise to a built-in positive charge exceeding in magnitude the initial built-in negative charge, which plays an important role at high temperatures.

It can be seen from Fig. 5 that the doping of structures with Au from aqueous solutions changes the photovoltage in the *por*-Si film insignificantly (both positive and negative values). The fact that $V_{ph}^{por\text{-}Si}$ is somewhat higher for negative values after doping is due to the fact that the doping leads to enhanced capture of holes in *por*-Si. The latter effect is especially pronounced when we compare the dependences $V_{ph}^{por\text{-}Si}(T)$

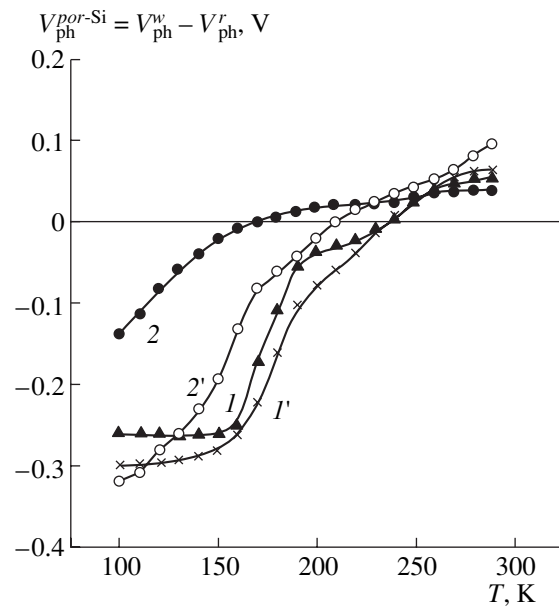$$V_{ph}^{por\text{-}Si} = V_{ph}^w - V_{ph}^r, \text{V}$$

Fig. 5. Temperature dependences of photovoltage in *por*-Si for the following structures: (*1*) initial, (*1'*) doped with Au from water, (*2*) treated in an HF solution (1%), and (*2'*) doped with Au from an HF solution (1%).

for the structures treated in an HF solution (1%) with (curve *2*) and without (curve *2'*) gold. It can be seen that in this case doping with Au significantly increases the magnitudes of both positive and negative values of $V_{ph}^{por\text{-}Si}$.

4. DISCUSSION

It can now be considered proven that the appearance of a noticeable photovoltage at room temperature in *por*-Si and in films of nanocrystalline Si is due to the quantum-confinement effect of increasing the band gap and the increased probability of radiative transitions in Si nanocrystals [11–13]. It is also ascertained that light is absorbed in nanocrystalline Si upon excitation of PL, due to which kinetically bound subsystems of free electron–hole pairs and excitons arise in Si nanocrystals [12, 13]. It was shown in many publications that the PL quantum yield at room temperature amounts to a few percent. This means that most excited electron–hole pairs recombine nonradiatively. It is suggested that the major mechanism of nonradiative recombination is the recombination through local centers in Si nanocrystals, which form dangling bonds ≡Si• [14].

The dominant mechanism of nonradiative recombination in *por*-Si is related to excitons. We suggest that the transformation of the PL spectra with time occurs as follows. After absorption of the excitation radiation in Si nanocrystals, the radiative recombination of free charge carriers and excitons occurs (the recombination times <250 ns). The subsequent microsecond PL decay with characteristic time τ_1, which contributes most significantly to the integrated PL spectra, is, in our opin-

ion, caused by the radiative annihilation of excitons localized at Si=O bonds on Si nanocrystals [11]. This is corroborated by the following facts: (i) the oxidation of *por*-Si nanocrystals of different size, which exhibit PL spectra in a wide frequency range (depending on the nanocrystal size) after hydrogen deposition, leads to the dominance of a red band in the PL spectra, which is almost independent of the size of Si nanocrystals [11]; (ii) in accordance with the calculations carried out in terms of different approximations [11, 15, 16], Si=O bonds form a band gap in the energy range 1.4–2.1 eV; (iii) the electroreflectance spectra of *por*-Si fabricated by stain etching demonstrate a direct transition at energies in the range 1.8–1.9 eV [17]; and (iv) in the case of absorption of materials with high permittivity onto *por*-Si, the PL intensity decreases significantly due to the decrease in the exciton binding energy in Si nanocrystals; however, the peak of integrated PL does not shift [18] since excitons are bound at local centers of the Si=O type.

The time τ_1 is found by solving the differential equations [18] describing the change in the density of free charge carriers and excitons bound to Si=O centers with time. The solution of these equations yields $\tau_1 = \tau_{nr}(1 + N_0/n_0)$, where τ_{nr} is the time of nonradiative recombination of free charge carriers and N_0 and n_0 are the densities of excitons bound to Si=O centers and free charge carriers, respectively, at the initial instant of the PL decay with time τ_1. The binding of electron–hole pairs into excitons and with Si=O centers in Si nanocrystals impedes their fast nonradiative recombination.

The tail in the PL falloff with characteristic time τ_2, observed by us, is obviously related to the recombination of nonequilibrium charge carriers, some of which are captured by traps in the oxide covering Si nanocrystals. The photovoltage measurements showed that these charge carriers are holes. The rejection of some portion of the captured holes from the traps back into the nanocrystalline Si layer results in their recombination with the electrons that were not removed from nanocrystalline Si. This phenomenon manifests itself in the PL decay with time τ_2, which is controlled by the hole-transport time.

It is well known that metal ions with positive standard electrochemical potential with respect to the potential of Si ions are reduced on a Si surface due to the redox reactions [6]. As a result, an island metal structure is formed on Si, which is controlled by the initial state of the Si surface, the composition of the solution from which the adsorption of metal ions occurs, the content of the metal salt in the solution, the metal type, and the deposition conditions (time, temperature, illumination). The size of islands ranges from nanometers to tens of nanometers [6]. It was shown in [19] using the deposition of silver as an example that such an island structure of a metal coating is also typical of *por*-Si formed by electrochemical etching. As was shown by Auger electron spectroscopy [3], Ag ions penetrate

through pores deep into the *por*-Si layer. If the concentration of deposited Ag islands is high, they may coagulate. When Ag ions are deposited onto a hydrated surface of Si nanocrystals, hydrogen is released and the nanocrystals are oxidized to form SiO_2 [19]. An increase in the time of deposition of Ag ions results in a decrease in the maximum intensity of the time-integrated PL and a small gradual shift of the PL peak to long waves [3].

In our previous studies, where the Au impurity was introduced into various nanocrystalline Si films by other methods, the Au dopant significantly increased the PL intensity [5, 20]. The PL intensity increased by a factor of 3 when the Au impurity was introduced into a solution of color etchant in the course of growing a *por*-Si layer on a *p*-Si substrate [20]. In this case, the introduction of Au hardly changed the PL decay time. Therefore, the increase in the PL intensity was attributed to the formation of conditions (due to the presence of gold) under which a large number of Si nanocrystals is formed per unit substrate area. The PL decay time increased by almost three orders of magnitude (from tens of nanoseconds to tens of microseconds) when gold was introduced into nanocrystalline Si films formed by laser ablation of a Si target from a backward [5] and forward [21] flow of erosion-torch particles onto a *p*-Si substrate. After doping with Au, the PL intensity also increased significantly. Before the doping, the PL intensity had a broad spectral distribution peaked at 2.5 eV, and, after the doping, two bands peaked at 2.5 and 1.6 eV arose. In this case, the intensity of the band at 1.6 eV could exceed that of the band at 1.6 eV by an order of magnitude. It should be noted that, among all the electropositive metals we studied (Ag, Au, Cu), only gold gave rise to a significant increase in the PL intensity and the PL decay time, which is related to the fact that Au atoms have a higher ionization energy and electron affinity compared to Si atoms. The significant increase in the PL intensity and decay time in the case of doping with Au was attributed to the saturation of dangling bonds of Si atoms on the surface of Si nanocrystals by gold and to the growing of a SiO_2 layer on nanocrystalline Si under the catalytic effect of gold.

In this study, in contrast to the above results, the introduction of a Au impurity decreases rather than increases the PL intensity, only slightly changing the PL decay time. In the case of doping from an HF solution (1%), the decrease in the PL intensity is mainly due to the fact that some of the nanocrystals of *por*-Si are etched away, which is caused by the presence of HF [22]. The red shift of the spectral dependence of the integrated PL can be attributed to the etching of small Si nanocrystals. The difference between the results of this study and those of [5, 21] is related to the fact that, in the experiments performed here, the dangling Si bonds on the surface of the Si nanocrystals were initially almost completely passivated by Si–H, Si–OH, Si–O, and Si=O bonds, which resulted in a relatively

small effect of Au on the PL properties. Nevertheless, the Au impurity, which somewhat reduces the PL intensity, enhances the contribution of fast ($\tau < 250$ ns) high-energy ($h\nu > 1.9$ eV) components of PL decay, which is reasonable to attribute to the reduction in the size of the Si nanocrystals due to their additional oxidation during doping [19].

As photovoltage measurements show, doping with Au affects the electronic states in *por*-Si and at the interface between *por*-Si and *p*-Si more significantly. After the doping, the density of boundary electronic states in *p*-Si increases severalfold, which indicates the penetration of Au ions through *por*-Si to the interface between *por*-Si and *p*-Si. Doping from water and an HF solution (1%) leads to changes in the concentrations of deep and shallow traps, respectively, for nonequilibrium electrons. In addition, doping with Au results in a significant increase in the positive and negative photovoltages on *por*-Si at room temperature and at $T \leq 200$ K, respectively. The increase in the positive photovoltage can be attributed to the additional oxidation of Si nanocrystals, whereas the increase in the negative photovoltage can be attributed to the higher density of states in *por*-Si that capture nonequilibrium holes.

CONCLUSION

The photovoltage method turned out to be rather sensitive to the effect of doping with Au on the characteristics of the structures formed from *por*-Si and *p*-Si. The data obtained on the electronic states in *por*-Si and at the interface between *por*-Si and *p*-Si in the Au-doped structures may be rather useful for studying the current transport in such structures with the aim of designing electroluminescent devices. In addition, since Au nanocrystals are formed during the doping of *por*-Si with Au, a system containing both Si and Au nanocrystals, which ensure a large internal-surface area, can be effectively used as a catalyst.

REFERENCES

1. L. L. Fedorenko, A. D. Sardaly, É. B. Kaganovich, *et al.*, Fiz. Tekh. Poluprovodn. (St. Petersburg) **31**, 6 (1997) [Semiconductors **31**, 4 (1997)].
2. E. F. Venger, É. B. Kaganovich, S. I. Kirillova, *et al.*, Fiz. Tekh. Poluprovodn. (St. Petersburg) **33**, 1330 (1999) [Semiconductors **33**, 1202 (1999)].
3. D. Andsager, J. Hilliard, and M. H. Nayfeh, Appl. Phys. Lett. **64**, 1141 (1994).
4. V. M. Maevskiĭ, V. E. Primachenko, O. V. Snitko, and N. G. Frolova, Poverkhnost, No. 1, 101 (1983).
5. É. B. Kaganovich, I. M. Kizyak, S. I. Kirillova, *et al.*, Fiz. Tekh. Poluprovodn. (St. Petersburg) **36**, 1105 (2002) [Semiconductors **36**, 1027 (2002)].
6. V. E. Primachenko and O. V. Snitko, *Physics of Semiconductor Surfaces Doped by Metals* (Naukova Dumka, Kiev, 1988).
7. Z. S. Gribnikov and V. I. Mel'nikov, Fiz. Tekh. Poluprovodn. (Leningrad) **2**, 1352 (1968) [Sov. Phys. Semicond. **2**, 1133 (1968)].
8. M. J. Winton, S. D. Russell, and R. Gronsky, J. Appl. Phys. **82**, 436 (1997).
9. S. I. Kirillova, V. E. Primachenko, E. F. Venger, and V. A. Chernobai, Semicond. Phys. Quantum Electron. Optoelectron. **4**, 12 (2001).
10. S. I. Kirillova, V. E. Primachenko, and V. A. Chernobaĭ, Optoélektron. Poluprovodn. Tekh., No. 21, 60 (1999).
11. M. V. Wolkin, J. Jorne, P. M. Fauchet, *et al.*, Phys. Rev. Lett. **82**, 197 (1999).
12. A. G. Gullis, L. T. Canham, and P. D. J. Calcott, J. Appl. Phys. **82**, 909 (1997).
13. D. Kovalev, H. Heckler, G. Polisski, and F. Koch, Phys. Status Solidi B **215**, 871 (1999).
14. M. Lannoo, C. Delerue, and G. Allan, J. Lumin. **57**, 243 (1993).
15. H. Kageshima and K. Shiraishi, Surf. Sci. **380**, 61 (1997).
16. A. Puzder, A. J. Williamson, J. C. Grossman, and G. Galli, Phys. Rev. Lett. **88**, 097401 (2002).
17. E. F. Venger, R. Yu. Holiney, L. A. Matveeva, and A. V. Vasin, Fiz. Tekh. Poluprovodn. (St. Petersburg) **37**, 104 (2003) [Semiconductors **37**, 103 (2003)].
18. P. K. Kashkarov, B. V. Kamenev, E. A. Konstantinova, *et al.*, Usp. Fiz. Nauk **168**, 577 (1998) [Phys. Usp. **41**, 511 (1998)].
19. I. Coulthard, R. Sammyniaken, S. J. Naftel, *et al.*, Phys. Status Solidi A **182**, 157 (2000).
20. É. B. Kaganovich, I. M. Kizyak, S. I. Kirillova, *et al.*, Optoélektron. Poluprovodn. Tekh., No. 37, 132 (2002).
21. S. I. Kirillova, V. E. Primachenko, É. G. Manoĭlov, and I. R. Bazylyuk, Optoélektron. Poluprovodn. Tekh., No. 37, 165 (2002).
22. E. F. Venger, T. Ya. Gorbach, S. I. Kirillova, *et al.*, Fiz. Tekh. Poluprovodn. (St. Petersburg) **36**, 349 (2002) [Semiconductors **36**, 330 (2002)].
23. T. Kawasaki, Y. Takai, and R. Shimizu, Appl. Phys. Lett. **79**, 3509 (2001).

Translated by Yu. Sin'kov

AMORPHOUS, VITREOUS,
AND POROUS SEMICONDUCTORS

Effect of a Fullerene Coating on the Photoluminescence of Porous Silicon

O. M. Sreseli*^, D. N. Goryachev*, L. V. Belyakov*, S. P. Vul'*, I. B. Zakharova**, and E. A. Alekseeva**

*Ioffe Physicotechnical Institute, Russian Academy of Sciences, St. Petersburg, 194021 Russia
^e-mail: Olga.Sreseli@mail.ioffe.ru
**St. Petersburg State Polytechnical University, St. Petersburg, 195251 Russia
Submitted July 10, 2003; accepted for publication July 14, 2003

Abstract—The interaction of a matrix of silicon nanocrystallites (porous silicon layer) with embedded fullerene molecules C_{60} was studied. The degradation of fullerene-containing layers as a result of irradiation with a strongly absorbed laser light was explored. It is shown that the layers with highest stability are obtained after high-temperature annealing in hydrogen. In this case, the photoluminescence spectra remain virtually unchanged when the layers are kept in air and irradiated with a high-intensity laser irradiation. Possible mechanisms of the phenomena studied are discussed. © 2004 MAIK "Nauka/Interperiodica".

1. INTRODUCTION

Owing to its strongly developed surface, porous silicon (*por*-Si) can be used in high-sensitivity sensors for gases, liquids, etc. [1, 2]. At the same time, this same property gives rise to a considerable instability of many parameters of *por*-Si, above all, its photoluminescent properties, which are defined by the degree of nanocrystallite passivation with hydrogen [3]. Storing the samples in air results in partial oxidation of the surface and changes in the properties of *por*-Si. These changes are particularly pronounced under high-intensity laser irradiation.

One of the methods of stabilizing a strongly developed and chemically active *por*-Si surface is to conserve it with different inert or passivating coatings. As is well known, under certain conditions (in particular, at high temperatures) silicon reacts with carbon to form silicon carbide SiC [4], which is stable against external actions. From various carbon modifications, we have selected fullerene C_{60}, which can be deposited onto *por*-Si both by vacuum evaporation and directly from a solution. It was expected that the deposition of fullerene onto *por*-Si with subsequent annealing can stabilize the optical properties of a porous layer.

2. FABRICATION OF *por*-Si LAYERS AND MEASUREMENT PROCEDURE

Layers of *por*-Si were produced using the standard technique of anodic etching of *p*-Si in HF : alcohol (1 : 1) solution in the dark. The current density was 20 mA/cm^2; the etching time, 5 min. Two methods of fullerene deposition were used: deposition in a vacuum by the hot-wall technique [5] and precipitation from

orthoxylene solution [6]. The results obtained by both methods were similar.

Time-resolved photoluminescence (PL) spectra were recorded using an FEU-79 photomultiplier under excitation by pulsed UV laser light ($\lambda = 337$ nm, 10 ns, 100 Hz). Fast PL (at the peak of the exciting pulse) and slow PL in quasi-stationary mode were recorded with a delay of ~1 μs between the laser pulse and the instant of the PL pulse recording.

Fast and slow PL spectra were studied before and after the deposition of C_{60}, as well as after the annealing of layers, with fullerene and without it, in hydrogen at 1000°C for 30 min. Furthermore, the modifications of spectra under the effect of intense laser irradiation (pulse power 100–300 kW cm^{-2}, average power 100–300 mW cm^{-2}) were studied. All the spectra below are presented without taking into account the spectral sensitivity of the photomultiplier (and the whole measuring setup), since this normalization is insignificant for the study of degradation effects.

3. RESULTS AND DISCUSSION

Figure 1 shows typical spectra of fast and slow PL before fullerene deposition (curves *1*, *2*) and after it (curves *3*, *4*). As can be seen, the intensity of the slow band decreases (in some cases, it disappears completely), but the spectrum shape remains unchanged. The quenching of the slow band after the fullerene deposition most probably indicates the formation of new channels of nonradiative recombination, for example, by suppressing the hydrogen passivation of the surface of nanocrystallites. At the same time, the fullerene coating can partially absorb the emitted light because of the small width of the fullerene band gap.
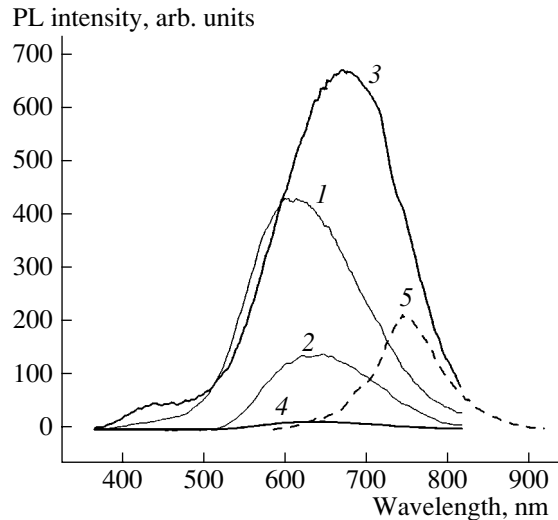
PL intensity, arb. units

Fig. 1. PL spectra of *por*-Si (here and below, the spectra are presented with the spectral dependence of the sensitivity of the experimental setup disregarded): (*1*, *2*) without fullerene, (*3*, *4*) after fullerene deposition, (*1*, *3*) fast PL component, (*2*, *4*) slow PL component, and (*5*) smooth Si surface after fullerene deposition.

After the deposition of C_{60}, the shape and intensity of the fast PL spectrum are considerably modified. The total intensity of the fast band increases noticeably due to the enhancement of the red wing, and a peak in the blue part of the spectrum appears (Fig. 1, curve *3*). The fast short-wavelength band (in the range 400–500 nm) is frequently attributed to radiative recombination via the levels on the interface between the silicon oxide and Si nanocrystallites. In our case, the emergence of an intense and broad emission band with short decay time can supposedly be accounted for by the formation of radiative-recombination centers related to the adsorption of fullerene molecules on the *por*-Si surface. In addition, the enhancement of the red wing of the spectrum is related to PL of fullerene itself (cf. Fig. 1, curve *5*, which shows the fast PL spectrum of C_{60} layer deposited onto polished Si).

Time dependences of the PL intensity under long-term irradiation by a laser (laser-induced degradation) were monitored at all stages of preparation of the samples (see Fig. 2). For freshly prepared *por*-Si samples, the PL intensity first decays fast and then slows down and the intensity levels off; the shape of the spectrum remains virtually unchanged (Fig. 3). It is worth noting the reversibility of the PL decay: the initial PL intensity is partially (by ~50%) restored after 1-h storage in the dark (Fig. 3, curve *3*).

After the deposition of fullerene, the character of the PL degradation changes. An unexpected result was that, in some cases, the intensity of fast PL increased under the influence of laser irradiation (Fig. 4, inset), and the spectrum blue-shifted (Fig. 4, curve 2). We attribute this effect to local heating of the *por*-Si surface. As is
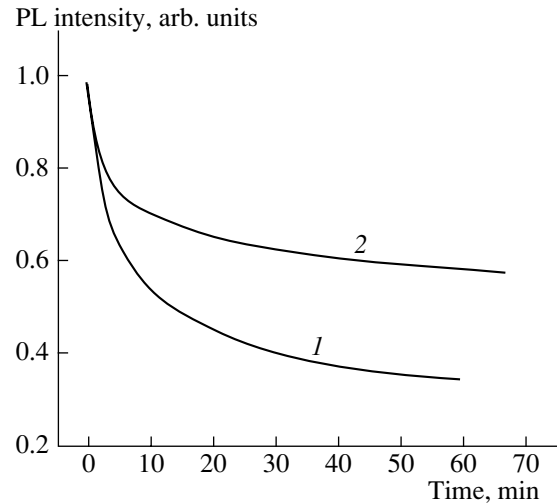
PL intensity, arb. units

Fig. 2. The decay of PL from freshly prepared *por*-Si under laser irradiation: (*1*) fast ($\lambda = 450$ nm) and (*2*) slow ($\lambda = 650$ nm) PL components.

shown in [7], the desorption of hydrogen from a *por*-Si surface begins at ~280°C, and C_{60} molecules are adsorbed directly by Si. This effect can result in the formation of fast radiative-recombination centers other than the fullerene centers. Local heating of *por*-Si may also cause the evaporation of the excess fullerene, which partially absorbs the emitted light. This explanation is also confirmed by the irreversibility of spectra modifications after storage in the dark.

Virtually all the decay curves of fast PL from freshly prepared samples are well approximated by two exponential functions, fast and slow, or by a well-extended exponential function (with the exponent to a power less than unity).
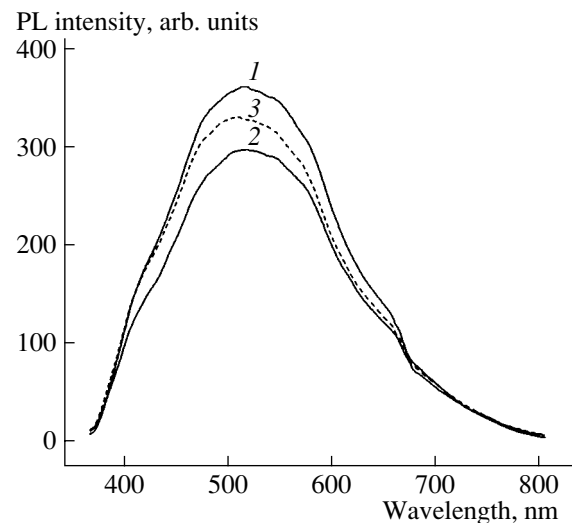
PL intensity, arb. units

Fig. 3. Temporal variation of the fast PL spectra of initial *por*-Si. The spectra were recorded (*1*) before irradiation, (*2*) 30 min after the beginning of irradiation, and (*3*) after 40-min storage in the dark.
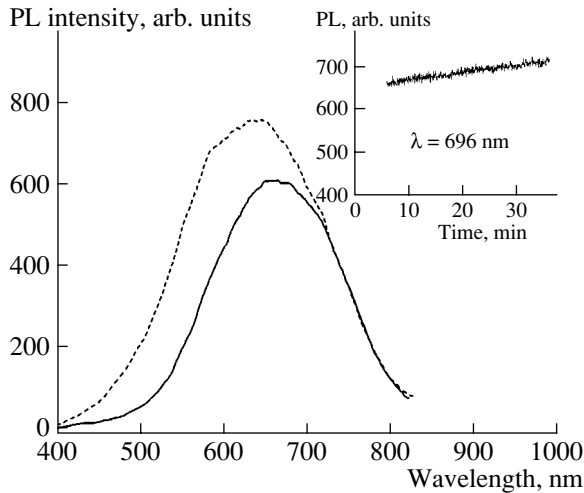
Fig. 4. Temporal variation of the fast PL spectra of *por*-Si with fullerene deposited: (*1*) initial spectrum, (*2*) recorded 20 min after the beginning of irradiation; inset: temporal variation of the PL intensity at $\lambda = 696$ nm.

Fig. 5. Fast PL spectra of (*1*) *por*-Si with fullerene after annealing and (*2*) initial *por*-Si sample.

The degradation of PL from *por*-Si suggests that the number of nonradiative-recombination centers increases. The PL intensity $I(t)$ at the instant t is inversely proportional to the number of these centers $N(t)$ [8]. Based on the exponential experimental decay curves, we can represent the $N(t)$ dependence as

$$N(t) = N(\infty) - [N(\infty) - N(0)]\exp[-(t/\tau)^{\beta}],$$

where $N(0)$ and $N(\infty)$ are the number of centers at the initial instant of time and at infinity; τ, the degradation time constant; and β, the stretching exponent of the stretched exponential ($\beta < 1$).

It may be suggested that the increase in the number of nonradiative-recombination centers under laser irradiation is related to weaker passivation of *por*-Si by hydrogen (to hydrogen desorption), but this does not account for the partial relaxation of PL after storage in the dark. Most likely, the reversible part of the PL decay is related to the Auger recombination of photoexcited carriers.

Annealing radically changes the character of the PL spectra: the whole wide spectrum from near-UV to near-IR is characterized by small decay times (Fig. 5, curve *1*). The PL color becomes white-blue, sometimes yellowish. For comparison, curve *2* in Fig. 5 shows the spectrum of fast PL from a freshly prepared sample without fullerene. The laser degradation of the PL spectrum in annealed samples is much weaker than in unannealed, and the samples annealed after fullerene deposition demonstrate the highest stability (Fig. 6).

After annealing, the PL decay almost follows the single-exponential law, with a very long decay time. The dramatic slowing down of degradation is indicative of a substantial reconstruction of the *por*-Si surface. Fullerene molecules decompose during annealing, and the formation of silicon carbide molecules becomes
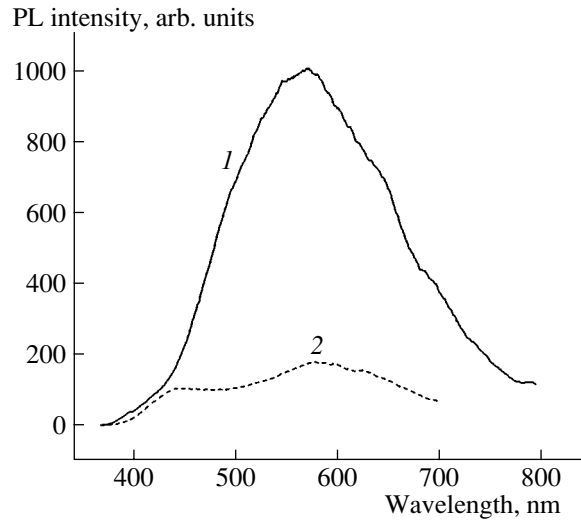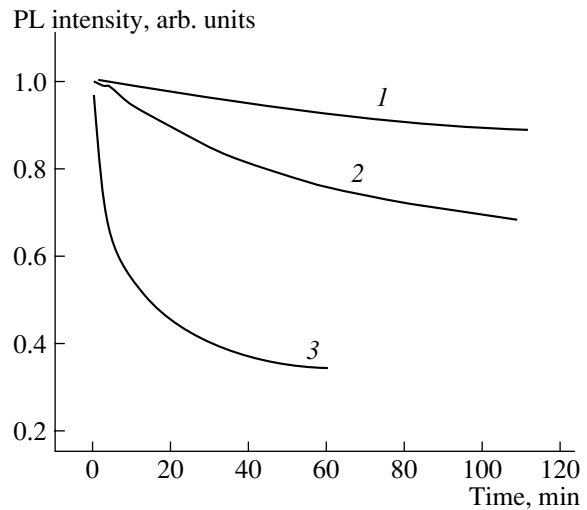

Fig. 6. The decay of fast PL from *por*-Si under laser irradiation: (*1*) annealed *por*-Si with fullerene, (*2*) annealed sample with a smaller amount of the fullerene deposited, and (*3*) initial *por*-Si.

possible. The stabilization of PL from annealed *por*-Si layers with fullerene is an indirect indication of the formation of a stable carbide phase.

Thus, it is shown that the luminescent properties of *por*-Si can be markedly stabilized by the deposition of fullerene with subsequent high-temperature annealing. An intense PL spectrum with fast decay is observed in the whole visible range, from near-UV to near-IR.

ACKNOWLEDGMENTS

REFERENCES

1. M. Y. Ghannam, A. A. Abouelsaood, and J. F. Nijs, Sol. Energy Mater. Sol. Cells **60**, 105 (2000).

2. C. Baratto, G. Faglia, E. Comini, *et al.*, Sens. Actuators B **77**, 62 (2001).

3. A. G. Cullis, L. T. Canham, and P. D. J. Calcott, J. Appl. Phys. **82**, 909 (1997).

4. L. Moro, A. Paul, D. C. Lorents, *et al.*, J. Appl. Phys. **81**, 6141 (1997).

5. T. L. Makarova, I. B. Zakharova, T. I. Zubkova, and A. Ya. Vul', Fiz. Tverd. Tela (St. Petersburg) **41**, 354 (1999) [Phys. Solid State **41**, 319 (1999)].

6. O. M. Sreseli, D. N. Goryachev, V. Yu. Osipov, *et al.*, Fiz. Tekh. Poluprovodn. (St. Petersburg) **36**, 604 (2002) [Semiconductors **36**, 574 (2002)].

7. M. De Seta, D. Sanvitto, and F. Evangelisti, Phys. Rev. B **59**, 9878 (1999).

8. I. M. Chang, S. C. Pan, and Y. F. Chen, Phys. Rev. B **48**, 8747 (1993).

Translated by D. Mashovets

===== **PERSONALIA** =====

Émmanuil Il'ich Adirovich
(On the 30th Anniversary of His Death)

Émmanuil Il'ich Adirovich (1915–1973) was born in Melitopol'. He graduated from Moscow State University. Adirovich worked at the Lebedev Physical Institute, USSR Academy of Sciences, from 1940 to 1962 and at the Physicotechnical Institute of the Uzbek Soviet Socialist Republic (Tashkent) from 1962 to 1973. Adirovich was one of the founders of the quantum-mechanical theory of luminescence in crystals. He is also known as a pioneer in the field of optoelectronics and dielectric electronics in the Soviet Union. In his scientific activity, Adirovich paid considerable attention to applied problems in the development of semi-conductor devices: he studied transient processes in transistors and diodes, and he contributed to the theory of optrons and optronic circuits. Adirovich, who was a doctor of science (physics and mathematics) and a full member of the Academy of Sciences of the Uzbek Soviet Socialist Republic, founded the Tashkent scientific school of solid-state physics.

Professor Yu.R. Nosov

Translated by A. Spitsyn

ATOMIC STRUCTURE AND NONELECTRONIC PROPERTIES OF SEMICONDUCTORS

The Evolution of Surface Structures in *p*-CdTe Crystals under Pulsed Laser Irradiation

A. Baĭdullaeva, M. B. Bulakh, A. I. Vlasenko, A. V. Lomovtsev, and P. E. Mozol'

Institute of Semiconductor Physics, National Academy of Sciences of Ukraine, Kiev, 03028 Ukraine
e-mail: baidulla@yahoo.com
Submitted April 1, 2003; accepted for publication April 29, 2003

Abstract—The dynamics of modification of the surface structure in *p*-CdTe (111) crystals subjected to nanosecond ruby laser pulses with a lasing wavelength within the fundamental-absorption region ($\hbar\omega = 1.78$ eV) is studied. It is shown that, depending on the radiation dose, the surface morphology changes in the following order: the formation of tellurium film, an increase in the density of dislocations under the tellurium film, and the formation of ordered quasi-periodic structures of both micrometer and nanometer size. The size of the structures and the character of their distribution are shown to be dose-dependent. © 2004 MAIK "Nauka/Interperiodica".

INTRODUCTION

Laser modification of semiconductor materials is one of the most promising methods of producing the components of present-day optoelectronic and microelectronic devices. It is well known that the high-power laser irradiation of a semiconductor surface may change the morphology of the surface layer structure. In this context, a new approach to controlling the properties of semiconductors has recently been actively developed. It is based on the laser-induced formation of low-dimensional structures (including intrinsic point and extended defects and the dopant atoms) in the matrix material.

Unlike the techniques for the production of low-dimensional structures, for example, from gaseous or liquid phases, the method considered here implies that these structures are formed in the semiconductor crystal lattice, which acts as a matrix and plays an essential role at each stage of the process.

In order to realize the high potential of this approach, further theoretical and experimental investigation of the low-dimensional structure formation is required. In this study, we trace the dynamics of the laser-induced structural changes, including the appearance of low-dimensional structures, in the surface layers of *p*-CdTe crystals. As the experimental samples, we used nominally undoped, scaly, and dislocation-free ($N_d \approx 10^2$ cm^{-2}) *p*-CdTe (111) crystals obtained by the vapor-phase synthesis of initial elements [1]. The samples were 100 μm thick. The crystals were irradiated at room temperature by a Q-switched ruby laser with pulse duration $\tau = 2 \times 10^{-8}$ s. The structural morphology of the as-prepared and irradiated samples was detected with the help of an optical MI-4 microscope and a NanoScope IIIa (Digital Instruments) atomic-force microscope (AFM) working in the tapping mode. For the AFM measurements, silicon probes with a tip nominal radius of ~10 nm were employed.

RESULTS

Figure 1a shows a micrograph of an island-like Te film appearing on a CdTe surface subjected to laser radiation with power density $I = 2$ MW/cm^2 and dose $D_1 = 0.08$ J/cm^2 (where $D = IN\tau$, N is the number of pulses, and τ is the pulse duration). The Te film is amorphous immediately after the irradiation and crystallizes with time [2]. The film was etched off using a methanol solution of 1N KOH. The subsequent selective etching of the surface revealed a dislocation-rich region that was formed under the Te film at a depth from ~3 to 5 μm. The irradiation dose at which the Te film is
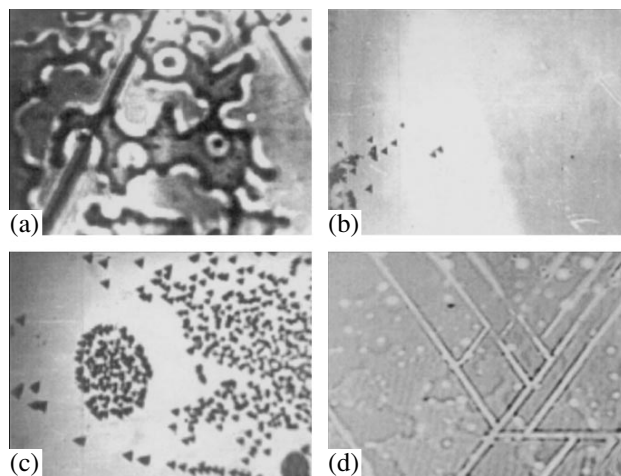

Fig. 1. Micrograph of a (111) *p*-CdTe crystal surface irradiated by ruby laser pulses: (a) the appearance of the islandlike Te film; (b, c, d) after the selective etching of the sample.
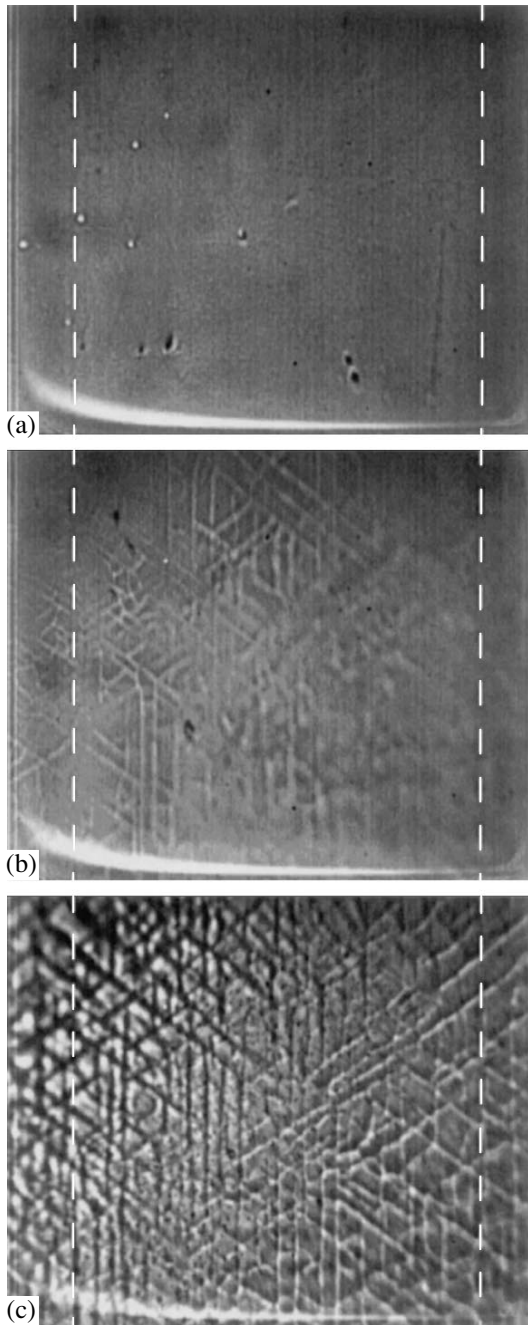
Fig. 2. Dislocation networks at the *p*-CdTe (111) crystal surface of (a) an as-prepared sample and the samples irradiated with a dose of (b) 0.32 and (c) 0.8 J/cm^2.

formed ($D_1 = 0.08$ J/cm^2) corresponds to the appearance of dislocations with random density distribution (Fig. 1b). As the irradiation dose increases to $D_2 = 0.16$ J/cm^2, the dislocation density grows to $N_d = 7 \times 10^3$ cm^{-2}, and the dose $D_3 = 0.32$ J/cm^2 brings about the formation of separate (uncoordinated) elements of the dislocation network (Figs. 1c, 1d). Similar dynamics of the surface structuring is observed at the same dose (D_3) attained by fewer pulses with a higher power den-

sity (but not exceeding the damage or melting threshold of the material) (Fig. 2b). A further increase in the irradiation dose to $D_4 = 0.8$ J/cm^2 leads to the formation of a dislocation network with its elements ordered and oriented at an angle of 120° with respect to each other (Fig. 2c).

The results of an AFM study show that the as-prepared samples are atomically smooth with arithmetic-mean roughness $R_a \approx 0.056$ nm, and uniformly distributed nanometer islands appear on the surface after irradiation. Figures 3a and 3b show the AFM image of a fragment (20×20 μm) of a *p*-CdTe (111) crystal surface after laser irradiation with doses D_3 and D_4. The linear dimensions of the islands vary in the range 25–350 nm, and their height ranges from 1 to 17 nm depending on the irradiation dose (Figs. 3c, 3d).

In the AFM image of a 1×1-μm fragment of the surface irradiated with dose D_3 (Fig. 3c), one can see quasi-periodic islands with linear dimensions of ~125–350 nm and a height of ~2 nm. As the dose increases to D_4, the structure becomes more distinct: small hills with linear dimensions ranging from 25 to 30 nm appear inside the large islands. At the same time, the height of the islands grows to 17 nm (Fig. 3d).

DISCUSSION

One of the causes of the formation of dislocations that one should consider is the appearance of thermal strain in surface layers, which are transformed into a plastic state upon laser heating. Because of the high surface absorption coefficient of ruby-laser radiation in CdTe crystals ($K \approx 10^5$ cm^{-1}), the crystal surface heats up to $T \approx 700$°C [3]. For comparison, the melting point of CdTe is $T_m = 1092$°C. As a result of the relaxation of thermal stress that is produced in the heated-up surface layer during the laser pulse, dislocations appear at the crystal surface [4]. Therefore, one should expect the interface between the heated-up surface layer and the cool bulk to be strained and to contain randomly distributed dislocation loops whose density depends on the temperature gradient and, hence, on the radiation density. The generation of dislocations is most efficient at the elastic-stress concentrators, where the absorptivity of the medium may increase. The most profound changes in the absorption factor take place in the vicinity of large-scale defects: inclusions, pores, dislocations, and microcracks. Such changes lead to an uncontrollable variation in temperature in the irradiated regions and, as a consequence, to nonuniform surface heating. The technology-conditioned inclusions of Cd and Te atoms in CdTe crystals are another source of strain in the crystal. This is because the melting points of Cd (312°C) and Te (450°C) are considerably lower than that of CdTe (1092°C) and, thus, the melting and the evaporation of these inclusions can occur even at a low density of laser radiation. This process additionally strains the surface layer and gives rise to excess dislocations. We note that, as the number of pulses with an
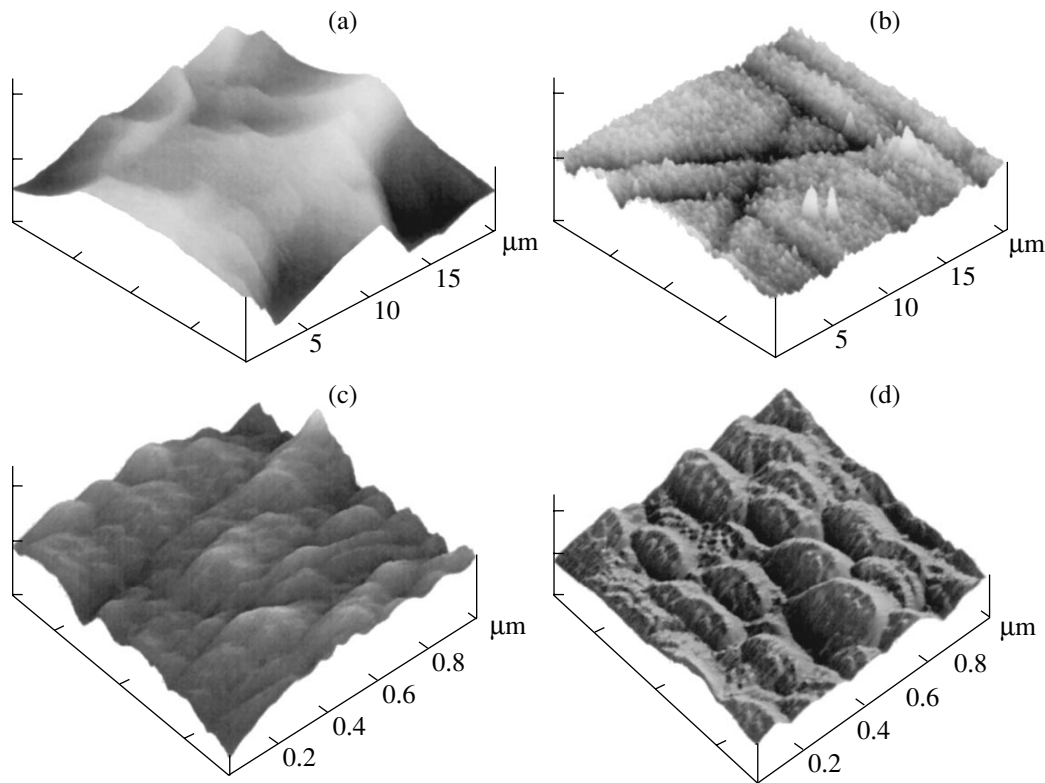
Fig. 3. AFM images of a *p*-CdTe (111) crystal surface after irradiation with a dose of (a, b) 0.32 J/cm^2 and (c, d) 0.8 J/cm^2. The scale chosen for the *x* axis is (a, b) 5 and (c, d) 0.2 μm/division; for the *z* axis, (a, b) 200 and (c, d) 50 nm/division.

energy below the damage threshold increases, an accumulation of damage is observed and the density of dislocations grows. The round clusters of dislocations shown in Fig. 3c may be due to the stress-induced gettering of dislocations in the elastic-stress fields at sites where there are deviations from the crystal stoichiometry.

It is worth noting that the formation of dislocations is also influenced by both the surface and the shock waves induced in the crystal by the pulsed laser irradiation [5, 6]. That is, the large number of excess vacancies produced by these waves cause additional deformation of the medium. The appearance of an elastically strained layer radically stimulates the vacancy diffusion rate via the up-diffusion mechanism, which results in vacancy clustering in the shock-produced regions of compression [5]. Depending on the number of vacancies, the clusters can be spherical or disc-shaped with a monatomic thickness (dislocation loops). Hence, it follows that the appearance of dislocations on the sample surface may stem from the combined effect of several laser-induced processes, such as thermal stress, the surface and the shock waves, and so on. The field of dislocations may become unstable with respect to the transformation into a spatially ordered state [7]. When a certain critical concentration of dislocations is exceeded, the system transforms into an ordered state that is determined by the self-consistent dislocation–strain interaction.

According to the available published data, the mechanisms of the laser-induced ordering of dislocation–deformation (DD) instabilities depend on the crystallographic orientation of the samples. For example, in the case of (111) Si wafers irradiated by neodymium laser pulses of millisecond duration [8], the ordering of DD instabilities was associated with the redistribution of dislocations between different atomic planes due to the deformation-induced drift of vacancies. A solid-phase formation of surface structures was assumed, and the regular surface structures that evolve during the transition of silicon to the plastic state were related to the local melting [8]. The theory described in [9] predicts that the gratings that appear in this case on the crystal surface should have an equilateral-triangle shape with grating period $d \approx 10^{-4}$ cm; this value was estimated theoretically and confirmed by experiments [7, 8]. It might be assumed that the same mechanism of dislocation ordering also appears in (111) CdTe crystals. However, in case of (111) CdTe, the linear dimensions of the structures that form depend on the power density of the laser or the irradiation dose and fall into the micro- and nanoranges; i.e., these dimensions are considerably smaller than in the case of Si. The formation of micrometer-size structures on the irradiated CdTe surface seem to occur by the mechanism of the self-organization of defects described above (Fig. 2c).

As for the formation of nanometer-size quasi-periodic structures, it seems reasonable to consider this process in terms of an increase in the density of point defects and a restructuring of the systems of point defects [9]. We suggest that the formation of nanometer-scale structures can be conceived as a three-stage process of self-organization of point defects that emerge in the irradiated crystal. An increase in the laser power density (or the irradiation dose) entails the growth of the spatially uniform concentration of defects, which is an externally controllable parameter. At the first stage, when the defect distribution remains spatially uniform, no self-organization of defects occurs. After the critical spatially uniform concentration of defects is attained, symmetrical clusters appear that consist of defects that are captured in self-consistent and symmetrical deformation wells; i.e., self-organization occurs. The sizes of such clusters are on the order of nanometers. Later, after the next critical value of the spatially uniform concentration of defects has been attained, a highly anharmonic periodic structure of nanometer size may result. In the case of laser-excited *p*-CdTe (111) crystals, the formation of nanometer-size structures may be caused by this mechanism of self-organization of defects.

CONCLUSIONS

Thus, subjecting a *p*-CdTe (111) crystal surface to ruby laser pulses of nanosecond duration leads to an essential change in the surface of the crystal. As the irradiation dose increases, the surface morphology passes through the following stages: the appearance of a tellurium film, the growth of the dislocation density, and the formation of ordered quasi-periodic structures of micrometer and nanometer size. The AFM study of the CdTe samples after irradiation allowed us to determine dose D_3, which results in the formation of quasi-periodic islands with linear dimensions of ~125–350 nm and a height of 2 nm, and dose D_4, which corresponds to the small (25–30 nm) "hills" that appear inside the large islands. At still higher doses, the height of the islands increases to 17 nm.

REFERENCES

1. B. M. Bulakh and S. M. Krasikova, Izv. Akad. Nauk SSSR, Neorg. Mater. **9**, 1112 (1973).
2. V. V. Artamonov, M. Ya. Valakh, V. V. Strel'chuk, *et al.*, Zh. Prikl. Spektrosk. **48**, 990 (1988).
3. V. V. Apallonov, A. M. Prokhorov, V. Yu. Khomich, and S. A. Chetkin, Kvantovaya Élektron. (Moscow) **9**, 343 (1982).
4. C. Kittel, *Introduction to Solid State Physics*, 5th ed. (Wiley, New York, 1976; Nauka, Moscow, 1978).
5. A. Baĭdullaeva, A. I. Vlasenko, B. L. Gorkovenko, *et al.*, Fiz. Tekh. Poluprovodn. (St. Petersburg) **34**, 443 (2000) [Semiconductors **34**, 429 (2000)].
6. A. Baĭdullaeva, A. I. Vlasenko, É. I. Kuznetsov, *et al.*, Fiz. Tekh. Poluprovodn. (St. Petersburg) **35**, 960 (2001) [Semiconductors **35**, 924 (2001)].
7. B. L. Volodin and B. I. Emel'yanov, Izv. Akad. Nauk SSSR, Ser. Fiz. **55**, 1274 (1991).
8. A. F. Banishev, B. L. Volodin, B. I. Emel'yanov, and K. S. Merzlyakov, Fiz. Tverd. Tela (Leningrad) **32**, 2529 (1990) [Sov. Phys. Solid State **32**, 1469 (1990)].
9. B. I. Emel'yanov and I. M. Panin, Fiz. Tverd. Tela (St. Petersburg) **39**, 2059 (1997) [Phys. Solid State **39**, 1815 (1997)].

Translated by A. Sidorova

ELECTRONIC AND OPTICAL PROPERTIES OF SEMICONDUCTORS

Fermi Level Pinning and Negative Magnetoresistance in PbTe:(Mn, Cr)

A. V. Morozov*, A. E. Kozhanov*, A. I. Artamkin*, E. I. Slyn'ko**, V. E. Slyn'ko**, W. D. Dobrovolski***, T. Story***, and D. R. Khokhlov*^

*Moscow State University, Vorob'evy gory, Moscow, 119899 Russia
^e-mail: khokhlov@mig.phys.msu.su
**Chernovtsy Branch, Institute of Materials Science Problems, National Academy of Sciences of Ukraine,
ul. Zhovtneva 5, Chernovtsy, 274001 Ukraine
***Institute of Physics, Polish Academy of Sciences, Warsaw, 02-668 Poland
Submitted March 24, 2003; accepted for publication April 1, 2003

Abstract—Fermi level pinning and persistent photoconductivity are observed in PbTe:(Mn, Cr) at $T < 35$ K. The impurity level that pins the chemical potential level shifts toward the bottom of the conduction band with increasing manganese content. Negative magnetoresistance at low temperatures is observed. The magnitude of this effect amounts to about 30% at $T = 4.2$ K. The effect is caused by the specific features of electron transport through the impurity band in a magnetic field. © 2004 MAIK "Nauka/Interperiodica".

1. INTRODUCTION

The modification of properties of semiconductors by doping with various impurities or by introducing crystal-lattice defects is one of the most important problems in condensed-matter physics. Of special interest in this field is the doping of semiconductors with magnetic impurities. As a rule, the existence of an intrinsic magnetic moment of impurity makes it possible to radically change the properties of a material in a magnetic field, such as energy-gap width, effective *g*-factor, and so on. The relative changes of the above parameters are particularly drastic in narrow-gap semiconductors. Apart from affecting the parameters of energy spectrum, magnetic impurities can form local and quasi-local states that considerably affect the concentration and scattering of charge carriers.

Narrow-gap IV–VI semiconductors are among the basic materials for IR optoelectronics and are widely used for manufacturing semiconductor lasers and photodetector arrays for middle and far IR regions of the spectrum. The feasibility of such a use is in many respects determined by specific properties of the impurity states that arise when narrow-gap IV–VI semiconductors are doped with certain elements, particularly with In and Ga [1]. These impurity states give rise to some radically new effects that are not characteristic of undoped material, in particular, the pinning of the Fermi level and persistent photoconductivity at low temperatures.

Similar impurity states were observed previously in PbTe doped with Cr [2] and Yb [3]. In PbTe:Cr, the Fermi level becomes pinned in the conduction band; in PbTe:Yb, in the valence band.

The doping of PbTe with Mn increases the band gap at a rate of $\partial E_g/\partial x \approx 40$ meV/(mol % of MnTe) but does not give rise to local and quasi-local impurity states near the energy gap [4].

In $Pb_{1-x}Mn_xTe$:Yb, a giant negative magnetoresistance was observed (the resistivity of the alloy increased by three orders of magnitude in a magnetic field) [5]. This effect was attributed in [5] to the specific features of conduction via the impurity band of Yb in a magnetic field. It was of interest how this effect would reveal itself in the case of a semi-insulating *n*-type state whose formation was expected in $Pb_{1-x}Mn_xTe$:Cr.

2. EXPERIMENTAL

Crystals of PbTe:(Mn, Cr) were grown by the Bridgman–Stockbarger method. The dopant content varied along the ingot axis. While Mn content N_{Mn} increased from the starting part of the ingot to its end, Cr content N_{Cr}, in contrast, decreased. Therefore, only the starting part of the ingot contained Cr in an amount sufficient to pin the Fermi level.

This part was cut perpendicularly to the ingot axis into disks about 1 mm in thickness. The impurity content in each disk was determined by energy-dispersive X-ray fluorescence analysis. The impurity distribution in each disk was uniform within the accuracy of the method (several percent of the impurity content). Samples with dimensions $5 \times 1 \times 1$ mm^3 were cut from the disks, and indium contacts were soldered. Galvanomagnetic properties were measured by the four-probe dc method in the conventional Hall configuration.
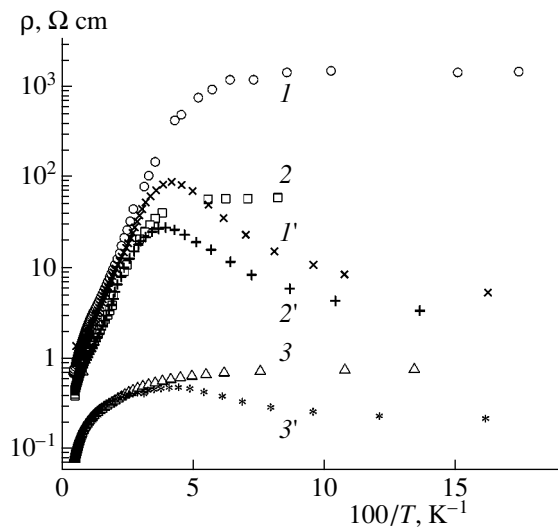
Fig. 1. Temperature dependences of resistivity measured (*1–3*) in the dark and (*1'–3'*) under IR irradiation. Mn content N_{Mn} = (*1, 1'*) 5.6, (*2, 2'*) 7.1, and (*3, 3'*) 9.1 mol %.
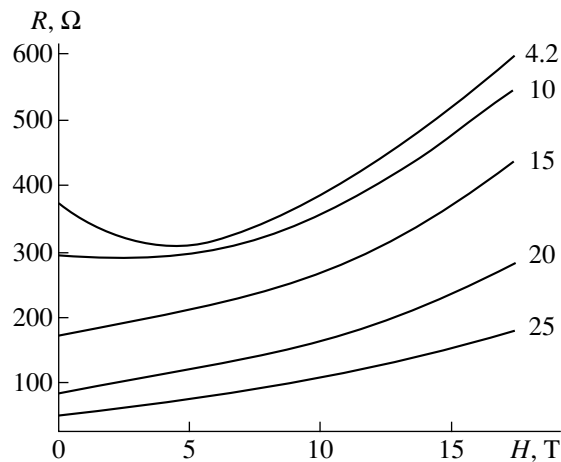

Fig. 2. Plots of resistivity versus field curves at various temperatures. Numbers denote the temperature in K; N_{Mn} = 9.1 mol %.

3. RESULTS

Temperature dependences of resistivity of the samples measured both in the dark and irradiated with IR photons are shown in Fig. 1. The temperature range 30–100 K corresponds to the activation process; a saturation of resistance is observed at lower temperatures. The activation energy decreases with increasing Mn content. Infrared irradiation results in persistent photoconductivity at temperatures below 35 K.

The application of magnetic field results in negative magnetoresistance at $T < 15$ K (Fig. 2). The magnitude of the effect is about 30%, which is much smaller than in the case of PbTe:(Mn, Yb) [5]. However, this magnitude is much larger than that of the negative magnetoresistance due to the quantum corrections to conduction

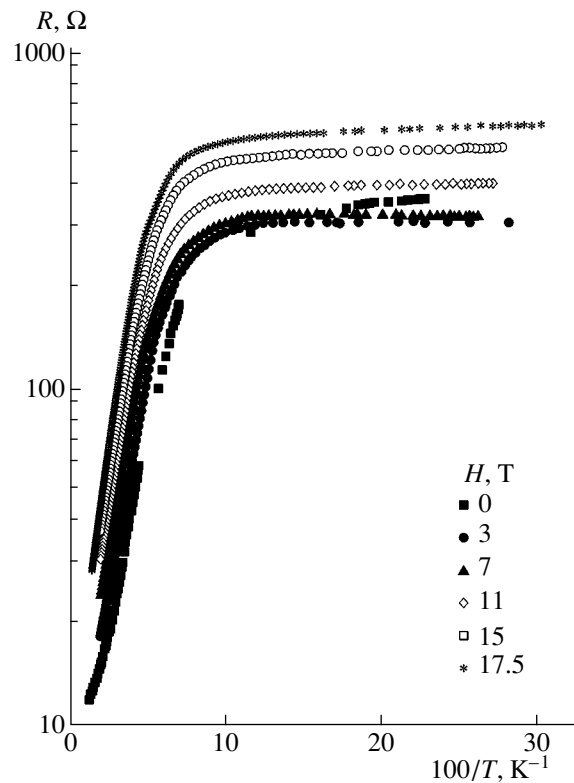**Fig. 3.** Temperature dependences of resistivity in various magnetic fields. N_{Mn} = 9.1 mol %.

usually observed in disordered systems. The reduction of resistance in magnetic field decreases with increasing temperature and disappears at $T > 15$ K.

As can be seen from Fig. 2, in the magnetic fields $H < 5$ T and $H > 7$ T, resistivity increases with decreasing temperature; however, in the range of fields 5 T < $H < 7$ T, the resistivity is virtually independent of temperature at $T < 10$ K. This effect is most distinctly observed in the temperature dependences of resistivity measured in different magnetic fields (Fig. 3). It is significant that the temperature dependence of resistivity in the range of magnetic fields $H < 5$ T includes two activation-type intervals. The activation energy corresponding to the region of relatively high temperatures, $T > 15$ K, is equal to 5–6 meV and increases slightly with increasing H, while the low-temperature activation energy decreases with increasing field and vanishes at $H \approx 5$ T. In the region $H > 7$ T, the increase in resistivity with decreasing temperature is observed again in low-temperature region $T < 15$ K.

The temperature dependence of the Hall mobility is shown in Fig. 4. Mobility increases as the temperature decreases, attains a maximum at $T \approx 35$ K, and then abruptly drops. Such a sharp decrease in the Hall mobility is usually observed in disordered systems or in systems whose conductivity is determined by the percolation effects [6]. The magnitude of mobility in the

maximum $\mu \approx 10^3$ cm^2/(V s) is typical of free electrons in the conduction band at temperatures of 30–40 K.

Similar data were obtained for other samples.

4. DISCUSSION

A number of unusual effects were observed in our experiments. First of all, the increase in the resistivity activation energy with increasing Mn content N_{Mn} is inconsistent with the expected tendency. Indeed, it is well known that the spacing between the pinned Fermi level in the PbTe:Cr conduction band and the bottom of the conduction band is about 100 meV. The increase in Mn content increases the band gap. It was anticipated that the impurity level at which the Fermi level is pinned is located at the midgap, as in the case of doping of PbTe with In [1]. In such a situation, an increase in N_{Mn} should decrease the spacing between the impurity level and the bottom of the conduction band, and this level (which pins the level of the chemical potential) should be incorporated into the band gap. As is clear from the experiment, the impurity level indeed enters the band gap at a certain value of N_{Mn}. However, it does not go deeper into the band gap with a further increase in Mn content but, on the contrary, moves in the opposite direction, thus reducing the activation energy of resistivity. Such a situation can exist if the band gap depends on the amount of Cr dopant; but no such dependence was observed in PbTe:Cr.

The second interesting effect is the negative magnetoresistance observed at temperatures $T < 15$ K. At higher temperatures, the magnetoresistance is positive; therefore, it would appear reasonable to assume that such a change in the behavior of resistivity in a magnetic field is associated with the fundamental mechanism of conduction. In all probability it is free electrons in the conduction band that make the main contribution to conductivity at temperatures above 15 K, and a high-temperature activation process is caused by the thermal excitation of electrons from the impurity level, which pins the level of chemical potential, to the conduction band. This assumption is supported by the high values of the Hall mobility of charge carriers in the range of temperatures under consideration. Consequently, the electrons in the conduction band contribute only to positive magnetoresistance.

The activation energy corresponding to the low-temperature process at $T < 15$ K in weak magnetic fields $H < 5$ T is much smaller than the energy difference between the impurity level, which pins the position of chemical potential, and the bottom of the conduction band. Moreover, the Hall effect data show that the charge carriers responsible for low-temperature activation have a much lower mobility than the conduction-band electrons. Therefore, it is reasonable to suggest the following mechanism of low-temperature activation. In contrast to the case of In doping for which impurity states are strongly pinned [7] and the width of
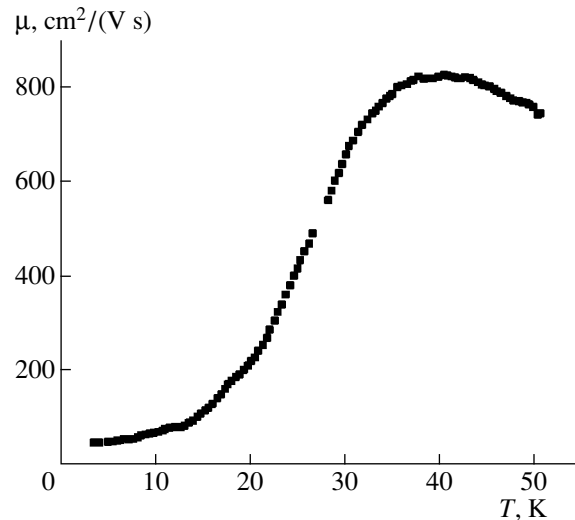

Fig. 4. Temperature dependence of the Hall mobility for the sample with $N_{Mn} = 9.1$ mol %.

the corresponding impurity level is very narrow (less than 1 meV), the impurity level for PbTe:(Mn, Cr), as well as for PbTe:(Ge, Yb), can be significantly broadened [8]. If the level of chemical potential is located at the midsection of the impurity band, percolation conduction can be observed. If this level is located in the "tails" of the density of states in this band, the conduction will be governed by the thermal activation of electrons from the Fermi level to the percolation level. In this case, the negative magnetoresistance can be caused by the shift of the chemical potential level with respect to the percolation level in a magnetic field.

The reason for such a shift may be the following. The application of magnetic field causes a noticeable splitting of the impurity states with different spin directions. The complete occupancy of the impurity band in these conditions remains unchanged. However, the occupancy of each spin-polarized impurity band can be drastically changed, which in turn can result in a shift of the Fermi level with respect to the percolation level of each of these bands. Other possibilities, in particular, those caused by the magnetic interaction of electrons in the d shells of Mn and Cr, also cannot be ruled out. In any case, it is clear that negative magnetoresistance is related to the specific features of charge transport through the impurity band and not to the electrons in the conduction band as in II–VI semiconductors [9].

ACKNOWLEDGMENTS

REFERENCES

1. B. A. Volkov, L. I. Ryabova, and D. R. Khokhlov, Usp. Fiz. Nauk **172**, 875 (2002) [Phys. Usp. **45**, 819 (2002)].

2. L. M. Kashirskaya, L. I. Ryabova, O. I. Tananaeva, and N. A. Shirokova, Fiz. Tekh. Poluprovodn. (Leningrad) **24**, 1349 (1990) [Sov. Phys. Semicond. **24**, 848 (1990)].

3. I. I. Ivanchik, D. R. Khokhlov, S. V. Ponomarev, *et al.*, in *Proceedings of 24th International Conference on Physics of Semiconductors* (Jerusalem, Israel, 1998), CD-ROM, VIII B-8.

4. J. Niewodniczańska-Zawadzka, J. G. Elsinger, L. Palmetshofer, *et al.*, Physica B & C (Amsterdam) **117–118**, 458 (1983).

5. I. I. Ivanchik, D. R. Khokhlov, A. V. Morozov, *et al.*, Phys. Rev. B **61**, R14889 (2000).

6. M. K. Sheĭnkman and A. Ya. Shik, Fiz. Tekh. Poluprovodn. (Leningrad) **10**, 208 (1976) [Sov. Phys. Semicond. **10**, 128 (1976)].

7. V. G. Golubev, N. I. Grechko, S. N. Lykov, *et al.*, Fiz. Tekh. Poluprovodn. (Leningrad) **11**, 1704 (1977) [Sov. Phys. Semicond. **11**, 1001 (1977)].

8. E. P. Skipetrov, N. A. Chernova, E. I. Slynko, and Yu. K. Vygranenko, Phys. Rev. B **59**, 12928 (1999).

9. A. Mycielsky and J. Mysielski, J. Phys. Soc. Jpn. **49**, 807 (1980).

Translated by A. Zalesskiĭ

Green Luminescence Band of Zinc Oxide Films Copper-Doped by Thermal Diffusion

Ya. I. Alivov*, M. V. Chukichev**, and V. A. Nikitenko***

*Institute of Microelectronic Technology and Ultra-High-Purity Materials, Russian Academy of Sciences,
Chernogolovka, Moscow oblast, 142432 Russia
e-mail: alivov@ipmt-hpm.ac.ru
**Moscow State University, Vorob'evy gory, Moscow, 119899 Russia
***Moscow State University of Communications, Moscow, Russia
Submitted April 2, 2003; accepted for publication April 21, 2003

Abstract—High quality ZnO single-crystal films were doped with copper by thermal diffusion, and their luminescent properties were studied by cathodoluminescence spectroscopy. Doping with copper increases the intensity of the green-emission band of the cathodoluminescence spectrum, whose peak, width, and shape at 78 and 300 K remain unchanged. At 4.2 K, a pronounced phonon structure with a phonon energy of 72 meV is detected in the cathodoluminescence green-emission band of the doped samples. In this case, the phonon peaks feature a triplet fine structure instead of the doublet one generally observed. This feature is attributed to radiative recombination of acceptor excitons that are localized at copper atoms and interact with each one of the subbands of the ZnO valence band. An analysis of the experimental data on the film cathodoluminescence and comparative studies of luminescence and electron spin resonance in single crystals allow one to conclude that the uncontrollable copper impurity typically existing in ZnO is responsible for green-emission luminescence in this material. © 2004 MAIK "Nauka/Interperiodica".

1. INTRODUCTION

Recently, interest in zinc oxide (ZnO) has significantly increased, since this material is considered as promising for the development of light-emitting structures and lasers of the blue and ultraviolet regions of the spectrum [1, 2]. Moreover, zinc oxide is a conventional low-voltage cathodoluminophore with green luminescence, which is used in various optoelectronic displays [3]. However, despite a large number of published papers on the growth of ZnO technology and studies of its physical properties, many of these properties remain unexplained. For example, the mechanism of *n*-type conduction generally observed is a subject of discussion [4]. The problem of the origin of the centers responsible for the green-emission band (the peak position wavelength is $\lambda_{max} = 500$–540 nm) that often exists in the photoluminescence and cathodoluminescence spectra has not yet been definitively solved. This band is associated with an uncontrolled copper impurity [5–9] or with singly charged oxygen vacancies that are analogues of F^+ centers in alkali halide crystals (see, e.g., [2, 3, 9, 10]).

For example, Vanheusden *et al.* [3] analyzed the preparation conditions for zinc oxide with green luminescence, as well as the measurement data on luminescence spectra and the electron spin resonance (ESR) data, and concluded that the centers responsible for the green luminescence band are oxygen vacancies singly positively charged with respect to the lattice. No less convincing are the experimental data [5–8] showing that the centers causing green luminescence in ZnO are individual copper atoms substituting zinc, which is always present in ZnO in small amounts.

Since the data on the origin of the green-emission band are rather contradictory, it is still necessary to ascertain definitively the mechanism of its appearance. In this study, ZnO films were doped with copper by thermal diffusion, and the influence of this impurity on the luminescence spectrum was studied. In addition, the photoelectron spin resonance (photo-ESR) and luminescence in ZnO single crystals with anion vacancies were studied.

2. EXPERIMENTAL

Initial high-quality ZnO films exhibited intense exciton luminescence at room temperature in the ultraviolet region of the spectrum and very weak luminescence in the green spectral region under medium excitation densities. The films, which were 3 μm thick, were grown by the method of chemical transport reactions on a buffer GaN layer on a sapphire substrate; i.e., the samples represented a ZnO/GaN/α-Al$_2$O$_3$ heteroepitaxial structure. Gallium nitride is a material whose physical properties and lattice parameters are close to those of ZnO. Therefore, the ZnO films grown on GaN exhibit good luminescence and thermally stable characteristics [11].
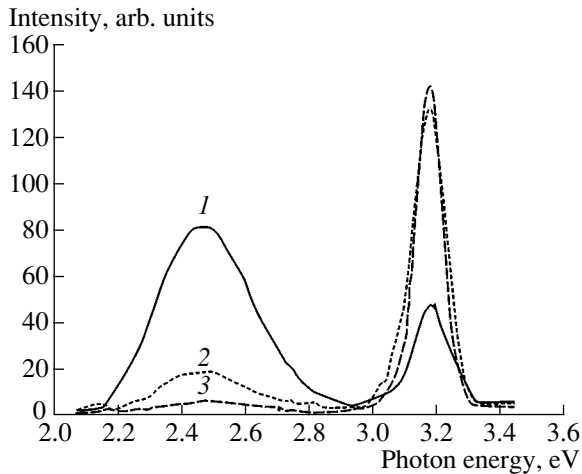
Intensity, arb. units

Fig. 1. Cathodoluminescence spectra of the (*1*) copper-doped, (*2*) undoped after annealing, and (*3*) as-grown samples at 300 K. The electron beam current is 1 μA; the accelerating voltage is 20 keV.
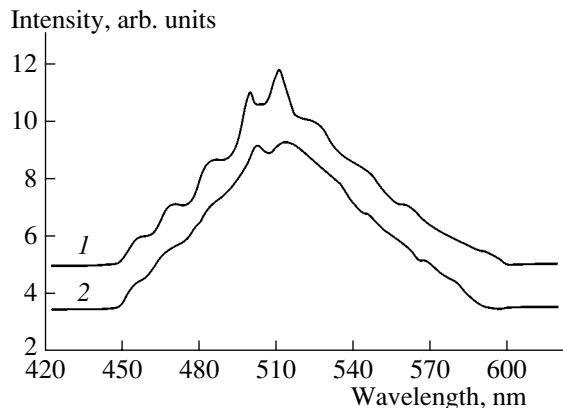
Intensity, arb. units

Fig. 2. Green spectral band of the cathodoluminescence spectrum of the (*1*) copper-doped and (*2*) undoped (magnified by a factor of 4) samples at 4.2 K. The electron beam current is 0.1 μA; the accelerating voltage is 20 keV.

Copper diffusion was carried out from a metal layer ~10 nm thick deposited onto the film surface by ion sputtering in an argon plasma. Diffusion annealing was carried out in air at 750°C for 20 h. To prepare a reference sample, a structure without a copper layer at the surface was annealed under the same conditions. After annealing, the sample resistivity was measured using the van der Pauw method. The copper content in the films after diffusion was estimated using secondary-ion mass spectroscopy (SIMS). The cathodoluminescence spectra were measured using a DFS-12 spectrometer at temperatures $T = 300$, 78, and 4.2 K. The crystals were excited at electron-beam currents of 0.05–1 μA and an accelerating voltage of 20 keV.

The ESR studies were carried out using an RE-1306 radio spectrometer with a 3-cm range and magnetic field modulation at a frequency of 100 kHz. In the case

when samples were exposed to light, a DKSSh-3000 xenon lamp was used, whose light was resolved by a monochromator of an SF-4 spectrophotometer in the required spectral region. The use of a helium flow-through cryostat (Oxford Instruments ESR-9) in the spectrometer allowed ESR measurements in the temperature range $T = 4$–300 K with a rapid (if necessary) change in the sample temperature (with an accuracy of 1 K). In most cases, an identical initial crystal state at low temperatures before each exposure to light was attained by sample annealing in the cryostat at room temperature for 5–10 min. The concentration $N(T)$ of paramagnetic centers in thermally stimulated processes of charge transport in the crystals under study was determined by the ESR intensity signal under conditions of pulsed heating. Simultaneously, thermal deexcitation was studied [12–14].

3. RESULTS

The resistivity measured in the copper-doped sample was higher than that in the undoped sample (equal to 0.25 Ω cm) by almost four orders of magnitude. Such an increase in the resistivity caused by doping with copper is also characteristic of ZnO [15]. The copper concentration measured by SIMS in the doped samples was 5×10^{17} cm^{-3}; in the undoped samples, the copper concentration was lower than the limit of detection (3×10^{16} cm^{-3}) of the measuring setup.

Figure 1 shows the cathodoluminescence spectra measured at $T = 300$ K in the copper-doped (curve *1*) and undoped (curve *2*) samples. For comparison, the cathodoluminescence spectrum of the unannealed sample (curve *3*) was also measured. The spectra of all the samples consisted of a narrow edge ultraviolet-emission band with a peak at 385 nm (~3.2 eV) and a broad green-emission band with a peak at 535 nm (~2.3 eV), whose position was identical for all the samples. The intensity of the ultraviolet-emission band decreased due to doping, while the green-emission band intensity increased almost by four times in comparison with that of the undoped sample. The green band width was the same (0.33 eV at $T = 300$ K) for all the samples; the band profile was almost unchanged (at $T = 300$ and 77 K). These data allow one to conclude that the centers of green luminescence in both doped and undoped samples are point defects of identical nature. They can be copper atoms or complexes including copper. A certain increase in the green-emission band intensity in the undoped sample after annealing (Fig. 1, curve *2*) in comparison with the initial one seems to be caused by the transition of a fraction of the uncontrollable copper impurity to a luminescence-active state (from interstitial to lattice sites) during annealing. The significant differences in the structures of the green cathodoluminescence spectral bands of the doped and undoped samples were detected at 4.2 K (see Fig. 2). We can see that the green-emission band of the sample intentionally doped with copper has pronounced equidistant peaks

spaced in energy by 72 meV; this distance is identical to the energy of longitudinal optical (LO) phonons in ZnO [9]. In this case, a fine triplet structure of equidistant peaks (Fig. 3) arises instead of the typically observed doublet one. We can see that the phonon structure of the sample without copper is significantly less pronounced. As will be shown below, the green-emission band is caused by radiative transitions in the excited d^9 shell of the Cu^{2+} ion. The exciton spectral regions of both sample types had identical structures and consisted of two series of equidistant lines: zero-phonon lines of the *A* exciton bound to the neutral donor and the free *A* exciton and their LO-phonon replicas with a periodicity of 72 meV.

4. DISCUSSION

The increase in the green-emission band intensity of the copper-doped sample, as well as its peak, half-width, and profile, which are identical to those of the undoped sample, is indicative of copper involvement in the formation of this luminescence band in all the samples under study. The mechanism of radiative recombination with the involvement of copper can be understood if the microscopic state of copper in the ZnO lattice is known. It follows from [9, 15] that copper atoms substituting zinc donate two electrons (like Zn) for the bond formation and are in a neutral state with respect to the Cu^{2+} lattice ($3d^9$). In this case, copper in the $3d^9$ state forms a deep acceptor level, which is spaced 0.17–0.19 eV away from the bottom of the conduction band [15, 16]. The population and depopulation of this level by an electron corresponds to the Cu^+ ($3d^{10}$) and Cu^{2+} ($3d^9$) states, respectively. Copper is in Group I of the periodic table and belongs to the family of transition $3d$ elements. Substituting cations in II–VI and III–V semiconductors, Cu as a rule donates the number of electrons to the valence band that is required to saturate all the chemical bonds within the nearest neighborhood. In this sense, Cu manifests itself as an isoelectronic impurity. As a result of perturbations introduced by such an impurity into the energy spectrum of semiconductor electrons, energy states of donor or acceptor types arise in the semiconductor band gap, and the impurity center itself is a trap for nonequilibrium holes or electrons, respectively. As a carrier is trapped, the impurity center acquires a charge with respect to the lattice, and a long-range Coulomb field arises in addition to the short-range potential of the isoelectronic impurity. This field promotes electron or hole trapping onto a weakly localized hydrogen-like orbital. These states $[d^{n+1}h]$ and $[d^{n-1}e]$ are excited unsteady hydrogen-like states of acceptor or donor types, which are referred to as the acceptor (AE) and donor (DE) excitons, respectively [17]. In this model, the valence electron is transferred to the *d* shell of the Cu^{2+} impurity as the electronic subsystem of the ZnO lattice is excited, and the hole is localized at the Cu^+ ion formed in this
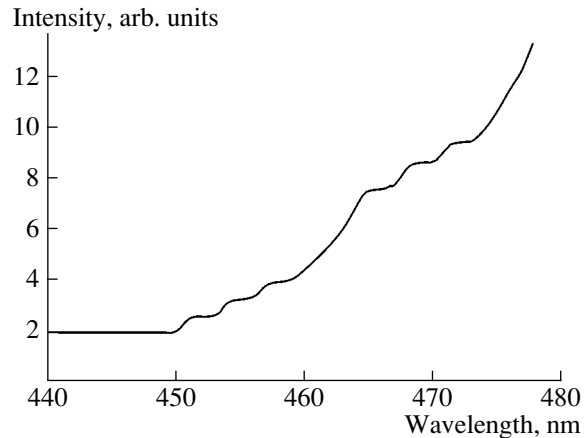
case at a hydrogen-like orbital of large radius. Thus, an exciton-like state of two $3d^{10}$ (Cu^+)h particles is formed at the impurity center due to such a transition. This is an acceptor exciton whose radiative decay gives rise to a leading line of green radiation in the spectrum. In this model, the doubling (tripling observed in specific cases) in the leading structure is associated with the splitting of the valence band due to the spin–orbit coupling and perturbation by the internal crystal field. The strong electron–phonon coupling, in which LO phonons are explicitly involved, forms a green-luminescence band with a peak, whose position depends on the existence of collateral channels of radiative recombination of carriers (e.g., yellow–orange luminescence [9]), the participation of local phonons in the process, and so on. Intracenter radiative transitions in the copper impurity (excited by radiative processes in AE) can also contribute to green band formation; however, this assumption calls for further research.

Returning to the vacancy model of green luminescence centers, in our opinion, this model has a number of drawbacks. For example, the vacancy model itself in many respects depends on the correct interpretation of the ESR signal attributed to anion vacancies in ZnO [9, 13, 14]. The fact is that, according to one interpretation, oxygen vacancies in the V_O^x state should be considered shallow-level donors with ionization energy $E_d \approx 0.03$–0.05 eV. These donors give rise to the ESR signal with the factor $g = 1.96$ (generation of F^+ centers) after the transition of electrons to the conduction band and cause high conductivity of zinc oxide [3, 9, 13, 14]. In this case, the green luminescence is assumed to be caused by the trapping of nonequilibrium electrons from the conduction band by the V_O^{++} states or by radiative transitions of electrons from anion vacancies in the V_O^+ state to the ZnO valence band [3, 9]. In the first version of this model, the very high ionization
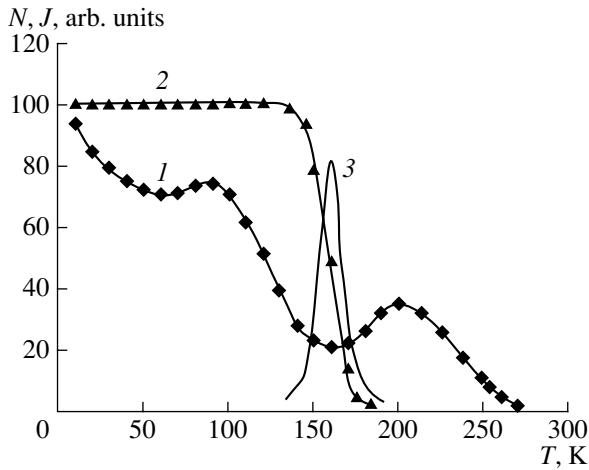
Intensity, arb. units

Fig. 3. Fine structure of the equidistant peaks of the green band at 4.2 K.

Fig. 4. Dependences of the concentration N of paramagnetic centers at 30 K (*1, 2*) and the thermal deexcitation intensities J (*3*) on the annealing temperature T of the ZnO single crystal irradiated with protons: (*1*) F^+ centers, (*2*) paramagnetic states ($Li_{Zn}^+ - O^1$), (*3*) deexcitation at the wavelength of 600 nm; preliminary excitation by 2.6-eV photons.

energy of the V_O^+ states, which is atypical of shallow hydrogen-like donors in semiconductors, raises doubts [18]. In the second version, the cross section of trapping of nonequilibrium holes by the V_O^+ states is too small, which is not favorable for the development of such a luminescence mechanism in *n*-type semiconductors [14, 18].

Currently, an alternative interpretation of ESR signals in zinc oxide seems to be convincing [9, 12–14, 19]. According to this interpretation, the signal (with the factor $g = 1.96$) is associated with electrons of the conduction band (or electrons in the band of shallow donors), and the photosensitive ESR signal (*f* signal) corresponding to centers with axial symmetry and $g_\parallel = 1.9948$ and $g_\perp = 1.9963$ is attributed to vacancies V_O^+ (F^+ centers). In this case, the detected hyperfine structure of the signal is attributed to the interaction of an unpaired spin of an electron with ^{67}Zn isotope nuclei (the content is 4.1%; the spin $J = 5/2$). The conditions of the ESR *f*-signal photoexcitation are such that one may conclude that V_O^x is a deep donor with a photoionization energy of 2.3 eV.

Nevertheless, as combined studies of photo-ESR and luminescence in ZnO single crystals with anion vacancies [13, 14] showed, these vacancies are not luminescence centers. As a confirmation of this, Fig. 4 shows the results of the ESR (pulsed-heating mode) study of point defect recharging, which allowed us to determine the temperature dependence of the relative concentration of paramagnetic centers causing the ESR *f* signal and reference ($Li_{Zn}^+ - O^1$) centers (lithium para-

magnetic states are described, e.g., in [14]) in ZnO:Li single crystals irradiated with protons. Simultaneously, thermal deexcitation was studied.

An important feature of these results is the retrapping of electrons released from traps at $T_1 \approx 30$–60 K and $T_2 \approx 110$–150 K by F^+ centers (Fig. 4, curve *1*), which completely corresponds to their charge state. Only when these centers become inefficient does the transformation of neutral lithium paramagnetic centers to the diamagnetic state ($T = 150$–180 K) begin, which is accompanied by yellow–orange thermal deexcitation (Fig. 4, curves *2, 3*). In the temperature range 180–200 K, lithium paramagnetic centers are populated by electrons of the valence band [9, 14]. Holes generated in the valence band are trapped by F centers via the reaction $F^x + e^+ \longrightarrow F^+$, which increases the ESR signal intensity (curve *7*). Further thermal population of the F^+ states by valence band electrons in the temperature range $T \approx 250$ K results in the total disappearance of the signal.

An important result of the experiments we carried out is the nonradiative nature of the transitions $F^+ + e^- \longrightarrow F^x$ and $F^x + e^+ \longrightarrow F^+$, which suggests that there is no relation between green luminescence and oxygen vacancies in ZnO.

We note that special doping of low-voltage ZnO cathodoluminophores exhibiting green luminescence with copper, as in the case we are considering with films, makes it possible to increase the brightness of the green photoluminescence and cathodoluminescence of zinc oxide [20].

5. CONCLUSION

Thermal diffusion of copper into high-quality ZnO films was carried out, and their luminescence properties were studied by the cathodoluminescence method. A significant increase in the intensity of the cathodoluminescence green spectral band of copper-doped ZnO films was detected compared to undoped samples. At 4.2 K the green-emission band of the doped sample has a more pronounced phonon structure with a periodicity corresponding to the energy of longitudinal optical phonons (72 meV). The results obtained showed that the copper impurity is responsible for the formation of the green band in the luminescence spectrum of zinc oxide. A model according to which the green luminescence in ZnO is a result of multiphonon radiative decay of acceptor excitons arising at the isoelectronic copper impurity was suggested and justified.

The combined studies of the ESR and luminescence showed that anion vacancies are centers of nonradiative recombination of nonequilibrium carriers.

REFERENCES

1. Y. R. Ryu, S. Zhu, Y. D. Budai, *et al.*, J. Appl. Phys. **88**, 201 (2000).

2. F. Leiter, H. Zhou, F. Henecker, *et al.*, Physica B (Amsterdam) **308–310**, 908 (2001).

3. K. Vanheusden, W. L. Warren, C. H. Seager, *et al.*, J. Appl. Phys. **79**, 7983 (1996).

4. C. G. Van de Walle, Phys. Rev. Lett. **85**, 1012 (2000).

5. R. Dingle, Phys. Rev. Lett. **23**, 579 (1969).

6. I. Broser, R. Germer, H. I. Shulz, and K. Wisznewski, Solid-State Electron. **21**, 1597 (1978).

7. R. Kuhnert and R. Helbig, J. Lumin. **26**, 203 (1981).

8. D. Y. Robbins, D. C. Herbert, and P. Y. Dean, J. Phys. C **14**, 2859 (1981).

9. I. P. Kuz'mina and V. A. Nikitenko, *Zinc Oxides: Production and Optical Properties* (Nauka, Moscow, 1984).

10. S. B. Zhang, S.-H. Wei, and Alex Zunger, Phys. Rev. B **63**, 75205 (2001).

11. M. V. Chukichev, B. M. Ataev, V. V. Mamedov, *et al.*, Fiz. Tekh. Poluprovodn. (St. Petersburg) **36**, 1052 (2002) [Semiconductors **36**, 977 (2002)].

12. K. Tarkpea, A. Ots, and V. A. Nikitenko, J. Phys. Chem. Solids **55**, 1353 (1994).

13. V. A. Nikitenko, K. É. Tarkpea, I. V. Pykanov, and S. G. Stoyukhin, Zh. Prikl. Spektrosk. **68**, 384 (2001).

14. V. A. Nikitenko, Zh. Prikl. Spektrosk. **52**, 367 (1992).

15. G. Muller, Phys. Status Solidi B **76**, 525 (1976).

16. Yasuo Kanai, Jpn. J. Appl. Phys. **30**, 703 (1991).

17. V. I. Sokolov, Fiz. Tekh. Poluprovodn. (St. Petersburg) **28**, 545 (1994) [Semiconductors **28**, 329 (1994)].

18. A. M. Gurvich, *Introduction to the Physical Chemistry of Phosphor Crystals* (Vysshaya Shkola, Moscow, 1971).

19. G. Neumann, Curr. Top. Mater. Sci. **7**, 269 (1981).

20. V. A. Nikitenko, S. V. Mukhin, S. P. Pivneva, *et al.*, Élektron. Tekh., Ser. 4, No. 2(137), 5 (1992).

Translated by A. Kazantsev

ELECTRONIC AND OPTICAL PROPERTIES OF SEMICONDUCTORS

Transformation of Luminescence Centers in CVD ZnS Films Subjected to a High Hydrostatic Pressure

N. K. Morozova*, I. A. Karetnikov, V. G. Plotnichenko, E. M. Gavrishchuk, É. V. Yashina, and V. B. Ikonnikov

Moscow Power Engineering Institute (Technical University), ul. Krasnokazarmennaya 17, Moscow, 111250 Russia
*e-mail: MorozovaNK@mpei.ru
Submitted April 15, 2003; accepted for publication April 22, 2003

Abstract—The cathodoluminescence and optical-transmission spectra of ZnS were analyzed to study the effect of a high hydrostatic gas pressure (1500 atm at 1000°C) on the equilibrium between intrinsic point defects in zinc sulfide grown by chemical vapor deposition (CVD) with an excess of zinc. The cathodoluminescence spectra were measured at 80–300 K and excitation levels of 10^{22} and 10^{26} cm^{-3} s^{-1}; the optical-transmission spectra were measured at 300 K in the wavelength range 4–12 μm. It is found that exposure to a high hydrostatic gas pressure transforms the self-activated emission in the cathodoluminescence spectrum: (i) a new short-wavelength band appears at 415 nm with its intensity increasing by one to three orders of magnitude; and (ii) the long-wavelength band that peaks at 445 nm and is observed in as-grown crystals becomes quenched. Simultaneously, the cathodoluminescence band peaked at 850 nm and related to vacancies V_S is no longer observed after high-pressure treatment. These effects are attributed to a partial escape of excess zinc (Zn_i) from crystals and additional incorporation of oxygen into lattice sites (O_S). A doublet band I_1, which peaked at ~331–332 nm at 80 K and at ~342–343 nm at 300 K and is related to excitons bound to acceptor levels of oxygen centers, was observed. This band is found to be dominant in the cathodoluminescence spectrum at an excitation level of 10^{26} cm^{-3} s^{-1}. Traces of the ZnO phase are apparent after the high-pressure treatment in both the cathodoluminescence spectra (the bands at 730 and 370 nm) and the transmission spectra (narrow bands in the region of 6–7 μm). © 2004 MAIK "Nauka/Interperiodica".

New gaseous-phase technology for growing II–VI compounds with a lowered impurity concentration and controlled composition makes it possible to obtain data on the origin of the deep-level oxygen centers responsible for so-called self-activated (SA) luminescence, as oxygen remains the only impurity that is present at high concentrations in these compounds. Morozova *et al.* [1] suggested a classification of oxygen-related bands. In this classification, all the main groups of SA bands in pure II–VI crystals are related to individual oxygen atoms at the lattice sites (O_S). According to the accepted crystallochemical model and its theoretical substantiation [1–3], O_S atoms form the nearest surroundings and the interrelated set of defects. This set of defects can be treated, on the one hand, as an individual isoelectronic center and, on the other, as a complex that exists only if there is interaction between its components. A change in the charge state of intrinsic point defects within the homogeneity region leads to a change in the charge state of the entire complex (oxygen-related center) and in the corresponding luminescence of the crystal. Three groups of oxygen-related bands are observed for impurity-free ZnS: (I) SA bands (blue emission) at 445 (415) nm; (II) SAL bands (ultraviolet emission) at ~(355–370) nm; and (III) the green-emission band at 510–520 nm. The first of these groups is observed if the oxygen-related center is found in the lattice with an excess of zinc; the

second group is observed in crystals with a stoichiometric composition; and the third group is observed in crystals with a significant excess of sulfur (a metalloid).

Morozova *et al.* [4] verified the interrelation between the spectral bands of bound excitons (BE) and acceptor levels of SAL oxygen-related centers in ZnSe. A similar BE band peaked at 329 nm (at 100 K) was also observed for ZnS samples that featured SAL emission [5] and were grown in hydrothermal conditions. The intensity of this band increased superlinearly with increasing intensity level and remained the only band in the spectrum.

In this context, we studied the polycrystalline ZnS condensates (layers) obtained by chemical vapor deposition (CVD) at a temperature of 600°C and with an excess of zinc (the ratio [Zn]/[H$_2$S] = 1.1–0.9) [6]. In accordance with the equilibrium in a system of intrinsic point defects [5], such a sulfide contains intrinsic donors: interstitial zinc in excess of the stoichiometry Zn_i and sulfur vacancies V_S.

The aforementioned ZnS layers were subjected to a high hydrostatic gas pressure (as high as 1500 atm) at a temperature of ~1000°C. High pressure is favorable for densification of the material and affects the equilibrium in a system of intrinsic point defects in such a way that the unit-cell volume decreases. As a result, one should expect a decrease in the concentration of all defects [7],

first and foremost, interstitial zinc atoms Zn_i; these are the dominant defects in as-grown ZnS crystals. In addition, the concentration of vacancies V_S can decrease or new defects with smaller sizes can be formed. For example, these new defects can include substitutional oxygen O_S formed according to the scheme $V_S + O_i \longrightarrow O_S$.

We initially studied the cathodoluminescence spectra measured at a low excitation level (10^{22} cm^{-3} s^{-1}), when the deep levels of defects and defect complexes contribute mainly to the spectra. The method for studying the CVD ZnS layers was described in detail elsewhere [1]. In addition, we report the results of studying the pulsed cathodoluminescence obtained at an excitation density of 10^{26} cm^{-3} s^{-1} (see [8]). It is noteworthy that oxygen with a concentration higher than 10^{18} cm^{-3} (almost at the solubility limit [9]) is inevitably present in ZnS [9]. The point is that oxygen is thermochemically related to the components of II–VI compounds, is easily incorporated into the corresponding crystal lattice, is present in the starting substances, and is typically not controlled.

According to the views expressed in [1] and mentioned above, oxygen should be responsible for the blue SA emission in the ZnS layers that were studied by us and had an excess of Zn. The cathodoluminescence spectra measured at 80 K for two initial CVD ZnS samples grown with differing degrees of H_2S purification with respect to O_2 are shown in Fig. 1.[1] As can be seen from Fig. 1, the self-activated emission does correspond to the band peaked at 445 nm. The relative intensity of this band I_{445}/I_{exc} (I_{exc} is the exciton-band intensity) decreases from 5 (curve 2) to 0.03 as a result of H_2S purification with respect to oxygen. The band peaked at 850 nm is related to sulfur vacancies V_S [5, 10, 11].

The band I_2, which peaks at 327.5 nm, is dominant in the excitonic region of the cathodoluminescence spectrum for pure ZnS crystals with an excess of Zn; this band is related to excitons bound to intrinsic donors $Zn_i^{\times(\cdot)}$ (see table). The edge emission (EE) and the band peaked at 520 nm are not observed in the cathodoluminescence spectrum of ZnS samples that are free of extraneous impurities (Fig. 1, curve 1). The high crystal quality of these samples is corroborated by the high intensity of the excitonic bands, for which as many as three LO-phonon replicas of the zero-phonon line I_2 are observed. An excitonic band peaked at 336.6 nm and very weak emission in the blue region of the spectrum are observed at 300 K.

The band I_1, which peaks at ~(331–332) nm with a binding energy of ~60 meV, is observed in the bound exciton spectral region for the samples with a higher concentration of oxygen (Fig. 1, curve 2). It can be seen that this band is not elementary. The intensity of the I_1
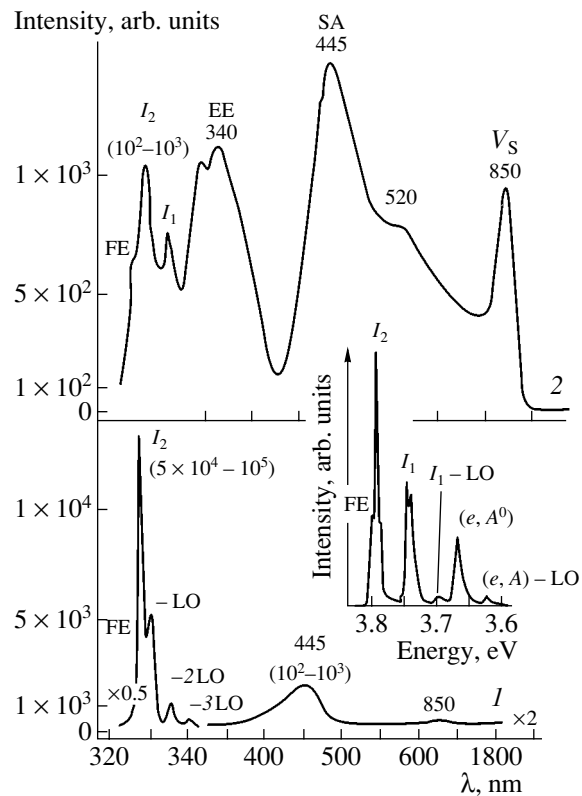

Fig. 1. Cathodoluminescence spectra of a CVD ZnS sample grown using (1) purified and (2) unpurified H_2S with the ratio [Zn]/[H$_2$S] $\approx$ 1.07. The spectra were measured at an excitation intensity of 10^{22} cm^{-3} s^{-1} and $T = 80$ K. The wavelengths (nm) and typical or specific intensities (in parentheses) of the main bands are indicated at the corresponding peaks. A fragment of a photoluminescence spectrum measured at 10 K is shown in the inset [13].

band is typically low at a cathodoluminescence-excitation level of 10^{22} cm^{-3} s^{-1}. However, this band overlaps with LO replicas of the main excitonic band as the intensity of excitonic spectrum increases for the samples depleted in oxygen (curve 1).

A shift of the I_1 band with temperature can be perceived from the data listed in the table. This band coincides with the doublet at ~331.8 and ~331.2 nm in the photoluminescence spectrum measured at 10 K and shown in the inset to Fig. 1 [12, 13]. The photoluminescence spectrum was measured for high-quality epitaxial ZnS layers under laser excitation. The origin of the doublet I_1 was not identified. The binding energies for the doublet components resolved at 10 K are equal to 61 and 54 meV (relative to FE$_{lh}$ [13]).

The effect of high-pressure high-temperature treatment on cathodoluminescence spectra of a typical CVD ZnS sample at the excitation intensity of 10^{22} cm^{-3} s^{-1} at 80 K is illustrated in Fig. 2. The cathodoluminescence spectrum changed drastically and diversely as a result of the treatment.

---

[1] The band intensities indicated in Figs. 1–4 are relative values obtained from experimental spectra that were recalculated for identical conditions of measurement.

Positions of the bands corresponding to free (FE) and bound (BE) excitons in ZnS

Band	Energy, eV (Wavelength, nm)			Binding energy ε, meV	Reference
	0 K	80 K	300 K		
FE_{lh}	3.7979 (326.46)	3.7929 (326.88)	3.6881 (336.18)	40.9	[12]
FE_{hh}	3.8012 (326.17)	3.7962 (326.6)	3.6915 (335.87)		
I_2 ($Zn_i^\bullet$)	3.790 (327.14)	3.7850 (327.56)	3.6803 (336.89)	8	[13]
I_1 (SA)	3.737 (331.77)	3.7320 (332.22)	3.6273 (342.1)	61–64	[13]
	3.744 (331.16)	3.7390 (331.59)	3.6343 (341.16)	54–57	
I_1 (SAL)	3.7734 (328.58)	3.7679 (329.05)	3.6437 (338.41)	24.5	[5]

Note: Variation in the energy of the split FE band with temperature [13] is given by $E(T) = E(0) - \alpha T^4/(\beta + T^3)$, where $E(0) = 3.7979$ eV (position of the free-exciton band at a temperature of 0 K), $\alpha = 4.04 \times 10^{-4}$ eV/K, and $\beta = 2.82 \times 10^6$ K^3 for FE_{lh}; and $E(0) = 3.8012$ eV, $\alpha = 4.15 \times 10^{-4}$ eV/K, and $\beta = 2.75 \times 10^6$ K^3 for FE_{hh}. The positions of BE bands were calculated on the basis of the known values of $E(T)$ at 10 K [13] and 100 K [5] taking into account the $FE_{lh}(T)$ dependence.

First, it was found that the short-wavelength component of SA emission at 410–415 nm appears with an intensity of 10^2–10^3. According to the accepted classification of luminescence centers [1], this short-wavelength component is related to the oxygen-containing complexes $\{O_S^* \cdot Zn_i^\bullet \cdot V_{Zn}''\}'$ that can be formed only if there a deficit of interstitial zinc in the crystal. An excess of zinc in the crystal results in the formation of donor–acceptor pairs $\{O_S^* \cdot Zn_i^\bullet \cdot V_{Zn}''\}'$–$Zn_i^\bullet$ that give rise to the long-wavelength component of the SA emission at 445 nm.

Second, in addition to the enhancement of SA emission, the band peaked at 850 nm and related to V_S vacancies is quenched as a result of the high-pressure high-temperature treatment. This behavior is possible if vacancies V_S are filled with oxygen, whose concentration in the crystals is $\sim 10^{20}$ cm^{-3}. The enhancement of 415-nm luminescence involving the oxygen-containing SA centers is consistent with an increase in the concentration of dissolved oxygen. We note in this context that the high-pressure high-temperature treatment is a more adequate method of affecting the equilibrium concentration and type of intrinsic point defects than annealing in the vapors of the compound constituents. Indeed, a decrease in the concentration of interstitial zinc $[Zn_i^\bullet]$ can also be attained by thermal annealing in sulfur

vapors; however, new defects appear as a result of annealing, in particular, zinc vacancies V_{Zn} [5].

Third, there is a correlation between the behavior of SA emission and that of the band in the spectral region that corresponds to the bound exciton; we refer to the doublet I_1, i.e., the band peaked at 331–332 nm and observed at 80 K. The observed spectral position of the bands of doublet I_1 corresponds to two acceptor levels of the SA center in the band gap of ZnS [1].

Since the bands related to bound excitons have a low intensity at a low excitation level (10^{22} cm^{-3} s^{-1}), we studied the cathodoluminescence of the same samples under conditions of higher excitation intensity (10^{26} cm^{-3} s^{-1}). Figure 3 shows the cathodoluminescence spectra measured at 300 K for an as-grown sample (spectrum *1*) and a sample subjected to the high-pressure high-temperature treatment (spectrum *2*) [11]. The band that is peaked at 342–343 nm and has a half-width at a half-height of ~60 meV is dominant at the high excitation level. The intensity of this band increases by an order of magnitude as a result of high-pressure high-temperature treatment. As can be seen from Fig. 3, this band of bound excitons is the only one in the cathodoluminescence spectra of ZnS after the high-pressure high-temperature treatment; i.e., this band is characteristic of "defect-free" ZnS (curve *2*). The band under consideration features a long-wavelength tail in the spectra of initial cleaved surfaces (curve *1*). The structure of this tail corresponds qualitatively to the bands observed in the cathodoluminescence spectra at the low excitation level (Fig. 2). The position of the main cathodoluminescence band at 300 K coincides with the calculated position of the doublet band I_1 (see table).

For pure ZnS containing a very high concentration of only oxygen-related SA centers after high-pressure high-temperature treatment, the observed band of bound excitons may be related to these centers. In addition, we observed a correlation between the positions of the peak of the band at 343 or 342 nm and those of the SA-emission components at 445 or 415 nm, respectively. This correlation is clearly seen in the cathodoluminescence spectra measured at a low excitation level. These spectra allow one to estimate the ratio between the intensities of the short-wavelength (415 nm) and long-wavelength (445 nm) components of SA emission. Our results are basically similar to the data reported in [15], which relate to studies of ZnSe. According to these data, the introduction of oxygen gave rise to bands of excitons bound to acceptor levels; in addition, recombination at donor–acceptor pairs was observed. Such an interpretation is also applicable to the results obtained previously [5, 16].

The bands of excitons bound to oxygen-containing SA centers that were observed by us make it possible to refine (using the binding energy ε) the position of acceptor levels $E_A = 10\varepsilon$ [14]. Taking into account two components of SA emission, we find that the energies

of the levels are equal to 0.61 and 0.54 eV, respectively. The values obtained are somewhat smaller than those obtained for E_A (0.69 and 0.59 eV) from the excitation and luminescence spectra according to the recombination model of emission [1]. If we also take into account the absence of spectral shift of oxygen-related bands [1, 4, 11] as the band gap varies with temperature, we should conclude that the SA emission corresponds to transitions from the excited level of the center to the ground level rather than from the conduction band. In particular, recombination at the donor–acceptor pairs that have a short distance between components and involve oxygen-containing complexes is possible.

Returning to the influence of high-pressure high-temperature treatment on the ZnS cathodoluminescence spectra at low excitation levels (Fig. 2), we note that, as a result of this treatment, the bands related to impurities of Group 1 (EE) and Cu (520–530 nm) are also intensified. Furthermore, new infrared bands peaked at 1475, 1635, and 1775 nm and caused by intracenter transitions in Cu_{Zn} ($3d^9$) ions appear in the spectrum. The appearance of these bands is consistent with the recharging of ions of residual copper $3d^{10} \longrightarrow 3d^9$ as the concentration of intrinsic donors decreases. Copper atoms in the lattice can fill zinc vacancies V_{Zn} at high external pressures. The presence of residual copper with a concentration of ~10^{16} cm^{-3} is possible in ZnS crystals.

It is especially noteworthy that a band peaked at 730 nm and related to ZnO inclusions in ZnS [9] appears in the cathodoluminescence spectrum after the high-pressure high-temperature treatment. This band is not observed in the cathodoluminescence spectra of as-grown samples. However, it is observed both at 80 K (Fig. 2) and at 300 K after the high-pressure high-temperature treatment, although the intensity of this band at 300 K is lower by approximately a factor of 2 than at 80 K. The fact that ZnO forms as a result of high-pressure high-temperature treatment is corroborated by the appearance of excitonic ZnO bands at 369, 380, and 385 nm [17] in a number of cathodoluminescence spectra (Fig. 4).

The band peaked at 730 nm has a higher intensity if the oxygen content in the crystals exceeds the corresponding solubility limit in ZnS, which is attained in the samples grown with a larger excess of sulfur. So the layers whose cathodoluminescence spectra are shown in Figs. 2 and 4 were grown under the conditions of $[Zn]/[H_2S] < 1$ (0.9) and > 1 (1.05). At a higher sulfur concentration, a decrease in the V_S concentration is confirmed by a decrease in the intensity of the cathodoluminescence band peaked at 850 nm (Figs. 2, 4; curves 2). In this case, the relative intensity of the ZnO band peaked at 730 nm (I_{730}/I_{exc}) increases from 0.1 to 0.3. It has been reported in previous publications that the ZnO emission at 730 nm is typical of the samples in which the formation of interstitial zinc is impeded [9].
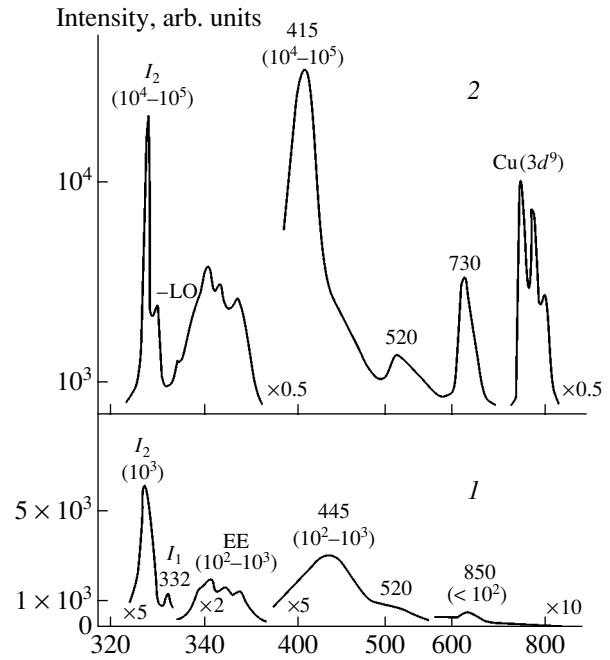
Fig. 2. Effect of high-pressure high-temperature treatment on the cathodoluminescence spectrum of CVD ZnS. Spectrum 1 corresponds to a cleaved surface before high-pressure high-temperature treatment and spectrum 2 corresponds to the same surface after this treatment. The excitation intensity was 10^{22} cm^{-3} s^{-1}. $T = 80$ K. $[Zn]/[H_2S] = 0.9$. The wavelengths (nm) and intensities (in parentheses) of the main bands are indicated at the corresponding peaks.

Fig. 3. The spectra of pulsed cathodoluminescence of the same cleaved surfaces as in Fig. 2 but at an excitation density of 10^{26} cm^{-3} s^{-1} and $T = 300$ K. Spectrum 1 corresponds to as-grown ZnS; spectrum 2, to ZnS subjected to high-pressure high-temperature treatment.
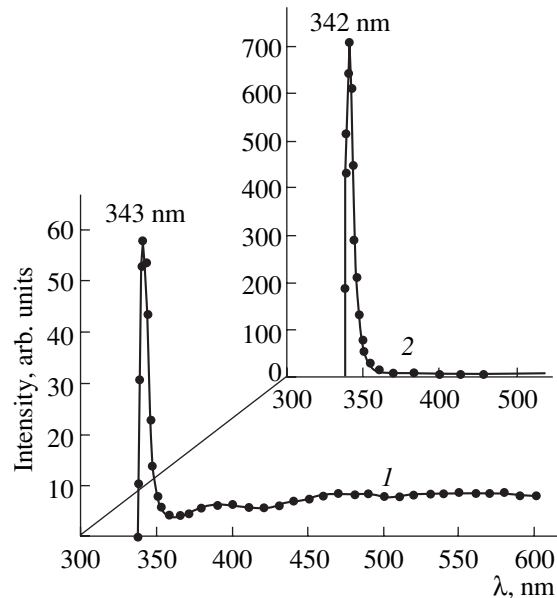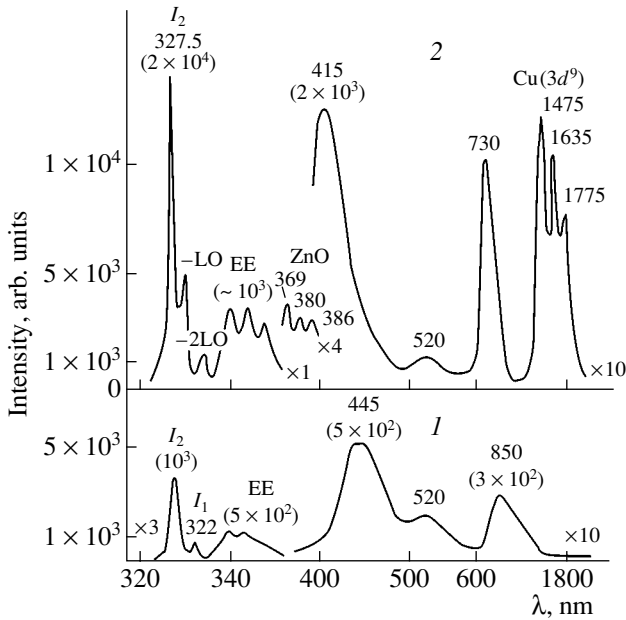
Fig. 4. Cathodoluminescence spectra of cleaved surfaces of CVD ZnS at an excitation density of 10^{22} cm^{-3} s^{-1} and $T = 80$ K. [Zn]/[H$_2$S] = 1.05. Spectrum *1* corresponds to as-grown ZnS; spectrum *2*, to the sample subjected to high-pressure high-temperature treatment. Wavelengths (nm) and intensities (in parentheses) of the main bands are indicated at the corresponding peaks.
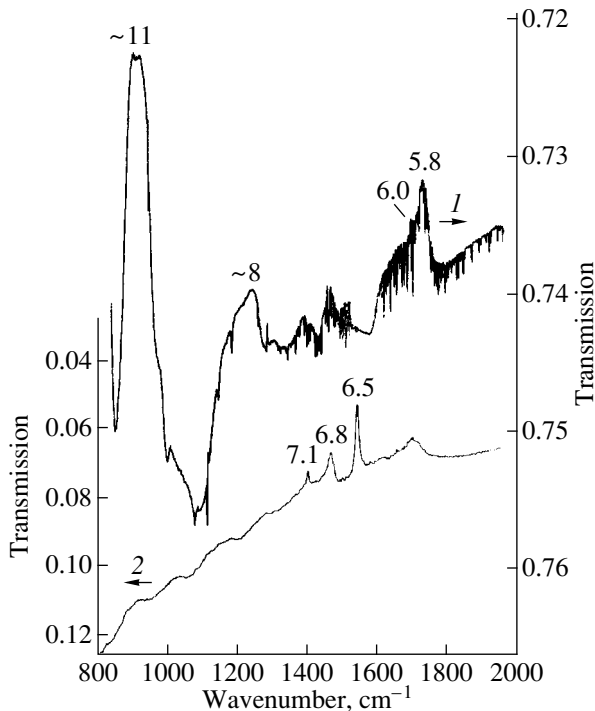

Fig. 5. Transmission spectra of ZnS at $T = 300$ K. Spectrum *1* corresponds to a sample after high-pressure high-temperature treatment (see Fig. 2); spectrum *2*, to a ZnS single crystal with ZnO inclusions after aging [5]. Wavelengths of the main bands expressed in micrometers are indicated.

In order to verify whether it is possible to estimate the presence of ZnO from the intensity of the cathodoluminescence band peaked at 730 nm, we studied the ZnS optical-transmission spectra, since it was previously shown [18] that even low concentrations of ZnO can be revealed from the Fourier spectra in the range 5–15 µm. In Fig. 5, we show the transmission spectra that are measured using the method described in [18]. A group of narrow absorption bands peaked at 5.8, 6.5, 6.8, and 7.1 µm and characteristic of ZnO inclusions is apparent in Fig. 5 (curve *1*). An analysis of the intensities of the aforementioned bands for various CVD ZnS layers showed that there was a correlation between these intensities and the intensity of the cathodoluminescence band peaked at 730 nm. For example, the transmission spectrum with a pronounced structure in the region 5–7 µm (Fig. 5, curve *1*) corresponds to a sample with a more intense cathodoluminescence band peaked at 730 nm after high-pressure high-temperature treatment. The group of bands under consideration is either not observed at all or is poorly pronounced against the background in the transmission spectra of as-grown samples.

A broad absorption band at a longer wavelength (~11 µm) was also observed in the transmission spectra in addition to the group of narrow bands. This band coincides with an intense absorption band of the (LO + TO) multiphonon spectrum of ZnO single crystals [18, 19] and is similar to the 10.2-µm ZnSe band that was observed at early stages of the formation of the oxide phase [18]. For comparison, Fig. 5 also shows a transmission spectrum (curve *2*) of a ZnS:Cu single crystal (10^{-3}% of Cu) after aging; the precipitation of the ZnO phase (most pronounced in the presence of copper) in this crystal is confirmed by studies of microcathodoluminescence in a scanning electron microscope [5]. In the aforementioned spectrum, the 11-µm broad band for ZnS is suppressed as in similar cases for ZnSe [18]. The band peaked at 11 µm becomes somewhat intensified after high-pressure high-temperature treatment of zinc sulfide layers.

We can draw the following conclusion on the basis of the results obtained.

The effects observed after the high-pressure high-temperature treatment are related to a decrease in the ZnS unit-cell volume, which is expected at a high pressure. The role of interstitial zinc atoms as rapidly diffusing native donors involved in the establishment of equilibrium interaction between intrinsic point defects is confirmed. High-pressure high-temperature treatment gives rise to an extremely uniform doping with the formation of stable centers or solid solutions in a perfect defect-free host.

The results of our studies reported above make it possible to confirm the accepted classification of oxygen-related centers. It is ascertained that oxygen-related centers (complexes) responsible for SA and SAL emission in ZnS have acceptor levels that can bind

excitons. These centers control luminescence at high excitation densities. We clarified the emission type and the depth of acceptor levels of oxygen-related centers: ~0.25 eV for SAL emission at 355–370 nm and 0.61 and 0.54 eV for two components (at 445 and 415 nm) of SA emission.

The relationship between the 730-nm luminescence band in ZnS that is free of extraneous impurities and the presence of the ZnO phase is confirmed.

REFERENCES

1. N. K. Morozova, I. A. Karetnikov, V. V. Blinov, and E. M. Gavrishchuk, Fiz. Tekh. Poluprovodn. (St. Petersburg) **35**, 25 (2001) [Semiconductors **35**, 24 (2001)].

2. Yu. N. Dmitriev, V. D. Ryzhikov, and L. P. Gal'chinetskiĭ, *Thermodynamics of Isovalent Doping of Crystals of the II–VI Semiconductor Compounds* (VNII Monokristallov, Khar'kov, 1990), No. IMK-90-16.

3. É. D. Aluker, D. Yu. Lusis, and S. A. Chernov, *Electron Excitations and Radioluminescence in Alkali Metals* (Zinatne, Riga, 1979).

4. N. K. Morozova, D. V. Zhukov, V. E. Mashchenko, and V. V. Blinov, in *Proceedings of XXXII International Scientific and Technical Seminar on Noise and Degradation Processes in Semiconductor Devices* (Mosk. Énerg. Inst., Moscow, 2002), p. 234.

5. N. K. Morozova and V. A. Kuznetsov, *Zinc Sulfide. Production and Optical Properties*, Ed. by M. V. Fok (Nauka, Moscow, 1987).

6. E. M. Gavrishchuk and É. V. Yashina, Vysokochist. Veshchestva, No. 5, 36 (1994).

7. C. M. J. Rooymans, *Structural Investigations on Some Oxide and Other Chalcogenides at Normal and Very High Pressures* (Philips, Eindhoven, 1968; Mir, Moscow, 1969).

8. V. M. Lisitsyn, V. I. Korepanov, V. I. Oleshko, and V. Yu. Yakovlev, Izv. Vyssh. Uchebn. Zaved., Fiz., No. 11, 5 (1996).

9. N. P. Golubeva and M. V. Fok, Zh. Prikl. Spektrosk. **17**, 261 (1972).

10. K. Leutwein, A. Rauber, and J. Schneider, Solid State Commun. **5**, 783 (1967).

11. N. K. Morozova, I. A. Karetnikov, E. M. Gavrishchuk, *et al.*, in *Proceedings of XXXIII International Scientific and Technical Seminar on Noise and Degradation Processes in Semiconductor Devices* (Mosk. Énerg. Inst., Moscow, 2003), p. 12.

12. Nam Sungun, Rhee Jongkwang, O. Byungsung, and Ki-Seon Lee, J. Korean Phys. Soc. **32** (2), 156 (1998).

13. N. Lovergine, P. Prete, G. Leo, *et al.*, Cryst. Res. Technol. **33**, 183 (1998).

14. *Physics and Chemistry of II–VI Compounds*, Ed. by M. Aven and J. S. Prener (North-Holland, Amsterdam, 1967; Mir, Moscow, 1970).

15. K. Akimoto, T. Miyajima, and Y. Mori, Phys. Rev. B **39**, 3138 (1989).

16. A. M. Akhekyan, V. I. Kozlovskiĭ, Yu. V. Korostelin, and Ya. K. Skasyrskiĭ, Kratk. Soobshch. Fiz., No. 3, 44 (1988).

17. I. P. Kuz'mina and V. A. Nikitenko, *Zinc Oxide* (Nauka, Moscow, 1984), p. 165.

18. N. K. Morozova, V. G. Plotnichenko, E. M. Gavrishchuk, and V. V. Blinov, Neorg. Mater. **39**, 1105 (2003).

19. R. J. Collins and D. A. Kleiman, J. Phys. Chem. Solids **11**, 190 (1959).

Translated by A. Spitsyn

ELECTRONIC AND OPTICAL PROPERTIES
OF SEMICONDUCTORS

The Influence of Impurities on Radiative Recombination via *EL*2 Centers in Gallium Arsenide Single Crystals

M. B. Litvinova

Institute of Semiconductor Physics, National Academy of Sciences of Ukraine, Kiev, 03028 Ukraine
e-mail: lmb@ist.com.ua

Abstract—The influence of Cd and Se atoms on the quantum efficiency of emission induced by *EL*2 defects in GaAs single crystals is studied in detail. The diffusion of impurities under conditions of vacuum is compared to that in an As atmosphere. It is ascertained that the character and degree of variation in the quantum efficiency are governed by the vacancy type and concentration in the crystals and are related to the probability of formation of complexes that consist of *EL*2 centers and impurities. © *2004 MAIK "Nauka/Interperiodica".*

1. INTRODUCTION

*EL*2 antisite defects play a fundamental role in determining the semi-insulating properties of undoped GaAs single crystals; notably, GaAs is widely used as a substrate material in microelectronics. Data on the structure and recombination properties of *EL*2 centers are favorable for the production of high-quality crystals with specified properties.

Recombination processes involving *EL*2 centers give rise to an emission band peaked at $h\nu_m \approx 0.65$ eV in the low-temperature ($T = 77$ K) GaAs photoluminescence (PL) spectra; this band is a superposition of the bands peaked at $h\nu_m \approx 0.63$ eV and $h\nu_m \approx 0.68$ eV (Fig. 1a) [1]. The 0.63-eV band is related to the radiative capture of free electrons e by charged $EL2^+$ defects (the transition $e \longrightarrow EL2^+$), whereas the 0.68-eV band is related to the radiative capture of free holes h by neutral $EL2^0$ defects (the transition $h \longrightarrow EL2^0$) (see inset in Fig. 1a). A number of factors affect the efficiency of recombination via the centers under consideration. First of all, we should take into account the self-diffusion in GaAs. Diffusion of As vacancies from the surface during high-temperature thermal annealing (TA) of GaAs in vacuum leads to a decrease in the concentration of *EL*2 centers (N_{EL2}) as a result of the reaction

$$As_{Ga} + V_{As} \Leftrightarrow V_{Ga} + As_{As} \tag{1}$$

and to a decrease in the intensity of emission with $h\nu_m = 0.65$ eV ($I_{0.65}$). In contrast, the formation of new *EL*2 centers during TA under conditions of an excess pressure of As vapors ($p_{As} > 9.8 \times 10^4$ Pa) results in an increase in $I_{0.65}$ [2].

It is also known that a decrease in the intensity of emission with $h\nu_m \approx 0.65$ eV occurs if Cu atoms are introduced into GaAs; this decrease is caused by passivation of *EL*2 defects as a result of the formation of *EL*2–Cu complexes [3]. However, the influence of other donor and acceptor impurities on the efficiency of

recombination via the centers under consideration has hardly been studied.

In this study, we show that copper is not the only impurity that causes a variation in the quantum efficiency of emission via *EL*2 defects. We investigate the origin of this variation by comparing the results of introducing the impurity in vacuum and in an As atmosphere. We then analyze the data obtained taking into account the structure of *EL*2 centers.

2. EXPERIMENTAL

The starting samples were semi-insulating nominally undoped *n*-GaAs (100) crystals grown by the Czochralski method; the crystals had resistivity $\rho = 7 \times 10^7$–2×10^8 Ω cm. The concentration of *EL*2 centers determined from optical absorption of photons with energy $h\nu = 1.04$ eV [1] was equal to $N = (1.2$–$1.8) \times 10^{16}$ cm^{-3}. The initial difference between the intensities of the PL bands with $h\nu_m \approx 0.63$ eV and $h\nu_m \approx 0.68$ eV at 77 K did not exceed 6%. Since the bands induced by oxygen atoms [4, 5] ($h\nu_m \approx 0.63$ eV) can also be present in the spectral region under consideration, we studied the selective-excitation spectra of PL. The data on the photoquenching of radiative recombination via the *EL*2 defects before and after the introduction of an impurity into the samples (see Appendix) made it possible to relate all the defects observed in this study to the *EL*2 centers.

The impurities (selenium or cadmium) were introduced into the samples with a thickness of ~2 mm at a temperature of 800°C for 4–8 h with subsequent rapid cooling. The impurity was introduced from a thermally deposited 1-μm-thick Cd (or Se) layer, which ensured diffusion from an inexhaustible source. The formed Ga$_2$Se$_3$ surface layer was removed using an acid etchant after Se diffusion.

The diffusion of impurities was carried out either in vacuum or under an excess pressure of arsenic vapors. The samples to be annealed were placed in quartz cells with an operating volume of ~4 cm^{-3}; the cells were preliminarily degreased and etched in aqua regia, which reduced the uncontrollable contamination of the crystals with copper. The cells were pumped out to a pressure of $<10^{-3}$ Pa. In order to provide an excess pressure of As, we put an As charge with a mass of 20 mg into the cells. The diffusion coefficients for impurities at $T = 800°C$ ($D_{Cd} \cong 3 \times 10^{-16}$ cm^2 s^{-1} and $D_{Se} \cong 7 \times 10^{-17}$ cm^2 s^{-1} [6]) are much smaller than those for As vacancies ($D_{VAs} \cong 1 \times 10^{-15}$ cm^2 s^{-1} [7]). Thus, diffusion in evacuated cells ensured that the impurity was introduced into crystals with a deficit of arsenic, whereas the impurity was introduced into crystals with an excess of As as result of diffusion under conditions of excess pressure of As vapors [2].

We also performed a control annealing of the samples without a Cd (or Se) layer on the surface. This annealing was carried out either in vacuum or under excess pressure of As vapors, in the same conditions as for diffusion of Se and Cd. The charge-carrier concentration at $n > 10^{16}$ cm^{-3} was determined from the half-width of the PL edge-emission band at 300 K [8].

We studied the PL and selective-excitation luminescence (SEL) spectra using conventional methods [8]. A He–Ne laser with an emission wavelength of 0.63 μm was used as the PL excitation source. In order to obtain the SEL spectra, we employed a KGM lamp with a power of 60 W. Selective resolution of excitation bands with a half-width $w_{exc} \le 0.8$ meV and a power of 4–6 mW in the range $h\nu = 1.0$–1.52 eV was accomplished using an MDR-2 monochromator. The emission intensity (I_m) at 77 K was detected by an FÉU-68 photomultiplier for the region $h\nu_m > 1$ eV and by a cooled FD-9G germanium photodiode for the region $h\nu_m < 1$ eV. The values of relative emission intensity $I_{arb} = I_m/I_{exc}$ (I_{exc} is the corresponding intensity of PL excitation) were then automatically recalculated.

When studying the emission photoquenching due to *EL*2 centers, we first heated the sample to $T = 155 \pm 5$ K and then kept the sample at this temperature for 10–11 min. After that, the sample was rapidly cooled to 77 K. The intensity I_m was measured only after the value of I_m was completely stabilized. This procedure was repeated before each new value of $I_m(h\nu_{exc})$ was determined; the step in measurements was $\Delta h\nu_{exc} = 2$ meV.

3. THEORETICAL EXPRESSIONS FOR THE INTENSITY OF EMISSION VIA THE *EL*2 CENTERS

3.1. Semi-Insulating Nominally Undoped n-GaAs

If PL is excited within the fundamental-absorption range, the intensities of the luminescence bands related
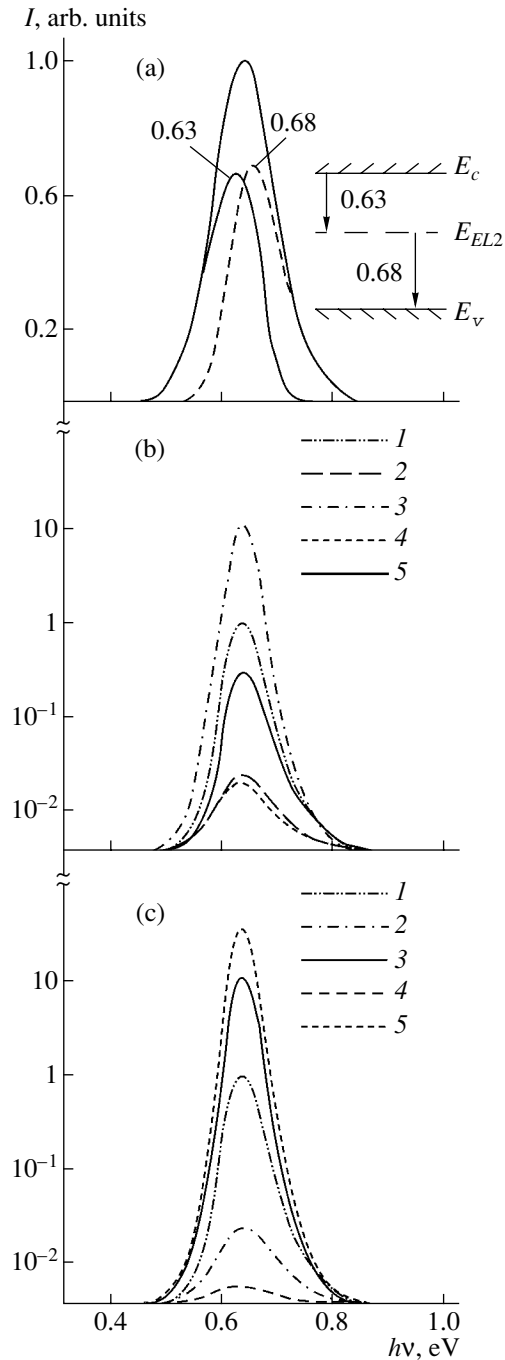
Fig. 1. The emission band with $h\nu_m \approx 0.65$ eV in the PL spectrum of gallium arsenide at $T = 77$ K: (a) resolution into components with peaks at 0.63 and 0.68 eV (the corresponding optical transitions are shown in the inset); (b) variation in $I_{0.65}$ as a result of introduction of cadmium ($N_{Cd} = 8 \times 10^{17}$ cm^{-3}); and (c) variation in $I_{0.65}$ as a result of introduction of selenium ($N_{Se} = 3 \times 10^{18}$ cm^{-3}). Spectrum *1* corresponds to as-grown semi-insulating nominally undoped crystals; spectrum *2* corresponds to a sample subjected to TA in vacuum without an impurity layer on the surface; spectrum *3* corresponds to a sample after TA in an As atmosphere without an impurity layer on the surface; spectrum *4* corresponds to a sample with an impurity introduced under conditions of vacuum; and spectrum *5* corresponds to a sample into which an impurity was introduced as a result of TA in an As atmosphere.

Fig. 2. Variation in $I_{0.65}$ as a function of the concentrations of (*4*) Cd and (*5, 6*) Se impurities introduced (*4, 5*) in an As atmosphere and (*6*) in vacuum. The broken lines correspond to $I_{0.65}$ (*1*) in an as-grown crystal, (*2*) in a crystal after TA in an As atmosphere without an impurity layer on the surface, and (*3*) in a crystal after TA in vacuum without an impurity layer on the surface.
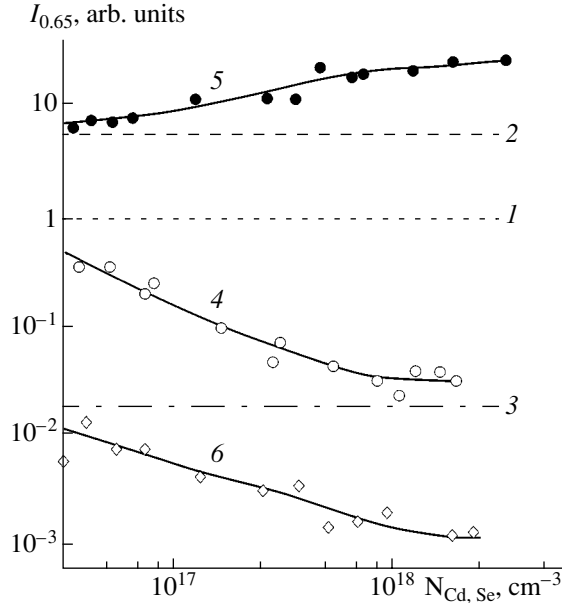
to the defects $EL2^+$ ($I_{0.63}$) and $EL2^0$ ($I_{0.68}$) (Fig. 1a) are equal in value under steady-state conditions [1, 3]; i.e.,

$$I_{0.68} = I_{0.63}. \tag{2}$$

For a high-resistivity undoped material, we then have

$$I_{0.68} = c_p^0 N_{EL2}^0 \delta p, \tag{3}$$

$$I_{0.63} = c_n^+ N_{EL2}^+ \delta n = c_n^+ (N_{EL2} - N_{EL2}^0)\delta n, \tag{4}$$

where δn and δp are the nonequilibrium concentrations of electrons and holes ($\delta p \gg n_0$ and $\delta p \gg p_0$; n_0 and p_0 are the corresponding equilibrium concentrations); c_n^+ and c_p^0 are the coefficients of radiative capture of electrons by the $EL2^+$ defects and of holes by the $EL2^0$ defects, respectively; N_{EL2}^+ and N_{EL2}^0 are the concentrations of corresponding defects; and N_{EL2} is the total concentration of these defects. It follows from expressions (2), (3), and (4) that

$$c_p^0 N_{EL2}^0 \delta p = c_n^+ (N_{EL2} - N_{EL2}^0)\delta n, \tag{5}$$

$$N_{EL2}^0 = (c_n^+ N_{EL2}\delta n)/(c_p^0 \delta p + c_n^+ \delta n). \tag{6}$$

Since $c_p^0 \ll c_n^+$, we obtain $N_{EL2}^0 \cong N_{EL2}$ and

$$I_{0.65} = c_p^0 N_{EL2}\delta p. \tag{7}$$

3.2. GaAs:Cd

All the centers are filled with holes in a low-resistivity material with *p*-type conductivity ($p_0 \gg \delta n, p_0 \gg \delta p$) in a state of equilibrium; as a result, the equilibrium concentration $N_{EL2}^0 = 0$ and the nonequilibrium concentration $\delta N_{EL2}^0 \ll N_{EL2}$. Therefore, under conditions of linear charge-carrier recombination via *EL2* centers, the emission intensity is given by

$$I_{0.65} = c_n^+ (N_{EL2} - \delta N_{EL2}^0)\delta n \approx c_n^+ N_{EL2}\delta n. \tag{8}$$

3.3. GaAs:Se

All the centers are filled with electrons in a low-resistivity *n*-type material ($n_0 \gg \delta n, n_0 \gg \delta p$), so that the equilibrium concentrations $N_{EL2}^+ = 0$ and $N_{EL2}^0 = N_{EL2}$. It then follows from (2) that

$$c_n^+ \delta N_{EL2}^+ \delta n = c_p^0 (N_{EL2}^0 + \delta N_{EL2}^0)\delta p. \tag{9}$$

Since $N_{EL2}^0 \gg \delta N_{EL2}^0$, the following formula is valid in conditions of linear charge-carrier recombination:

$$I_{0.65} = c_p^0 N_{EL2}\delta p. \tag{10}$$

4. RESULTS AND DISCUSSION

4.1. Introduction of Cadmium

After the diffusion of cadmium atoms, the surface of the crystals had *p*-type conductivity. Doping under conditions of vacuum caused a decrease in $I_{0.65}$ to the same extent as in the case of TA without an impurity layer on the surface (Fig. 1b, curves *2, 4*). If diffusion of Cd was carried out under conditions of an excess pressure of As vapors, the intensity of emission related to *EL2* centers decreased, whereas the annealing of control samples without an impurity layer on the surface led to an increase in this intensity (see Section 1). The values of intensity $I_{0.65}$ on the surface of doped crystals were two to three orders of magnitude smaller than those typically obtained after annealing a sample without a surface impurity layer (Fig. 1b, curves *3, 5*).

The dependence of $I_{0.65}$ on the impurity concentration indicates (Fig. 2, curve *4*) that $I_{0.65}(N_{Cd})$ decreases as the concentration of cadmium atoms in the crystal increases.

Since linear recombination of charge carriers is observed at the surface of doped crystals and the lifetime of charge carriers ($\tau_n = (2-3) \times 10^{-10}$ s) changes only slightly compared to that observed in semi-insulating nominally undoped GaAs (this behavior suggests that new and more efficient channels of radiative and nonradiative recombination are not introduced), it follows from formulas (8) and (10) that $I_{0.65} \propto N_{EL2}$. Therefore, a decrease in $I_{0.65}$ after TA in an As atmosphere (as

in the case of doping with Cu [3]) is caused by a decrease in the concentration of individual *EL2* centers due to the formation of the *EL2*–Cd complexes.

Indeed, since Cd atoms in GaAs occupy Ga vacancies, these atoms can be involved in the above complexes as $EL2$–Cd_{Ga}.[1] As was mentioned above, the diffusion coefficient for Cd atoms is much smaller than that for arsenic vacancies. Therefore, we may expect that cadmium diffuses into the crystal region where the concentration $[V_{As}]$ decreases in the presence of excess pressure of As vapors; thus, according to the expression [2]

$$[V_{As}][V_{Ga}] = k p_{As}^{1/2} \qquad (11)$$

($[V_{As}]$ and $[V_{Ga}]$ are the concentrations of the As and Ga vacancies), $[V_{Ga}]$ increases (there is a deficit of gallium) [6]. An increase in the number of V_{Ga} vacancies near the antisite As_{Ga} defects favors the formation of $EL2$–Cd_{Ga} complexes. At the same time, under conditions of vacuum, the impurity diffuses into the surface crystal region with a high $[V_{As}]$ concentration and, accordingly, a low $[V_{Ga}]$ concentration. This circumstance accounts for the low probability of forming As_{Ga}–Cd_{Ga} complexes; the introduction of Cd does not affect $I_{0.65}$.

4.2. Introduction of Selenium

The surface of the crystals had *n*-type conductivity after the introduction of selenium atoms. Diffusion under conditions of vacuum led to a greater decrease in $I_{0.65}$ than was observed after annealing the samples without impurity surface layers (Fig. 1c, curves *2*, *4*). At the same time, the diffusion of Se in an atmosphere of As resulted in an increase in $I_{0.65}$ compared to that observed after annealing without impurities (Fig. 1c, curves *3*, *5*). Both effects became more pronounced as the impurity concentration (N_{Se}) increased (Fig. 2, curves *5*, *6*).

When the charge-carrier recombination is linear and the lifetime in the region doped with Se corresponds to the lifetime in semi-insulating nominally undoped GaAs, it follows from (8) and (11) that $I_{0.65} \propto N_{EL2}$; thus, the variation in $I_{0.65}$ is caused by a change in N_{EL2}.

An increase in the intensity of emission related to *EL2* centers after diffusion of Se in an atmosphere of As vapors is most probably caused by partial replacement of As atoms by the impurity that is introduced into the As sublattice [9]. In this case, the displaced atoms can occupy Ga vacancies and form antisite defects (as mentioned above, the concentration $[V_{Ga}]$ increases at the crystal surface as a result of TA in the atmosphere of As vapors).

The decrease in $I_{0.65}$ caused by selenium diffusion as a result of TA in vacuum can be related (as in the case of the introduction of cadmium and copper) to a

decrease in the efficiency of emission via *EL2* defects due to the formation of *EL2*–Se complexes. Indeed, selenium atoms diffuse over the lattice sites of the As sublattice [7] and can form $EL2$–Se_{As} complexes (see footnote 1). If TA is carried out in vacuum, the impurity is found in the crystal region with a high concentration of $[V_{As}]$ (with a deficit of As) as a result of the escape of As. In this case, the formation of the complexes is caused by the fact that As vacancies are present near the antisite defects As_{Ga}. The above behavior is possible if the probability of recombination between As_{Ga} and V_{As} [see expression (1)] is lower than unity, i.e., if there is a potential barrier for such recombination.[2]

4.3. Comments on the Structure of EL2 Defects

Despite prolonged research into *EL2* centers, which were first detected in 1963 [11] and were then identified with a deep-level donor in 1976 [12], there is so far no unified opinion about the structure of this center [13–18]. From 1982 onward, various models of the *EL2* center were based on the assumption that this center is an antisite As_{Ga} defect [19–21]. However, some scientists still believe that *EL2* centers are individual As_{Ga} defects [15], whereas other scientists identify these centers with complexes of As_{Ga} with As interstitial atoms As_i ($As_{Ga}As_i$) [16] and with gallium vacancies V_{Ga} ($As_{Ga}V_{Ga}$) [17] or with the vacancy association $V_{As}V_{Ga}$ ($As_{Ga}V_{As}V_{Ga}$) [18]. There are also data that make it possible to consider *EL2* centers as a family of $As_{Ga} + X$ defects [22, 23] whose composition can change depending on element X as a result of thermal treatment [23].

The results of this study show that Ga vacancies are located in the vicinity of As_{Ga} antisite defects in crystals with a deficit of gallium. At the same time, an increase in the concentration of arsenic vacancies governs the localization of these vacancies in the vicinity of antisite defects. Consequently, a possible solution to the issue concerning the composition of complexes with As_{Ga} defect is the assumption that the probability of formation of these complexes is controlled by the concentration of specific point defects in the crystal. A variation in the point-defect concentration brings about either a change in the structure of a complex consisting of As_{Ga} and a point defect in favor of the dominant defect or the absence of a point defect in the vicinity of As_{Ga}.

5. CONCLUSIONS

1. Copper is not the only impurity that affects the quantum efficiency of emission via *EL2* defects in GaAs crystals. The introduction of a cadmium acceptor impurity results in a decrease in this efficiency in crystals with a deficit of gallium and does not affect it in crystals with a deficit of arsenic. This effect is caused

---

[1] Diffusion of Cd and Se proceeds according to the dissociative mechanism, and the probability of forming complexes with interstitial impurity atoms is low [7].

[2] The data reported in [9, 10] indicate the existence of a potential barrier for recombination between As_i and V_{As} in the crystal bulk. At the GaAs crystallization temperature, the barrier height exceeds 5 eV.
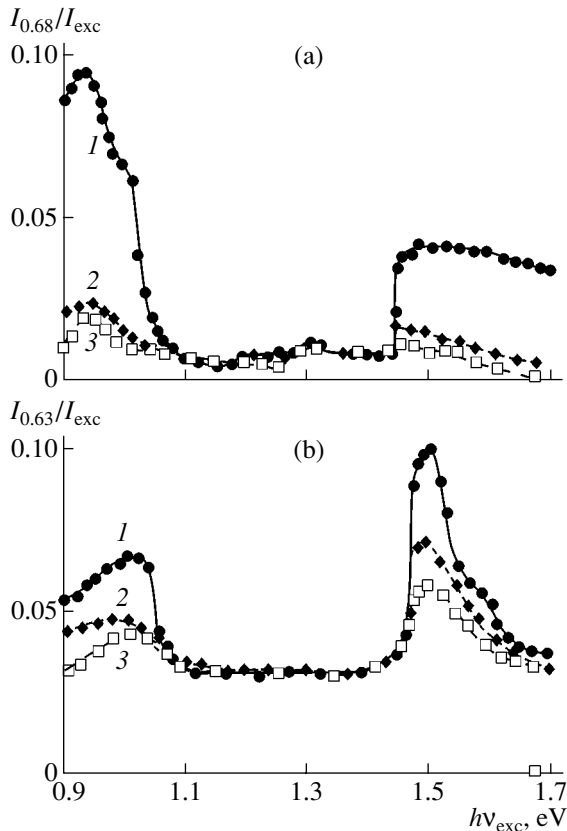
Fig. 3. The spectrum of selective excitation of luminescence at $T = 77$ K for (a) the band with $h\nu_m = 0.68$ eV and (b) the band with $h\nu_m = 0.63$ eV. Spectrum *1* corresponds to the as-grown semi-insulating nominally undoped GaAs crystal; spectrum *2* was measured after diffusion of cadmium in the atmosphere of As vapors ($N_{Cd} = 1.12 \times 10^{18}$ cm^{-3}); and spectrum *3* was measured after diffusion of selenium ($N_{Se} = 2 \times 10^{18}$ cm^{-3}) in an atmosphere of As vapors.

by a decrease in the concentration of individual *EL*2 centers as a result of the formation of *EL*2–Cd$_{Ga}$ complexes.

2. The introduction of a selenium donor impurity increases the quantum yield of emission via *EL*2 defects in crystals with a deficit of gallium and reduces this yield in crystals with a deficit of arsenic. The former effect is most probably caused by an increase in the concentration of *EL*2 centers as a result of displacement of As atoms from the arsenic sublattice sites by the impurity; the latter effect is probably caused by the formation of *EL*2–Se$_{As}$ complexes.

3. We can clarify the issue concerning the composition of complexes that consist of *EL*2 centers and point defects by assuming that a variation in the concentration of point defects (vacancies and interstitial atoms) in the crystal brings about a corresponding variation in the structure of complexes in favor of a dominant defect or the absence of point defects in the vicinity of As$_{Ga}$.

PHOTOQUENCHING OF EMISSION RELATED TO *EL*2 DEFECTS

As was mentioned above (see Section 2), oxygen atoms (along with *EL*2 defects) can make a certain contribution to the emission with $h\nu_m \approx 0.63$ eV. In order to clarify the extent of the effect of oxygen impurity (or any other defects related to the emission with $h\nu_m \approx 0.63$–0.68 eV [18]) based on the results obtained in this study, we studied the spectra of selective excitation of luminescence bands with $h\nu_m = 0.63$ eV ($I_{0.63}$) and $h\nu_m = 0.68$ eV ($I_{0.68}$) in several control GaAs crystals before and after introducing the impurity.[3] It can be seen from the spectrum of selective excitation of luminescence for semi-insulating nominally undoped GaAs at $T = 77$ K (Figs. 3a, 3b, curve *1*) that almost complete quenching of $I_{0.68}$ and incomplete quenching of $I_{0.63}$ takes place in the range $h\nu_{exc} \approx 1.102$–1.458 eV. The values of $I_{0.68}$ and $I_{0.63}$ (Fig. 3, curves *2*, *3*) in the photoquenching region were no different from the corresponding values in initial crystals after the introduction of Se and Cd atoms with the highest concentrations of N_{Se} (or N_{Cd}) attained in this study.

It is known that the effect of quenching the emission with $h\nu_m = 0.63$ and 0.68 eV at $h\nu_{exc} \approx 1.1$–1.45 eV is governed by the transformation of *EL*2 defects into an inactive metastable state [24]. Residual (after photoquenching) emission with $h\nu_m = 0.63$ eV is most probably caused by oxygen atoms [5] (the magnitude of the effect of quenching for the oxygen-related band with $h\nu_m = 0.63$ eV is very small compared with that for the band associated with the *EL*2 defect [24]). The existence of photoquenching and the fact that the introduction of both cadmium and selenium does not affect the residual intensities $I_{0.63}$ and $I_{0.68}$ indicate that the variations in $I_{0.65}$ observed in this study in the region doped with impurities are related to *EL*2 defects.

REFERENCES

1. K. D. Glinchuk, V. I. Goroshev, and A. V. Prokhorovich, Optoélektron. Poluprovodn. Tekh., No. 24, 66 (1992).

2. I. I. Pokaznoĭ, F. S. Shishiyanu, I. M. Tiginyanu, *et al.*, Fiz. Tekh. Poluprovodn. (Leningrad) **22**, 1108 (1988) [Sov. Phys. Semicond. **22**, 699 (1988)].

3. K. D. Glinchuk, A. V. Prokhorovich, and F. M. Vorobkalo, Cryst. Res. Technol. **31**, 1045 (1996).

4. P. W. Yu and D. S. Wallers, Appl. Phys. Lett. **41**, 863 (1982).

5. T. Kazuno, Y. Sawada, and T. Y. Yokoyama, Jpn. J. Appl. Phys. **25**, L878 (1986).

6. M. G. Mil'vidskiĭ, O. V. Pelevin, and B. A. Sakharov, *Physicochemical Fundamentals of Production of Decaying Semiconductor Compounds* (Metallurgiya, Moscow, 1974).

[3] As was mentioned in Section 1, the band with $h\nu_m \approx 0.65$ eV is a superposition of the bands with $h\nu_m \approx 0.63$ eV and $h\nu_m \approx 0.68$ eV.

7. F. S. Shishiyanu, *Diffusion and Degradation in Semiconductor Materials and Devices* (Shtiintsa, Kishinev, 1978).

8. G. P. Peka, V. F. Kovalenko, and V. N. Kutsenko, *Luminescence Methods of Contol of Parameters of Semiconductor Materials and Devices* (Tekhnika, Kiev, 1986).

9. V. V. Voronkov, A. Yu. Bol'sheva, R. I. Gloriozova, *et al.*, Kristallografiya **32**, 208 (1987) [Sov. Phys. Crystallogr. **32**, 118 (1987)].

10. K. M. Luken and R. A. Morrow, J. Appl. Phys. **79**, 1388 (1996).

11. N. G. Ainsle and J. F. Woods, J. Appl. Phys. **35**, 1469 (1963).

12. A. Mircea, A. Mitonneay, L. Mollan, and A. Briere, Appl. Phys. **11**, 153 (1976).

13. K.-H. Wietzke, F. K. Koschnick, and J.-M. Spaeth, Mater. Sci. Forum (Vols. Switzerland), 1061 (1995).

14. S. A. Goodman, F. K. Koschnick, C. Weber, *et al.*, Solid State Commun. **110**, 593 (1999).

15. Q. M. Zhang and J. Bernholc, Phys. Rev. B **47**, 1667 (1993).

16. H. E. Ruda, Q. Liu, M. Ozawa, *et al.*, J. Phys. D: Appl. Phys. **25**, 1538 (1992).

17. R. A. Morrow, J. Appl. Phys. **78**, 5166 (1995).

18. Chen Chao, M. A. Bykovskiĭ, and M. I. Tarasik, Fiz. Tekh. Poluprovodn. (St. Petersburg) **28**, 35 (1994) [Semiconductors **28**, 19 (1994)].

19. E. R. Weber, H. Ennet, V. Kaufmann, *et al.*, J. Appl. Phys. **53**, 6140 (1982).

20. D. E. Holmes, R. T. Chen, K. R. Elliott, and G. Kirkparrick, Appl. Phys. Lett. **40**, 46 (1982).

21. J. Lagowski, H. C. Gatos, J. M. Parsey, *et al.*, Appl. Phys. Lett. **40**, 342 (1982).

22. D. W. Fischer, Phys. Rev. B **37**, 2968 (1988).

23. Hoon Young Cho, Eun Kyu Kim, and Suk-Ki Min, Phys. Rev. B **39**, 10376 (1989).

24. M. Tajima, Jpn. J. Appl. Phys. **26**, L885 (1987).

Translated by A. Spitsyn

Structurally Complex Two-Hole and Two-Electron Slow Traps with Bikinetic Properties in *p*-ZnTe and *n*-ZnS Crystals

M. A. Rizakhanov*, E. M. Zobov*, and M. M. Khamidov**

*Amirkhanov Institute of Physics, Dagestan Scientific Center, Russian Academy of Sciences,
ul. 26 Bakinskikh Komissarov, Makhachkala, 367003 Russia
e-mail: zob_em@mail.ru
**Dagestan State University, Makhachkala, 367000 Russia
Submitted March 11, 2003; accepted for publication May 12, 2003

Abstract—Thermal-activation and photoactivation methods were used to ascertain the existence of two-hole traps in *p*-ZnTe crystals and two-electron traps in *n*-ZnS. It was found that these traps have a large number of energy states that are grouped in two series of levels: $E_V + (0.46–0.66)$ eV and $E_V + (0.06–0.26)$ eV in *p*-ZnTe and $E_C – (0.6–0.65)$ eV and $E_C – (0.14–0.18)$ eV in *n*-ZnS. Both the hole and the electron traps belong to the class of slow traps with bikinetic properties. These traps feature normal kinetic properties in the state with a single trapped charge carrier and feature anomalous kinetic properties in the state with two charge carriers. Multiple-parameter models allowing for a relation of traps in *p*-ZnTe and *n*-ZnS to the vacancy–impurity pairs distributed according to their interatomic distances and localized in the region of microinhomogeneities with collective electric fields that repel the majority charge carriers are suggested. The main special features of behavior of electron and hole traps are explained consistently using the above models. © 2004 MAIK "Nauka/Interperiodica".

1. INTRODUCTION

Methods of thermally stimulated currents (TSCs) and induced extrinsic photoconductivity (IEP) were used to study two-hole and two-electron traps with closely coinciding photoelectric parameters in *p*-ZnTe and *n*-ZnS. The thermodynamic properties of intrinsic defects in II–VI compounds suggest that these traps can be formed [1]. The main properties of electron and hole traps are explained assuming that these traps are related to vacancy–impurity pairs, which incorporate the cationic (V_C) and anionic (V_A) vacancies for the electron and hole traps, respectively. The suggested model concepts of hole and electron traps, when taken as a whole, also include the idea that microinhomogeneities of point defects and macroinhomogeneities in *p*-ZnTe and *p*-ZnS crystals affect the characteristic parameters of the traps. It is shown that both the electron and hole centers belong to the class of slow traps. In the state with a single charge carrier, the traps under consideration exhibit normal kinetic properties, whereas these properties are anomalous if two charge carriers reside in the trap.

2. THERMALLY STIMULATED CURRENTS

2.1. Estimation and Control of Characteristic Parameters of the Traps Using Thermally Stimulated Currents

The value of TSC caused by thermal ionization of a slow trap (the ratio between the rate of capture of a majority charge carrier by a trap and the recombination rate $R \ll 1$) is given by [2]

$$I(T) = I_0 \exp\left(-\frac{E_t}{kT}\right)$$
$$\times \exp\left[-\frac{\vartheta N_{\text{eff}} S_t}{\beta}\left(\frac{kT^2}{E_t}\right)\exp\left(-\frac{E_t}{kT}\right)\left(1 + \frac{4kT}{E_t}\right)\right], \quad (1)$$

where

$$I_0 = \gamma \vartheta N_{\text{eff}} S_t n_{t0}; \quad (2)$$

E_t is the ionization energy for the trap; S_t is the capture cross section for a majority charge carrier; n_{t0} is the initial number of charge carriers in the trap; ϑ is the thermal velocity of charge carriers; N_{eff} is the effective density of states in the band of majority charge carriers; β is the rate of heating the sample when the TSC spectrum is recorded; and γ is a factor that depends on the geometric parameters of the sample, the external electric field, and on the charge, lifetime, and mobility of majority charge carriers.

In the initial stage of thermal ionization of the trap, the contribution of the second exponential function in expression (1) to the dependence $I(T)$ is small. The increase in TSC is exponential at this stage. This result was used to introduce into practice the methods for determining the energy E_t from the slope of the straight line [3, 4],

$$\log I(T) = \log I_0 - \frac{E_t}{kT}, \quad (3)$$

and the cross section from the formula [5, 6]

$$S_t = \frac{\beta I_{ext}}{\vartheta N_{eff} \Delta T}.\qquad(4)$$

Formula (4) follows from expressions (2) and (3) when the quantity I is replaced by its extrapolated value I_{ext} at the point of intersection of straight line (3) with the vertical axis $T^{-1} = 0$, the concentration n_{t0} is replaced by the ratio $\theta/\gamma\beta$, and the area θ under a specific TSC band is replaced by the band half-width ΔT. The equality $\theta = \Delta T$ is valid for a model (pure triangular) TSC band with the amplitude $I_{max} = 1$ (in arbitrary units) and the pedestal width $\Delta T_0 = 2\Delta T$. Replacement of the area θ by ΔT when estimating S_t from formula (4) introduces an error no larger than 10%; this error only affects the factor multiplying the quantity that defines the order of magnitude of the cross section S_t. In the case of complex TSC spectra, the half-width ΔT can be estimated as double the width of the low-temperature portion of an elementary band separated using the "thermal decontamination" method [7].

Direct estimation of I_{ext} includes procedures for normalizing the TSC spectrum and extrapolating the straight line $\log I = f(T^{-1})$ to the vertical axis $T^{-1} = 0$. A simple expression for the estimate of I_{ext} follows from the shape of the right-angled triangle (Fig. 1, inset) in the coordinate system [$\log I$, $10^3/T$]. The base of the triangle lies in the horizontal axis $\log I = 0$ and passes through the peak of the TSC band. The length of this base is $10^3/T_0$ and equals the abscissa of the point of intersection of the horizontal axis with the straight line defined by expression (3); the extrapolated portion of this straight line forms the hypotenuse of the triangle. The length of the vertical cathetus is equal to $\log I_{ext} = 10^3/T_0 \tan\alpha$ (Fig. 1, inset). The tangent of the angle of inclination of straight line (3) to the horizontal axis defines E_t. Another result following from the expression for $\log I_{ext}$ is of practical importance (and was hitherto unknown): $\tan\alpha$ (via the quantity $I_{ext} = 10^{\frac{10^3}{T_0}\tan\alpha}$) makes it possible to determine the cross section S_t of capture of charge carriers by slow traps [see formula (4)].

Transition from the TSC spectrum given by (1) to the point of its maximum, where $T = T_m$ and $dI/dT = 0$, yields the approximate equality [8]

$$\log\frac{S_t}{S_0} \cong \frac{E_t}{kT_m}\log e.\qquad(5)$$

In dimensionless coordinates $\left[\log\dfrac{S_t}{S_0}, \dfrac{E_t}{kT_m}\right]$, this equality represents a universal diagram for characteristic parameters of both slow traps (E_t, S_t) and corresponding
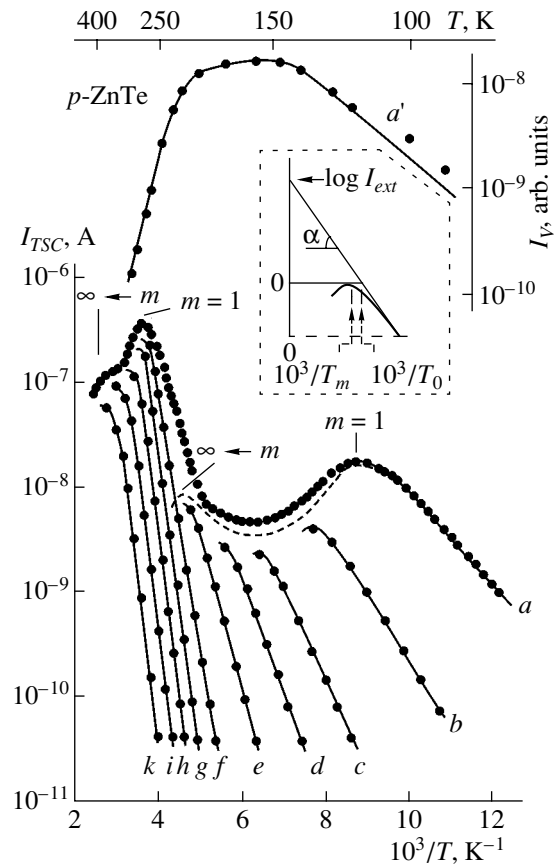

Fig. 1. Curve a corresponds to an integrated TSC spectrum for a p-ZnTe crystal; in spectra b–k, solid lines represent low-temperature portions of theoretical TSC bands according to (1), and filled circles represent experimental values of TSC obtained using "thermal decontamination." The dashed line is the envelope of elementary bands b–e. The rate of recording the TSC spectra was $\beta = 0.2$ K s^{-1}. Curve a' reproduces the temperature dependence of the IEP-spectrum intensity. The inset shows an arbitrary TSC spectrum in coordinates $\log I$ –$10^3/T$ (the solid thick line); the triangle has corners located at [0, 0], [$\log I_{ext}$, 0], and [0, $10^3/T_0$].

thermally stimulated bands (β, T_m) in semiconductors and insulators. The parameter S_0 is defined as $S_0 = \beta/\vartheta N_{eff} T_m$.

The accuracy of estimates for parameters E_t and S_t can be judged by checking whether these estimates are consistent with diagram (5) and whether the shape of the experimental bands coincides sufficiently with that of the bands given by (1) and calculated using the above parameters.

2.2. TSCs and Characteristic Parameters of the Traps

Integrated TSC spectra in the temperature range 90–300 K both in p-ZnTe (Fig. 1, curve a) and in n-ZnS (Fig. 2, curve a) consist of two broad bands. Resolution of these bands into elementary bands (Fig. 1, curves b–k; Fig. 2, curves b–d) employing the "thermal decontami-
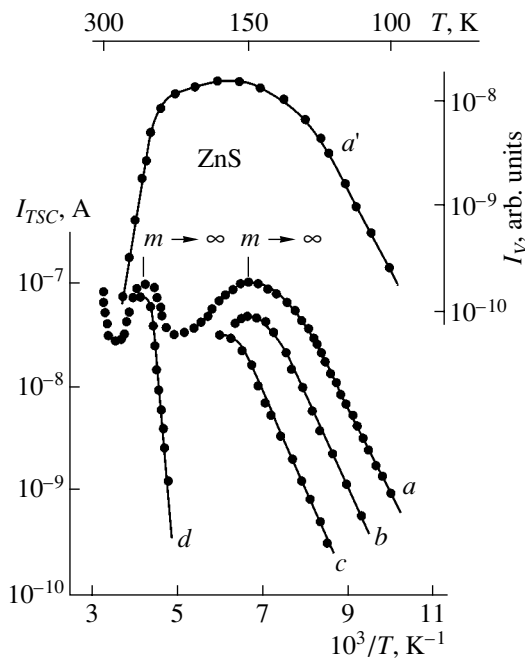
Fig. 2. Curve *a* corresponds to an integrated TSC spectrum of an *n*-ZnS crystal. In spectra *b–d*, solid lines represent low-temperature portions of theoretical TSC bands according to (1), and filled circles represent experimental values of TSC obtained using "thermal decontamination." The rate of recording the TSC spectra was $\beta = 0.2$ K s^{-1}. Curve *a'* shows the temperature dependence of the IEP-spectrum intensity.
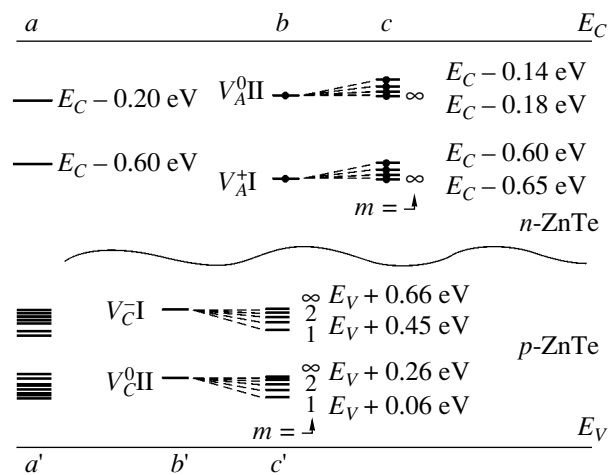

Fig. 3. (*a*) Scheme of electronic levels of vacancy V_A that were predicted theoretically for *n*-ZnS [1]. (*b*, *c*) Schemes of electronic levels of an individual vacancy V_A (*b*) and of a vacancy–impurity pair formed of a vacancy V_A and a shallow ionized acceptor ($r_m \geq 30$ Å) in an *n*-ZnS crystal (experimental results of this study). (*a'*) A scheme of hole-trapping levels in *p*-ZnTe according to published data [9–16]. (*b'*, *c'*) Schemes of hole-trapping levels of an individual vacancy V_C (scheme *b'*) and a vacancy–impurity pair composed of a vacancy V_C and a shallow-level ionized donor located at a cationic site in *p*-ZnTe (experimental results of this study). The numbers $m = 1, 2, \ldots, \infty$ correspond to the numbers of coordination shells within which the components of vacancy–impurity pairs are located.

nation" method [7] and estimation of the energy E_t using formula (3) indicate that energy states grouped quasi-continuously in two zones, which have almost equal widths but are quite far apart, exist in the band gaps of both compounds (Fig. 3, schemes *c*, *c'*). The states $E_V + (0.45–0.66)$ eV (hole levels I) in *p*-ZnTe are responsible for the high-temperature integrated TSC band, whereas the states $E_V + (0.06–0.26)$ eV (hole levels II) are responsible for the low-temperature integrated TSC band (Fig. 1, curve *a*). A similar relation is also observed between integrated TSC bands (Fig. 2, curve *a*) and the states $E_C - (0.6–0.65)$ eV (electron levels I) and $E_C - (0.14–0.18)$ eV (electron levels II) in *n*-ZnS.

The cross sections S_t were calculated using formula (4). These cross sections increase in *p*-ZnTe as energy E_t increases; this behavior of S_t is observed both when we pass from one level to another within each group of levels and when we pass from levels I to levels II (Fig. 4). The width of energy intervals containing levels I and II in *n*-ZnS is very small (Fig. 3). Taking this circumstance into account, we cannot estimate with confidence the type of dependence of S_t on the energy E_t within the systems of levels I and II in *n*-ZnS. In contrast, when we pass from levels II to levels I in *n*-ZnS, a jumplike increase in S_t is observed. The cross sections for the deepest states $E_C - 0.65$ eV and $E_C - 0.18$ eV in systems of electron levels I and II, which, according to

the suggested model (Section 4), are related to individual vacancies V_A^+ and V_A^0, are equal to $S_t \cong 10^{-15}$ cm^2 and $S_t \cong 10^{-22}$ cm^2, respectively.[1]

The parameters E_t and S_t of traps are consistent with universal diagram (5) (Fig. 4, inset). The accuracy of determination of these parameters is also indicated by the agreement between the shapes of experimental bands (the latter are represented by filled circles in Figs. 1 and 2) and the bands calculated using the values of E_t and S_t for bands (1) (for calculated bands, see Fig. 1, the low-temperature portion of curve *a* and curves *b–k*, and Fig. 2, the low-temperature portion of curve *a* and curves *b–d*).

3. THE IEP SPECTRA: SPECTRAL SHIFT OF IEP BANDS

An IEP spectrum for *p*-ZnTe features a peak at $h\nu_{max} \cong 0.84$ eV (Fig. 5, curve *a*); the spectrum was measured at 295 K in conditions of successive excitation with the band-gap and extrinsic-absorption light. A band peaked at $h\nu_{max} = 0.85$ eV is observed in the IEP spectrum as a result of similar measurements for *n*-ZnS (Fig. 5, inset, curve *a'*). In conditions of combined

---

[1] Unless otherwise specified, the states of vacancies V_C and V_A are hereafter denoted taking into account their charge acquired when majority carriers are localized at these vacancies.
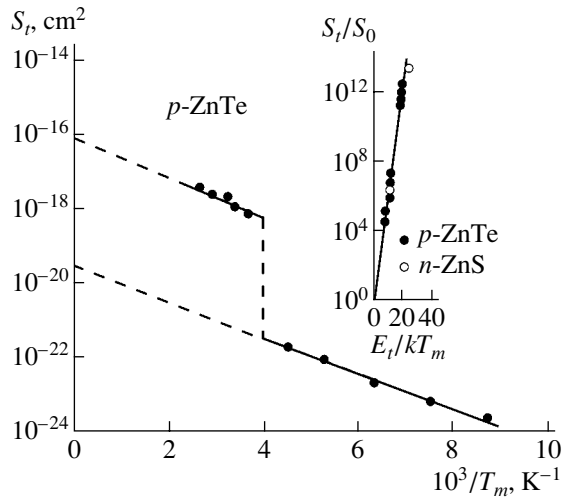
Fig. 4. Dependences of capture cross sections S_t for traps in p-ZnTe on reciprocal temperatures of the peaks for corresponding discrete TSC bands resolved using "thermal decontamination" (Fig. 1). In the inset, the straight line corresponds to the universal diagram $[S_t/S_0, E_t/kT_m]$ for characteristic parameters of traps (E_t and S_t) and of TSC spectra (T_m and β); filled and unfilled circles correspond to experimental parameters of the traps and corresponding TSC bands in p-ZnTe and n-ZnS.
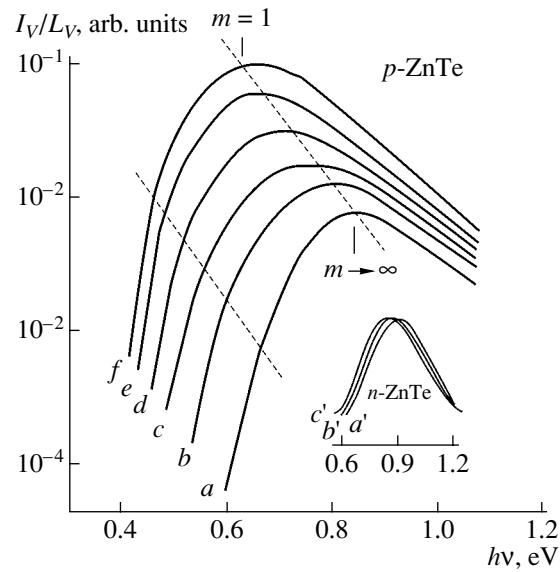

Fig. 5. (a–f) IEP spectra measured in p-ZnTe in relation to the intensity of background excitation with band-gap light. In the inset, curves a'–c' represent IEP spectra in n-ZnS measured using the same method. The increase in the intensity of background excitation corresponds to alphabetical order in the designations of the spectra.

excitation, the IEP bands in both compounds exhibit a spectral j shift to lower energies (Fig. 5, curves a–f; inset, curves a'–c'). The magnitude of the j shift depends on the intensity of background irradiation with band-gap light. The largest magnitude of the effect in each of the compounds is equal to the width of the corresponding system of levels I: $\Delta \cong 0.2$ eV for p-ZnTe and $\Delta \cong 0.05$ eV for n-ZnS (Fig. 3).

Optical-ionization energies for photoelectrically active traps (E_0) are determined from photon energies $h\nu$ that correspond to low-energy points in the IEP band with intensity $I = 0.1I_{max}$ (Fig. 4). The common origin of integrated TSC bands and IEP spectra is indicated by the fact that the values of E_0 are found within the range of thermal-ionization energies E_t of levels I for each of the compounds. The magnitude of the Frank–Condon effect is small for levels I, despite the fact that these levels are fairly deep ($\Delta E = E_0 - E_t \leq 0.03$ eV).

In Section 5, we report data that show that not only the IEP spectra and high-temperature TSC bands but also the entire range of studied nonequilibrium phenomena in each of the compounds have a common origin.

4. THE VACANCY–IMPURITY MODELS OF THE TRAPS

According to previous publications (see, for example, [9–16]), the hole traps in p-ZnTe can be related to cationic vacancies, acceptor impurities of Group I elements, and such like. The number of levels observed so far in each of the publications ranged from one to four. All these levels taken together form a spectrum that is

rich in features; the width of this spectrum and the distribution of hole levels in it correspond to the spectrum ascertained in this study in a specific p-ZnTe crystal (cf. schemes a' and c' in Fig. 3). The high informativeness of the results reported in this paper is the result of using thermal and photoelectric spectroscopic methods simultaneously. It is also important that these methods were implemented in conditions of varying the position of quasi-Fermi levels over a wide energy range.

According to the model we suggest, the hole traps $E_V + (0.45$–$0.66)$ eV and $E_V + (0.06$–$0.26)$ eV in p-ZnTe are related to the vacancy–impurity pairs with various interatomic distances (r_m). These pairs consist of atoms of a shallow-level ionized donor at a cationic lattice site (D_C^+) (for example, the residual Al impurity) and a vacancy V_C. The deepest donor states $E_V + 0.66$ eV and $E_V + 0.26$ eV in the systems of levels I and II are related to individual vacancies V_C^- and V_C^0.

It is assumed that the electron traps in n-ZnS are also related to the vacancy–impurity pairs but, in contrast to these pairs in p-ZnTe, consist of randomly distributed ($r_m \geq 30$ Å) atoms of acceptor A_C^- (atoms of residual impurities of the elements of Groups I and V) and vacancies V_A. Studies of n-ZnS annealed in the Zn melt confirm the view that intrinsic defects are involved in the formation of electron traps (Fig. 6, inset, curve a) in accordance with the suggested model. The energy positions of the deepest states in the system of electron levels I and II, which are attributed to individual V_A^+ and
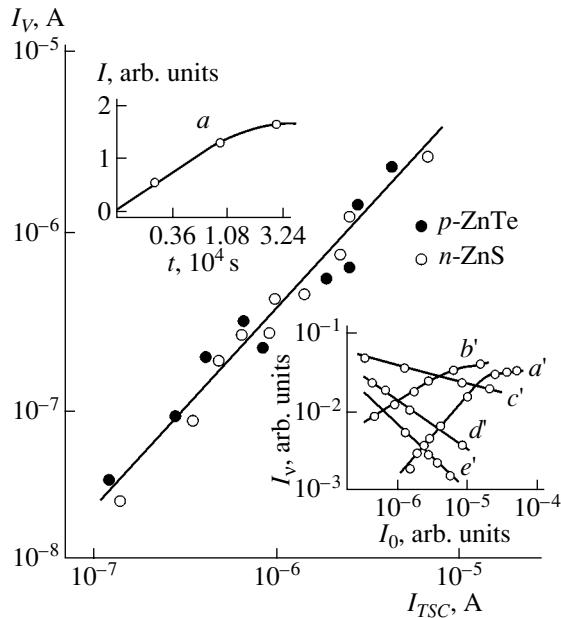
Fig. 6. Intensities of the IEP spectrum and low-temperature TSC band for various *p*-ZnTe and *n*-ZnS samples. In the upper inset, curve *a* represents the dependence of IEP-spectrum intensity in *n*-ZnS on the duration of annealing in the Zn melt at 920 K; the lower inset shows the dependences of the IEP-spectrum intensity in *n*-ZnS on the intensity of background excitation with band-gap light (this intensity was estimated using the value of intrinsic photoconductivity) at temperatures $T = (a')$ 293, (b') 233, (c') 203, (d') 138, and (e') 100 K.

V_A^0 centers, are close to those of theoretically predicted [1] levels of these centers (cf. Fig. 3, schemes *a*, *b*).

The proposed models involve not only concepts concerning the microstructure and physicochemical origin of traps in *p*-ZnTe and *n*-ZnS. It is assumed at the same time that the traps in *p*-ZnTe and *n*-ZnS (as well as those in CdS, CdSe [17], ZnSe [18], and γ-La$_2$S$_3$ [9]) are located in the region of macroscopic inhomogeneities with collective electric fields that repel the majority charge carriers; due to these fields, the cross sections S_t become effective.

5. DISCUSSION

5.1. Photoelectric Properties

Two series of hole traps in each of the studied compounds (Fig. 3) are the result of the two-electron and two-hole nature of vacancies V_C and V_A. The low-temperature TSC bands (Figs. 1, 2, curves *a*) appear as a result of thermal ionization of levels II that are in the $(V_C^0 - D_C^+)^+$ state in *p*-ZnTe and in the $(V_A^0 - A_C^-)^-$ state in *n*-ZnS. After a single ionization, levels I of vacancy–impurity pairs $(V_C^- - D_C^+)^0$ are activated in *p*-ZnTe and those of vacancy–impurity pairs $(V_A^+ - A_C^-)^0$ are acti-

vated in *n*-ZnS. The aforementioned thermal ionization gives rise to high-temperature TSC bands. The TSC spectra are composed of elementary bands, each of which is related to a vacancy–impurity pair with a specific configuration. An analysis performed by the method of thermal decontamination supports the conclusion that the TSC spectra are integrated (Fig. 1, curves *b–k*; Fig. 2, curves *b–d*).

The *j* shift of IEP bands, which is observable as *p*-ZnTe and *n*-ZnS are irradiated with band-gap light, is caused by a gradual increase in the occupation of levels I with majority charge carriers (beginning with the deepest levels).

Levels II in both *p*-ZnTe and *n*-ZnS do not manifest themselves in the measurements of IEP. However, these levels can indirectly affect the photoelectric activity of levels I owing to an important special feature of multicharged centers. Specifically, the capture of a second charge carrier by a vacancy–impurity pair results in a situation where levels I cannot manifest themselves owing to a strong interaction between the two charge carriers and the fact that they are indistinguishable [20].

An increase in the IEP-spectrum intensity (Figs. 1, 2, curves *a'*) with increasing temperature is observed both for *p*-ZnTe and for *n*-ZnS with levels I and II that are occupied at low temperatures in nonequilibrium conditions. This increase has an activation energy equal to the depth of the shallowest level in the system of corresponding states II (Fig. 3). This result is a consequence of an increase in the number of photoactive levels I in the course of gradual thermal ionization of levels II. Levels II are unoccupied, and levels I are filled with majority charge carriers in the temperature range between the peaks of TSC bands. In this state, both compounds exhibit the most pronounced nonequilibrium sensitization. Thermal depopulation of levels I and quenching of IEP occur at high temperatures. The activation energy for the IEP quenching in *p*-ZnTe (*n*-ZnS) is equal to the ionization energy E_t of the level $E_V + 0.66$ eV ($E_C - 0.65$ eV) that is most widely spaced from the valence (conduction) band in the system of levels I.

The IEP-spectrum intensity increases in both compounds in the temperature range that corresponds to an efficient occupation of levels I with increasing intensity of background irradiation with band-gap light; this intensity is determined from the magnitude of intrinsic photocurrent (Fig. 6, inset, curves *a'*, *b'*). In contrast, an inverse dependence of the IEP-spectrum intensity on the intrinsic photocurrent (curves *c'–e'* in the same inset) is observed in the temperature range where the charge carriers are captured by levels II.

In Fig. 6, we show the values of conductivity at the points that correspond to the peaks of IEP bands and low-temperature TSC bands in the 19 *p*-ZnTe and *n*-ZnS samples studied by us. It can be seen that there exists a distinct correlation between the TSC and IEP peak values, which follows directly from the fact that

both phenomena in each of the compounds are related to the same traps.

5.2. Energy Spectrum of Traps

The ionization energy for a hole (electron) trap that interacts with a donor D^+ (acceptor A^-) is given by $E_{tm} = E_{t\infty} - e^2/\varepsilon r_m$ in the first approximation. Here, $E_{t\infty}$ is the depth of the level of an individual hole (electron) trap and $e^2/\varepsilon r_m$ is the shift of this level due to the proximity of the ionized donor (acceptor). In accordance with experimental data, the calculated values of E_{tm} for both p-ZnTe (the relative permittivity $\varepsilon = 11.6$, $r_m = a(m/2)^{1/2}$, and the lattice parameter $a = 6.01$ Å [21]) and for n-ZnS ($\varepsilon = 8.4$ [21] and $r_m \geq 30$ Å) fall within two groups of levels (Fig. 3, schemes c, c'). The values of $E_{t\infty}$ are equated to the ionization energies of individual ($m \longrightarrow \infty$) vacancies V_C^- and V_C^0 in p-ZnTe and V_A^+ and V_A^0 in n-ZnS (Fig. 3). The difference $E_{tm} - E_t$ for each of the levels in p-ZnTe increases as r_m decreases; this difference amounts to about 0.1 eV in a system of levels I and II for shallower hole states ($m = 1$). The difference under consideration is caused by the fact that the deviation of the defect potential from a simple Coulomb potential is disregarded in calculations; the Coulomb potential is important for a vacancy–impurity pair with closely spaced components.

5.3. The Concentration Distribution of Vacancy–Impurity Pairs $\rho(r)$

Two peaks are characteristic of the distribution $\rho(r)$ of donor–acceptor pairs composed of simple atoms [22]. One of these peaks corresponds to compact pairs ($m = 1$), whereas the second peak corresponds to randomly distributed pairs ($m \longrightarrow \infty$). However, in the case of the vacancy–impurity pairs under consideration, which include two-hole (V_C) and two-electron (V_A) centers, a doublet structure for each of the peaks $\rho(r)$ should be expected.

Indeed, all four expected peaks in the TSC spectrum in p-ZnTe with a complete set of vacancy–impurity pairs are observed. These peaks are indicated by arrows at $m = 1$ and $m \longrightarrow \infty$ (Fig. 1, curve a). In contrast to integrated TSC bands attributed to vacancy–impurity pairs formed of closely spaced components ($m = 1$), integrated bands attributed to randomly distributed vacancy–impurity pairs ($m \longrightarrow \infty$) are less pronounced. It is noteworthy that the existence of a single (low-temperature) peak of the two aforementioned peaks can only be judged by the behavior of elementary bands that are resolved using thermal decontamination (Fig. 1, dashed line; this line envelopes the discrete bands b–e).

The vacancy–impurity pairs are photoelectrically active only in the $(V_C^- - D_C^+)^0$ state. Therefore, only two of the four expected peaks of the $\rho(r)$ distribution are observed in the IEP spectra of p-ZnTe (Fig. 5). The IEP and TSC spectra clearly show that the vacancy–impurity pairs are distributed with the predominance of pairs with closely spaced components.

The TSC and IEP spectra in n-ZnS are related to randomly distributed vacancy–impurity pairs that are photoelectrically active only in the $(V_A^+ - A_C^-)^0$ state. Two bands in the integrated TSC spectrum (Fig. 2, curve a) and a single IEP band with characteristic j shift (Fig. 5, inset) correspond to these pairs.

Studies of TSC in a high-temperature region ($T > 300$ K) show that not only the vacancy–impurity pairs but also deeper traps exist in n-ZnS. The concentration of these traps far exceeds that of vacancy–impurity pairs, so that the former ensure the constancy of electron lifetimes and the equality of intensities of integrated TSC bands (Fig. 2, curve a). High-temperature TSCs exceed low-temperature TSCs (despite their common origin) in p-ZnTe where there are no other traps except for those studied (cf. peaks denoted as $m = 1$ in curve a in Fig. 1). This phenomenon may be caused by two factors: (i) the lifetime of holes in the state with simultaneously occupied levels I and II is shorter than that in the state with only levels I filled with holes and (ii) the low-temperature TSC band has a slightly reduced intensity owing to the fact that the temperature of its peak is close to the temperature of preliminary excitation of p-ZnTe.

5.4. Kinetic Properties

We now consider the facts that support the assumption (Section 4) that macrobarriers have an effect on the kinetic parameters of traps in p-ZnTe and n-ZnS.

(i) The dependence $S_t = f(T_m^{-1})$ in p-ZnTe is exponential, i.e., $S_t = S_{t0}\exp(-\varphi/kT_m)$ (Fig. 4). The parameters $\varphi \cong 0.1$ eV, $S_{t0} \cong 10^{-16}$ cm^2, and $S_{t0} \cong 3 \times 10^{-20}$ cm^2 can be interpreted as the height of the recombination barrier and the intrinsic cross sections for levels I and II, respectively.

(ii) The cross section S_t is larger for levels I than for levels II (by four orders of magnitude in p-ZnTe and by almost seven orders of magnitude in n-ZnS). It is difficult to explain this behavior based only on the assumption that there are differences in the charge states or the mechanisms of capture of charge carriers between levels I and II.

(iii) Low-temperature irradiation of p-ZnTe with fairly intense band-gap light results in the reversal of the sign of the photocurrent variation under exposure to IR light. Spectral regions corresponding to the stimulation and quenching of the photocurrent coincide, which undoubtedly indicates that both phenomena are related to the same centers of type I. The defects responsible for the photocurrent quenching are known as the r recombination centers with large cross sections for hole

capture $S_p = 10^{-14}$–10^{-16} cm^2 [23]. The reversal of the sign of variation in the intrinsic photocurrent in *p*-ZnTe is most likely indicative of the increase in the cross section for centers of type I to the value characteristic of the intrinsic cross section $S_{t0} \cong 10^{-16}$ cm^2 (see above). The cause of this behavior is the considerable decrease in the height of macrobarriers as the quasi-Fermi levels shift to the edges of the allowed bands and the resulting transformation of centers of type I into *r* centers.

Expressions (1) and (5) are derived assuming that the capture factor $R = 0$. The agreement between theoretical and experimental results of studying TSCs (Figs. 1, 2; Fig. 4, inset) is important evidence that the traps in *p*-ZnTe and *n*-ZnS belong to the class of slow traps. The same conclusion can be drawn on the basis of direct estimations of the factor *R*. For example, the cross sections S_t for levels II are smaller (Subsection 2.2.) than those for recombination centers $S_r \geq 10^{-20}$ cm^2 [23]. Taking into account also that thermal depopulation of levels II occurs in a situation where at least levels I are occupied (the concentration of active recombination centers is high), we realize that the condition $R \ll 1$ is satisfied with a large margin for these levels.

Systematization of single-electron traps according to their kinetic properties allowed us to conclude that slow traps with both normal kinetic properties and anomalous kinetic properties exist in semiconductors [17–19]. Two-hole traps in *p*-ZnTe and two-electron traps in *n*-ZnS exhibit bikinetic properties.

According to the suggested model, the capture of majority charge carriers by levels I in *p*-ZnTe and *n*-ZnS occurs in an attraction field of charges V_C^{2-}, V_A^{2+}, $(V_C^{2-}-D_C^+)^-$, and $(V_A^{2+}-A^-)^+$. This circumstance makes it possible to explain the fairly large extrinsic cross sections of the centers under consideration, $S_{t0} \cong 10^{-16}$ cm^2 (in *p*-ZnTe) and $S_{t0} > 10^{-15}$ (in *n*-ZnS) (see above), despite the larger depth of these levels and the higher temperature of measurements. If we also take into account that the traps in *p*-ZnTe and *n*-ZnS are photoelectrically active in the state with a single captured charge carrier, we may state that the traps in this state exhibit normal kinetic properties.

In contrast, the capture of majority charge carriers by levels II occurs either in an attraction field of V_C^- and V_A^+ centers or in the zero field of neutral $(V_C^--D_C^+)^0$ and $(V_A^+-A_C^-)^0$ centers. Nevertheless, the measured values of cross sections for levels II $S_t = 10^{-22}$–10^{-24} cm^2 are much smaller than theoretically predicted cross sections $S_t \approx 10^{-16}$–10^{-13} cm^2 for the centers with the aforementioned charge states. It is also difficult to explain the values of S_t taking into account the dynamic aspect of the mechanism of the charge-carrier capture by the centers under consideration. For example, the event of localization of holes at the shallowest level $E_V + 0.06$ eV

in a system of states II in *p*-ZnTe (Fig. 3) can be assigned to a single-phonon process with a large degree of confidence. However, the measured value of cross section for this level is extremely small ($S_t \cong 10^{-24}$ cm^2, see Fig. 4). The fact that the traps in the state with two charge carriers in *p*-ZnTe and *n*-ZnS do not exhibit photoelectric activity is also indicative of the anomalous kinetic properties of these traps.

When evaluating the kinetic properties of states II in *p*-ZnTe and *n*-ZnS, we should also take into account that not only the directly measured but also the extrapolated (intrinsic) cross sections for these states are extremely small: $S_t < 10^{-19}$ cm^2 (Fig. 4). This fact suggests that the observed anomalous kinetic properties of traps in the state with two charge carriers may be a result of not only the effect of macrobarriers. It is not inconceivable that the two-hole and two-electron centers under study exhibit specific quantum-mechanical special features; as a result, the elementary processes of capture of majority charge carriers and photons at levels II of these centers are hampered.

6. HYPOTHESIS ON THE TYPE OF SPATIAL DISTRIBUTION OF COMPONENTS OF VACANCY–IMPURITY PAIRS IN A MACROINHOMOGENEITY STRUCTURE

If the cross section S_t of a trap interacting with a large-scale inhomogeneity in a crystal (dislocation, intercrystal boundary, and so on) with a collective electric field that repels the majority charge carriers expands into a range of values with the energy E_t remaining unchanged, then this circumstance is important evidence that the traps are distributed throughout the entire volume of this macroinhomogeneity [18, 19]. The hole and electron states in *p*-ZnTe and *n*-ZnS are specific in that each of these states has a discrete cross section S_t. Therefore, it is not excluded that the components of vacancy–impurity pairs, which act as traps (V_C and V_A) in the above compounds, occupy quasi-equipotential sites in the structure of macroinhomogeneity, whereas the other components (which are not traps) are distributed randomly in this structure. A model that is close in essence to the above model and allows for the existence of ordering in the distribution of point defects in a structure of large-order disorder (dislocation) was also suggested by us for the electron trap $E_C - 0.2$ eV, which was also related to the donor–acceptor pairs but in a γ-La$_2$S$_3$ crystal [19]. Only the distribution of atoms of nontrapping (acceptor) type is ordered in γ-La$_2$S$_3$. In contrast, the atoms of the trapping (donor) component occupy sites that are located at different distances from the dislocation core; as a result, the cross section expands into a range of values.

REFERENCES

1. F. A. Kröger, *The Chemistry of Imperfect Crystals* (North-Holland, Amsterdam, 1964; Mir, Moscow, 1969).

2. Ch. B. Lushchik, *Investigation of Capture Centers in Alkali–Halogen Crystallophosphors* (Tartu, 1955).

3. V. V. Antonov-Romanovskiĭ, Izv. Akad. Nauk SSSR, Ser. Fiz. **10**, 477 (1946).

4. G. F. T. Garlic and A. F. Gibson, Proc. Phys. Soc. **60**, 574 (1948).

5. M. A. Rizakhanov, Izv. Vyssh. Uchebn. Zaved., Fiz., No. 1, 153 (1971).

6. M. A. Rizakhanov, *Electron–Oxygen Quasi-Particles in Proteins. Electron–Atomic Theories of Primary Photobiological Effects* (Bari, Makhachkala, 1998).

7. W. Hoogenstraaten, Philips Res. Rep. **13**, 515 (1958).

8. M. A. Rizakhanov, Fiz. Tverd. Tela (Leningrad) **31**, 193 (1989) [Sov. Phys. Solid State **31**, 1946 (1989)].

9. A. E. Tsurkman and V. I. Berlan, in *New Semiconductor Compounds and Their Properties* (Shtiintsa, Kishinev, 1975), p. 83.

10. T. L. Larsen, C. F. Varotto, and D. A. Stevenson, J. Appl. Phys. **43**, 172 (1972).

11. M. Aven and B. Segall, Phys. Rev. **130**, 81 (1963).

12. I. K. Andronik, A. V. Bochkarev, P. G. Mikhalash, *et al.*, in *Electroluminescence of Solids and Its Application* (Naukova Dumka, Kiev, 1972), p. 33.

13. D. I. Kennedy and M. J. Russ, J. Appl. Phys. **38**, 4387 (1967).

14. D. L. Losee, Appl. Phys. Lett. **21**, 54 (1972).

15. J. B. Webb and D. E. Brodie, Can. J. Phys. **53**, 1415 (1975).

16. P. N. Koval'skiĭ, M. K. Sheĭnkman, and A. D. Shneĭder, Fiz. Tekh. Poluprovodn. (Leningrad) **5**, 1653 (1971) [Sov. Phys. Semicond. **5**, 1449 (1971)].

17. M. A. Rizakhanov, F. S. Gabibov, G. M. Gasanbekov, *et al.*, Available from VINITI No. 7781-84 (1984).

18. M. A. Rizakhanov and M. M. Khamidov, Fiz. Tekh. Poluprovodn. (St. Petersburg) **27**, 725 (1993) [Semiconductors **27**, 397 (1993)].

19. E. M. Zobov and M. A. Rizakhanov, Fiz. Tekh. Poluprovodn. (St. Petersburg) **35**, 171 (2001) [Semiconductors **35**, 164 (2001)].

20. S. M. Ryvkin, *Photoelectric Effects in Semiconductors* (Fizmatgiz, Leningrad, 1962; Consultants Bureau, New York, 1964).

21. *Physics and Chemistry of II–VI Compounds*, Ed. by M. Aven and J. S. Prener (North-Holland, Amsterdam, 1967; Mir, Moscow, 1970).

22. H. Reiss, C. S. Fuller, and F. J. Morin, Bell Syst. Tech. J. **35**, 535 (1956).

23. V. E. Lashkarev, A. V. Lyubchenko, and M. K. Sheĭnkman, *Nonequilibrium Processes in Photosemiconductors* (Naukova Dumka, Kiev, 1981).

Translated by A. Spitsyn

Universal Analytical Approximation of the Carrier Mobility in Semiconductors for a Wide Range of Temperatures and Doping Densities

T. T. Mnatsakanov*, M. E. Levinshtein**, L. I. Pomortseva*, and S. N. Yurkov*

*All-Russia Electrotechnical Institute, Moscow, 111250 Russia
**Ioffe Physicotechnical Institute, Russian Academy of Sciences, St. Petersburg, 194021 Russia
e-mail: melev@nimis.ioffe.ru
Submitted June 2, 2003; accepted for publication June 4, 2003

Abstract—A simple analytical method is suggested to calculate the mobility of majority carriers in semiconductors. The method allows one to adequately describe experimental data in a wide range of temperatures and doping levels in various kinds of semiconductors: elementary (Si), III–V (GaAs), IV–IV (various SiC polytypes), and III–N (GaN). The high accuracy of the results of the calculation suggests that the method is universal, and it may be used to calculate the mobility of majority carriers in other semiconductor materials. The simplicity and accuracy of the technique make it promising for computer simulations of multilayer semiconductor structures. © 2004 MAIK "Nauka/Interperiodica".

1. INTRODUCTION

Nowadays, there is no need to convince anyone of the efficiency and utility of numeric simulation of characteristics of semiconductor structures. On the contrary, trust in the results of computer simulation is often so high that it becomes necessary to remind oneself that computer simulation describes the processes inside semiconductor structures correctly only when the model equations, the boundary and initial conditions, and the relations approximating the dependence of the electrical parameters of a material on external factors are adequate for the problem under study.

Meanwhile, the description of such important characteristics as electron and hole mobilities, μ_n and μ_p, in a wide temperature range encounters certain difficulties that make it impossible to adequately describe these parameters. It is noteworthy that detailed studies of various mechanisms of charge scattering in semiconductors have been performed (scattering by ionized and neutral impurities; by acoustic phonons, including intravalley and intervalley processes; by polar and nonpolar optical phonons; piezoelectric scattering on acoustic phonons; carrier–carrier scattering) [1–5], which allow one to determine with sufficient accuracy the temperature dependence of μ_n and μ_p. However, this calculation of mobility requires precise values of a set of physical constants of a material, which are known with satisfactory precision only for silicon. For other materials, including such promising materials as SiC and GaN, the unknown values of physical constants turn into fitting parameters [5]. Furthermore, the mathematical complexity of the relations used in these calculations makes them almost impossible to apply in

developing numerical models of the characteristics of semiconductor devices. This is the reason why the majority of known software packages, such as DESSIS [6], ATLAS [7], and MEDICI [8], use models of the well-known Caughey–Thomas [9] type to describe carrier transport.

One should note that the Caughey–Thomas model was initially suggested and applied to describe the dependence of mobility on the doping level in Si [9, 10]. However, later it was used to describe mobility in GaAs [11] and various polytypes of SiC [12, 13]. The Caughey–Thomas model is simple, and it describes well the dependence of mobility on the doping level at room temperature. Nevertheless, formal attempts to take into account the temperature dependence of mobility in terms of this model [10–13] result in considerable errors in the model's predictions at low temperatures and heavy doping.

In fact, the method of introducing the temperature dependence of mobility, suggested in [10–13], allows one to describe only the portion of the dependence where mobility decreases with increasing temperature in the high-temperature range. This circumstance may be regarded as the most serious disadvantage of the approach used in [10–13], especially given the rising interest in cryogenic applications of semiconductor devices and devices based on structures made of a semiconductor and a high-temperature superconductor [14].

Recently, a new approach to the calculation of the temperature dependence of mobility was suggested in [15]. It was successfully used to describe the mobility of majority carriers in SiC [16] and GaN [17]. Virtually all the available experimental data on carrier mobility

Table

Semiconductor material	Carrier type	μ_{max}, cm^2 V^{-1} s^{-1}	μ_{min}, cm^2 V^{-1} s^{-1}	N_g, cm^{-3}	γ	α	β
Si	Electrons	1414.0	68.5	9.2×10^{16}	0.71	2.42	0.26
	Holes	470.5	44.9	2.2×10^{17}	0.72	2.20	0.36
GaAs	Electrons	9400.0	750.0	7×10^{16}	0.50	2.30	0.50
	Holes	450.0	30.0	5×10^{17}	0.50	2.30	0.45
4H-SiC	Electrons	880.0	30.0	2×10^{17}	0.67	2.60	0.50
	Holes	117.0	33.0	1×10^{19}	0.50	–	–
6H-SiC	Electrons	400.0	25.0	1×10^{18}	0.80	2.10	0.70
	Holes	95.0	25.0	5×10^{18}	0.40	2.00	–
3C-SiC	Electrons	750.0	50.0	2×10^{17}	0.80	2.50	0.30
	Holes	–	–	–	–	–	–
GaN	Electrons	1000.0	55.0	2×10^{17}	1.00	2.00	0.70
	Holes	170.0	3.0	3×10^{17}	2.00	5.00	–

in these materials were adequately described in a wide range of temperatures (50 K $\leq T \leq$ 1000 K) and doping levels (10^{13} cm$^{-3} \leq N \leq 10^{20}$ cm^{-3}).

In this study, the approach suggested in [15] is extended to silicon and GaAs. The calculated results are compared with the experimental data.

2. KEY EQUATIONS OF THE MODEL

The starting relation describing the dependence of mobility on the doping level at room temperature ($T = 300$ K) has the form

$$\mu_i(N) = \mu_{min,\,i} + \frac{\mu_{max,\,i} - \mu_{min,\,i}}{1 + (N/N_{g,\,i})\gamma_i}, \qquad (1)$$

where $i = n, p$ for electrons and holes, respectively; the parameters $\mu_{max,\,i}$, $\mu_{min,\,i}$, $N_{g,\,i}$, and γ_i depend on the semiconductor material; and N is the dopant concentration.

The parameter $\mu_{max,\,i}$ in Eq. (1) characterizes mobility in lightly doped samples, where the principal scattering mechanism is scattering on lattice vibrations, whereas $\mu_{min,\,i}$ characterizes mobility under heavy doping conditions, when impurity scattering dominates. Taking into account these factors and the difference between the temperature dependences of mobility associated with lattice $\mu_L(T) = \mu_L(T_0)(T/T_0)^{-\alpha}$ and impurity $\mu_I(T) = \mu_I(T_0)(T/T_0)^{\beta}$ scattering, a relation that simultaneously describes the mobility dependence on N and T was obtained in [15] based on Eq. (1):

$$\mu_i(N, T) = \mu_{max,\,i}(T_0)\frac{B_i(N)\left(\dfrac{T}{T_0}\right)^{\beta_i}}{1 + B_i(N)\left(\dfrac{T}{T_0}\right)^{\alpha_i + \beta_i}}, \qquad (2)$$

where

$$B_i(N) = \left[\frac{\mu_{min,\,i} + \mu_{max,\,i}\left(\dfrac{N_{g,\,i}}{N}\right)^{\gamma_i}}{\mu_{max,\,i} - \mu_{min,\,i}}\right]_{T = T_0}, \qquad (3)$$

$T_0 = 300$ K.

It is easily seen that relations (2) and (3) give a correct qualitative description of the temperature dependence of mobility within light and heavy doping limits. At a fixed doping level, relation (2) describes the experimentally observed nonmonotonic temperature dependence of mobility. The dependence of the extremum point $T = T_{mi}$, where $\dfrac{d\mu_i}{dT} = 0$, on the doping level and other parameters can be represented as

$$T_{im} = T_0\left[\frac{\beta_i}{\alpha_i}\frac{1}{B_i(N)}\right]^{\frac{1}{\alpha_i + \beta_i}}. \qquad (4)$$

One should note that Eq. (2) becomes directly Eq. (1) at $T = T_0$.

Below, we will compare the results calculated from Eqs. (2) and (3) with the available experimental data for each particular material.

3. CALCULATED RESULTS AND DISCUSSION

The relations presented in the preceding section were used to calculate hole and electron mobility in four semiconductor materials: elementary Si and compounds, GaAs (III–V), SiC (IV-IV), and GaN (III–N). All the parameters necessary to describe the mobility of the majority holes or electrons in these materials are listed in the table. Figures 1–5 show the mobility of the
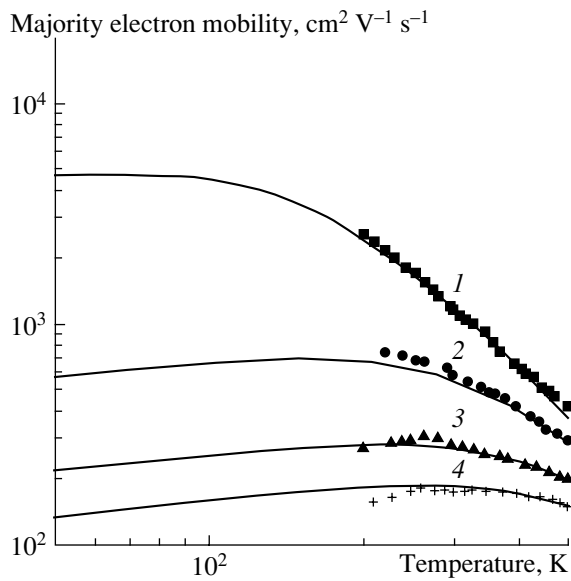
Majority electron mobility, cm^2 V^{-1} s^{-1}

Fig. 1. Temperature dependences of electron mobility in *n*-Si at different donor concentrations: $N = (1)$ 9×10^{15}, (2) 2×10^{17}, (3) 1×10^{18}, and (4) 2.5×10^{18} cm^{-3}. Solid lines: calculated from (2), (3) and the data from the table; the same in Figs. 2–5. Points: experimental data from [18, 19].

majority carriers in different materials. Solid lines show the results calculated using Eqs. (2) and (3) and the data listed in the table. The points are the experimental data [18–20]. As can be seen in the figures, Eqs. (2) and (3) describe adequately the mobility of majority carriers in Si, GaAs, SiC, and GaN over a wide range of temperatures (50 K ≤ *T* ≤ 1000 K).

One should note that the application of Eqs. (2) and (3) suggests a one-to-one correspondence between the mobility at *T* = 300 K and the doping level. Meanwhile, a considerable scatter in the experimental doping levels *N* corresponding to a given mobility μ is obtained in nearly all new semiconductor materials, which is mainly caused by the lack of control over the level of compensation in the samples under study. This circumstance may present difficulties in the use of Eqs. (2) and (3). In this study, this problem was solved as follows.

The doping level N_0 was determined for a chosen experimental value of μ at *T* = 300 K using Eq. (1). Then the dependence μ(N_0, *T*) was calculated from (2), (3) for the chosen N_0.

It is interesting that in the case of Si, where the compensation level is usually well controlled, the inaccuracy in the mobility description in a wide temperature range does not exceed 7%.

4. CONCLUSION

A simple analytical method is suggested to calculate the mobility of majority carriers in semiconductors. The method allows one to adequately describe experimental data in a wide range of temperatures and doping
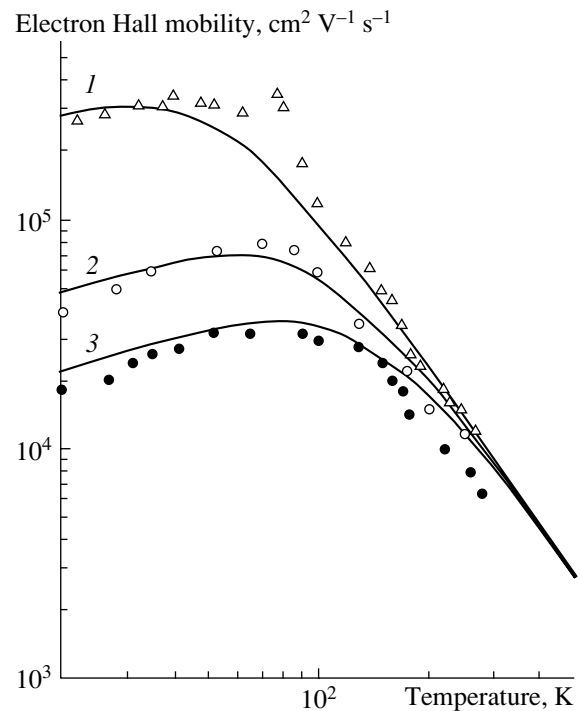
Electron Hall mobility, cm^2 V^{-1} s^{-1}

Fig. 2. Temperature dependences of electron mobility in *n*-GaAs at different donor concentrations: $N = (1)$ 5×10^{13}, (2) 1×10^{15}, and (3) 5×10^{15} cm^{-3}. Points: experimental data from [19].
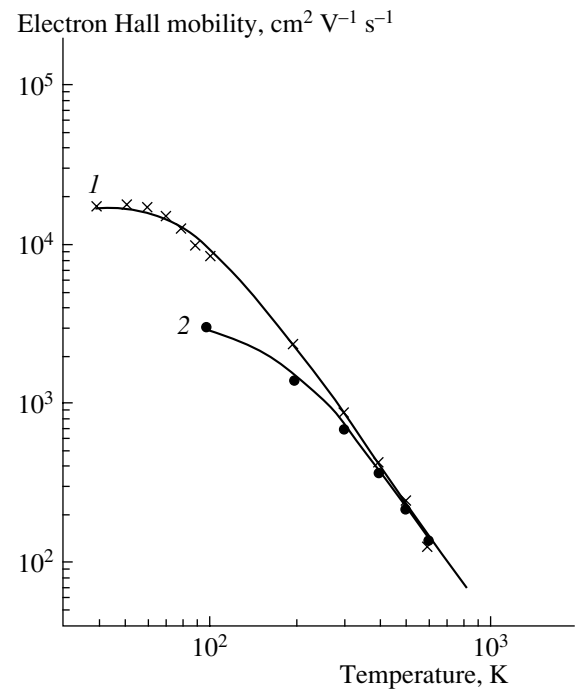
Electron Hall mobility, cm^2 V^{-1} s^{-1}

Fig. 3. Temperature dependences of electron mobility in *n*-4*H*-SiC (axis **C** ⊥ **E**) at donor concentrations (1) 5×10^{14} and (2) 4×10^{16} cm^{-3}. Points: experimental data from [20]; the same in Figs. 4 and 5.
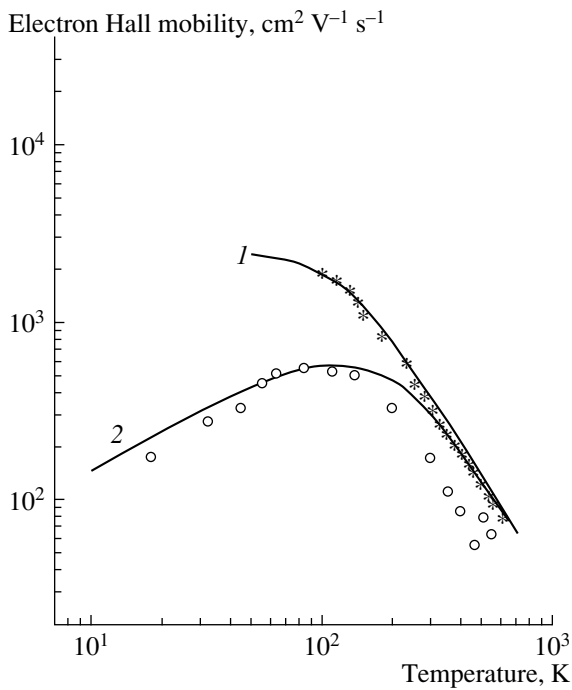
Electron Hall mobility, cm^2 V^{-1} s^{-1}

Fig. 4. Temperature dependences of electron mobility in *n*-6*H*-SiC (axis **C** $\perp$ **E**) at donor concentrations (*1*) 2×10^{16} and (*2*) 2×10^{17} cm^{-3}. Experimental points were taken from [20].
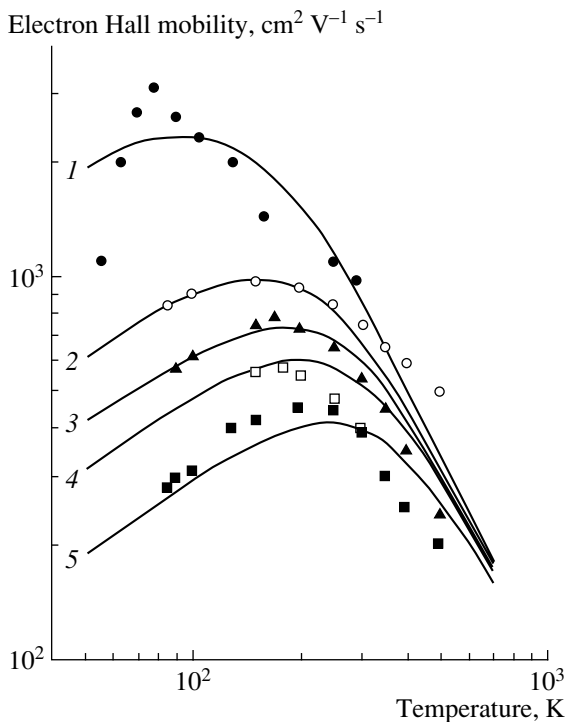
Electron Hall mobility, cm^2 V^{-1} s^{-1}

Fig. 5. Temperature dependences of electron mobility in *n*-GaN (wurtzite) at different donor concentrations: $N = $ (*1*) 3×10^{16}, (*2*) 1×10^{17}, (*3*) 1.5×10^{17}, (*4*) 2.0×10^{17}, and (*5*) 3.5×10^{17} cm^{-3}. Experimental points were taken from [20].

levels in various semiconductors, including an elementary semiconductor (Si) and semiconductors of the III–V (GaAs), IV–IV (various polytypes of SiC), and III–N (GaN) types. The high accuracy of calculation suggests that the method is universal and can be used to calculate the mobility of majority carriers in other semiconductor materials.

One should note that the simplicity and accuracy of the method suggested make it a promising instrument for computer simulation of multilayer semiconductor structures. This method is already being used to analyze static and dynamic characteristics of structures based on silicon carbide [21–25].

REFERENCES

1. V. L. Bonch-Bruevich and S. G. Kalashnikov, *Physics of Semiconductors* (Nauka, Moscow, 1977).
2. R. A. Smith, *Semiconductors*, 2nd ed. (Cambridge Univ. Press, Cambridge, 1978; Mir, Moscow, 1982).
3. B. K. Ridley, *Quantum Processes in Semiconductors* (Clarendon Press, Oxford, 1982; Mir, Moscow, 1986).
4. M. S. Shur, *Devices and Circuits* (Plenum, New York, 1987; Mir, Moscow, 1991).
5. J. Pernot, W. Zawadski, S. Contreras, *et al.*, J. Appl. Phys. **90**, 1869 (2001).
6. *ISE Integrated Systems Engineering AG. DESSIS Ref. Manual* (1988), Available: http://www.ise/ch/products/dessis.
7. *Silvaco International. ATLAS User's Manual* (Santa Clara, CA, 1997), Available: http://www.silvaco.com/.
8. *MEDICI User's Manual* (Technology Modeling Associates, 1999), Available: http://www.avanticorp.com/product.
9. D. M. Caughey and R. E. Thomas, Proc. IEEE **55**, 2192 (1967).
10. N. D. Arora, J. R. Hauser, and D. J. Roulston, IEEE Trans. Electron Devices **29**, 292 (1982).
11. M. Sotoodeh, A. H. Khalid, and A. A. Rezazadeh, J. Appl. Phys. **87**, 2890 (2000).
12. M. Roschke and F. Schwierz, IEEE Trans. Electron Devices **48**, 1442 (2001).
13. M. Ruff, H. Milehner, and R. Helbig, IEEE Trans. Electron Devices **41**, 1040 (1994).
14. E. A. Guttierrez-D, C. Claeys, E. Simoen, and S. V. Koshevaya, in *Workshop on Low Temperature Electronics (WOLTE 3), San Miniato, Tuscany, Italy* (1998); J. Phys. IV **8**, 315 (1998).
15. T. T. Mnatsakanov, L. I. Pomortseva, and S. N. Yurkov, Fiz. Tekh. Poluprovodn. (St. Petersburg) **35**, 406 (2001) [Semiconductors **35**, 394 (2001)].
16. T. T. Mnatsakanov, M. E. Levinshtein, L. I. Pomortseva, and S. N. Yurkov, Semicond. Sci. Technol. **17**, 974 (2002).

17. T. T. Mnatsakanov, M. E. Levinshtein, L. I. Pomortseva, *et al.*, Solid-State Electron. **47**, 111 (2003).

18. S. S. Li and W. R. Thurber, Solid-State Electron. **20**, 609 (1997).

19. M. E. Levinshtein, S. L. Rumyantsev, and M. S. Shur, in *Handbook Series on Semiconductor Parameters* (World Sci., Singapore, 1996), Vol. 1.

20. M. E. Levinshtein, S. L. Rumyantsev, and M. S. Shur, in *Properties of Advanced Semiconductor Materials GaN, AlN, InN, SiC, SiGe* (Wiley, New York, 2001).

21. M. E. Levinshtein, T. T. Mnatsakanov, P. A. Ivanov, *et al.*, IEEE Trans. Electron Devices **48**, 1703 (2001).

22. T. T. Mnatsakanov, M. E. Levinshtein, S. N. Yurkov, *et al.*, Solid-State Electron. **46**, 525 (2002).

23. M. E. Levinshtein, T. T. Mnatsakanov, S. N. Yurkov, *et al.*, Solid-State Electron. **46**, 1953 (2002).

24. T. T. Mnatsakanov, M. E. Levinshtein, P. A. Ivanov, *et al.*, J. Appl. Phys. **93**, 1095 (2003).

25. M. E. Levinshtein, P. A. Ivanov, T. T. Mnatsakanov, *et al.*, Solid-State Electron. **47**, 699 (2003).

Translated by D. Mashovets

Effect of Hydrogen on the Electronic Structure and Properties of Boron Nitrides

S. E. Kul'kova[1, 2], D. V. Chudinov[2], and D. V. Khanin[1, 2]

[1]*Institute of Strength Physics and Materials Science, Siberian Division, Russian Academy of Sciences,*
Akademicheskii pr. 2/1, Tomsk, 634021 Russia
[2]*Tomsk State University, Tomsk, 634050 Russia*
e-mail: kulkova ms.tsc.ru
Submitted April 10, 2003; accepted for publication April 29, 2003

Abstract—The electronic structure of three polymorphic modifications of boron nitride is calculated using the full-potential linear augmented plane wave method with exchange-correlation potential within the framework of the local density and generalized gradient approximation. The calculated values of the bulk modulus obtained from the three equations of state are in reasonable agreement with experimental data. The effect of hydrogen on the electronic structure and physicochemical properties of hexagonal and cubic boron nitride is studied. © *2004 MAIK "Nauka/Interperiodica".*

1. INTRODUCTION

The problem of the formation of wear-resistant surfaces of superhard materials is now attracting great attention. Among these materials, one should especially distinguish diamond, which has the highest hardness and strength, as well as an extremely high elastic modulus value [1, 2]. The unique physical properties and high thermal conductivity of diamond and diamond-like materials are widely used in microelectronics [3]. Accordingly, the interest in the study of materials based on dense modifications of boron nitride BN has considerably increased [1–4]. At the same time, hexagonal or graphite-like boron nitride (BN-*h*) (which is a stable modification of BN under normal conditions) is also of great interest, since it is an analogue of graphite and has similar mechanical characteristics; for this reason BN-*h* is often called "white graphite." Such materials have strong bonding inside the layers and weaker bonding between the layers (Fig. 1). For elevated pressures and temperatures, there are diamond-like modifications of boron nitride, namely, wurtzite (BN-*w*) and zincblende (BN-*z*) [4–9]. The formation of the hexagonal tetrahedral phase (BN-*w*) requires lower energy and is considered to be a high-pressure martensite phase [8, 9]. The mechanism of the direct phase transition determines not only the structure of the new phase but also the degree of its crystalline perfection, which varies widely, depending on the conditions of synthesis [1, 2, 4, 9]. It is known that the synthesis of diamond-like boron nitride in the presence of alkali and alkaline-earth metal hydrides allows one to grow crystals with a more perfect structure also at lower pressures [10]. At the same time, this procedure can result in the subsequent contamination of boron nitride with hydrogen. When graphite-like boron nitride is in a medium with high hydrogen content and is exposed to intense radiation, hydrogenation of this material cannot be excluded [11]. It is known that heat treatment of boron nitride powders in hydrogen appreciably lowers the sintering temperature of the samples and increases the density and strength of the material [12]. All this together is the reason why there is such interest in studying the effect of hydrogen on the electronic structure (ES) and physicomechanical properties of boron nitride at the microscopic level; this effect is the main subject of this paper.

The electronic structure of various modifications of boron nitride was repeatedly studied by numerous authors using methods based on first principles [13–18], and most of the papers dealt with hexagonal boron nitride. Since the minimal basis of wave functions was used in the early papers, the calculations did not correctly reproduce the conduction band (CB) nor even the structure of the valence bands (VBs). The scatter in theoretical values of the dielectric gap is as high as 10 eV (from 2.4 to 12.7 eV), whereas experiments yield values in the range 3.2–5.8 eV [19]. The electronic structures of the three modifications of boron nitride were most consistently studied in [15, 16, 18]. However, the conclusions concerning the nature of the gap drawn in [14, 15], using the same full-potential linear augmented plane wave (APW) method, differ. Thus, in [14] a direct gap was obtained at the point *H* (4.3 eV) and an indirect gap equal to 3.9 eV corresponded to the points *H–M*, whereas according to [15], the VB edge is not at the point *H* but at the point (1/4, 3/8, 0). In this case, the term lies 0.2 eV higher that at the point *M*, and the direct gap was obtained at the point *M* (4.5 eV). In [16] an indirect gap *H–M* equal to 4.1 eV was obtained. The same value was obtained in [18] in the context of the pseudopotential approach. One should note that the cal-
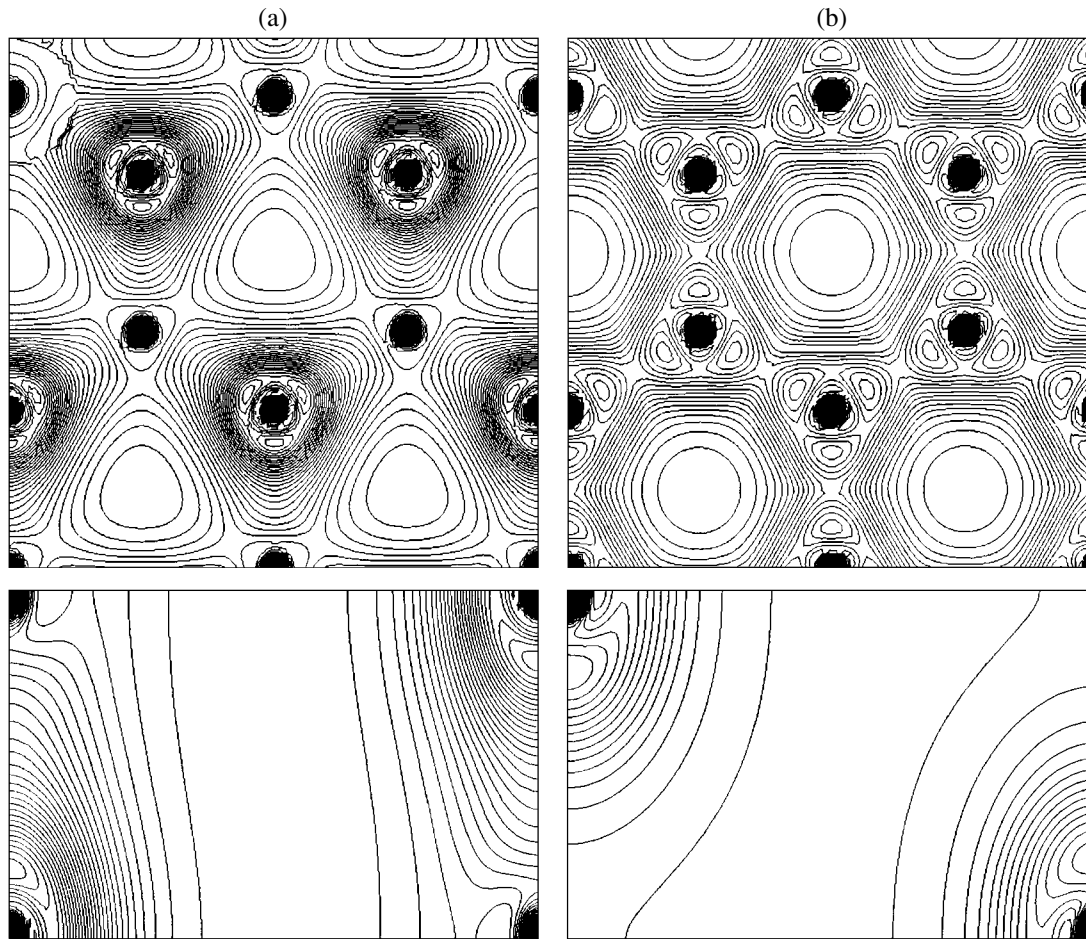
Fig. 1. Distribution of charge density in the basal and prismatic planes for (a) hexagonal boron nitride and (b) graphite.

culated values of the bulk modulus B for BN-h in [16, 18] are an order of magnitude larger than the experimental values, whereas the values obtained for the two other phases (BN-w and BN-z) are in reasonable agreement with the experiment.

In this paper, we describe the results of the calculations of the ES for the three modifications of ideal boron nitride using the generalized gradient approximation for the exchange-correlation potential in which nonlocal effects are partially taken into account, and we study the effect of hydrogen on the ES and properties of hexagonal and cubic boron nitride.

2. METHOD OF CALCULATION

The electronic structure of ideal boron nitride and of boron nitride with interstitial hydrogen atoms was calculated by the full-potential linear APW method [20]. For the exchange-correlation potential, we used the local density approximation (LDA) and generalized gradient approximation (GGA) [21]. The radii of the "muffin-tin" (MT) spheres for N and B were chosen to be equal to 1.4 and 1.2 au, respectively, and remained

the same for all the structures studied. The expansion of crystal potential and charge density inside the MT spheres was restricted to the value $l_{max} = 10$. The nonspherical contributions to the charge density and potential inside the spheres were taken into account up to $l_{max} = 4$. The plane waves with vectors up to $K_{max} = 6$ au^{-1} were included in the space between the spheres. The potential in the space between the spheres was Fourier-expanded and the summation over the vectors of the reciprocal lattice was restricted to $G_{max} = 14$. Self-consistency was attained for 72, 60, and 172 k-points for BN-h, BN-w, and BN-z, respectively. It was assumed that hydrogen does not appreciably affect the parameters of the hexagonal and cubic phases. The radius of the hydrogen sphere was assumed to be equal to the radius of the boron sphere. Several hydrogen sites were simulated for hexagonal boron nitride. Tentative estimates of the total energies were obtained using the linear MT-orbital (LMTO) method, which allows us to considerably reduce the computation time. Then the two cases in which a hydrogen atom was found to be inside a layer in the basal plane and between layers were recalculated using the full-potential linear APW

Table 1. Electronic characteristics of boron nitride in eV (the LDA results are given in brackets)

	BN-*h*	BN-*w*	BN-*z*
Lower VB width			
This calculation	3.9 (3.8)	5.8 (5.9)	5.7 (5.9)
Furthmuller *et al.* [18]	4.0	6.3	6.2
Xu and Ching [16]	4.0	6.3	6.9
Park *et al.* [15]	3.8	6.0	5.9
Experiment	5.8 [23]		5.2 [24]
Upper VB width			
This calculation	9.1 (8.9)	10.9 (10.9)	10.1 (10.6)
Furthmuller *et al.* [18]	9.0	11.3	11.0
Xu and Ching [16]	10.4	11.8	10.9
Park *et al.* [15]	9.0	11.0	10.7
Experiment			13.5 [24]
Total VB width			
This calculation	18.1 (17.6)	20.4 (20.2)	20.2 (20.0)
Furthmuller *et al.* [18]	17.8	20.6	20.4
Xu and Ching [16]	18.8	21.0	21.1
Park *et al.* [15]	17.7	20.3	20.1
Experiment	15–20 [19]		22.0 [19]
Band gap			
This calculation	4.26 (4.24)	5.17 (5.02)	4.47 (4.35)
Furthmuller *et al.* [18]	4.1 (H–M)	4.9	4.4
Xu and Ching [16]	4.1 (H–M)	5.8	5.2
Park *et al.* [15]	4.0	4.9	4.4
Catellani *et al.* [14]	3.9 (H–M)		
Experiment	4.3 [25]		6.0–6.4 [24]
	5.0–5.7 [28]		
Direct gap γ–γ			
This calculation	6.55 (6.23)	8.36 (8.17)	8.81 (8.66)
Park *et al.* [15]		8.2	8.8
Xu and Ching [16]	8.9	8.0	8.7

method. In the cubic phase, the atom H was placed at the site with coordinates a(3/4, 3/4, 3/4); for high hydrogen concentrations, the calculation was performed using the fcc unit cell. For low hydrogen concentrations, a simple cubic cell was used in which boron atoms occupied sites of the fcc cell. Nitrogen atoms occupied the sites with coordinates a(1/4, 1/4, 1/4), a(3/4, 3/4, 1/4), a(3/4, 1/4, 3/4), and a(1/4, 3/4, 3/4). To evaluate the bulk modulus, we calculated the dependence of the total energy on the cell volume for each structure; in the case of BN-*h* additional c/a-optimization was performed for each of the calculated cell volumes. The equilibrium lattice parameters were determined by the total-energy minimization. The bulk modulus was calculated by numerical differentiation of the approximating curve using three different equations of state: a

fourth-degree polynominal, Murnagan's equation, and the equation of state from [22].

3. BORON NITRIDE ELECTRONIC STRUCTURE

Since the ES of ideal boron nitride modifications is discussed in sufficient detail in the early papers [15, 16, 18], we only briefly describe the main results. Our calculations show that BN-*h* is an indirect-gap insulator: the top of the VB lies close to the point K rather than at a symmetry point of the Brillouin zone (BZ) and the edge of the CB lies at the point M. In contrast to the results of [15, 16, 18], the direct gap (4.63 eV) corresponds to the point H, whereas the gap at the point M is 4.73 eV (4.5 eV [15, 18] and 4.6 eV [16]). In Table 1, the main electronic characteristics of the three phases of BN are given, together with the results of our earlier
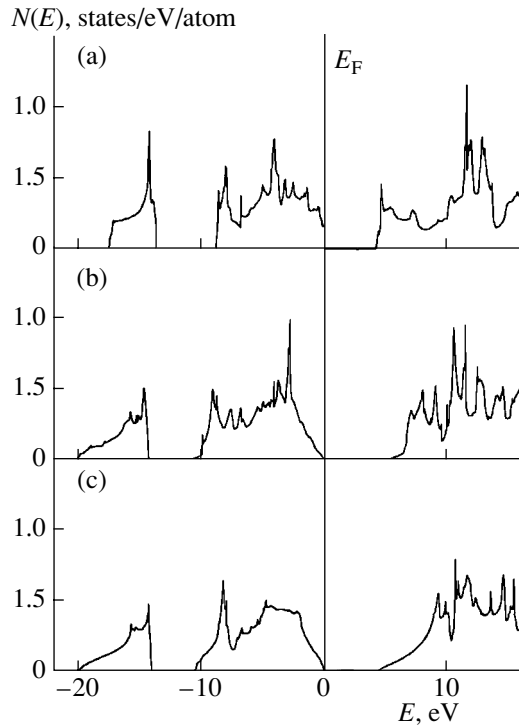
N(E), states/eV/atom

Fig. 2. Total densities of electronic states for boron nitride: (a) BN-*h*, (b) BN-*w*, and (c) BN-*z*.

bottom of the CB in the direction *K–H* and at the point *M* is rather small, and the difference in the energies of the top of the VB at the same points is even smaller, on the order of 0.02–0.05 eV, i.e., almost within the accuracy of calculation. At the same time these data show that the gap in BN-*h* is indirect. Our calculation using the full-potential LMTO method also predicts an indirect gap of 4.6 eV but between the points (0.289, 0.167, 0) and (0.192, 0.333, 0.108).

In Fig. 2 we show the total densities of electronic states (DoS) for the three phases of BN plotted with respect to the top of the VB. The calculation of partial DoS demonstrated that the structure of the VB is almost completely determined by nitrogen; the contribution of boron is small but its effect on the formation of states at the edge of the CB is greater. The values of the effective charge at nitrogen and boron spheres indicate a tendency for the charge to be transferred from boron to nitrogen. In Fig. 1, the charge density distributions in the basal and prismatic planes for BN-*h* and for graphite are shown. We can see that the extent of the charge region for boron is greater than for nitrogen. As regards chemical bonding, charge transfer implies the appearance of the ionic component in boron nitride, which profoundly affects its physical properties. The charge redistribution both inside the layers and between them is more complicated in boron nitride than in graphite (Fig. 1b).

The values of the bulk modulus for the three phases of BN are given in Table 2. For a more rigorous estimate, we used the three equations to find the total energy as a function of volume $E_{tot}(V)$. Whereas for

studies and the experimental data of [19, 23–26]. The use of the GGA approximation does not appreciably change the dielectric gap (see Table 1). We note that the difference between the values of energy terms near the

Table 2. Bulk modulus *B*, its first derivative with respect to pressure *B'* in GPa, and lattice parameters for the three phases of boron nitride in Å

	BN-*h*		BN-*w*		BN-*z*	
	B	*B'*	*B*	*B'*	*B*	*B'*
Murnagan's equation	24.6	14.7	404.5	3.9	398.2	3.7
Equation of state [22]	25.4	11.2	404.0	3.7	402.9	3.7
Fourth-degree polynomial	25.4	11.5	404.6	4.0	397.7	3.7
Park *et al.* [15]	[251.4*]		349.0		353.0	
Xu and Ching [16]	335	2.48	390	6.3	370	3.8
Furthmuller *et al.* [18]	261	3.66	401	3.59	397	3.59
Cohen [27]					367	
Experiment	25.5[a]	15[a]			410 ± 80[b]	
			410 ± 80[b]		369[c]	
Lattice parameters	*a*	*c*	*a*	*c*	*a*	
Our calculation	2.480	6.493	2.528	4.164	3.582	
Experiment	2.500	6.660	2.550	4.200	3.615	
Furthmuller *et al.* [18]	2.486	6.439	2.521	4.165	3.576	

Note: The superscripts *a*, *b*, and *c* denote the experimental values from [28–30], respectively; * denotes the result of the calculation with fixed *c/a* equal to the experimental value.

BN-w and BN-z after the optimization of the structure with respect to volume the results are in good agreement with experimental data, for BN-h the difference between theory and experiment is practically an order of magnitude (the value in the square brackets in Table 2). Even greater values of B were obtained in [16, 18]. For this reason, in addition to volume optimization (for a constant ratio c/a), we carried out c/a optimization for each value of the volume for BN-h. The minimal values of the energy obtained for each volume were used to approximate the curve $E_{tot}(V)$. In this case, good agreement with experiment was obtained for the first time, both for B and for B' (the first derivative of B with respect to pressure). The optimized values of the lattice parameters for the three structures are also given in Table 2.

On the whole, the results of the calculations show that the ES for all three phases is reproduced quite correctly and can be used for calculations and for interpreting various electronic properties of boron nitride.

4. EFFECT OF HYDROGEN ON THE ELECTRONIC STRUCTURE OF GRAPHITE- AND DIAMOND-LIKE BORON NITRIDE

In order to analyze the effect of hydrogen on chemical bonding and the properties of hexagonal and cubic BN, it is necessary to determine the possible hydrogen sites in the unit cell. The corresponding experimental data are not known. This may indicate either that such hydrogen structures are not formed or that such experiments were not performed. By analogy with graphite, in which the hydrogen molecule can occupy the position of one of the carbon atoms at hexagon sites [31], we may assume that a similar configuration is also possible in hexagonal boron nitride. Moreover, a compound is known $(BNH_2)_3$ whose molecule has a structure of benzene type (a hexagon ring with alternating B and N atoms and with hydrogen atoms located normally to the ring plane). A similar location of hydrogen is also characteristic of boron hydrides. We may assume that the location of hydrogen in BN-h is most probably in the interlayer space but very close to the basal planes. However, in the context of the supercell approach, a detailed analysis of such models requires considerable computation time; thus, we used simplified models to describe the behavior of atomic hydrogen in hexagonal boron nitride. Hydrogen atoms were placed in the basal plane, in the interlayer space, and on the faces and edges of the unit cell parallel to the c axis. The results of the evaluative calculations of the total energy by the LMTO method show that the most favorable positions with lowest energy lie between the layers and at the centers of the faces. Fig. 3 shows the electron energy spectra for two hydrogen positions in boron nitride, one between the layers (case 1) and the other at the center of the hexagon (case 2). The calculation of the total and partial DoS shows that the contributions of hydrogen
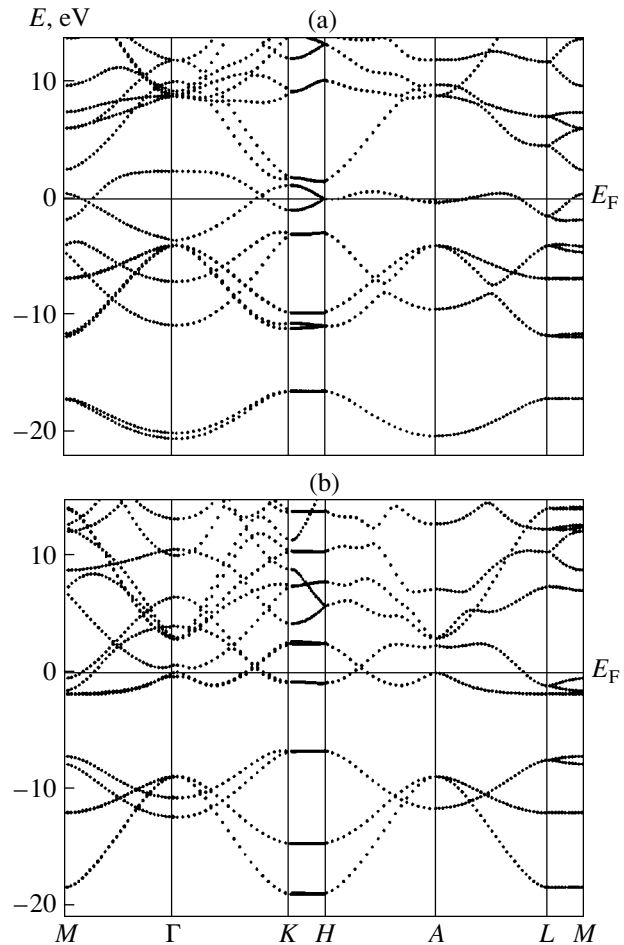

Fig. 3. Electron energy spectra for hexagonal boron nitride with atomic hydrogen (a) in the interlayer space and (b) in the basal plane.

are comparable to those of boron. In the first case (Fig. 3a), hydrogen states in the gap appear, and near the Fermi level E_F there are regions where $E(k)$ is flat, which may be an indication of the instability of the structure. Since in this case the hydrogen concentration is high, we have a band of finite width, but the dispersion in this band tends to zero with decreasing H concentration. Indeed, in this case hydrogen, which is located between the layers, cannot ensure the stability of bonds with boron or nitrogen atoms because of the large interplanar distances; the same behavior is observed if hydrogen is located in the centers of the faces. The calculation of the volume dependence of the total energy using the c/a optimization does not reveal a minimum on the curve $E_{tot}(V)$; this is also evidence against the model under consideration.

If a hydrogen atom is located in the basal plane, then there is a gap between the bands, just as for ideal BN-h, and hydrogen mainly contributes to DoS in the energy region near the bottom of the CB. The position of the Fermi level coincides with the DoS peak. The calculation of the total energy predicts that in this case isolated
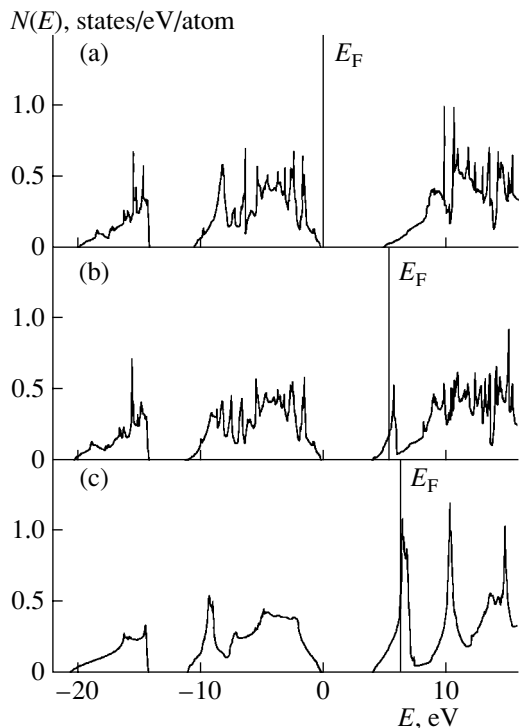
$N(E)$, states/eV/atom

Fig. 4. Total DoS of (a) cubic (diamond-like) boron nitride, (b) boron nitride with low (about 11.1%), and (c) high (about 33.3%) hydrogen concentrations.

most probable. In this case, the H_2 molecule can be located between the layers and fill in the volume like a ball; i.e., the hydrogen molecule can be found between layers as in a potential well. Similar behavior is observed in the recent experiments with graphite, although the origin of this behavior is not quite clear and requires further research.

In the case of cubic boron nitride, the situation is slightly simpler, since hydrogen can be introduced into a free tetrahedral interstitial space. The results of the calculation of the DoS for BN-z with different hydrogen concentrations are shown in Fig. 4. In cubic boron nitride, hydrogen mainly contributes to the DoS at the bottom of the CB. The volume dependence of the total energy of an electronic subsystem with a high hydrogen content (about 33%) has no minimum, but if the hydrogen concentration decreases (less than 11%), equilibrium states can exist, with an increase in volume of less than 3.3%. In Fig. 4b we see that the decrease in H concentration shifts the sharp peak of the DoS away from E_F. Nevertheless, the large value of $N(E_F)$ and the existence of flat regions in the spectrum indicate that this state is metastable. On the whole, hydrogen only slightly affects the bulk modulus of cubic boron nitride, which is already quite large in the case of a diamond-like modification of boron nitride (382.1 GPa in pure BN-z and 383.3 GPa in BNH).

5. CONCLUSION

Our calculations for ideal modifications of boron nitride show that taking into account nonlocal effects in the context of the generalized gradient approximation for the exchange-correlation potential only slightly affects the electronic characteristics of boron nitride. Our procedure for optimizing the structure of hexagonal boron nitride allowed us to obtain for the first time a value of the bulk modulus that was in good agreement with experiment. It is shown that dissolved hydrogen can be present in cubic boron nitride; however, such structures are extremely unstable with respect to external factors. The structure of hexagonal boron nitride that has a composition close to BNH with hydrogen in the basal plane (case 2) is metastable under the above-specified conditions. If the volume of the unit cell is decreased by about 10%, the bulk modulus increases by more than a factor of 2 compared to ideal BN-h, in agreement with experiment [12]. We note that the location of hydrogen in hexagonal boron nitride is more likely near the surface. In [11] it was shown that hydrogen is mainly located in the intergrain space. The location of hydrogen at the surface can result in an increase in hydrogen reactivity to impurity atoms, which are initially present in powders before the synthesis of boron nitride. This assumption is supported by the formation of the gas phase in the reaction space of the compression chamber [10]. Cleaning the surface of impurities, hydrogen increases the density and strength of the material. The interaction of hydrogen with the (001)

monolayers are more favorable. If we consider the dependence of the total energy on the parameters a and c, then a minimum appears only in the case where the parameter a is fixed and $a \geq a_0$, where a_0 is the experimental value of the lattice parameter for BN-h. In this case, the volume of the unit cell changes because of the decrease in the interplanar spacing. The minimum is observed if c decreases by about 10%. Such a variation in the parameter c is possible for high pressures, under which the phase transition can set in. It is well known that the change in the volume of graphite-like boron nitride with pressure is mainly determined by the lattice compressibility along the c axis and that the presence of hydrogen decreases the pressure at which the transition occurs first to the martensite phase BN-w and then to BN-z [10]. It is possible that even low hydrogen concentrations in the basal plane (or near it) may stimulate the onset of the martensite transformation, which in turn may lead to a sharp increase in the bulk modulus. The estimate for case 2 (for $V/V_0 = 0.892$, where V_0 is the experimental equilibrium volume of BN-h) shows that B is increased by more than a factor of 2 compared to pure BN-h. The following values were obtained: $B = 57.7$ GPa from Murnagan's equation and 67.9 GPa by the method of [22].

Thus, the results of the calculations indicate the "transparency" of the hexagonal modification of boron nitride to atomic hydrogen. At elevated hydrogen concentrations, the formation of molecular hydrogen is

surface of cubic boron nitride can proceed according to the scheme suggested in [32] for diamond. In this case, it is necessary to consider the formation of boron or nitrogen dimers due to the variation in the coordination number of the nearest neighbors at the surface. The interaction of hydrogen with the (0001) surface in BN-*h* can be more complicated and can strongly depend on the nitrogen and boron content in the plane considered. All these problems require detailed study and will be discussed in our future publications.

ACKNOWLEDGMENTS

REFERENCES

1. A. V. Kurdyumov and A. N. Pilyankevich, *Phase Transformations in Carbon and Boron Nitride* (Naukova Dumka, Kiev, 1979).
2. A. V. Kurdyumov, V. G. Malogolovets, N. V. Novikov, A. N. Pilyankevich, and L. A. Shul'man, *Polimorphous Modifications of Carbon and Boron Nitride* (Metallurgiya, Moscow, 1994).
3. J. H. Edgar, J. Mater. Res. **7**, 235 (1992).
4. R. B. Heimann and J. Kleiman, *Shock-Induced Crowth of Superhard Materials* (Springer, Berlin, 1988).
5. R. H. Wentof, J. Chem. Phys. **34**, 809 (1961).
6. F. P. Bundy and R. H. Wentorf, J. Chem. Phys. **38**, 1144 (1963).
7. T. Sato, T. Ishii, and N. Setaka, Commun. Am. Ceram. Soc. C **65**, 162 (1982).
8. A. V. Kurdyumov, N. F. Ostrovskaya, and A. N. Pilyankevich, Dokl. Akad. Nauk SSSR **229**, 338 (1976) [Sov. Phys. Dokl. **21**, 402 (1976)].
9. E. Tani, T. Soma, A. Sawaoka, and S. Saito, Jpn. J. Appl. Phys. **14**, 1605 (1975).
10. L. F. Vereshchagin, I. S. Gladkaya, G. A. Dubitskiĭ, and V. N. Slesarev, Izv. Akad. Nauk SSSR, Neorg. Mater. **15**, 256 (1979).
11. V. A. Dedkov, Candidate's Dissertation in Physics and Mathematics (Tomsk, 1996).
12. I. A. Morosov, R. A. Morosova, T. D. Dubovik, *et al.*, in *Abstract Book of NATO International Conference on Hydrogen Materials Science and Chemistry of Metal Hydrides* (Katseveli, Ukraine, 1997), p. 70.
13. J. Robertson, Phys. Rev. B **29**, 2131 (1984).
14. V. A. Catellani and M. Pasternak, Phys. Rev. B **32**, 6997 (1985).
15. K. T. Park, K. Terakura, and N. Hamada, J. Phys. C: Solid State Phys. **20**, 1241 (1987).
16. Yong-Nian Xu and W. Y. Ching, Phys. Rev. B **44**, 7787 (1991).
17. O. V. Boev and S. E. Kul'kova, Fiz. Tverd. Tela (St. Petersburg) **34**, 2218 (1992) [Sov. Phys. Solid State **34**, 1184 (1992)].
18. J. Furtmuller, J. Hafner, and G. Kresse, Phys. Rev. B **50**, 15606 (1994).
19. V. A. Fomichev and M. A. Pumsh, J. Chem. Phys. **29**, 1015 (1968).
20. P. Blaha, K. Shwartz, and J. Luits, in *WIEN97* (Vienna Univ. of Technology, Vienna, 1997); P. Blaha, K. Schwartz, P. Sorantin, and S. B. Trickey, Comput. Phys. Commun. **59**, 399 (1990).
21. J. P. Perdew, S. Burke, and M. Ernzerhof, Phys. Rev. Lett. **77**, 3865 (1996).
22. D. M. Teter, G. V. Gibbs, M. B. Boisen, Jr., *et al.*, Phys. Rev. B **52**, 8064 (1995).
23. E. Teleger, N. Kosuch, G. Wiech, and A. Faessler, Phys. Status Solidi B **91**, 223 (1979).
24. *Landolt–Bornstein. New Series Physics of Group IV Elements and III–V Compounds Group*, Ed. by O. Madelung (Springer, Berlin, 1982), Vol. 17a.
25. J. Zuman and D. Kolar, J. Phys. C **5**, 3097 (1972).
26. R. Leapman, P. Fejes, and J. Silcox, Phys. Rev. B **28**, 2361 (1983).
27. M. L. Cohen, Mater. Sci. Eng. A **209**, 1 (1996).
28. H. G. Driskamer and R. W. Lynch, Solid State Phys. **19**, 135 (1966).
29. V. A. Pesin, Sverkhtverd. Mater. **6**, 5 (1980).
30. E. Knittle, R. M. Wentzcovitch, R. Jeanloz, and M. L. Cohen, Nature **337**, 349 (1989).
31. H. Freimuth, H. Wiechert, H. P. Schildberg, and H. J. Lauter, Phys. Rev. B **42**, 587 (1990).
32. M. D. Winn, M. Rassinger, and J. Hafner, Phys. Rev. B **55**, 5364 (1997).

Translated by I. Zvyagin

SEMICONDUCTOR STRUCTURES, INTERFACES, AND SURFACES

Diffusion of Zinc into InP with an Unprotected Surface

V. F. Andrievskiĭ, E. V. Gushchinskaya, and S. A. Malyshev

Institute of Electronics, Belarussian Academy of Sciences, Minsk, 220090 Belarus

Submitted March 11, 2003; accepted for publication April 18, 2003

Abstract—The results of experimental studies of InP:Zn obtained by diffusion of zinc in an open system into InP with an unprotected surface are reported. The effects of heat treatment in a nitrogen and a hydrogen atmosphere performed prior to the Zn diffusion on the InP parameters are studied. It is ascertained that a surface layer saturated with nitrogen is formed as a result of thermal annealing in a nitrogen atmosphere. It is shown that this layer retards the phosphorus evaporation, reduces the generation of recombination centers in indium phosphide, and increases the concentration of the electrically active zinc impurity in the *p*-type region of indium phosphide. © *2004 MAIK "Nauka/Interperiodica".*

1. INTRODUCTION

The main method of producing p^+-type regions in the production technology of optoelectronic and microelectronic devices based on InP is the diffusion of zinc. A low concentration of the electrically active zinc impurity and a high concentration of defects generated in the course of this diffusion result in a low yield of devices and a deterioration in their parameters and reliability. A high concentration of defects is caused by an intense process of phosphorus evaporation from the semiconductor bulk [1, 2].

A high concentration of phosphorus vacancies as a result of the evaporation of phosphorus atoms determines a low concentration of electrically active zinc ions. In the course of diffusion, zinc atoms migrate over the interstitial lattice sites and not only become incorporated into the sites of indium sublattice and act as an electrically active impurity [3–5], but are also found to be bound by phosphorus vacancies and form neutral complexes that include zinc atoms and phosphorus vacancies (V_P–Zn–V_P or Zn–V_P) [6]. Since the formation of neutral complexes is more likely than the incorporation of zinc into indium vacancies [7], the concentration of electrically active zinc is low compared to the total concentration of diffusing zinc.

In order to reduce the phosphorus evaporation from the bulk of indium phosphide during the diffusion process, an increased pressure of phosphorus vapors is usually provided over the InP wafer surface. The problem of phosphorus evaporation is solved most simply by using pulsed diffusion [8]. However, this method has a low throughput and reproducibility, which results in a low yield of devices and, accordingly, a high production cost. For a long time, researchers endeavored to discover a more efficient method for carrying out zinc diffusion (diffusion from a solid source, diffusion through a protective dielectric coating, and diffusion from polymeric zinc-containing films).

Zinc diffusion into indium phosphide with an unprotected surface is the most attractive method from the standpoint of simplicity, ease of production, and output. The purpose of this paper is to study the special features of formation of p^+-type regions using the above method for diffusion.

2. EXPERIMENTAL

Diffusion of Zn into InP with an unprotected surface was carried out in a flow-through system in a quartz reactor mounted in a diffusion furnace. The crucible with zinc and wafers of single-crystal InP with an electron concentration of 2.6×10^{16} cm^{-3} were placed in the reactor. The ends of the reactor were sealed using metal lids in which mobile molybdenum rods were incorporated. The system was first purged with hydrogen; the rods were then used to place wafers and the crucible with zinc at the tube center, where the required temperature was maintained. The diffusion of zinc was carried out for 60 min at a temperature of 470°C.

The concentration profile of zinc in the bulk of indium phosphide was measured by secondary-ion mass spectroscopy (SIMS) using an IMF-4F (Cameca) system. The concentration of zinc atoms was calibrated using the ion-implanted InP samples. Chemical elements on the InP surface were detected using an electron spectrometer. In order to determine the concentration profiles of majority charge carriers and the profiles of diffusion length and effective lifetime of minority charge carriers, we used photoelectrochemical *C–V* profiling [9–11].

3. RESULTS AND DISCUSSION

We now consider the effect of thermal annealing (TA) in a nitrogen and a hydrogen atmosphere on the electrical properties of single-crystal indium phosphide. Studies of the effective lifetime of minority charge carriers τ_{eff} in the surface region of InP samples subjected to TA without special protection of the semi-
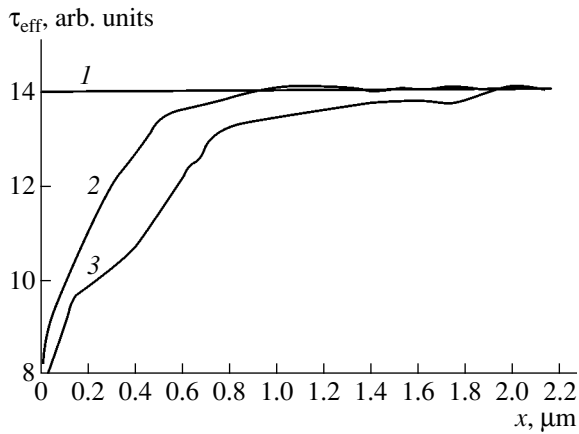
τ_{eff}, arb. units

Fig. 1. Depth distribution of the effective lifetime of minority charge carriers in InP ($n = 3.4 \times 10^{16}$ cm^{-3}) (*1*) before thermal annealing, (*2*) after thermal annealing in a nitrogen atmosphere, and (*3*) after thermal annealing in a hydrogen atmosphere.

N_N, arb. units

Fig. 2. Concentration profiles of nitrogen atoms in InP (*1*) before thermal annealing and (*2*) after thermal annealing in a nitrogen atmosphere. The profiles were obtained using secondary-ion mass spectroscopy.

conductor surface showed that the atmosphere in which the TA was carried out had a significant effect on the τ_{eff} distribution (Fig. 1). For example, the effective lifetime of minority charge carriers near the InP surface decreases as a result of TA at 470°C for 60 min in atmospheres of hydrogen and nitrogen. The thickness of the layer within which this decrease is observed after TA in a nitrogen atmosphere is much smaller than that after TA in a hydrogen atmosphere. The decrease in τ_{eff} in the surface layer is attributed to the generation of recombination centers in the course of TA; these centers are formed as a result of phosphorus evaporation from the bulk [12–14]. Studies of the as-grown sample show that the effective lifetime of minority charge carriers in the surface region of this sample is no different from the corresponding value in the semiconductor bulk. The shape of the τ_{eff} distribution in thermally annealed samples is indicative of a decrease in the probability of formation of recombination centers over the depth of the sample during TA in a nitrogen atmosphere compared to TA in a hydrogen atmosphere.

An analysis of the indium phosphide surface using an ÉS-2401 electron spectrometer showed that the surface layer of the samples that were thermally annealed in a hydrogen or a nitrogen atmosphere consisted of native InP oxide composed of In_2O_3, P_2O_5, and $InPO_4$ oxygen compounds. The emergence of the native oxide is probably caused by oxidation of the InP surface prior to TA and by thermal InP oxide that is formed owing to the presence of impurities (oxygen and water) in the gas in the flow-through system. A SIMS analysis of the state of the surface of the InP samples that were thermally annealed in a nitrogen atmosphere showed that nitrogen was present in the surface region of this sample (Fig. 2); i.e., a surface layer saturated with nitrogen was formed. Nitrogen was not detected in the surface region of the as-grown sample.
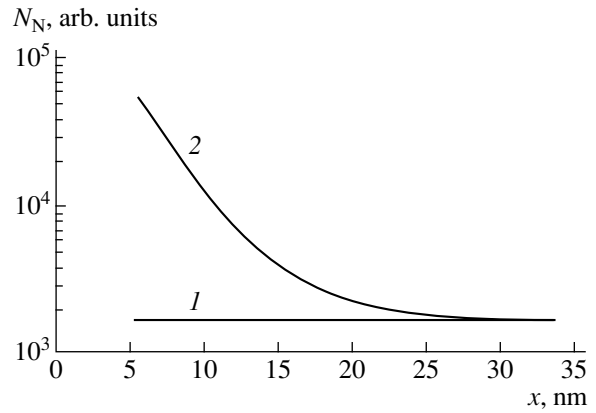
Let us consider the effect of the surface layer saturated with nitrogen on Zn diffusion (carried out in an open system) into the bulk of InP through an unprotected surface. Concentration profiles of the electrically active impurity and zinc atoms in InP for as-grown samples and samples subjected to TA in a nitrogen atmosphere are shown in Fig. 3 (the profiles were obtained using SIMS). Thermal annealing in a nitrogen atmosphere was carried out at a temperature of 300°C for different periods of time. As can be seen from Fig. 3, the duration of TA has a considerable effect on the distribution of the electrically active impurity. The SIMS concentration profiles of zinc atoms for all the studied samples after diffusion without annealing and
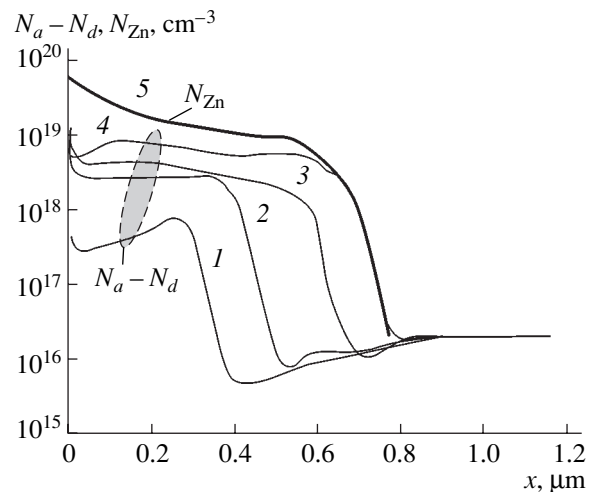
$N_a - N_d$, N_{Zn}, cm^{-3}

Fig. 3. Profiles of N_a–N_d concentration after Zn diffusion (*1*) without preliminary thermal annealing and (*2–4*) with preliminary thermal annealing in a nitrogen atmosphere at 300°C for (*2*) 10, (*3*) 20, and (*4*) 30 min. Curve *5* represents the concentration profile of zinc atoms $N_{Zn}(x)$ according to the SIMS measurements.
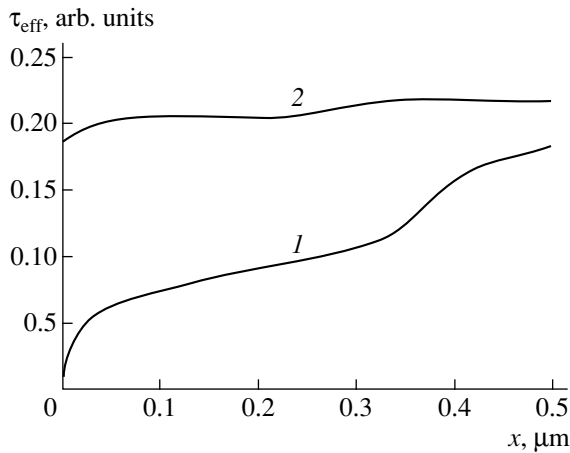
Fig. 4. The depth distribution of the effective lifetime of minority charge carriers in the *n*-type region of the *p–n* junction after Zn diffusion (*1*) without preliminary thermal annealing and (*2*) with preliminary thermal annealing in a nitrogen atmosphere for 30 min at 300°C.

Fig. 5. Schematic representation of Zn diffusion into InP through an unprotected surface (*a*) without thermal annealing and (*b*) with thermal annealing in a nitrogen atmosphere.

after preliminary TA in a nitrogen atmosphere are identical (Fig. 3, curve *5*). Measurements of nitrogen concentration in the samples under consideration by SIMS show that nitrogen is preserved in the surface layer after zinc diffusion; i.e., zinc diffusion does not result in the disappearance of the nitrogen-saturated surface layer.

For an unannealed sample, the concentration of the electrically active impurity (Fig. 3, curve *1*) is much lower than the total concentration of zinc atoms (curve *5*). In this case, the depth of the *p–n* junction was 0.35 μm, whereas the penetration depth of zinc atoms was 0.7 μm. In the layer extending from 0.35 to 0.7 μm in depth from the surface, zinc atoms are in an electrically inactive state. This state is probably related to phosphorus vacancies that form the V_P–Zn–V_P and Zn–V_P neutral complexes. It can also be seen from Fig. 3 that TA in a nitrogen atmosphere affects the concentration profile of the electrically active impurity (Fig. 3, curves *2–4*). As the duration of TA increases, both the hole concentration and the *p–n*-junction depth increase. If the duration of TA exceeds 30 min, the *p–n*-junction depth coincides with the diffusion length of Zn atoms. The increase in the degree of activation of Zn atoms in the course of TA in a nitrogen atmosphere indicates that the concentrations of neutral complexes V_P–Zn–V_P and Zn–V_P and, accordingly, the concentration of phosphorus vacancies V_P decrease. The depth distribution of the effective lifetime of minority charge carriers indicates that the recombination of charge carriers is fairly intense in the *n*-type region of a *p–n* junction for the unannealed InP sample (Fig. 4). Thermal annealing in an atmosphere of nitrogen reduces the probability of forming these recombination centers.

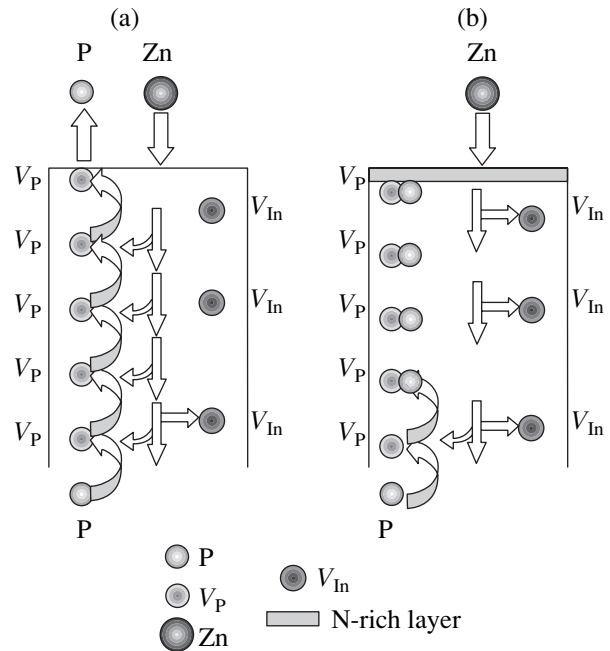Thus, thermal annealing in an atmosphere of nitrogen prior to zinc diffusion into the InP bulk through an unprotected surface gives rise to a surface layer saturated with nitrogen; this layer reduces the generation rate of phosphorus vacancies and increases the degree of activation of zinc during its diffusion.

On the basis of these studies, we may assume that the following processes occur during Zn diffusion into InP with an unprotected surface.

Phosphorus atoms migrate over phosphorus vacancies with subsequent phosphorus evaporation from the InP surface in addition to penetration of zinc atoms into the semiconductor bulk over the interstitial space. As a result, phosphorus vacancies are generated; the concentration of these vacancies becomes much higher than that of indium vacancies (Fig. 5a). The formation of neutral complexes containing zinc atoms and phosphorus vacancies is more probable than the incorporation of zinc into vacant indium sites. As a result, if the concentration of phosphorus vacancies is high, zinc forms the aforementioned neutral complexes. In this case, the concentration of electrically active zinc in the p^+-type region of InP amounts to no more than 5% of the total zinc concentration.

A layer saturated with nitrogen is formed at the InP surface as a result of preliminary thermal annealing in an atmosphere of nitrogen. This layer prevents evaporation of phosphorus from the InP bulk and thus reduces the concentration of phosphorus vacancies in the surface region of the semiconductor (Fig. 5b). If the concentration of phosphorus vacancies is lower than a certain critical value, the incorporation of zinc atoms into the indium sublattice and the resulting formation of the

electrically active impurity becomes the dominant process. The concentration of electrically active zinc in a p^+-type InP region at a depth of 0.5 μm amounted to 50% of the total zinc concentration in the samples subjected to thermal annealing for 30 min. The value of the critical concentration of phosphorus vacancies determines the depth of penetration of the electrically active impurity; i.e., the p–n-junction depth. In the n-type region of the p–n junction in the unannealed samples and the samples subjected to TA for less than 30 min (Fig. 3, curves *1–3*), the process of formation of neutral complexes is more probable because the concentration of phosphorus vacancies exceeds the critical value. A fraction of the zinc atoms incorporated into the indium sublattice forms an impurity of the acceptor type and compensates the residual donor concentration. As a result, a layer with an electron concentration that is lower than the corresponding value in the semiconductor bulk is formed in the n-type region of the p–n junction.

4. CONCLUSIONS

A surface layer saturated with nitrogen is formed as a result of thermal annealing in a nitrogen atmosphere. This layer prevents phosphorus evaporation, reduces the probability of generation of recombination centers in indium phosphide, and brings about an increase in the concentration of the electrically active zinc impurity during zinc diffusion (in an open system) into the bulk of InP through an unprotected surface.

ACKNOWLEDGMENTS

REFERENCES

1. M. Wada, K. Sakakibqara, M. Higuchi, and Y. Sekiguchi, J. Cryst. Growth **114**, 321 (1991).
2. Yu Kin Man, L. Y. Chan, R. Leon, *et al.*, J. Appl. Phys. **74**, 86 (1993).
3. P. N. Favennec, L. Henty, M. Gauneau, *et al.*, Electron. Lett. **16**, 882 (1980).
4. S. Aytac and A. Schachetzki, Solid-State Electron. **24**, 57 (1981).
5. H. Ando, N. Susa, and H. Kanbe, Jpn. J. Appl. Phys. **20** (3), L197 (1981).
6. K. Kasmierski, A. M. Huber, G. Morillot, and B. de Gremoux, Jpn. J. Appl. Phys. **23**, 628 (1984).
7. G. van Gurp, T. van Dongen, G. M. Fontijn, *et al.*, J. Appl. Phys. **65**, 553 (1989).
8. *Atomic Diffusion in Semiconductors*, Ed. by D. Shaw (Plenum, London, 1973; Mir, Moscow, 1975).
9. A. T. Gorelenok, V. F. Andrievskii, A. V. Kamanin, *et al.*, in *Proceedings of 2001 European Microwave Week: GaAs2001 Conference* (London, 2001), p. 13.
10. V. F. Andrievskiĭ, A. T. Gorelenok, N. A. Zagorel'skaya, *et al.*, Pis'ma Zh. Tekh. Fiz. **27** (23), 68 (2001) [Tech. Phys. Lett. **27**, 1013 (2001)].
11. A. T. Gorelenok, V. F. Andrievskii, A. V. Kamanin, *et al.*, Nucl. Instrum. Methods Phys. Res. B **186**, 240 (2001).
12. T. Kamijoh, H. Takang, and M. Sakuta, J. Appl. Phys. **55**, 3756 (1984).
13. V. F. Andrievskii, E. V. Gushchinskaya, Yu. S. Emelyanenko, and S. A. Malyshev, in *Heterostructure Epitaxy and Devices—HEAD'97*, Ed. by P. Kordos and J. Novak (Kluwer Academic, Dordrecht, 1998), p. 149.
14. V. F. Andrievskii, E. V. Gushchinskaya, and S. A. Malyshev, in *Proceedings of 10th IEEE International Symposium on Electron Devices for Microwave and Optoelectronics: Applications-EDMO'2002* (Manchester, UK, 2002), p. 5.

Translated by A. Spitsyn

SEMICONDUCTOR STRUCTURES, INTERFACES, AND SURFACES

Donor Compensation in the Depletion Layer of CdF$_2$ Crystals with a Schottky Barrier

A. S. Shcheulin, A. K. Kupchikov, A. E. Angervaks, and A. I. Ryskin*

Vavilov State Optical Institute, All-Russia Research Center, St. Petersburg, 199034 Russia
*e-mail: alex@ryskin.spb.su
Fax: (812) 328 3720
Submitted April 8, 2003; accepted for publication April 21, 2003

Abstract—RF response and capacitance–voltage and current–voltage characteristics of *n*-type semiconductor crystals CdF$_2$:In, CdF$_2$:Ga, and CdF$_2$:Y with a Schottky barrier were studied. Specific features of these characteristics are accounted for based on the assumption that the charge transport from the metal to the depletion layer is due to the formation of Cd^0 excitations in the contact layer, which occurs because of the supply of electron pairs from the metal (Au). These excitations compensate donors in the space-charge region of ~1 μm thickness, adjacent to the contact. © *2004 MAIK "Nauka/Interperiodica"*.

1. INTRODUCTION

Measurements of the Schottky barrier impedance are widely used to study electron states in semiconductors and, in particular, to determine the concentration of electrically active impurities. One of the methods used for this purpose is the measurement of the capacitance–voltage (*C–V*) characteristic of the Schottky barrier under reverse bias. For the case of an impurity that is uniformly distributed in a sample and forms a discrete donor level, the quantity C^{-2} is a linear function of *V*:

$$\frac{1}{C^2} = \frac{2(V + V_k)}{\varepsilon\varepsilon_0 e N_d S^2}, \tag{1}$$

where V_k is the barrier height; $\varepsilon\varepsilon_0$, the permittivity of the crystal; *e*, the elementary charge; N_d, the concentration of ionized donors, which defines the space charge density; and *S*, the metal–semiconductor contact area. If the capacitance is measured by applying a small ac voltage to the sample, the frequency used must be low enough so that the measurement process does not distort the equilibrium occupancy of donor levels at the interface between the depleted layer and the sample bulk.

In the presence of several donor levels with different binding energies, the plot of the $C^{-2} = f(V)$ dependence consists of several linear portions, and their slope decreases as the bias voltage increases. This is because the Fermi level successively crosses at increasingly deeper levels of the impurity. For discrete levels with the energy $E_j > E_F$, $j = 1\ldots m$ (E_F is the Fermi energy) and the density of corresponding centers N_j, Eq. (1) is replaced by [1]:

$$\frac{1}{C^2} = \frac{2(V + V_k)}{\varepsilon\varepsilon_0 e \left(\sum_{j=1}^{m} N_j\right) S^2} + \text{const}(V). \tag{2}$$

The levels N_j are numbered in order of increasing binding energy. The higher the binding energy of a level, the closer the coordinate x_j at which the level intersects the Fermi level is to the contact. Since the rate of thermal emission from donors, which determines the time at which equilibrium occupancy is established, depends on the binding energy, the capacitance measured by the modulation technique is frequency-dependent. To determine the total concentration of donors in the crystal, the voltage modulation frequency must be low enough so that the rate of thermal emission from the deepest donors ensures their equilibrium occupancy at the boundary of the layer limited by the coordinates $x = 0$ (contact) and x_m.

In the case of inhomogeneous doping of a semiconductor, the profile of the concentration distribution $N_d(x)$ can be determined using the differential form of the dependence of the capacitance on the reverse bias [2]:

$$N_d(x) = \frac{C^3}{S^2 e\varepsilon\varepsilon_0\left(\dfrac{dC(x)}{dV}\right)}. \tag{3}$$

In this paper, we study the temperature dependences of the RF response, as well as capacitance–voltage (*C–V*) and current–voltage (*I–V*) characteristics of semiconductor CdF$_2$ crystals with a Schottky barrier. It is shown that the compensation mechanism operative in these crystals is associated with the presence in the depleted layer of excitations that provide the transport of the charge from the metal to this layer.

2. ELECTRONIC PROPERTIES OF SEMICONDUCTING CdF$_2$

CdF$_2$ is an insulator of high ionicity with a band gap of 7.8 eV. The fluorine atoms are located at sites on a

simple cubic lattice. The Cd atoms occupy half the central positions in fluorine cubes, which alternate with "unfilled" cubes (interstices of the cation sublattice). Free or weakly bound electrons are introduced into the crystal by doping it with donor impurities and subsequent calcination in a reducing atmosphere, so the crystal becomes an *n*-type semiconductor. Group-IIIa impurities (rare-earth elements according to modern chemical terminology) form hydrogen-like donor states in the crystal with a binding energy of ~0.1 eV. In and Ga, elements belonging to Group IIIb of the periodic table, form bistable centers in CdF_2 [3, 4]. These centers are identical to *DX* centers in III–V and II–VI semiconductors: along with shallow donor states, they form deep two-electron *DX* states [5, 6] (as for the difference between these two groups of donor impurities, see [7]). The formation of these states is accompanied by deep relaxation of the lattice, which gives rise to potential barrier between the deep and shallow states of the center. Owing to this barrier, the shallow state is metastable. The microscopic nature of the *DX*-state in CdF_2 was defined by Park and Chadi [8]. Their calculations show that the impurity atom is shifted along the fourfold axis toward the neighboring interstice by about 3/4 of the length of the edge of the fluorine cube [8]. According to [8], the deep level energy is 0.25 eV for In and 0.70 eV for Ga. The crystal is compensated: nearly equal quantities of In or Ga ions are in "deep," In^+ or Ga^+, and ionized, In^{3+} or Ga^{3+}, states. The concentration of trivalent impurity ions is higher than that of univalent ions owing to the presence of a certain number of interstitial F^- ions (see, e.g., [9]). At low temperature the majority of impurity centers are in a deep state, and the crystal conductivity is low.

Strong photoionization absorption bands are associated with both states of a bistable center. For shallow donor centers this is a long-wavelength band covering the IR part of the spectrum, as far as ~10 μm. The "tail" of this band extends into the visible range; its shape is well described by the hydrogen-like impurity model [10, 11]. The deep state is responsible for the band covering the UV part of the spectrum, from the fundamental absorption edge of CdF_2 (~160 nm), and a considerable part of the visible spectral range [12, Fig. 1]. The photoexcitation of a crystal in this band at low temperature transforms deep centers into shallow ones, $(In^{3+} + e_H)$ or $(Ga^{3+} + e_H)$ (here e_H denotes an electron bound on a hydrogen-like orbital near the impurity). Due to the presence of the barrier, a photoinduced shallow state can persist for an infinitely long time if the temperature is low enough. As the temperature rises above ~40 K for In and ~200 K for Ga, this state dissociates, and two shallow centers form one deep and one ionized ("empty") center [5]. The energies of deep levels estimated from the analysis of kinetics of thermal dissociation of shallow levels are in agreement with the theoretical values mentioned above [12, 13].
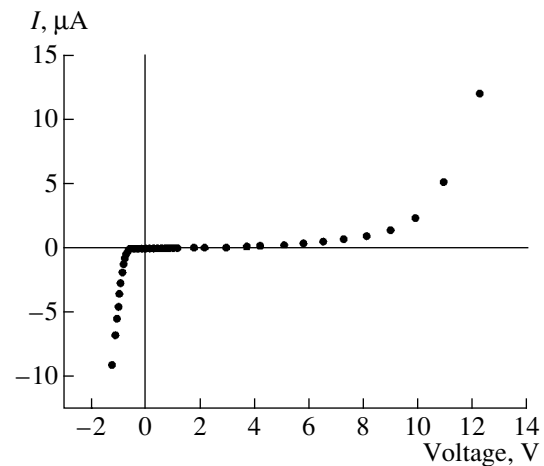

Fig. 1. *I–V* characteristic of a CdF_2:In crystal ($n = 4.5 \times 10^{18}$ cm^{-3}) with a Schottky barrier; $T = 150$ K. The positive current and voltage correspond to a reversely biased barrier.

The absorption spectra of crystals with rare-earth impurities contain only the IR band. These crystals are virtually transparent in most of the visible spectrum, with the exception of its long-wavelength portion.

3. SAMPLES AND EXPERIMENTAL PROCEDURE

CdF_2 samples doped with In, Ga, or Y were grown in graphite crucibles by the modified Stockbarger–Bridgman technique. Donor centers in the grown crystals were formed by heating in Cd vapor (additive coloration). In this procedure, electrons localized on dopants or in the conduction band replace interstitial fluorine atoms, which compensate the charge of trivalent impurities. The density *n* of electrons introduced into a crystal during coloration was estimated from the absorption by shallow donor centers in the IR spectral range under the conditions when virtually all the electrons are localized on these centers [10, 11]. Some other methods of determining density were used for the case of In and Ga doping, and similar values were obtained [9, 14]. To investigate the depletion layer characteristics, we chose crystals with a relatively high resistivity. The electron density *n*, equal to the concentration of donor centers, was 4.5×10^{18}, 3×10^{17}, and 1.5×10^{17} cm^{-3} in the CdF_2:In, CdF_2:Ga, and CdF_2:Y samples, respectively. The samples were wafers 1–3 mm thick with polished wide faces. The Schottky barrier was formed with Au electrodes (the work function of Au is ~5 eV; that of CdF_2, ~4 eV [15]). Before the deposition of the Au contacts, the samples were etched in HCl. Ohmic indium contacts were deposited onto the opposite face. When contacts of both types were deposited, the crystals were moderately heated at temperatures that did not cause bleaching (which is observed during heating in vacuum or in air at temperatures >250°C). Thus, the concentration of electrically active impurities in the bulk and on the surface of samples

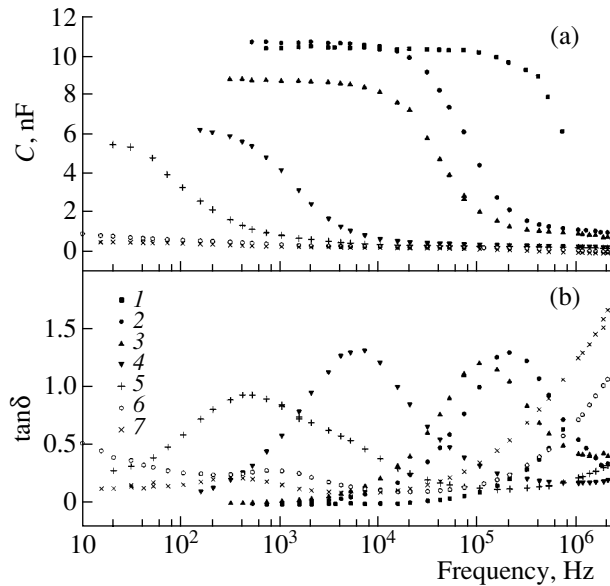**Fig. 2.** RF response of a CdF$_2$:Y crystal ($n = 1.5 \times 10^{17}$ cm^{-3}) with a Schottky barrier. T = (*1*) 297, (*2*) 241, (*3*) 201, (*4*) 120, (*5*) 100, (*6*) 76, and (*7*) 63 K; (a) capacitance, (b) dissipation factor.
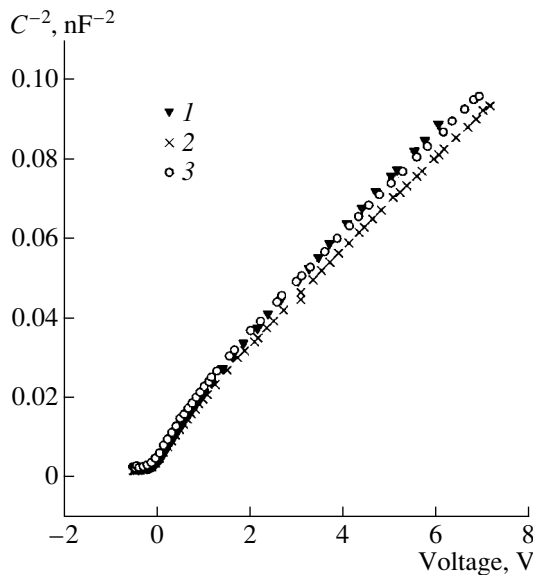

Fig. 3. C–V characteristic of a CdF$_2$:In crystal ($n = 4.5 \times 10^{18}$ cm^{-3}) with a Schottky barrier; $\nu = 1$ kHz; T = (*1*) 246, (*2*) 220, and (*3*) 196 K.

could be considered constant with a good degree of accuracy.

Dielectric measurements were taken using a universal bridge by the method of substituting the sample with a simulator in the frequency range 10–10^6 Hz. The bias voltage was applied to the sample by connecting a voltage source in the diagonal of a bridge. A crystal in an electrometric cell was placed in a UTREX cryostat

in which the temperature was controlled within the limits T = 64–320 K. The I–V characteristics of the samples under study were asymmetric with respect to the sign of the voltage applied (Fig. 1), which indicates the formation of a Schottky barrier at the Au contact. The barrier height at room temperature is estimated as ~1.5 V [16–18]. This barrier determines the resistance of the samples studied under reverse and small forward biases.

4. C–V AND I–V CHARACTERISTICS OF CdF$_2$ CRYSTALS WITH A SCHOTTKY BARRIER

To choose the frequency for studies of C–V characteristics, we measured the temperature and frequency dependences of impedance for CdF$_2$:In, CdF$_2$:Ga, and CdF$_2$:Y samples with the contacts described above. Figure 2 shows the example of the RF response of a CdF$_2$:Y crystal, where two features can be distinguished in the frequency dependence: two steps in the capacitance (Fig. 2a) and corresponding peaks in the dissipation factor (Fig. 2b).[1] These features shift to a higher frequency as the temperature rises. This behavior of the RF response is usually attributed to the effect of two donor levels with different binding energies [19]. This interpretation contradicts the fact that there is only one hydrogen-like donor level in a CdF$_2$:Y crystal. Similar behavior is observed in the frequency dependences of impedance for crystals with DX-centers, CdF$_2$:In and CdF$_2$:Ga; their spectra also demonstrate two, and at some temperatures even three, features. As shown in [9, 20], the high-frequency feature in a CdF$_2$:In crystal is associated with the interface between the depleted layer and the bulk; it corresponds to the Fermi level intersection with the shallow center level. Presumably, the high-frequency feature in CdF$_2$:Ga and CdF$_2$:Y crystals is of the same nature. The present study did not aim to identify all the features in the impedance spectra for the crystals studied, but rather concentrated on the low-frequency feature, since it characterizes the depleted layer region in which donors are ionized to the maximum extent (see Introduction).

C–V characteristics were recorded at the frequency ν corresponding to the low-frequency step in the $C(\nu)$ dependence. In all the samples under study, the $C^{-2}(V)$ dependences are S-shaped, which indicates the nonuniformity of the space-charge region (Figs. 3–5); this behavior is most prominent in the CdF$_2$:Y crystal (Fig. 5). With a certain degree of conventionality, these dependences can be divided into three portions that have different dC^{-2}/dV slopes: portion 1 corresponds to the region of small forward bias 0.1–0.5 V; portion 2, small reverse bias <1 V; and portion 3, high reverse bias >2 V. The concentrations N_d corresponding to these three portions at $T \approx 200$ K are listed in Table 1. The maximum N_d values are obtained for portions 1; the minimum, for portions 2. All these values are on one to

---

[1] The geometrical capacitance of the sample is on the order of a picofarad.
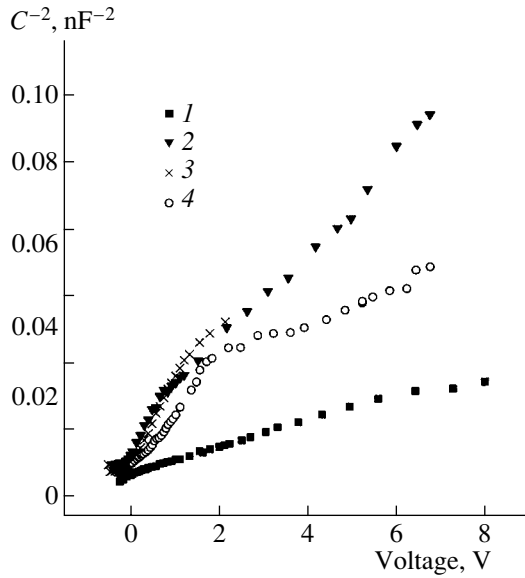
Fig. 4. $C–V$ characteristic of a CdF$_2$:Ga crystal ($n = 3 \times 10^{17}$ cm^{-3}) with a Schottky barrier; $\nu = 60$ Hz; $T = (1)$ 295, (2) 248, (3) 222, and (4) 210 K.

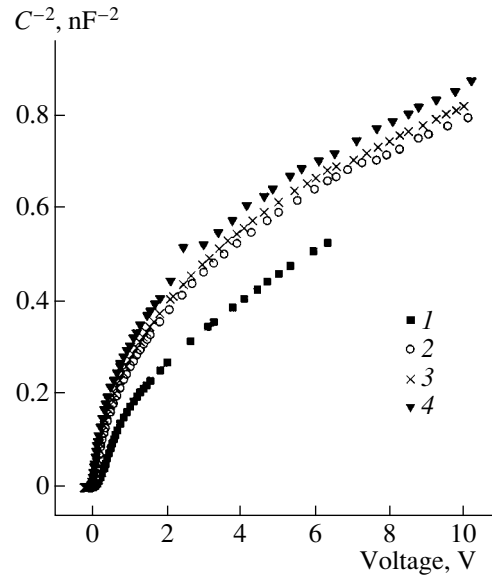**Fig. 5.** $C–V$ characteristic of a CdF$_2$:Y crystal ($n = 1.5 \times 10^{17}$ cm^{-3}) with a Schottky barrier; $\nu = 500$ Hz; $T = (1)$ 245, (2) 200, (3) 160, and (4) 121 K.

three orders of magnitude smaller than the "optical" (bulk) electron densities n in the corresponding samples (see Section 3). In all cases, the N_d values determined from $C–V$ characteristics have a weak temperature dependence, which increases slightly as one approaches room temperature. Note that N_d must be completely temperature-independent for the situations described by Eqs. (1) and (2).

Table 2 presents typical thicknesses w calculated using Eq. (1) for several biases. The thicknesses vary in limits from several tenths of a micrometer to several micrometers; therefore, the surface states cannot be invoked to account for features in the response and $C–V$ characteristics in the frequency range under study.

If the difference between the concentrations of donor centers in the bulk (n) and in the depletion layer (N_d) are taken into account, it would appear reasonable that, in the latter case, the centers are compensated through the transition of electrons from the metal to the semiconductor, which decreases the effective concentration of ionized donors in the space-charge region. In this case, the two features in the frequency dependence of response in CdF$_2$:Y can be attributed to the depletion of shallow donor centers (the high-frequency feature) and compensation in the depletion layer region adjacent to the metal (the low-frequency feature). The compensation of donors in this region expands it; the higher the degree of donor compensation, the more it expands (Fig. 6).

A plausible mechanism of compensation in the depletion layer is the formation of two-electron excitations Cd^0 in the region adjacent to the metal; their appearance may be stimulated by the modification (rupture) of chemical bonds at the metal–semiconductor interface.

As it is isoelectronic to the deep In$^+$ center, this excitation should be characterized by strong lattice relaxation similar to that in a deep In center (see above). Thus, it should give rise to a short-wavelength absorption band related to its photoionization, similar to the absorption band of deep In$^+$ levels (see Fig. 1 in [12]). The lack of this band in the CdF$_2$:Y absorption spectrum indicates that there are no Cd^0 excitations in the bulk of this semiconductor. They arise only in the

Table 1. Donor concentrations characterizing the depletion layer (N_d) and the crystal bulk (n), as determined from $C–V$ characteristics and optical properties of crystal

Crystal and conditions of ($C–V$)	N_d, cm^{-3}	n, cm^{-3}
CdF$_2$:In	5.70×10^{16} (portion 1)	4.5×10^{18}
($\nu = 1$ kHz, $T = 195$ K)	0.63×10^{16} (portion 2)	
	0.98×10^{16} (portion 3)	
CdF$_2$:Ga	9.0×10^{16} (portion 1)	3.0×10^{17}
($\nu = 60$ Hz, $T = 210$ K)	1.3×10^{16} (portion 2)	
	2.7×10^{16} (portion 3)	
CdF$_2$:Y	9.7×10^{14} (portion 1)	1.5×10^{17}
($\nu = 500$ Hz, $T = 200$ K)	0.41×10^{14} (portion 2)	
	3.8×10^{14} (portion 3)	

Note: Second column lists the portions of $C–V$ characteristics used for N_d determination. In calculations with Eq. (3), $\varepsilon = 8$ was used.
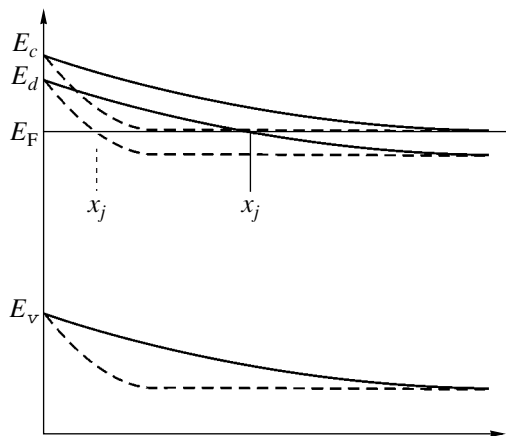
Crystal and the conditions of $(C–V)$ measuring	w, μm
CdF$_2$:In ($\nu = 1$ kHz, $T = 195$ K)	0.21 ($V = 0$)
	0.68 ($V = 4$ V)
	0.84 ($V = 7$ V)
CdF$_2$:Ga ($\nu = 60$ Hz, $T = 210$ K)	0.18 ($V = 0$)
	0.40 ($V = 4$ V)
	0.54 ($V = 7$ V)
CdF$_2$:Y ($\nu = 500$ Hz, $T = 200$ K)	0.90 ($V = 0$)
	5.43 ($V = 4$ V)

region of the depletion layer that is adjacent to the metal.

With a small forward bias, the external field causes an outflow of electrons into the metal and an increase in the capacitance because of the decreasing thickness of the depletion layer, and the barrier field increases. When it passes to negative bias, the current across the crystal drops sharply and the capacitance decreases because of the increase in the thickness of the layer. In this situation, the electric field in the barrier is stabilized at 10^4–10^5 V/cm. Under the effect of this field, Cd^0 excitations that form on the crystal surface transfer electron pairs from the surface to a considerable part of the depletion layer.
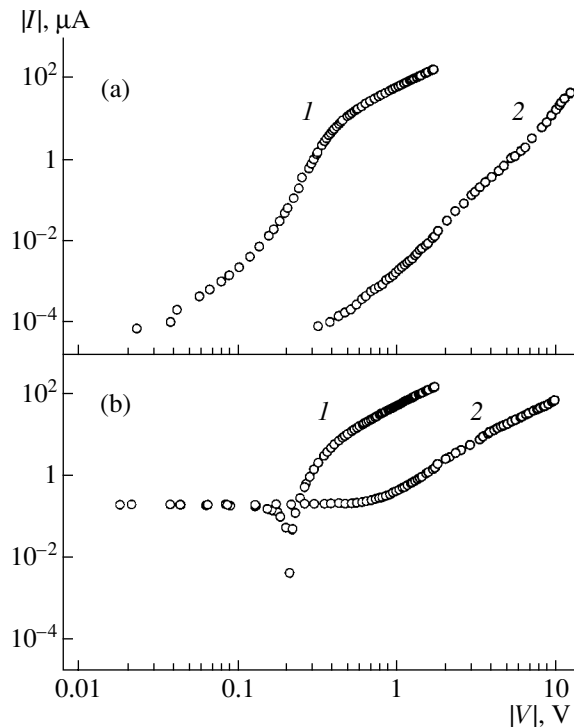
It is precisely these excitations that are responsible for the current in the reverse $I–V$ characteristic (Fig. 1). Their sensitivity to short-wavelength light suggests that the $I–V$ characteristic strongly depends on the crystal illumination due to the occurrence of photovoltage. The mechanism of photovoltage formation may be presented as follows. Photons absorbed by strongly

relaxed Cd^0 states excite electrons to the conduction band. These electrons outflow into the crystal bulk under the effect of the Schottky barrier field, and Cd^0 excitations destroyed by the light are replaced by new ones generated in the atomic layers of the semiconductor in direct contact with the metal.

Figure 7 shows $I–V$ characteristics of a CdF$_2$:Y crystal (a) in the dark and (b) illuminated by a 436-nm line of a DRSh-250 high-pressure mercury lamp. The dark and light characteristics virtually coincide under forward bias $V > 0.3$ V. At $V \approx 0.2$ V, the bias applied to the illuminated sample is compensated by photovoltage, and the current drops sharply. As the forward bias further decreases and subsequently passes to reverse bias, the current stabilizes. In this range of biases it is determined by photovoltage, and all the electrons excited by light are pulled out from the depletion layer into the bulk. Under reverse bias $|V| > 0.5$ V, an avalanche rise in both dark current and photocurrent is observed. The photocurrent is generated by light of nearly the whole visible range, with the exclusion of its long-wavelength portion; it is not generated by $\lambda > 1$ μm illumination, while the crystal bulk containing shallow donor centers is sensitive to this light.

In principle, another source of photovoltage is possible, specifically, the photoemission of electrons from the metal to the semiconductor. This assumption, however, is inconsistent with the behavior of photocurrent

Fig. 6. Energy band bending at the metal–n-semiconductor contact for (dashed line) weak and (solid line) strong donor compensation; x_j is the coordinate of the Fermi level E_F intersection with the donor level E_d.

Fig. 7. $I–V$ characteristic of a CdF$_2$:Y crystal ($n = 1.5 \times 10^{17}$ cm^{-3}) with a Schottky barrier; (a) in the dark, (b) illuminated with a 436-nm line of a high-pressure mercury lamp; (*1*) forward bias, (*2*) reverse bias; $T = 210$ K.

relaxation after the illumination is switched off: at first, the current drops sharply, and then over a long time interval (up to several hours) it decreases to the dark value. Photoemission is incompatible with such a residual effect.

5. CONCLUSION

Studies of dielectric response, *C–V* and *I–V* characteristics of CdF_2 semiconductor crystals with a Schottky barrier, reveal a series of specific features that might appear strange at first glance. The dielectric response behavior indicates the presence of a structure in the depletion layer that should not exist in a semiconductor with only one donor level (CdF_2:Y). The concentration of ionized donors, which is determined from *C–V* characteristics at a frequency that should have allowed all the donor centers to be observed, turns out to be one to three orders of magnitude smaller than the donor concentration in the crystal bulk. The conduction observed when reverse bias is applied cannot be related to minority carriers in a CdF_2 crystal, which has an exceedingly wide (7.8 eV) band gap. These specific features can be accounted for if we assume that donors in the depletion layer are compensated by electron pairs generated by a golden electrode. These pairs are localized on Cd^{2+} ions, which are thus converted to Cd^0 excitations. The formation of these excitations, accompanied by a considerable relaxation of the crystal lattice, is apparently caused by a modification of chemical bonds. The electric field of the barrier stimulates the diffusion of these excitations to a depth determined by their lifetime. Thus, two regions are present in the depleted region: one adjacent to the contact, in which these excitations are formed and carry a charge, and a more distant one that is free of these excitations, as is the crystal bulk. Cd^0 excitations are responsible for the conduction in a crystal when reverse bias is applied. The lattice relaxation associated with Cd^0 excitations is similar to the relaxation of an isoelectronic In^+ state (deep state of an In center). The presence of these excitations in the depletion layer determines its sensitivity to short-wavelength light, including the case of a CdF_2:Y crystal, which is virtually transparent in this spectral range. The disintegration of Cd^0 excitations by a short-wavelength light stimulates their formation at the contact and generates photovoltage.

In CdF_2:In and CdF_2:Ga crystals, the compensation in the depletion layer and in the bulk occurs via deep (*DX*) centers, which are more stable than Cd^0 excitations. However, the existence of the latter is of fundamental importance in this case also, because they provide the transport of electron pairs from the metal to impurity ions.

In conclusion, we note that the structure of the depletion layer in the crystals under consideration is rather complex, and its detailed analysis is beyond the scope of this paper. This study concerns that region in the depletion layer in which complete ionization of the impurity atoms should have occurred. However, as the present study has demonstrated, a compensation mechanism limiting the electric field in the barrier region is operative in this part of the depletion layer.

REFERENCES

1. I. Balberg, J. Appl. Phys. **58**, 2603 (1985).
2. P. N. Brunkov, A. A. Suvorova, N. A. Bert, *et al.*, Fiz. Tekh. Poluprovodn. (St. Petersburg) **32**, 1229 (1998) [Semiconductors **32**, 1096 (1998)].
3. F. Nrautweiler, R. Moser, and R. P. Khoshla, J. Phys. Chem. Solids **29**, 1869 (1968).
4. J. E. Dmochowski, W. Jantsch, D. Dobosz, and J. M. Langer, Acta Phys. Pol. A **73**, 27 (1988).
5. A. S. Shcheulin, A. I. Pyskin, K. Swialek, and J. M. Langer, Phys. Lett. A **222**, 107 (1996).
6. A. I. Ryskin and P. P. Fedorov, Fiz. Tverd. Tela (St. Petersburg) **39**, 1050 (1996) [Phys. Solid State **39**, 943 (1996)].
7. D. E. Onopko and A. I. Ryskin, Phys. Rev. B **61**, 12952 (2000).
8. C. H. Park and J. D. Chadi, Phys. Rev. Lett. **82**, 113 (1999).
9. A. S. Shcheulin, A. K. Kupchikov, A. E. Angervaks, *et al.*, Phys. Rev. B **63**, 205207 (2001).
10. F. Moser, D. Matz, and S. Lyu, Phys. Rev. **182**, 808 (1969).
11. J. M. Kanger, T. Langer, G. L. Pearson, *et al.*, Phys. Status Solidi B **66**, 537 (1974).
12. S. A. Kazanskii, A. I. Ryskin, A. S. Shcheulin, *et al.*, Physica B (Amsterdam) **308–310**, 1035 (2001).
13. R. A. Linke, A. S. Shcheulin, A. I. Ryskin, *et al.*, Appl. Phys. B: Lasers Opt. **72**, 677 (2001).
14. A. I. Ryskin, A. S. Shcheulin, E. V. Miloglyadov, *et al.*, J. Appl. Phys. **83**, 2215 (1998).
15. B. A. Orlowski and J. M. Langer, Acta Phys. Pol. A **63**, 107 (1983).
16. R. Mach and E. U. Messerschmidt, Phys. Status Solidi A **42**, K187 (1977).
17. J. Garbarczyk, B. Krukowska-Fulde, T. Langer, and J. M. Langer, J. Phys. D: Appl. Phys. **11**, L17 (1978).
18. A. Singh, Solid-State Electron. **26**, 815 (1983).
19. L. S. Berman and A. A. Lebedev, *Deep-Level Transient Spectroscopy of Semiconductors* (Nauka, Leningrad, 1981).
20. A. I. Ritus, A. V. Pronin, A. A. Volkov, *et al.*, Phys. Rev. B **65**, 165209 (2002).

Translated by D. Mashovets

Formation of Ohmic Contacts on Semi-Insulating GaAs by Laser Deposition of In

V. Kazlauskienė[1], V. Kažukauskas[2]*, J. Miškinis[1], A. Petravičius[1], R. Pūras[2], S. Sakalauskas[2],
J. Sinius[1], J.-V. Vaitkus[1, 2], and A. Žindulis[1, 2]**

[1]*Vilnius University, Faculty of Physics, Institute of Materials Science and Applied Research, 2040 Vilnius, Lithuania*
[2]*Vilnius University, Faculty of Physics, 2040 Vilnius, Lithuania*
*e-mail: vaidotas.kazulauskas@ff.vu.lt
**e-mail: antanas.petravicius@ff.vu.lt
Submitted April 10, 2003; accepted for publication April 21, 2003

Abstract—A method for producing ohmic contacts on semi-insulating GaAs by laser ablation with subsequent laser deposition of In is proposed. The contacts are formed at room temperature; thus, the high-temperature annealing used in other technologies is excluded. The ohmic properties of the contacts are retained in a range of currents that is several orders of magnitude wide, regardless of the direction of current. The electric potential is distributed linearly along the sample, and the current is limited only by the bulk resistivity of the material itself. The method is promising for the formation of high-precision arrays of ohmic contacts that penetrate the whole thickness of the sample in the fabrication of microelectronic devices. © 2004 MAIK "Nauka/Interperiodica".

1. INTRODUCTION

The formation of ohmic contacts on semi-insulating GaAs is a topical problem in the fabrication of a number of practically important electronic devices, particularly, radiation detectors. Currently, the deposition of Sn–Ge–Au, Au–Ge–Ni, or Pd–Ge layers by thermal evaporation with subsequent annealing is used to fabricate ohmic contacts. This technology includes several deposition stages and a high-temperature (>300°C) annealing. Moreover, this method produces planar contacts (electrodes), though in many cases contacts that extend all the way through the crystal bulk would be more appropriate. Modern laser technology allows for high-precision processing of materials, including the "drilling" of small-diameter (less than 50 μm) openings in a semiconductor wafer. It would be practically promising to form ohmic contacts in such openings to produce groups of devices with minimum mutual interference and leakage currents. No practically applicable technology for fabricating electrodes of this type has yet been proposed. Laser annealing by low-power pulses was used to restore the crystal structure of III–V semiconductors after ion implantation [1]. The application of high-power laser irradiation for GaAs treatment has been less successful, because the surface stoichiometry is modified.

The goal of the present study is to determine how stable ohmic In contacts on semi-insulating GaAs can be fabricated using laser annealing, laser etching (ablation), and laser evaporation.

2. EXPERIMENTAL

Indium was chosen as the material for ohmic contacts on semi-insulating GaAs owing to its physical properties. As an isovalent impurity in GaAs, it reduces the concentration of dislocations and other defects [2] and thus improves the conditions of charge carrier transport. Because of the isovalency of In, a fundamental difference exists between In/GaAs and other types of contacts, e.g., AuGe/GaAs. In the latter case, the contact is ohmic owing to n^+ doping of the near-contact region. In contrast, the introduction of In atoms into the contact region does not produce n^+ doping; therefore, the contact is ohmic owing to some other mechanism. As shown in [3, 4], a graded InGaAs junction is formed in this case. Such junctions were produced by MBE [5]. The formation of a graded junction with an ohmic contact was also confirmed in [6], but in this case the contacts were produced by ion-beam sputtering, so that thermal annealing at 375°C was necessary to obtain ohmic properties. We have set ourselves the task of excluding high-temperature annealing by applying laser irradiation. This is favored by the low melting temperature of In, which allows one to reduce the necessary laser power and thus significantly reduce the probability of uncontrollable crystal damage. Mechanically, In is rather a strong material and is suitable for the production of a stable joint between a crystal and Au or Al contact wires.

In order to produce electrodes and study contact properties, several technological procedures and methods have been used. First, In electrodes were deposited onto a chemically cleaned GaAs surface by standard high-vacuum thermal evaporation. To improve the
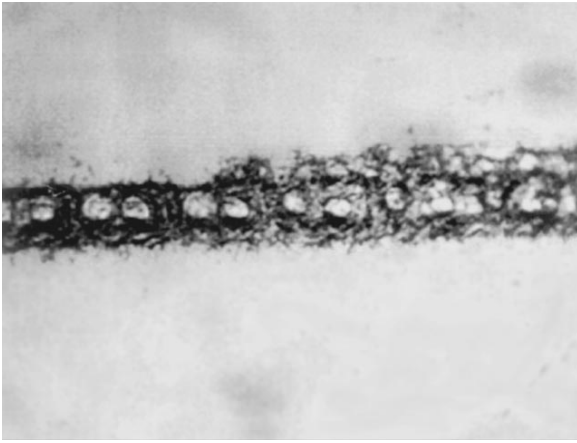
Fig. 1. A micrograph of a GaAs surface in the vicinity of a contact groove produced by laser ablation. The right half of the groove is covered with In by laser evaporation. The diameter of the laser beam trace is ~100 μm. The bright area around the whole laser-treated surface is the thermally recrystallized surface of GaAs.

Fig. 2. Distribution of the concentration of chemical elements in the contact and near-contact regions. The distance is measured from the edge of the GaAs wafer. (a) Distribution of In: the points and dashed line are the experimental data; the solid line is the Gaussian distribution. (b) Distributions of other defined elements.

mechanical strength of the electrodes, the In layers were covered with thicker layers of Cr or Al. Electrodes fabricated in this way were unstable, and their current–voltage ($I–V$) characteristics were nonlinear. Thus, to accelerate the diffusion of In into GaAs and improve the electrical properties of the contact, we used intermediate low-temperature (120°C) thermal or laser annealing. The properties of these contacts were compared with the properties of contacts produced by laser evaporation of In and its deposition onto a locally etched (by laser ablation) surface of a GaAs crystal. Laser ablation of GaAs was performed by pulses of the second harmonic of a Nd:YAG laser ($\lambda = 532$ nm, pulse width 30 ns, peak energy 6 J/cm^2). The beam was focused onto a spot 50 or 100 μm in diameter (the irradiation intensity was reduced when necessary). Prior to contact formation, the GaAs surface was cleaned chemically and by ion-beam milling for 45 min. Then, the contact area was subject to etching (by laser ablation) and an In layer was deposited from a glass plate covered with In. Figure 1 shows traces of the impact of the laser on the GaAs surface after etching and In deposition. It was necessary to perform this procedure with a precisely adjusted laser intensity[7], because with excessive power In was spattered over the plate surface in the form of separate droplets. We have also tried to produce electrodes without preliminary laser treatment of the GaAs surface; In was simply deposited by evaporating it from a glass plate with a high-intensity beam, but this also led to In spattering. After the deposition of the In layer onto the surface pretreated with laser ablation, an additional In layer of ~50 nm in thickness was deposited to improve the electrical and mechanical properties of the contacts, and it was covered with a thick Al layer to improve its mechanical strength. The distribution of elements in the contact region was ana-
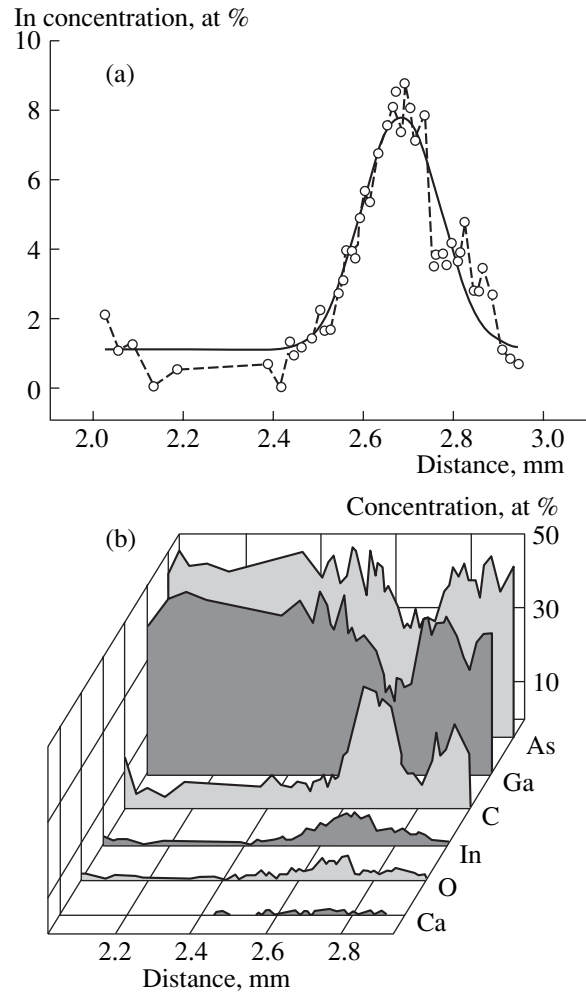
lyzed by Auger spectroscopy. The electrical properties of contacts were studied by measuring $I–V$ characteristics and the surface potential distribution. The surface potential was measured by the no-contact capacitance method [8], the essence of which is as follows. A charge is induced in the testing microelectrode, which vibrates immediately above the surface area studied. The magnitude of this charge, which is defined by the local properties of the surface, is transformed into ac voltage. Further processing of this signal and the use of 100% negative feedback automatically provides a self-compensation mode, which improves the metrological characteristics of the measuring device.

3. RESULTS AND DISCUSSION

Figure 2 shows the profiles of the distribution of chemical elements in the contact region, including the
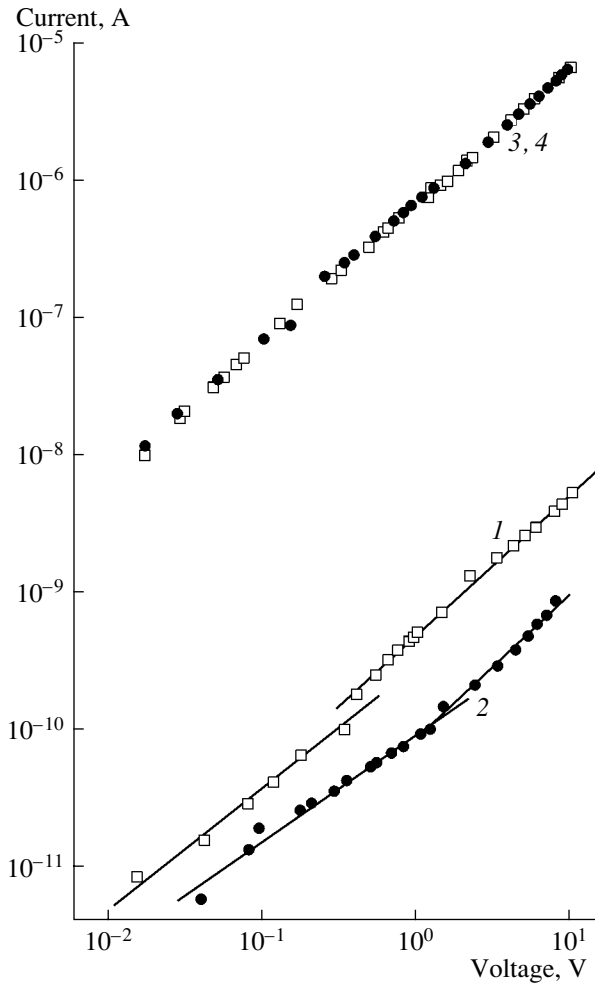
Fig. 3. *I–V* characteristics for (*1*, *3*) forward and (*2*, *4*) reverse bias. Contacts were produced by (*1*, *2*) thermal evaporation and (*3*, *4*) laser evaporation.
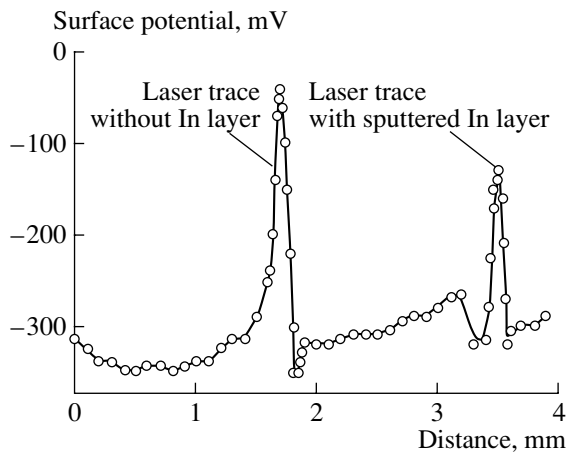

Fig. 4. Distribution of surface potential along a sample with two transverse grooves etched by laser ablation at places where the electrodes are formed: the left groove is not covered with In; the right was covered with In by laser pulse deposition in a high vacuum.

contact groove etched by laser pulses on the GaAs surface. As can be seen in Fig. 2a, In is distributed according to the Gauss law, most likely because of the corresponding distribution of intensity in the laser beam. The significant fluctuation deviations are due to the difference in size of the ablation craters, which form as a result of irradiation by laser pulses. A similar distribution is observed for other easily adsorbed impurities—C, O, and Ga (Fig. 2b)—which presumably appeared during treatment of the crystal, for example, from the residual gases in the vacuum system, or were brought together with the indium from the glass plate, the intermediate source of In. These impurities are not removed by the cleaning flow of Ar ions.

Figure 3 shows the *I–V* characteristics of samples fabricated by the two methods described above. As can be seen, laser treatment significantly improves the ohmic properties and reduces the contact resistance. Usually, the *I–V* characteristics of contacts deposited without additional thermal treatment are strongly asymmetric owing to the strong influence of the potential barrier in the contact region. At the same time, estimating the potential barrier energy is a complicated task, because the contacts are not clearly pronounced Schottky barriers, their *I–V* characteristic is linear on a log-log scale with a slope of 0.75–0.8. The resistance of such contacts at small (up to 0.1 V) bias was $(2.6-3.3) \times 10^9$ Ω. At a high bias, *I–V* characteristics are linear, which is indicative of the influence of the ohmic resistance of the contact region itself, because the current remains significantly lower than in the case of contacts formed with laser treatment of GaAs. A characteristic step and a change in the slope are observed at smaller biases. Most probably, this can be attributed to the breakdown of a thin potential barrier at the surface, which is caused by surface states directly at the metal–semiconductor interface. This effect should be enhanced in a semi-insulating material with nonuniform In distribution over the surface due to the spatially nonuniform compensation of defects in GaAs with In.

Contacts fabricated by our technology, including laser ablation and In deposition, remain ohmic and have a bias and current that varies within three orders of magnitude; the current is limited only by the bulk resistance of the sample (~1.5×10^6 Ω, which is typical of high-resistivity GaAs). When the samples are strongly illuminated, photovoltage is observed, which indicates the existence of a potential barrier. The negative sign of photovoltage appears at the electrode that was enriched with indium during laser deposition. In semi-insulating samples, the photovoltage was ~150 mV, and it decreased as the GaAs conductivity increased. This is consistent with the known fact that fluctuations of band edges (potential profile) with nearly the same magnitude are formed in semi-insulating GaAs [2] and are screened by free carriers that appear through generation or doping.
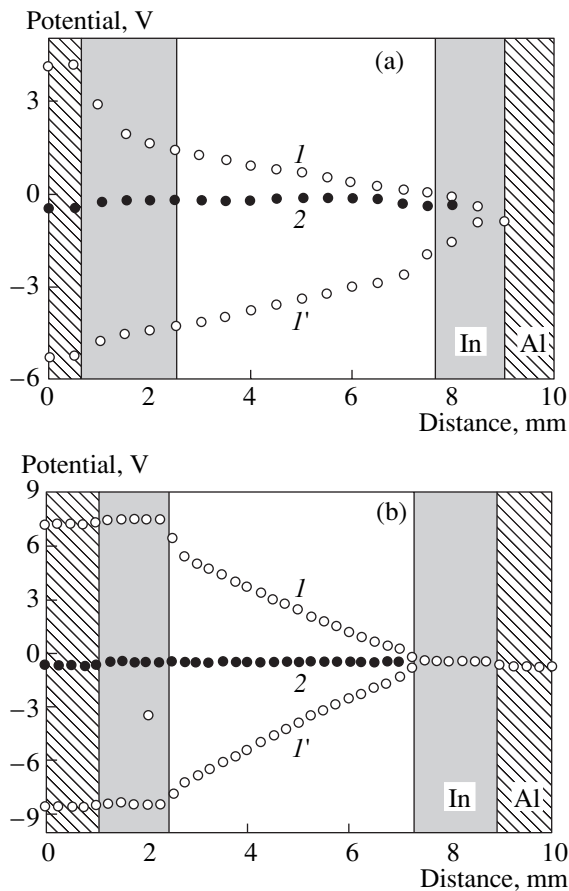
Fig. 5. Distribution of surface potential along a sample with contacts produced by (a) thermal and (b) laser deposition of In. (*1*, *1'*) correspond to the two polarities of the applied bias; (*2*) corresponds to zero bias. The distance is measured from the left edge of the crystal. The geometry of a sample with two electrodes at both ends (front view) is shown schematically. Some portions of the In layer (near the edges of the sample) are covered with Al to improve their mechanical strength.

Measurements of the distribution of the surface potential along the sample (Fig. 4) demonstrated that the surface potential barrier changes as a result of In deposition in the regions subjected to laser treatment. As can be seen, the deposition of In into the groove formed by laser ablation significantly reduces the barrier. Figure 5 shows the potential distribution along the samples with contacts fabricated by thermal evaporation (Fig. 5a) and laser-pulse deposition of In (Fig. 5b). It can be seen that, in the first case, the potential distribution remains asymmetrical with different directions

of the applied electric field, like the *I–V* characteristics. A specific feature of these contacts is that the potential also changes on a crystal surface covered with an In layer. This effect is presumably related to the nonuniform "islandlike" distribution of indium during the deposition of a thin In layer, so that barriers are formed between GaAs and this layer. These data are in good agreement with the formation of contact barriers described above, which affect the run of the *I–V* characteristics.

In the case of In deposition onto laser-etched areas, the quality of contacts is much better: the potential distribution along the sample is linearized, and it becomes symmetrical in respect to the electric field direction. An insignificant potential step is seen only near the interface with the In contact, where the GaAs surface is recrystallized as a result of the laser annealing. The recrystallized region in the vicinity of the ablation zone is seen as a brighter halo in Fig. 1.

4. CONCLUSION

A method for the formation of ohmic contacts on high-resistivity GaAs is suggested, which includes laser etching of the surface and In deposition. The contacts produced in this way exhibit ohmic behavior in a wide range of currents, regardless of the bias polarity. The distribution of the electric potential along the sample length is linear. This method is promising for the formation of precise grids of ohmic contacts that pass through the whole thickness of the crystal in the production of microelectronic devices and elements.

REFERENCES

1. G. Vitali, I. Palumbo, M. Rossi, *et al.*, Phys. Rev. B **53**, 4757 (1996).
2. V. Kažukauskas, J. Storasta, and J.-V. Vaitkus, Phys. Rev. B **62**, 10882 (2000).
3. A. Lakhani, J. Appl. Phys. **56**, 1888 (1984).
4. T. Sebestyen, Solid-State Electron. **25**, 543 (1982).
5. J. M. Woodall, J. L. Freeouf, G. D. Pettit, *et al.*, J. Vac. Sci. Technol. **19**, 626 (1981).
6. D. W. Davies, D. V. Morgan, and H. Thomas, Semicond. Sci. Technol. **14**, 615 (1999).
7. V. Kazlauskienyė, V. Kažukauskas, J. Miškinis, *et al.*, J. Phys. **41**, 357 (2001).
8. S. Sakalauskas and A. Sodeika, Rev. Sci. Instrum. **69**, 466 (1998).

Translated by D. Mashovets

SEMICONDUCTOR STRUCTURES, INTERFACES, AND SURFACES

The Investigation of Structural Perfection of $Cd_xHg_{1-x}Te$/CdZnTe Epitaxial Layers by the Raman Scattering Method

A. I. Belogorokhov*, I. A. Denisov*, N. A. Smirnova*, and L. I. Belogorokhova**

*Scientific Research Center of the Russian Federation Institute of Rare Metals,
Bol. Tolmachevskii per. 5, Moscow, 119017 Russia
e-mail: belog@mig.phys.msu.ru
**Faculty of Physics, Moscow State University, Vorob'evy gory, Moscow, 119899 Russia
Submitted April 21, 2003; accepted for publication April 23, 2003

Abstract—The distribution and character of variations in the intensity of lattice vibrations that are induced by structural defects of various nature over the layer depth of $Cd_xHg_{1-x}Te$/CdZnTe epitaxial structures are investigated. The results are discussed in detail. Experimental results are obtained by the Raman scattering method in a micromode over the cleaved surface of the sample formed normally to the [111] face immediately prior to measurements. Special attention is paid to the possibility of obtaining information on the presence of structural defects in the cation sublattice and tellurium precipitates in $Cd_xHg_{1-x}Te$ epitaxial layers. © *2004 MAIK "Nauka/Interperiodica".*

1. INTRODUCTION

Liquid-phase epitaxy has been successfully used to obtain $Cd_xHg_{1-x}Te$/CdZnTe heterostructures of various compositions over the last thirty years. As a rule, in most cases it is of interest to investigate the concentration profile of material components and/or residual and doping impurities over the thickness of an epitaxial layer (epitaxial layer), as well as electrical, optical, and other properties of the semiconductor structure grown. Considerably less information is available on the distribution of structural defects over the layer thickness. These are tellurium precipitates, antisite defects, and inclusions of different nature. Scanning or transmission electron microscopy is usually used for such investigations [1]. The Raman scattering method has practically not been used for these purposes, since it is not a local method of analysis in a conventional variant. The use of an optical microscope in a setup (the so-called micro-Raman method of recording the spectra) allows one to apply it in studying the distribution of structural defects over the thickness of the $Cd_xHg_{1-x}Te$ epitaxial layer [2]. Such information is very important for assessing the quality of the material and for predicting the properties of a device fabricated based on the structure grown. Raman scattering is most sensitive to variations in the vibrational properties of crystals, which are controlled, specifically, by the structural imperfections in a sample. Therefore, we used this method to study the structural quality of the $Cd_xHg_{1-x}Te$ epitaxial layers.

An analysis of the available published data shows that inclusions of a second phase based on Te, Hg, or Cd are present to some extent in single-crystal samples of p-$Cd_{1-y}Zn_yTe$ and p-$Cd_xHg_{1-x}Te$ solid solutions. Local agglomerates that differ from the other part of the crystal in composition and tellurium precipitates can also take place. Inclusion sizes can vary over a wide range from 3 to 50 μm. After etching in the structure-selective etchant, inclusions of the second phase are observed as pits with a characteristic dislocation rosette around them [3]. The existence of similar inclusions and tellurium precipitates is confirmed using the methods of X-ray diffraction, Auger spectroscopy for CdTe [4], infrared (FTIR) spectroscopy for CdZnTe [4–6], and Raman spectroscopy for bulk $Cd_xHg_{1-x}Te$ [7].

It is assumed that large (3–50 μm) Te-based inclusions are caused by concentration supercooling of the melt during crystal growth both due to the deviation of the melt composition from stoichiometry and because of an unfavorable combination of growth conditions. The emergence of inclusions can be caused by rapid cooling of the solid solution to room temperature and by the retrograde character of Te solubility in the solid phase. The density of such inclusions can be decreased to a few inclusions per ~1 cm² of sample area by selecting the optimal temperature conditions of growth and subsequent thermal treatment of $Cd_xHg_{1-x}Te$ and $Cd_{1-y}Zn_yTe$. A considerable decrease in the density of inclusions can be attained by providing the smallest possible excess of Te (relative to stoichiometry) in the composition of the melt and by decreasing the degree of overheating of the melt.

It is known that additional resonance peaks, which correspond to phonon modes of a lattice of a particular Te modification, are present in the Raman spectra of $Cd_xHg_{1-x}Te$ crystals that contain Te precipitates [7]. The problem of detecting Te precipitates and analyzing their distribution over the sample thickness is still of relevant interest.

2. EXPERIMENTAL

The p-$Cd_xHg_{1-x}Te$ ($0.21 < x < 0.23$) epitaxial layers grown on $Cd_{0.96}Zn_{0.04}Te$ (111) substrates by liquid-phase epitaxy (LPE) in a sealed quartz cell from Te-based solution-melts were investigated. In contrast to bulk $Cd_xHg_{1-x}Te$, no inclusions of the second phase were found after selective etching of epitaxial layers. This is associated with the fact that the temperature of epitaxial growth is below the growth temperature for bulk $Cd_xHg_{1-x}Te$ and below the point of the highest retrograde solubility of Te (630°C).

The $Cd_{0.96}Zn_{0.04}Te$ (111) substrates were cut from crystals grown by the Bridgman–Stockbarger vertical method using a near-stoichiometric melt. After grinding and chemical–mechanical polishing, the samples were 30–50 mm in diameter and 750 ± 50 μm thick. The structural quality of the CdZnTe samples was investigated using metallographic methods. The dislocation density in the $Cd_{0.96}Zn_{0.04}Te$ substrates used by us was $N_d \leq 4 \times 10^4$ cm^{-2}; twins and inclusions of the second phase were absent.

The secondary-ion mass spectroscopy (SIMS) results (Perkin-Elmer PHI 550) enabled us to conclude that no residual impurities were found in the epitaxial layers. Electrical parameters were measured at room temperature and at liquid-nitrogen temperature by the van der Pauw method. The Hall coefficient was measured with the induction of a magnetic field of 1.5 T, and resistivity was measured with a switched off magnetic field. For as-grown samples, at $T = 77.3$ K, the hole density was $(1.0–2.0) \times 10^{17}$ cm^{-3}, and the mobility was ~300 cm^2 V^{-1} s^{-1}. To decrease the carrier density to a level of $(0.5–2.0) \times 10^{16}$ cm^{-3}, the samples were thermally treated in saturated Hg vapors. However, in some cases, we did not manage to decrease the hole density in the epitaxial layers to the magnitude required. The parameters of some epitaxial layers are given in Table 1. To carry out the study, we chose three samples with an approximately identical composition to facilitate the procedure of identifying resonance peaks in the Raman spectra. These samples differed in free-carrier density.

The Raman spectra were obtained in the geometry of photon backscattering with pumping by an Ar$^+$ laser at wavelengths of 488 and 514.5 nm. The setup included a Jobin-Yvon T64000 double monochromator and a GaAs photomultiplier cooled to 78 K. To investigate the microstructure of the samples, an Olympus metallographic microscope was used. In this case, the laser beam was focused on the surface of the sample in a spot 2 μm in diameter. Optical spectra were detected on a freshly cleaved surface of the sample from the epitaxial layer to the substrate with a step of 2 μm. Several measurements were made on the substrate itself. To avoid irreversible thermal effects on the sample or its degradation, the sample was cooled to 85 K, and the pumping power of the Ar$^+$ laser was varied from 1 to 10 mW. Thus, the power density of laser emission at the

Table 1. Parameters of epitaxial layers in $Cd_xHg_{1-x}Te/Cd_{0.96}Zn_{0.04}Te$ structures

Sample number	Composition x	Conductivity type	Hole concentration 10^{16} cm^{-3} ($T = 77.3$ K)	Layer thickness, μm
2–4	0.217	p	1.6	30
5–1	0.229	p	6.4	30
8–2	0.212	p	16	28

material surface was as high as 30–140 kW/cm^2. The surface degradation and other irreversible processes in the samples investigated were observed with densities of laser radiation that were an order of magnitude higher than the energy used for the detection of the Raman spectra. A CCD camera combined with a microscope allowed one to visually observe on a monitor the state of the object's surface during the detection of the Raman spectra. In some cases, measurements were repeatedly carried out at the same point of the sample to make sure that the results of the measurements were completely reproducible and that there were no variations in spectral dependences.

3. RESULTS AND DISCUSSION

For materials with a zinc blende structure, specifically, for $Cd_xHg_{1-x}Te$ with an orientation $\langle 111 \rangle$ and $\langle 122 \rangle$, longitudinal LO and transverse TO optical modes of lattice vibrations, according to selection rules, manifest themselves in the Raman spectra. For other configurations, scattering of photons by longitudinal vibrations can occur only in the case of some distortions of the crystal structure, which may be caused, for example, by the presence of impurity centers and structural defects in the sample. In the first case, Frelich-type vibrational modes also become active. These modes manifest themselves along with the vibration modes allowed by the selection rules. For $Cd_{0.25}Hg_{0.75}Te$, the frequencies of the main optical phonons should have the following values ($T = 295$ K): $\omega_{TO}^{HgTe} = 119.5$ cm^{-1}, $\omega_{LO}^{HgTe} = 140.5$ cm^{-1}, and $\omega_{LO}^{CdTe} = 158$ cm^{-1}.

The Raman peaks, which are revealed in the region of the first-order active phonon modes of $Cd_xHg_{1-x}Te$, had a complex shape (Fig. 1). In the course of fitting the calculated curve to the experimental one, it became clear that it is possible to find the best result using the procedure of summation of seven Gaussian functions. An example of a similar breakdown of the experimental Raman spectrum into constituent Gaussian components is shown in Fig. 1 for sample 5–1. The spectral position of each of the seven peaks corresponds to a certain resonance vibration in $Cd_xHg_{1-x}Te$ (Table 2). Analysis of the Raman spectra, which were obtained using the radiation of an Ar$^+$ laser at a wavelength of 514.5 cm^{-1}, also provided information on the vibrational spectra of the
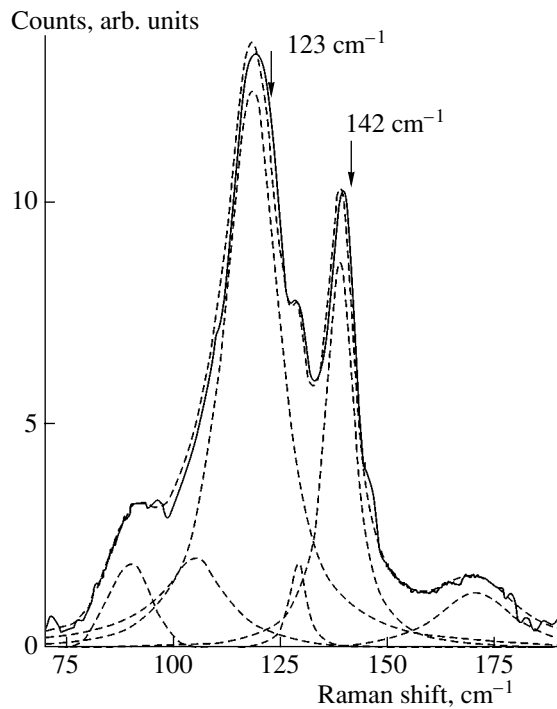
Counts, arb. units

Fig. 1. Raman spectrum of sample 5–1. Dashed lines show the Gaussian curves into which the experimental spectrum was decomposed.

HgTe sublattice. As the composition of $Cd_xHg_{1-x}Te$ varies from $x = 0$ to $x = 0.25$, the energy gap E_1 approaches the energy of radiation of the Ar^+ laser, which operates at a wavelength of 514.5 nm (2.401 eV). Thus, the mode of longitudinal optical vibrations of the HgTe sublattice (LO_{HgTe}), which is forbidden by selection rules, should not emerge in the Raman spectra up to $x = 0.25$. However, such resonance vibration is rather stable in the spectra of the samples investigated. Shyama Rath *et al.* [8] reported similar results for a study of Raman scattering in single-crystal $Cd_xHg_{1-x}Te$ samples. In our case, the emergence of the LO_{HgTe} mode should be expected with a higher degree of probability since epitaxial films were studied, which are known to be of poorer quality compared with bulk $Cd_xHg_{1-x}Te$. The disordering of the crystal structure, which is caused by a particular factor, introduces variations into scattering of photons in actual solid solutions. This causes broadening of resonance peaks and gives rise to vibrational modes, which are forbidden by the selection rules.

It should be noted that two possible identifications of peaks *4* and *6* are noted in Table 2. They are either trigonal Te or Te precipitates. The latter case refers to a region of the crystal several nanometers in size with a high density of atoms of a particular type (or all types combined) in the cation sublattice. This region should comprise an agglomeration of excess Te atoms with respect to the remaining volume of the crystal; the Te atoms are somewhat shifted from their equilibrium state. To determine the magnitude of this shift exactly, it is necessary to carry out additional experiments, preferably using EXAFS spectroscopy. No phase boundary exists between the Te nanoprecipitate and the surrounding region of the crystal. On the one hand, this should affect the spectral positions of the Raman peaks with respect to metal Te. On the other hand, we may assume that the peaks mentioned will be shifted due to elastic strains that emerge in this region of the crystal. In our opinion, the absence of the phase boundary is caused by the absence of the local reconstruction of the crystal structure that occurs in the region of the Te nanoprecipitate. Therefore, the effect of elastic strains will not be so significant. Let us consider the case when the Te atoms agglomerate spontaneously during the cooling of as-grown $Cd_{1-y}Zn_yTe$ or $Cd_xHg_{1-x}Te$ crystals in the form of clusters or phase formations of several micrometers in size. In this case, the pattern will be dif-

Table 2. Frequencies corresponding to resonance peaks in the Raman spectra and assignment of these peaks to vibrational modes of $Cd_xHg_{1-x}Te$

Peak number	Spectral position (cm⁻¹)	Assignment	Reference
1	85	Longitudinal acoustic vibration in the HgTe sublattice	[7]
	90	*E* mode of vibrations of crystalline Te	[4]
2	107–108	Hg atoms at the sites of the Te sublattice (antisite defect)	[11]
	105	Te atoms at the sites of the HgTe sublattice	[8]
	107	Hg vacancies	[7]
3	116.5	TO_{HgTe}	[10]
4	123	Trigonal Te (mode A_1)	[12]
	126	Te precipitates	[4, 7]
5	139.5	LO_{HgTe}	[8]
6	142	Trigonal Te (*E* mode of vibrations)	[7]
	144	Te precipitates	[7]
7	157.5	LO_{CdTe} (TO_{CdTe})	[8]

ferent. The tellurium atoms line up in an order that differs from that of the crystal bulk (and with a different symmetry) and form densely packed chains with their own crystal structure. As a result of this, elastic strains emerge in the boundary layer (inclusion/matrix), whose effect increases as the linear dimension of this inclusion decreases. This is caused by an increase in the ratio of the number of atoms that form the transition layer to the number of atoms that are located in the Te agglomerates. Authors of studies [5, 9] consider that these agglomerates have a trigonal structure. Alternatively, Shin *et al.*, based on the results of X-ray diffraction analysis, concluded that the Te precipitates form a local rhombohedral crystal lattice in CdTe [4]. It should be noted that in the same study [4] additional X-ray diffraction peaks were observed, which may indicate the existence of Te inclusions of other modifications in the sample. We carried out a number of studies to clarify the various Te phases in $Cd_xHg_{1-x}Te$ crystals. These phases are easily distinguishable from the selective etching pattern. In some cases, Te inclusions of the rhombohedral phase occurred, while in other cases inclusions of the trigonal phase occurred. Simultaneously, variations in the corresponding Raman spectra were observed. Thus, we assumed that it is possible to interpret in different ways the nature of the emergence of resonance peaks in the Raman spectra in the region of Te vibrational modes.

In our case, it is possible to exclude completely the presence of any modifications of amorphous Te in the epitaxial layer bulk. First, amorphous Te crystallizes at $T = 280$ K; second, its Raman spectrum is generally similar to the spectral dependence of the total density of vibrational states. In this case, an intense broad peak should be observed in the spectrum at a frequency of 157 cm^{-1}, which is considerably higher than any single-phonon excitation in a Te crystal.

It should be noted that second-order resonance scattering peaks were absent in the experimental Raman spectra for all the samples. Given the power and wavelengths of laser radiation used, we might have expected the emergence of $2TO_{HgTe}$, $2LO_{HgTe}$, $2TO_{CdTe}$, LO_{HgTe} + LO_{CdTe}, and TO_{HgTe} + LO_{HgTe} resonance peaks in the Raman spectra. Similar vibrational modes were observed, but for single-crystal samples [8]. This required that the Raman spectra be detected using prolonged signal integration times and an extremely low scanning rate. In our case, for the $Cd_xHg_{1-x}Te$ samples with composition $x \approx 0.2$, the peaks mentioned should be observed at frequencies ≈233, 279, 315, 297, and 256 cm^{-1}, respectively. Such is the case if we take into account that the vibrational modes of the CdTe sublattice are located at frequencies ($x \approx 0.22$, $T = 85$ K) $\omega_{LO1}(\omega_{TO1}$ [8]) = 157.5 cm^{-1}, whereas the modes of the HgTe sublattice are positioned at frequencies $\omega_{LO2} = 139.5$ cm^{-1} and $\omega_{TO2} = 116.5$ cm^{-1} [10]. Instead of this, in the experimental Raman spectra obtained from the side of the surface, as well as over the cleaved plane in the immediate proximity of the surface of the sample, a peak in the frequency region $\omega \approx 415$ cm^{-1} was observed. Its emergence may be caused by the third-order phonon scattering ($3LO_1$), which seems unlikely at first glance. To reveal the nature of this peak completely, further research is required. Furthermore, as follows from the above, this peak emerged in the Raman spectra from various crystallographic planes. We may assume that the aforementioned peak is related to the combination of LO and TO phonons, which correspond to the Brillouin zone boundary.

The emergence of local vibrations in the experimental optical spectra can be caused by antisite defects, such as the incorporation of Cd atoms into the HgTe sublattice or the emergence of Hg atoms at Cd sites in the CdTe sublattice, and, finally, by antisite Te in one of these sublattices. Frequencies of these vibrations can be calculated using the following relationships for the specific value of x:

$$\omega^2(Cd : HgTe) = \frac{1}{m_{Cd}}(d_{Cd-Te} + d_{Hg-Cd}), \qquad (1)$$

$$\omega^2(Hg : CdTe) = \frac{1}{m_{Hg}}(d_{Cd-Te} + d_{Cd-Hg}), \qquad (2)$$

$$\omega^2(Te : HgTe) = \frac{1}{m_{Te}}(d_{Hg-Te} + d_{Te-Te}), \qquad (3)$$

$$\omega^2(Te : CdTe) = \frac{1}{m_{Te}}(d_{Cd-Te} + d_{Te-Te}). \qquad (4)$$

Here, d_n are the force constants, whose values are the following ($x = 0.22$, $T = 78$ K): $d_{Cd-Te} = 95.4$ N/m, $d_{Hg-Cd} = 95.4$ N/m, $d_{Hg-Te} = 104.8$ N/m [9], $d_{Te-Te} = 68.1$ N/m; and m_n are the masses of the corresponding ions. From the calculations carried out, the following wave numbers of the aforementioned local modes were found: $\omega_{Te:HgTe} = 152.9$ cm^{-1}, $\omega_{Te:CdTe} = 146.9$ cm^{-1}, and $\omega_{Hg:TeTe} = 107.1$ cm^{-1} for $x = 0.22$. The calculation for a single atomic Te–Te pair, for example, in a one-dimensional chain of Te atoms, yields $\omega_{Te-Te} = 179$ cm^{-1} [13].

It should be noted that there are several interpretations as to which particular mode of vibrations Raman peak number *2* belongs. Three possibilities are given in Table 2, two of which are practically opposite. In addition to them, it is possible to add the possibility of scattering photons under a two-phonon combination of the LO–*TA* type in the same spectral range [14]. In this case, it should be taken into account that the frequencies of transverse optical phonons at the *X* and *L* points of the Brillouin zone of $Cd_xHg_{1-x}Te$ ($x \approx 0.2$) are equal to $TA(X) = 29$ cm^{-1} and $TA(L) = 25$ cm^{-1} [15]. Hill pointed out that this vibrational mode (105–108 cm^{-1}) should correspond to Hg vacancies [7]. This mode was observed in the Raman spectra of p-$Cd_xHg_{1-x}Te$ and was not observed in the spectra of n-$Cd_xHg_{1-x}Te$ [7]. In our experiments, this mode was observed at various

energies of laser excitation at wavelengths of 488 and 514.5 cm^{-1} in the *p*-Cd$_x$Hg$_{1-x}$Te epitaxial layers, which were subjected to postgrowth thermal annealing in Hg vapors at $T = 350$°C. As a rule, after such a procedure, the concentration of Hg vacancies decreases, which should suppress the mode at 107 cm^{-1}, if its emergence is caused by these vacancies. It is also necessary to take into account that the frequency of the last of the vibrational modes listed, which was calculated according to Eqs. (1)–(4), coincides with that given in Table 2 (mode *2*). Based on the above, we believe that its presence in the Raman spectra is caused by antisite defects of the Hg$_{Te}$ type [11].

Figures 2a–2c show the spectral position of all the vibrational modes listed in Table 2. The origin of the abscissa scale coincides with the epitaxial layer surface. Accordingly, the Cd$_x$Hg$_{1-x}$Te/CdZnTe interface is located at a distance of 28–30 μm from the epitaxial layer surface. In Figs. 2a–2c, this interface is shown by a vertical straight line. Let us first consider the structural quality of the HgTe sublattice by analyzing the position of the Raman peaks that correspond to its vibrational modes *3* and *5*. In samples 1 and 2 (Figs. 2a, 2b), a similarity is observed in the behavior of the low-frequency and high-frequency vibrational modes of HgTe. Their spectral positions practically coincide with the frequencies of the main optical phonons of HgTe, which are listed in Table 2. There are slight deviations (~0.5–1 cm^{-1}) in the surface (~3 μm) region of the epitaxial layer. In the case of sample 3, such deviations are much larger, ~1–2 cm^{-1} for TO$_{HgTe}$ and ~1–3 cm^{-1} for LO$_{HgTe}$, and they are more noticeable in the central region of the epitaxial layer. We may assume from the character of the shift of these modes that the HgTe sublattice in sample 3, especially in the midsection of the layer, is elastically stressed (compressed). However, this conclusion could not be confirmed or disproved unambiguously based on the results of the behavioral analysis of other vibrational modes. Let us consider mode *2* (107 cm^{-1}). Its position varies from the surface to the epitaxial layer boundary in samples 2 and 3. The deviations from the value predicted (107 cm^{-1}) are very large (as large as 5.5 cm^{-1} at certain points of the layer). Therefore, it is possible to question the assignment of this mode to vibrations of Hg atoms in the sites of the Te sublattice.

It is noteworthy that any structure caused by the LO-phonon intersubband resonance in the inversion layer is not observed in the Raman spectra of the samples at a frequency of 132 cm^{-1}. It is sometimes assumed that the intensity of this mode can serve as a parameter that characterizes the quality of the crystal surface [16]. In our case, it is more logical to interpret it in the context of the surface of the Cd$_x$Hg$_{1-x}$Te epitaxial layers free of the inversion layer. The next point we should mention is associated with the absence of any peaks in the Raman spectra of the samples at frequencies of 133–

135 cm^{-1}. In some studies, these peaks are associated with a cluster mode, which has Γ_1 symmetry [17], or with the resonance mode of a cluster, which consists of one Cd atom and three atoms in the Te sublattice [16]. The absence of this vibrational mode in the spectra of the samples investigated in our study can be considered as indirect proof of the statistically microscale-uniform distribution of the major components in the bulk of the Cd$_x$Hg$_{1-x}$Te solid solution.

Let us consider the analysis of a possible distribution of excess Te in the epitaxial layer bulk and in the adjoining interfacial region in more detail. It can be seen from Figs. 2a–2c that the position of some peaks, namely, *1*, *4*, and *6*, vary in the vicinity of the layer–substrate interface. All these peaks, to a certain extent, are associated with the presence of excess Te in the epitaxial layer. It should be noted that Te precipitates in the samples investigated accumulate in the vicinity of the layer–substrate interface and in the surface region. These precipitates are practically absent in the central (~10–15 μm) part of the epitaxial layer. This is not surprising since, during the heat treatment of as-grown epitaxial layers at $T = 340$–380°C for 6 h in saturated Hg vapors, the diffusion of structural defects into the epitaxial layer boundaries should occur. The results obtained are in agreement with the data reported by Sochinskii *et al.* [2]. When analyzing the Raman and cathodoluminescence spectra of bulk CdTe samples, which were thermally treated in Ga and Cd vapors at $T = 500$–600°C, they concluded [2] that Te precipitates start to vanish in the central part of the sample by migrating to its boundaries. Additionally, it was noted that small Te precipitates are annealed out in several hours, whereas heat treatment of about 22 h is required to anneal large (5–10 μm) precipitates.

If Te inclusions are in a stressed compressed state, their resonance peaks should be shifted to lower wave numbers [12]. Alternatively, if tensile elastic stresses occur, the peaks shift to the opposite side. The thermal expansion coefficient for trigonal Te is anisotropic and attains its largest value in the direction coinciding with the axis of the Te chain. Therefore, assuming that the Te inclusions form the extended structure, we can predict to a first approximation their preferential spatial orientation from the shift of corresponding peaks in the Raman spectra with decreasing sample temperature. Let the *C* axis of the chain of Te atoms be oriented normally to the sample surface. In this case, the spectral shift of the vibrational mode A_1 (123 cm^{-1}) should not be so noticeable compared with the case when this axis is parallel to the surface. In contrast with bulk Cd$_{1-y}$Zn$_y$Te and Cd$_x$Hg$_{1-x}$Te crystals, Te inclusions were not observed in the Cd$_x$Hg$_{1-x}$Te epitaxial layers investigated by us. Therefore, the different variation in the spectral position of modes *E* and A_1 can be attributed to the variation in the preferential geometry shape and average size of Te nanoprecipitates. Consequently,
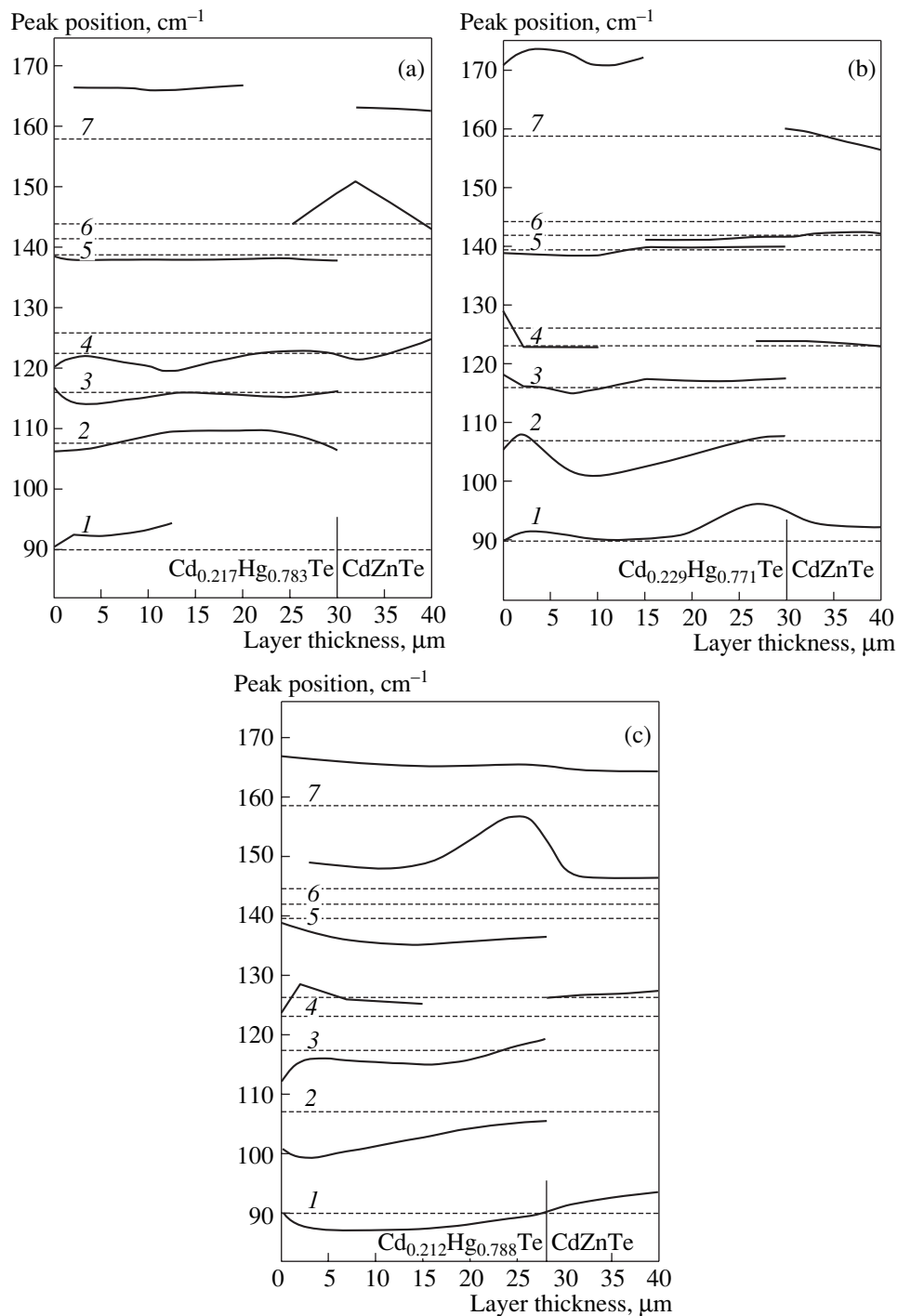
Fig. 2. Mutual arrangement of resonance peaks into which the Raman spectra were decomposed. The compositions of the $Cd_xHg_{1-x}Te$ samples over the epitaxial layer depth: (*a*) $x = 0.217$, (*b*) $x = 0.229$, and (*c*) $x = 0.212$. The numbers of peaks correspond to the vibrational modes listed in Table 2.

analyzing the difference of frequencies, which correspond to the vibrational modes discussed, over the layer thickness, we can gain the information as to whether the shape of Te precipitates varies or not.

Let us now consider the experimental data. It can be seen that the A_1 mode is absent in the Raman spectra of sample 3. In sample 2, this mode is observed only in the immediate vicinity of the epitaxial layer boundaries, and it is observed over the entire distance from the film surface to its boundary, extending into the substrate, only in the first sample. The behavior of this mode is not monotonic. It shifts by 2–2.5 cm^{-1} in the interfacial

region and in the middle of the epitaxial layer, at a distance of 12–15 μm from the epitaxial layer surface (Fig. 2a). Consequently, we may assume that the shape of Te precipitates in the first sample varies from the layer–substrate interface to the surface. Therefore, the spectral behavior of other Te vibrational modes (modes *1* and *6*) in this epitaxial layer, depending on the spatial coordinate, correlate with the A_1 mode (mode *4*). It should be noted that resonance scattering peaks of photons are practically absent in the Raman spectra of the first epitaxial layer. These peaks correspond precisely to Te inclusions in bulk $Cd_xHg_{1-x}Te$ and are located at frequencies of 126 and 144 cm^{-1}. Therefore, the E vibrational mode (90 cm^{-1}) emerges only in the near-surface region. This mode is shifted to higher wave numbers, and this shift is the largest for that part of the sample where the A_1 mode is subjected to the largest shift, but it is directed oppositely. A similar situation may be caused by the existence of local elastic stresses of the crystal lattice in the epitaxial layer. This is a quite consistent conclusion, which is also confirmed to a certain extent by the behavior of vibrational mode *3* (TO_{HgTe}). Its spectral position over the epitaxial layer length varies out-of-phase with mode *4* discussed above. In samples *2* and *3*, the A_1 mode emerges only in the interfacial region from the substrate side and in the surface region of the epitaxial layer. In the substrates of the samples mentioned, the spectral position of this mode varies with decreasing sample temperature in the opposite direction relative to 123 cm^{-1} (Figs. 2b, 2c). This fact, as was noted in the previous paragraph, may indicate differences in the spatial orientations of Te inclusions. As one approaches the $Cd_xHg_{1-x}Te/Cd_{1-y}Zn_yTe$ interface, this vibrational mode tends to ~123 cm^{-1}.

Vibrational mode *6* (142, 144 cm^{-1}) behaves quite differently. Thus, for example, it is practically absent for epitaxial layer *1*, transfers from the substrate bulk into the layer and is located at frequencies 142–142.5 cm^{-1}, extends to the middle of epitaxial layer *2*, and exhibits complex behavior in the third case. The complexity lies in the fact that, both for the $Cd_{1-y}Zn_yTe$ substrate and for the $Cd_xHg_{1-x}Te$ epitaxial layer, this mode is considerably shifted to higher frequencies. Moreover, as can be seen from Fig. 2c, over a distance of approximately 18 μm from the layer–substrate interface, this shift is so substantial that assigning mode *6* to vibrations of atoms constituting the Te precipitate can be questioned. It is most likely that the vibrational mode, which is related to LO_{CdTe} (TO_{CdTe}), can manifest itself in this region of the epitaxial layer. Specifically, epitaxial layer *3* may contain not only Te nanoprecipitates but also more complex agglomerates, which affect the vibrational properties of the CdTe sublattice. This conclusion can be partially confirmed by the results of research into the character of variations in vibrational mode *1* (E mode of Te vibrations, 90 cm^{-1}). As in the previous case, this mode is practically absent in the first epi-

taxial layer. In the second epitaxial layer, this mode occupies a position close to equilibrium and deviates from it only in the near-boundary region of the layer. In the third layer, this mode is shifted by several inverse centimeters to the lower side from the equilibrium value (ω = 90 cm^{-1}). This mode starts to shift in the opposite direction as one crosses the $Cd_xHg_{1-x}Te/Cd_{1-y}Zn_yTe$ boundary. This may be associated with the reversed sign of elastic stresses for the layer–substrate region in the third epitaxial layer. Judging from the shift of Raman peaks *1* and *6*, the effect of stresses on the vibrational properties of the Te sublattice is considerable, which also affects the vibrations of the cation sublattice.

Figures 3a–3c show data that reflect the character of variations in the vibrational modes listed in Table 2 over the epitaxial layer depth. Comparing these results, we may assume that, for the first sample, the structural imperfections of the HgTe sublattice occur mainly in the surface region of the epitaxial layer, with the depth ranging from 0 to 7 μm. This concerns vibrational modes *3* and *5*; their intensity falls abruptly as one approaches the layer–substrate interface. For sample *2*, these modes are extended over almost the entire layer depth and most strongly manifest themselves in the half of the epitaxial layer that adjoins the substrate. In the third case (Fig. 3c), a situation that combines the first two variants is realized. Comparing this conclusion with the above analysis of the data shown in Figs. 2a–2c, it can be seen that the frequency shift of the aforementioned modes from the undisturbed state is largest for the third epitaxial layer. Consequently, from all the reasoning given above, one may conclude that the elastic stresses in the HgTe sublattice are the most substantial for the third sample. Indirect confirmation of this conclusion can be found by analyzing variations in the intensity of vibrational mode *2*, which corresponds to the Hg vacancies, over the layer depth. For samples 2 and 3, as can be seen from Figs. 3b and 3c, the distribution of intensity of vibrations of this mode over the epitaxial layer is generally similar to that for modes *3* and *5*. Alternatively, for the first epitaxial layer (Fig. 3a), no such similarity is observed. Moreover, starting from the middle of the layer and up to its surface, the behavior of vibrational modes *3*, *5*, and *2* is substantially different. Thus, we may assume that the Hg vacancies are at least not the main source of elastic stresses in the HgTe sublattice. Here, attention should be paid to the manifestation of mode *7*, which reflects the state of the CdTe sublattice (LO_{CdTe}) in the epitaxial layer. In all three cases, the variation in intensity of this mode follows the same law as for the HgTe sublattice. Consequently, we may state with a high degree of confidence that it is not so much single cation vacancies that may be responsible for elastic stresses in the $Cd_xHg_{1-x}Te$ epitaxial layers investigated by us, but their complexes. It should be noted that, based on our data, it seems impossible to trace the possible participation of impurity atoms in the
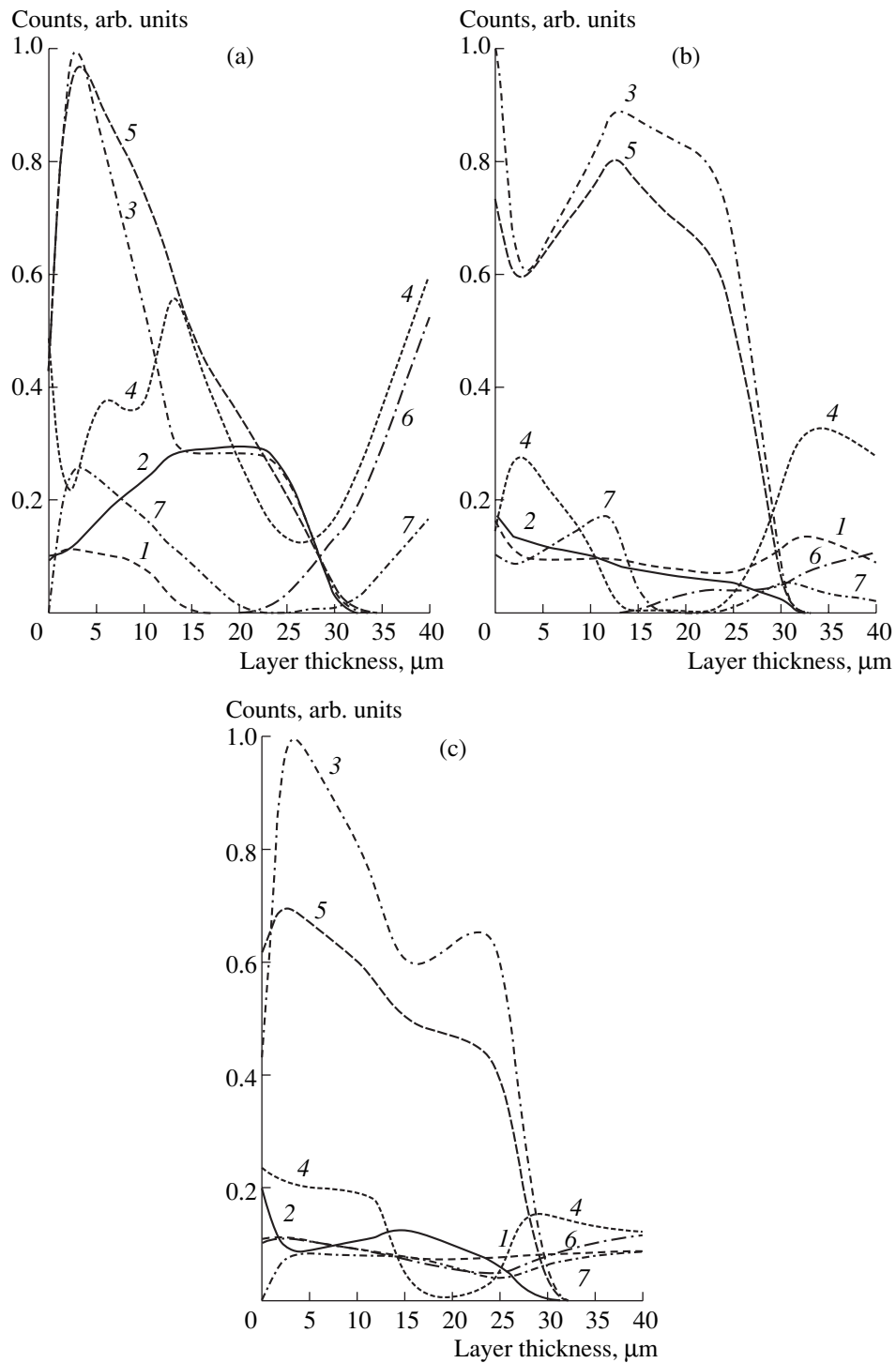
Fig. 3. Distribution of intensity of vibrational modes listed in Table 2 in the Raman spectra of the $Cd_xHg_{1-x}Te$ epitaxial layers investigated. Notation corresponds to Fig. 2.

formation of similar agglomerates. However, it should be noted that we failed to reveal the presence of any prevailing impurity both in the $Cd_{1-y}Zn_yTe$ substrates and in the $Cd_xHg_{1-x}Te$ layers using the SIMS method. The question of possible Zn diffusion from the substrate during growth of the epitaxial layer and its distri-

bution over the epitaxial layer bulk will be considered in a separate paper.

By analyzing the form of distribution of intensity of the vibrational modes listed in Table 2 over the depth of the $Cd_xHg_{1-x}Te/Cd_{1-y}Zn_yTe$ epitaxial layers, we may assume that the lattice vibrations caused by vacancy

complexes are the most active among these modes. In our view, the Te nanoprecipitates may play the role of the aforementioned complexes.

4. CONCLUSION

In this paper, the results of investigating the distribution profile and the features of variations in the lattice vibrations, which are initiated by structural defects of various nature, over the layer depth in $Cd_xHg_{1-x}Te/Cd_{1-y}Zn_yTe$ epitaxial structures are discussed in detail. Based on the results obtained, we may conclude that, in contrast to bulk crystals, LPE-grown $Cd_xHg_{1-x}Te$ epitaxial layers contain no extended Te inclusions, but nanometer-size Te precipitates occur in them. Direct proof of such a conclusion can be obtained using transmission electron microscopy or EXAFS spectroscopy. After the thermal annealing of the samples at 340–380°C, the Te nanoprecipitates are redistributed in the surface and interfacial regions of the epitaxial layer. Experimental results are obtained using the Raman scattering method in a micromode over the sample cleaved surface prepared immediately prior to measurements. Low-temperature micro-Raman spectroscopy is experimentally complex, and the interpretation of the results obtained is ambiguous. However, this method provided unique information that was sometimes inaccessible to other experimental methods of investigating the morphology of epitaxial layers in $Cd_xHg_{1-x}Te/Cd_{1-y}Zn_yTe$ epitaxial structures over their depth with localization as small as 2 μm.

ACKNOWLEDGMENTS

REFERENCES

1. M. S. Kwon and J. Y. Lee, J. Cryst. Growth **191**, 51 (1998).
2. N. V. Sochinskii, M. D. Serrano, E. Dieguez, *et al.*, J. Appl. Phys. **77**, 2806 (1995).
3. *Etching of Semiconductors* (Mir, Moscow, 1965).
4. S. H. Shin, J. Bajaj, L. A. Moudy, and D. T. Cheung, Appl. Phys. Lett. **43**, 68 (1983).
5. A. I. Belogorokhov, V. M. Lakeenkov, and L. I. Belogorokhova, Fiz. Tekh. Poluprovodn. (St. Petersburg) **35**, 808 (2001) [Semiconductors **35**, 773 (2001)].
6. J. Zhu, X. Zhang, B. Li, and J. Chu, Infrared Phys. Technol. **40**, 411 (1999).
7. I. Hill, J. Appl. Phys. **67**, 4270 (1990).
8. Shyama Rath, K. P. Jain, S. C. Abbi, *et al.*, Phys. Rev. B **52**, 17172 (1995).
9. D. N. Talwar and M. Vandevyver, J. Appl. Phys. **56**, 1601 (1984).
10. P. M. Amirtharaj, N. K. Dhar, J. Baars, and H. Seelewind, Semicond. Sci. Technol. **5**, S68 (1990).
11. P. M. Amirtharaj, K. K. Tiong, P. Parayanthal, and F. H. Pollack, J. Vac. Sci. Technol. A **1**, 1744 (1983).
12. W. Richter, J. B. Renucci, and M. Cardona, Phys. Status Solidi B **56**, 223 (1973).
13. R. D. Yadava, R. K. Bagai, and W. N. Borle, J. Electron. Mater. **21**, 1001 (1992).
14. A. Polian, R. Le Toullec, and M. Balkanski, Phys. Rev. B **13**, 3558 (1976).
15. S. C. Shen and J. H. Chu, Solid State Commun. **48**, 1017 (1983).
16. A. Ksendzov, F. H. Pollak, P. M. Amirtharaj, and J. A. Wilson, Semicond. Sci. Technol. **5**, S78 (1990).
17. K. K. Tiong, P. M. Amirtharaj, P. Parayanthal, and F. H. Pollask, Solid State Commun. **50**, 891 (1984).

Translated by N. Korovin

LOW-DIMENSIONAL
SYSTEMS

Electron Transfer between Semiconductor Quantum Dots via Laser-Induced Resonance Transitions

A. V. Tsukanov and L. A. Openov*

Institute of Physics and Technology, Russian Academy of Sciences, Moscow, 117218 Russia
e-mail: tsukanov@ftian.oivta.ru
*Moscow Engineering Physics Institute, Moscow, 115409 Russia
e-mail: opn@supercon.mephi.ru
Submitted March 17, 2003; accepted for publication April 15, 2003

Abstract—The effect of a resonant laser pulse on the quantum dynamics of an electron in a system of two semiconductor quantum dots (QDs) is studied theoretically. The pulse characteristics (frequency, amplitude, and duration) corresponding to the highest probability of electron transition from the ground state of one QD to the ground state of the other QD are determined with regard to possible difference in the QD sizes. A specific model with QDs of near cubic shape is considered. © *2004 MAIK "Nauka/Interperiodica".*

1. INTRODUCTION

In recent years, much attention has been paid to semiconductor nanostructures: quantum wells (QWs), quantum dots (QDs), etc. (see, e.g., [1–5]). Further miniaturization of the basic elements of semiconductor devices requires a deeper understanding of the physical processes in nanostructures. One such process is the interaction of electrons in nanostructures with an RF electromagnetic field. This interaction is fundamental for the operation of quantum-cascade lasers [6], resonant tunneling diodes [7], certain models of quantum computers [8], and so on. Recently, a number of new effects occurring in QWs and QDs under the action of laser radiation were predicted theoretically: electron localization in one of the QWs of a double-well structure [9], the emission of single photons by a QD [10], etc.

It was suggested in [11] that the action of a laser pulse on a system of two spatially separated QDs can be used to transfer electrons from one dot to the other. The essence of the mechanism that causes this effect can be outlined as follows. An electron occupying initially the ground quantum-confinement level in the conduction band of one of the QDs (localized in this QD) interacts resonantly with the field of the laser pulse, which causes a transition of the electron to an excited state. If the energy of this excited state is close to the top of the potential barrier separating the QDs (see Fig. 1), the electron becomes delocalized between the dots. In such a state, the probability amplitudes for finding the electron in the first and the second QDs are equal. Therefore, under the action of the same laser pulse, the electron can make a transition to the ground quantum-confinement energy level of the second dot and remain there after the pulse. Thus, the excited level serves as a "transport state" for the electron. It was shown previously for a simple model system consisting of two identical QDs [11] that the parameters of a laser pulse (its frequency, duration, and intensity) can be chosen in such a way that the probability of an electron transition from one QD to the other exactly equals unity. It was suggested, in particular, that this effect can be used in designing schemes for quantum computation based on semiconductor nanostructures [11, 12].

It should be noted, however, that, at the current level of technology, it is virtually impossible to fabricate two absolutely identical QDs [13]. Thus, it is necessary to consider how important the difference in the geometric parameters of the QDs is for the resonance electron transfer between them. We need to examine whether a
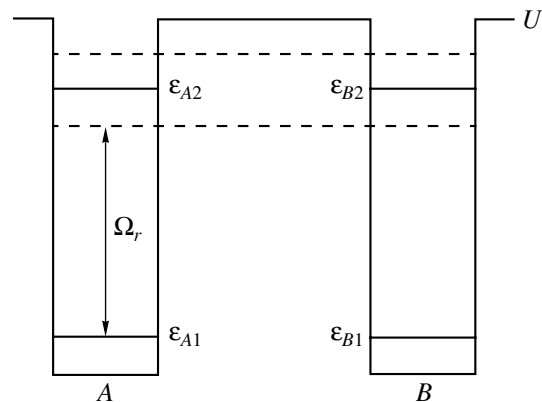
Fig. 1. Energy-level diagram for a nanostructure consisting of two QDs, *A* and *B*. Here, ε_{A1}, ε_{A2}, ε_{B1}, and ε_{B2} are the energies of the ground and excited quantum-confinement levels in the corresponding isolated QDs; *U* is the height of the potential barrier separating the QDs; and Ω_r is the resonance frequency. Dashed lines indicate the energies of the states delocalized between the QDs, which arise due to the tunneling effect.

small difference in the sizes of the QDs may result in considerable, or even complete, suppression of this effect. The purpose of this study is to extend the results obtained in [11] to systems of two QDs with nearly, but not exactly, equal sizes. For the case of a nanostructure consisting of two QDs of near cubic shape, we find the conditions for the existence of the effect of laser-induced resonance electron transfer between the dots.

2. MODEL AND BASIC EQUATIONS

Let us consider two QDs (A and B). We assume that, if the dots were isolated, each of them would have at least two quantum-confinement levels with the energies ε_{Ai} and ε_{Bi} (here, $i = 1$ or 2 is the number of a level) (see Fig. 1). When the spacing between the QDs is sufficiently large and/or the barrier separating the QDs is sufficiently high, the wave functions of the ground states of both dots $\varphi_{A1}(\mathbf{r})$ and $\varphi_{B1}(\mathbf{r})$ are strongly localized in the corresponding dots and the overlap between them is weak. Thus, the matrix element V characterizing the electron tunneling between the $|A1\rangle$ and $|B1\rangle$ states is exponentially small, and an electron localized in one of the dots will stay there for a macroscopically long time, $\tau \sim 1/V$ (hereafter, we set the Plank constant $\hbar = 1$).

Next, we choose the energy levels ε_{A2} and ε_{B2} of the excited states $|A2\rangle$ and $|B2\rangle$ to be close to the top of the potential barrier separating the QDs. Then, the matrix element of electron tunneling between the $|A2\rangle$ and $|B2\rangle$ states will be large, which leads to their strong hybridization, i.e., to the formation of two states (a bonding and an antibonding state) extended between the dots. Let us enumerate all of the levels considered in order of increasing energy: states $|1\rangle = |A1\rangle$ and $|2\rangle = |B1\rangle$ are localized, and states $|3\rangle$ and $|4\rangle$ are delocalized. As the subsequent consideration is based on the resonance-field approximation, we disregard the possible existence of other quantum-confinement levels whose energies differ notably from the energies ε_1, ε_2, ε_3, and ε_4 of the four above levels (accordingly, we skip the "insignificant" levels and enumerate only the four resonant or near resonant levels).

Taking these considerations into account, we can write the Hamiltonian of an electron in an electromagnetic field in the following form:

$$\hat{H}(t) = \sum_{i=1}^{4} \varepsilon_i \hat{a}_i^+ \hat{a}_i + (e/m^*c)\mathbf{A}(t)(\mathbf{p}_{31}\hat{a}_3^+\hat{a}_1 \quad (1)$$
$$+ \mathbf{p}_{32}\hat{a}_3^+\hat{a}_2 + \mathbf{p}_{41}\hat{a}_4^+\hat{a}_1 + \mathbf{p}_{42}\hat{a}_4^+\hat{a}_2 + \text{h.c.});$$

here, $\hat{a}_i^+$ and $\hat{a}_i$ are the operators of creation and annihilation of an electron in the corresponding states, $\mathbf{p}_{ij} = \langle i|\hat{\mathbf{p}}|j\rangle$ are the matrix elements of the momentum operator, and $\mathbf{A}(t)$ is the vector potential (we use the Lorenz gauge with zero scalar potential and disregard the interaction term quadratic in the vector potential).

Let the frequency Ω of the laser pulse be close to the resonance frequency $\Omega_r = \varepsilon_3 - \varepsilon_1$, which equals the difference between the energies of one of the excited states (for definiteness, we choose state $|3\rangle$) and the ground state $|1\rangle$ of dot A. We assume that $\delta \ll \varepsilon_4 - \varepsilon_3$, where $\delta = \Omega - \Omega_r$ is the detuning from the resonance. Level $|3\rangle$ serves as the transport level. In the resonance approximation, Hamiltonian (1) can be written as

$$\hat{H}(t) = \varepsilon_1 \hat{a}_1^+ \hat{a}_1 + \varepsilon_2 \hat{a}_2^+ \hat{a}_2 + \varepsilon_3 \hat{a}_3^+ \hat{a}_3$$
$$+ \left\{ \frac{1}{2}\exp(-i\Omega t)(\lambda_1 \hat{a}_3^+\hat{a}_1 + \lambda_2 \hat{a}_3^+\hat{a}_2) + \text{h.c.} \right\}, \quad (2)$$

where we introduced $\lambda_1 = -(ie/m^*\Omega)\mathbf{E}_0\mathbf{p}_{31}$ and $\lambda_2 = -(ie/m^*\Omega)\mathbf{E}_0\mathbf{p}_{32}$ using the well-known relationship between the vector potential and the strength of an electric field with frequency Ω and amplitude $\mathbf{E}_0$.

The electron wave function $\Psi(t)$ satisfies the Schrödinger equation

$$i\frac{\partial \Psi(t)}{\partial t} = \hat{H}(t)\Psi(t) \quad (3)$$

with the Hamiltonian (2). It can be written in the form

$$\Psi(t) = \sum_{i=1}^{3} A_i(t)\exp(-i\varepsilon_i t)|i\rangle. \quad (4)$$

At the initial moment ($t = 0$), the electron is localized in the ground state of QD A; i.e., $A_1(0) = 1$ and $A_2(0) = A_3(0) = 0$. Our goal is to determine the probabilities $p_i(t) = |A_i(t)|^2$ of finding the electron in state $|i\rangle$ at the moment t. Note that the quantities $p_1(t)$ and $p_2(t)$ are the probabilities of finding the electron in the ground states of QDs A and B, respectively.

Let us pass to the representation $\Psi(t) = \hat{U}(t)\tilde{\Psi}(t)$ in (3), where the unitary operator $\hat{U}(t)$ has the form

$$\hat{U}(t) = \exp\left[\frac{i\Omega t}{2}(\hat{a}_1^+\hat{a}_1 + \hat{a}_2^+\hat{a}_2 - \hat{a}_3^+\hat{a}_3)\right]$$

(see [14]). The wave function $\tilde{\Psi}(t)$ satisfies the equation

$$i\frac{\partial \tilde{\Psi}(t)}{\partial t} = \hat{\tilde{H}}\tilde{\Psi}(t). \quad (5)$$

The Hamiltonian $\hat{\tilde{H}}$ is time-independent:

$$\hat{\tilde{H}} = \hat{U}^+(t)\hat{H}(t)\hat{U}(t) - i\hat{U}^+(t)\frac{\partial \hat{U}(t)}{\partial t}$$
$$= \left(\varepsilon_1 + \frac{\Omega}{2}\right)\hat{a}_1^+\hat{a}_1 + \left(\varepsilon_2 + \frac{\Omega}{2}\right)\hat{a}_2^+\hat{a}_2 + \left(\varepsilon_3 - \frac{\Omega}{2}\right)\hat{a}_3^+\hat{a}_3 \quad (6)$$
$$+ \frac{1}{2}(\lambda_1 \hat{a}_3^+\hat{a}_1 + \lambda_2 \hat{a}_3^+\hat{a}_2 + \text{h.c.});$$

thus, the solution to the time-dependent equation (5) can be written as

$$\tilde{\Psi}(t) = \sum_{k=1}^{3} B_k \exp(-i\tilde{\varepsilon}_k t)|\tilde{k}\rangle. \tag{7}$$

Here, $|\tilde{k}\rangle$ and $\tilde{\varepsilon}_k$ are, respectively, the eigenfunctions and eigenvalues of the time-independent Schrödinger equation

$$\hat{\tilde{H}}|\tilde{k}\rangle = \tilde{\varepsilon}_k|\tilde{k}\rangle. \tag{8}$$

The coefficients B_k are determined from the condition $\tilde{\Psi}(0) = \Psi(0) = |1\rangle$. Expanding state $|\tilde{k}\rangle$ in states $|i\rangle$, we obtain

$$|\tilde{k}\rangle = \sum_{i=1}^{3} C_{ki}|i\rangle. \tag{9}$$

Taking into account (6), we derive from (8) and (9) a system of equations for the coefficients C_{ki} and an equation for the eigenvalues $\tilde{\varepsilon}_k$:

$$\begin{pmatrix} \varepsilon_1 + \dfrac{\Omega}{2} - \tilde{\varepsilon}_k & 0 & \dfrac{\lambda_1^*}{2} \\ 0 & \varepsilon_2 + \dfrac{\Omega}{2} - \tilde{\varepsilon}_k & \dfrac{\lambda_2^*}{2} \\ \dfrac{\lambda_1}{2} & \dfrac{\lambda_2}{2} & \varepsilon_3 - \dfrac{\Omega}{2} - \tilde{\varepsilon}_k \end{pmatrix} \begin{pmatrix} C_{k1} \\ C_{k2} \\ C_{k3} \end{pmatrix} = \begin{pmatrix} 0 \\ 0 \\ 0 \end{pmatrix}, \tag{10}$$

$$\left(\varepsilon_1 + \frac{\Omega}{2} - \tilde{\varepsilon}_k\right)\left[\left(\varepsilon_2 + \frac{\Omega}{2} - \tilde{\varepsilon}_k\right)\left(\varepsilon_3 - \frac{\Omega}{2} - \tilde{\varepsilon}_k\right) - \frac{|\lambda_2|^2}{4}\right]$$
$$- \frac{|\lambda_1|^2}{4}\left(\varepsilon_2 + \frac{\Omega}{2} - \tilde{\varepsilon}_k\right) = 0. \tag{11}$$

Using expansion (9), we derive from (7) the expression

$$\tilde{\Psi}(t) = \sum_{i=1}^{3} D_i(t)|i\rangle. \tag{12}$$

Here,

$$D_i(t) = \sum_{k=1}^{3} B_k C_{ki} \exp(-i\tilde{\varepsilon}_k t), \tag{13}$$

with the initial conditions being $D_i(0) = \delta_{1i}$. The required probabilities of finding the electron in state $|i\rangle$ at time t are equal to $p_i(t) = |D_i(t)|^2$ (here, $i = 1, 2, 3$).

In the general case ($|\lambda_1| \neq |\lambda_2|$ and $\varepsilon_1 \neq \varepsilon_2$), the expressions for the probabilities $p_i(t)$ are very awkward.

In the particular case $\varepsilon_1 = \varepsilon_2$, these expressions can be written as

$$\begin{cases} p_1(t) = 1 - \dfrac{2|\lambda_1|^2}{|\lambda_1|^2 + |\lambda_2|^2} f_1(t) + \left(\dfrac{2|\lambda_1|^2}{|\lambda_1|^2 + |\lambda_2|^2}\right)^2 f_2(t), \\[3mm] p_2(t) = \left(\dfrac{2|\lambda_1||\lambda_2|}{|\lambda_1|^2 + |\lambda_2|^2}\right)^2 f_2(t), \\[3mm] p_3(t) = \dfrac{\lambda_1^2}{16\omega_R^2} \sin^2(2\omega_R t), \end{cases} \tag{14}$$

where

$$\omega_R = \frac{1}{4}\sqrt{\delta^2 + |\lambda_1|^2 + |\lambda_2|^2},$$

$$f_1(t) = 1 - \cos\left(\frac{\delta t}{2}\right)\cos(2\omega_R t)$$
$$- \frac{\delta}{4\omega_R}\sin\left(\frac{\delta t}{2}\right)\sin(2\omega_R t), \tag{15}$$

$$f_2(t) = \sin^4(\omega_R t) + \sin^2\left(\frac{\delta t}{4}\right)\cos(2\omega_R t)$$
$$+ \frac{\delta^2}{64\omega_R^2}\sin^2(2\omega_R t) - \frac{\delta}{8\omega_R}\sin\left(\frac{\delta t}{2}\right)\sin(2\omega_R t).$$

If level $|4\rangle$ is chosen as the transport level, the above results remain valid, with the only difference that $\lambda_1 = -(ie/m^*\Omega)\mathbf{E}_0 p_{41}$ and $\lambda_2 = -(ie/m^*\Omega)\mathbf{E}_0 p_{42}$ in this case.

When $\lambda_2 \longrightarrow 0$, expressions (14) and (15) describe the Rabi oscillations between the ground and excited states in the first QD; the transitions between the QDs do not occur. When $\varepsilon_1 = \varepsilon_2$ and $\lambda_1 = \lambda_2$, expressions (14) and (15) yield the same results as obtained in [11] for identical QDs. In this case, $p_2(T) = 1$, provided that $\delta = 0$ and $\omega_R T = \pi/2 + \pi n$ (where n is an integer). In other words, adjusting the laser pulse duration T, one can ensure that the electron definitely makes a transition from one dot to the other within the pulse duration.

It can be seen from (14) and (15) that the probability $p_2(t)$ is always less than unity if $\lambda_1 \neq \lambda_2$. The difference in the energies ε_1 and ε_2 of the ground states of two nonidentical QDs leads to an even larger decrease in the maximum value of $p_2(t)$. Assuming $|\varepsilon_2 - \varepsilon_1|$, $||\lambda_2| - |\lambda_1||$, and $\delta \ll |\lambda_1|$, we find that $p_2(T)$ attains its maximum value

$$p_2^{max} \approx 1 - \{(|\lambda_2| - |\lambda_1|)^2 + (\varepsilon_2 - \varepsilon_1)^2$$
$$+ (\pi^2/8)[\delta + (\varepsilon_2 - \varepsilon_1)/2]^2\}/|\lambda_1|^2 \tag{16}$$

at $T = \pi/2\omega_R$, where

$$\omega_R$$
$$= \sqrt{|\lambda_1|^2 + |\lambda_2|^2 + [\delta + (\varepsilon_2 - \varepsilon_1)/2]^2 + (\varepsilon_2 - \varepsilon_1)^2/4}. \tag{17}$$
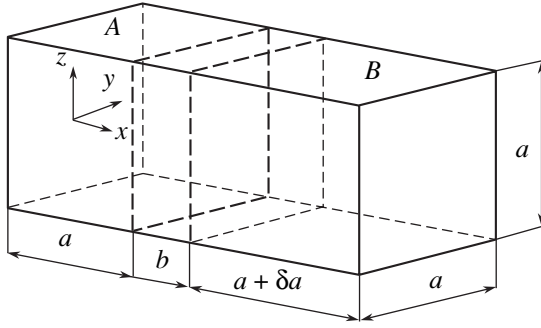
Fig. 2. Model of a double-QD nanostructure: dot A has a cubic shape, dot B has the shape of a rectangular parallelepiped, and they are separated by a barrier of thickness b. QD A occupies the region $0 < x < a$, $|y| < a/2$, $|z| < a/2$; QD B occupies the region $a + b < x < 2a + \delta a + b$, $|y| < a/2$, $|z| < a/2$. The electron potential energy $V(\mathbf{r}) = 0$ for $\mathbf{r} \in A$ and $\mathbf{r} \in B$; $V(\mathbf{r}) = U$ for $|y| < a/2$, $|z| < a/2$ and $x < 0$, $a < x < a + b$, $x > 2a + \delta a + b$; and $V(\mathbf{r}) = +\infty$ for $|y| > a/2$, $|z| > a/2$.

In order to check the sensitivity of the effect of resonance electron transfer between QDs to a spread in the QD sizes, we have to calculate the quantities ε_1, ε_2, λ_1, and λ_2 as functions of the geometric parameters of the QDs, i.e., to consider some specific model of a double-QD nanostructure and determine the electron-energy spectrum and the wave functions. Below, we present such a consideration for QDs of near cubic shape.

3. ELECTRON-ENERGY SPECTRUM AND THE MATRIX ELEMENTS OF ELECTRON TRANSITIONS IN A SYSTEM OF TWO NEAR CUBIC QUANTUM DOTS

Let us consider the following model [15] (see Fig. 2). Two QDs A and B are located at distance b from each other along the x axis. The shape of QD A is a cube with edge length a, and the shape of QD B is a rectangular parallelepiped with edge length a along the y and z directions and $a + \delta a$ along the x direction. The electron potential energy $V(\mathbf{r})$ in the dots is assumed to be zero. The QDs are separated by a potential barrier that has finite height U in the x direction and is infinitely high in the y and z directions (see Fig. 2). For simplicity, we assume that the electron effective mass m^* in the dots and within the barrier is the same.

In this case, the variables in the time-independent Schrödinger equation can be separated. The wave function has the form

$$\Psi(x, y, z) = \frac{2}{a}\Psi(x)\cos\left(\frac{\pi n_2 y}{a}\right)\cos\left(\frac{\pi n_3 z}{a}\right), \quad (18)$$

where $n_2 \geq 1$ and $n_3 \geq 1$ are integers. The energy eigenvalues are equal to

$$\varepsilon = \varepsilon_x + \frac{\pi^2 n_2^2}{2m^* a^2} + \frac{\pi^2 n_3^2}{2m^* a^2}, \quad (19)$$

where ε_x is determined by the dispersion relation, which results from the conditions of continuity of the wave function $\Psi(x)$ and its derivative (this dispersion relation is rather awkward and we omit it here). Thus, the problem is reduced to solving a one-dimensional Schrödinger equation.

Consider the subband corresponding to $n_2 = 1$ and $n_3 = 1$ (see (18) and (19)). Let us assume the value $\pi^2/m^* a^2$ to be the new energy reference point; then, $\varepsilon = \varepsilon_x$. We assume that (i) the difference in the linear dimensions of dots A and B is small (i.e., $\delta a \ll a$) and (ii) the dot spacing b and the height U of the barrier separating the dots are sufficiently large, so that $(2m^* b^2 U)^{1/2} \gg 1$, which means that the overlap between the wave functions of the deep levels of the QDs is very small. In what follows, we assume that $b \gg a$. Let us determine the energies ε_1 and ε_2 of the two lower (localized) levels of this nanostructure (ε_1, $\varepsilon_2 \ll U$) and the energies ε_3 and ε_4 of the two levels close to the barrier top ($U - \varepsilon_3 \ll U$, $U - \varepsilon_4 \ll U$), which are delocalized between the QDs (see the energy diagram in Fig. 1).

The energies ε_1 and ε_2 coincide very closely with the ground-state energies ε_{A1} and ε_{B1} of isolated QDs A and B, respectively; the discrepancy is exponentially small with respect to the parameter $(2m^* b^2 U)^{1/2} \gg 1$. To calculate the probability and the time of the resonance electron transfer between the QDs (see (16) and (17)), we need to determine the difference $\varepsilon_2 - \varepsilon_1$. For $\delta a/a \ll 1$, we find that

$$\varepsilon_2 - \varepsilon_1 \approx \frac{\delta a}{a}\frac{\xi^2}{m^* a^2}\frac{1}{1 + 2(2m^* a^2 U - \xi^2)^{-1/2}}. \quad (20)$$

Here, ξ is the numerical coefficient in the expression $\varepsilon_1 = \xi^2/2m^* a^2$ for the energy of the ground state in an isolated QW of width a and depth U. This coefficient depends on the QW parameter $m^* a^2 U$ and can be determined in each specific case by solving the corresponding dispersion equation; the value of ξ increases from zero to π as U increases from zero to infinity.

It is known that the second discrete level in an isolated one-dimensional QW of width a appears when the height of the potential barrier attains the critical value $U_c = \pi^2/2m^* a^2$. In a double-well system, splitting this level subsequently leads to the appearance of the third and the fourth levels, both delocalized between the QWs. The barrier height U_{c3}, corresponding to the appearance of the third level, depends on the parameter

$$\alpha = \frac{\pi^2}{2}\frac{\delta a}{a}\frac{b}{a}. \quad (21)$$

For $\alpha \ll 1$, which corresponds to the case of interest (where we have two QDs of nearly equal size, although probably rather distant from each other), the solution of the dispersion equation yields $U_{c3} \approx U_c(1 - \delta a/a)$. It should be noted that U_{c3} differs from the critical value
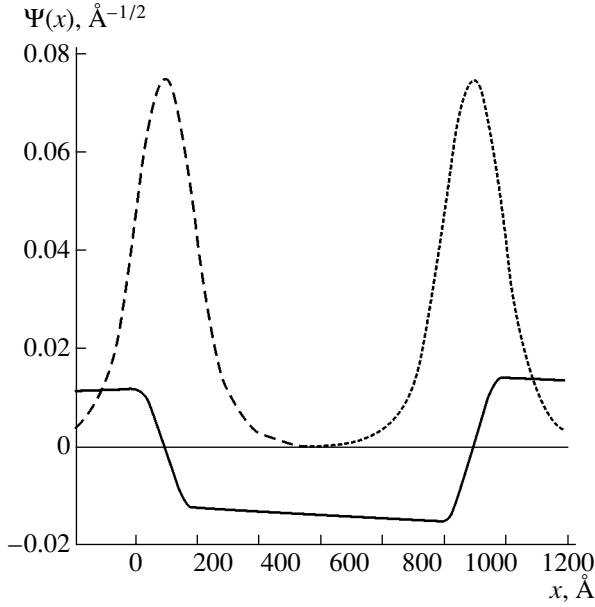
Fig. 3. Wave functions of an electron in a double-QD system (see Figs. 1, 2). The nanostructure parameters are $a = 20$ nm, $b = 80$ nm, $\delta a = 0.2$ nm, and $(U - U_{c3})/U_c = 10^{-2}$; here, $U_c = \pi^2/2m^*a^2$ and $U_{c3} = U_c(1 - \delta a/a)$. The long-dashed and short-dashed lines show the wave functions of the two lowest states localized in the different QDs (the first and the second energy levels in the nanostructure); the solid line shows the wave function of the state delocalized between the QDs (the third level).

Fig. 4. Wave function of an electron at the third (transport) level of the double-QD structure (see Figs. 1, 2) with $a = 60$ nm, $b = 240$ nm, $\delta a = 0.2$ nm. $(U - U_{c3})/U_c = 10^{-3}$ (long-dashed line), 10^{-2} (thick solid line), 10^{-1} (short-dashed line), and 0.3 (thin solid line); here, $U_c = \pi^2/2m^*a^2$ and $U_{c3} = U_c(1 - \delta a/a)$.

U_c for a single QW of width $a + \delta a$; the reason is that, for $\alpha \ll 1$, the QWs cannot be treated as isolated.

The third level in a double-well system corresponds to the bonding state that arises due to the hybridization of the wave functions of the two levels of separate QWs. Its wave function is nearly symmetric with respect to the center of the structure (exact symmetry exists for $\delta a = 0$). If $U - U_{c3} \ll U_{c3}$, the energy of the third level can be expressed as

$$\varepsilon_3 \approx U - \frac{\pi^2}{4} \frac{(U - U_{c3})^2}{U_c}, \qquad (22)$$

which is confirmed by numerical calculations. With a further increase in U up to $U_{c4} \approx U_c(1 + 4a/\pi^2 b)$, the fourth level appears; it corresponds to the antibonding state, whose wave function is nearly antisymmetric with respect to the center of the structure. At this stage, this level is of no importance for us, as the third level was chosen as the transport one (the results remain virtually unchanged if the fourth level is chosen as the transport level).

In Fig. 3, the wave functions of the three single-electron levels under consideration are shown for a nanostructure with $a = 20$ nm, $b = 80$ nm, $\delta a = 0.2$ nm, and $(U - U_{c3})/U_c = 10^{-2}$. For this set of parameters, $\varepsilon_1 \approx 0.350U$, $\varepsilon_2 \approx 0.354U$, and $\varepsilon_3 \approx 0.9998U$. We do not present the analytical expressions for the wave func-
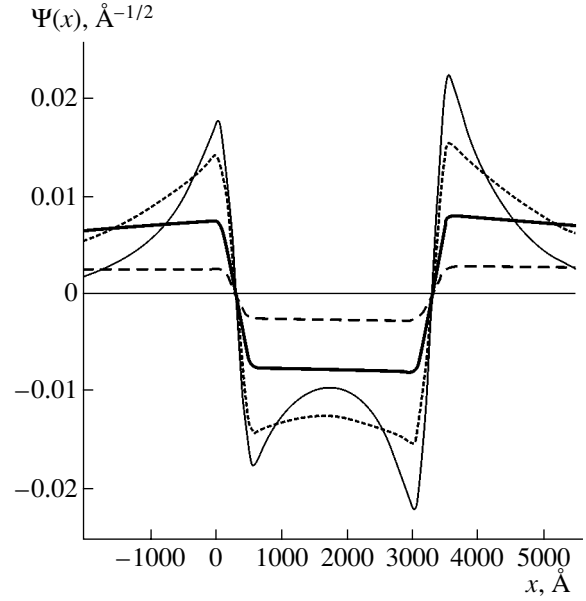
tions, which are simple but too lengthy. Knowing the wave functions, one can easily calculate the matrix elements λ_1 and λ_2 for the electron transitions $1 \longleftrightarrow 3$ and $2 \longleftrightarrow 3$, respectively (see Section 2). Assuming that the electric field is polarized along the x axis (i.e., $\mathbf{E}_0 = E_0\mathbf{e}_x$), we find for the case of $U - U_{c3} \ll U_c$ that

$$\lambda_1 = \beta e a E_0 \sqrt{\frac{U - U_{c3}}{U_c}}, \quad \lambda_2 = -\lambda_1(1 + \alpha); \quad (23)$$

here, the parameter $\alpha \ll 1$ was defined above (see (21)), and the numerical coefficient β depends on the QW parameter m^*a^2U and the coefficient ξ (also defined previously). For the case under consideration ($U \approx U_c$; i.e., $m^*a^2U \approx \pi^2/2$), $\xi \approx 1.85$. Then, $\beta \approx 0.94$ and expression (20) for the difference $\varepsilon_2 - \varepsilon_1$ can be written as

$$\varepsilon_2 - \varepsilon_1 = \gamma\frac{\delta a}{a} U_c, \qquad (24)$$

where $\gamma \approx 0.39$. Numerical calculations indicate that the relation $(|\lambda_2| - |\lambda_1|)/|\lambda_1| = \alpha$ between the matrix elements λ_1 and λ_2, which is given by formula (23), is satisfied with good accuracy for $(U - U_{c3})/U_c \leq 0.1$. If $(U - U_{c3})/U_c$ increases to 0.2–0.3, the difference between $|\lambda_1|$ and $|\lambda_2|$ grows, so that $(|\lambda_2| - |\lambda_1|)/|\lambda_1| = (2-3)\alpha$. This circumstance is related to the growing asymmetry of the wave function of the third level due to the tendency for it to be localized in the deeper well (see Fig. 4). Nevertheless, if $\alpha \ll 1$, the absolute values

of λ_1 and λ_2 remain close to each other even in the case of $(U - U_{c3})/U_c \approx 0.5$.

4. DISCUSSION

First of all, we note that the probability of electron transfer between the QDs can be increased by changing the resonance frequency from $\Omega_r = \varepsilon_3 - \varepsilon_1$ to $\Omega'_r = \varepsilon_3 - (\varepsilon_1 + \varepsilon_2)/2$, which follows from formula (16) and is also reasonably understood from physical considerations. Then, taking into account (23), one can rewrite Eq. (16) for the probability p_2^{max} as

$$p_2^{max} \approx 1 - \left[\alpha^2 + \frac{(\varepsilon_2 - \varepsilon_1)^2}{|\lambda_1|^2} \right]; \qquad (25)$$

the corresponding pulse duration T (see (17)) now equals

$$T \approx 2\pi / \sqrt{2(1 + \alpha)|\lambda_1|^2 + (\varepsilon_2 - \varepsilon_1)^2}. \qquad (26)$$

Provided the resonance frequency is appropriately readjusted, the deviation of p_2^{max} from unity is due only to the differences between the matrix elements λ_1 and λ_2 and the energies of the localized states ε_1 and ε_2, i.e., ultimately, the difference in the size and/or shape of the QDs. In our model, this difference is characterized by the quantity $\delta a/a$ (see Fig. 2). Let us compare the contributions from the terms α^2 and $(\varepsilon_2 - \varepsilon_1)^2/|\lambda_1|^2$ in Eq. (25) for the probability p_2^{max}. First, we evaluate the parameter α (see (21)), having chosen some reasonable set of geometric characteristics of the structure under consideration. Let us assume that the sizes of the QDs differ by $\delta a = 0.2$ nm, which is of the same order of magnitude as the thickness of a single atomic layer; this is an "optimistic" but still realistic estimate. Then, for example, for $a = 20$ nm and $b = 80$ nm, we obtain $\alpha \approx 0.2$. Thus, the corresponding term in (26) is only responsible for a decrease in p_2^{max} as small as 4%. An increase in the QD size a and a decrease in the spacing b between them leads to a decrease in α and, accordingly, to an increase in p_2^{max}.

As far as the term $(\varepsilon_2 - \varepsilon_1)^2/|\lambda_1|^2$ in (25) is concerned, the condition $\varepsilon_2 - \varepsilon_1 \ll |\lambda_1|$ (along with the condition $\alpha^2 \ll 1$) is not sufficient to make resonance electron transfer possible. The fact is that the electromagnetic field acts on the nanostructure over a finite time interval T and, thus, contains harmonics in the frequency range $\delta\omega \sim 1/T \sim |\lambda_1|$. Hence, the necessary condition for the validity of the resonance approximation (2) is the relationship $\delta\omega \ll \Delta\varepsilon$, or, in fact, $|\lambda_1| \ll \Delta\varepsilon$; here, $\Delta\varepsilon$ is the energy spacing between the transport level (in the case under consideration, level 3) and the closest level of the spectrum. Under this condition, levels 1 and 2 are in resonance only with the transport level and out of reso-

nance with any other level. Thus, the following double inequality has to be satisfied:

$$\varepsilon_2 - \varepsilon_1 \ll |\lambda_1| \ll \Delta\varepsilon. \qquad (27)$$

It should be stressed that the value of $|\lambda_1|$ can be varied by a corresponding change in the pulse power (see (23)), while the quantities $\varepsilon_2 - \varepsilon_1$ and $\Delta\varepsilon$ are determined only by the parameters of the nanostructure. Therefore, the latter have to be chosen in such a way that $\varepsilon_2 - \varepsilon_1 \ll \Delta\varepsilon$.

The value of $\varepsilon_2 - \varepsilon_1$ is given by (24). The value of $\Delta\varepsilon$ can be estimated as follows. As was shown in Section 3, for $U_{c3} < U < U_{c4}$ there is only one delocalized excited level (close to the barrier top), and the levels closest to this level belong to the continuous spectrum. Then, according to (22),

$$\Delta\varepsilon = U - \varepsilon_3 \approx \frac{\pi^2 (U - U_{c3})^2}{4 U_c}.$$

Thus, $\Delta\varepsilon$ increases with increasing U. If $U > U_{c4}$, the level closest to level 3 is level 4 and $\Delta\varepsilon = \varepsilon_4 - \varepsilon_3$. In this case, depending on the parameters of the structure (a, b, δa, U), this difference may either increase or decrease as U increases. However, with large values of U, the difference in the matrix elements λ_1 and λ_2 is significant, and the probability p_2^{max} of resonance electron transfer decreases (see (16) and Section 3). Thus, the value $U \approx U_{c4}$ can be used as the optimum barrier height. Since $(U_{c4} - U_{c3}) \ll U_c$ at $a/b \ll 1$ (see Section 3), we can use formula (22) to estimate the corresponding optimum value of $\Delta\varepsilon$; the result is

$$\Delta\varepsilon = \frac{\pi^2}{4} \frac{(U_{c4} - U_{c3})^2}{U_c} \approx \frac{\pi^2}{4} U_c \left(\frac{\delta a}{a} + \frac{4}{\pi^2} \frac{a}{b} \right)^2.$$

Then, taking into account (24), we find that the condition $\varepsilon_2 - \varepsilon_1 \ll \Delta\varepsilon$ can be written as

$$\frac{\delta a}{a} \ll \frac{\pi^2}{4\gamma} \left(\frac{\delta a}{a} + \frac{4}{\pi^2} \frac{a}{b} \right)^2. \qquad (28)$$

The validity of this inequality requires that the two small parameters $\delta a/a$ and $4a/\pi^2 b$ satisfy the condition $\delta a/a \ll 4a/\pi^2 b$. In this case, inequality (28) takes the form

$$\frac{\delta a}{a} \ll \left(\frac{a}{b} \right)^2, \qquad (29)$$

where we took into account that $4/\gamma\pi^2 \approx 1$. For example, for $a = 20$ nm, $b = 80$ nm, and $\delta a = 0.2$ nm, we have $\delta a/a = 0.01$ and $(a/b)^2 \approx 0.06$; thus, condition (29) is satisfied, albeit without a margin. Indeed, numerical calculations indicate that, for this set of parameters, the ratio $(\varepsilon_2 - \varepsilon_1)/\Delta\varepsilon$ cannot be smaller than 0.3, which means that double inequality (27) cannot be satisfied. If, keeping a constant, we reduce the spacing b between the QDs, the inequality $(2m^* b^2 U)^{1/2} \gg 1$ (which is a necessary condition for localization of the wave func-

tions of the ground levels in the two QDs) will be violated: at $U \approx U_c = \pi^2/2m^*a^2$, we have $(2m^*b^2U)^{1/2} \approx \pi(b/a)$, and the ratio $b/a \approx 4$ is close to the lowest acceptable value. Thus, the only way to meet the above criteria for the possibility of resonance electron transfer through the third level is to consider a structure with the QD size a increased severalfold at least, with the value of b/a kept unchanged. For example, for $a = 60$ nm, $b = 240$ nm, and $\delta a = 0.2$ nm, the ratio $(\varepsilon_2 - \varepsilon_1)/\Delta\varepsilon$ can be decreased to ~0.1; then, double inequality (27) is satisfied, albeit marginally, for $(\varepsilon_2 - \varepsilon_1)/|\lambda_1| \approx 0.3$.

A further increase in a (with the ratio b/a kept constant) leads to an even stronger reduction in the value of $(\varepsilon_2 - \varepsilon_1)/\Delta\varepsilon$, which makes it easier to satisfy inequality (27). However, in this case, the height of the barrier between the QDs $U \approx \pi^2/2m^*a^2$ decreases rapidly. For example, $U \approx 14$ meV for $m^* = 0.067m_0$ and $a = 20$ nm. At the same time, $U \approx 0.14$ meV for $a = 200$ nm, and the structure should be cooled to ultralow temperatures to avoid detrimental thermal effects. Thus, the values $a = 60$ nm and $b = 240$ nm (with $\delta a = 0.2$ nm) are, apparently, close to optimum: on the one hand, the necessary conditions for the resonance electron transfer are satisfied (although not rigorously); on the other hand, the experiment can be carried out at liquid-helium temperatures. Assuming that $(\varepsilon_2 - \varepsilon_1)/|\lambda_1| \approx 0.3$ and taking into account the smallness of the parameter $\alpha \approx 0.07$, we find from (25) that the probability of electron transfer can be as high as $p_2^{max} \approx 0.9$. Since the right-hand part of inequality (27) is not rigorously satisfied, the value of p_2^{max} may actually be somewhat lower; nevertheless, it is obvious that a slight difference in the sizes of the QDs does not lead to complete suppression of the effect of resonance electron transfer between the dots.

If the barrier height is increased to $U \approx \pi^2n^2/2m^*a^2$ ($n = 2, 3, \ldots$), levels $2n + 1$ or $2n + 2$ play the role of the transport level (the one close to the top of the barrier). These levels are formed due to the splitting of the $(n + 1)th$ levels in the individual QDs (note that n must be odd: for even n, the matrix elements λ_1 and λ_2 are anomalously small, because the deep and the excited levels of the structure have wave functions of nearly the same parity with respect to the centers of the corresponding QW). When the barrier height increases, it becomes easier to satisfy the condition $(2m^*b^2U)^{1/2} \gg 1$ for the localization of the ground states of individual QDs, and the spacing b between the dots can be reduced by about a factor of n. In turn, this circumstance makes it easier to satisfy inequality (29) and, accordingly, inequality (27). However, in this case, the parameter a/b is no longer small, and some of the approximations made become invalid. Thus, the issue of laser-induced electron transfer between the ground states of deep QWs requires a separate analysis, which we plan to do in the course of future research.

Finally, let us estimate the optimum value of the amplitude E_0 of the electric-field strength for the electromag-

netic wave. Let us assume again that $(\varepsilon_2 - \varepsilon_1)/|\lambda_1| \approx 0.3$; then, for a nanostructure with $a = 60$ nm, $b = 240$ nm, $\delta a = 0.2$ nm, and $(U - U_{c3})/U_c \approx 0.1$, we obtain from (23) and (24) $E_0 \approx 3$ V/cm, which corresponds to the pulse intensity $I \approx 10^{-2}$ W/cm^2. Note that, for such a value of E_0, disregarding the term in (1) that is quadratic with respect to the vector potential is justified.

Estimation of the optimum duration of the laser pulse for the above set of nanostructure parameters by formula (26) yields $T \sim 1$ ns. The value of T must be smaller than the lifetime τ of an electron in the excited state with respect to a spontaneous transition to the ground state with emission of a photon or phonon, since the unitary evolution of an electron in the field of an electromagnetic wave is otherwise broken. According to [15], the value of τ depends heavily on the nanostructure parameters and may attain 1 μs, so that the condition $T \ll \tau$ will be satisfied.

5. CONCLUSION

We studied theoretically the quantum dynamics of an electron in a nanostructure consisting of two tunneling-coupled QDs under the action of a laser pulse. We derived an analytical expression for the probability of an induced transfer of an electron between the states localized in different QDs, with the possible spread in the QD sizes taken into account. Such a transfer occurs through resonance excitation of an electron to a level that, being close to the top of the barrier, has a wave function that is delocalized between the QDs. This effect is an analogue of the Rabi oscillations for a three-level system. We determined the dependences of the frequency and the duration of a laser pulse corresponding to the maximum probability of the electron transfer on the nanostructure energy spectrum and dipole matrix elements. Within the model considering QDs of near cubic shape, we formulated the criteria that the nanostructure characteristics (the QD size, the spacing between the QDs, and the barrier height) have to comply with in order to make resonance electron transfer possible. We concluded that a slight processing spread in the QD sizes results in only an insignificant reduction in the electron-transfer probability ($p_2^{max} \approx 0.9$). We believe that, with the current level of nanostructure technology, this effect can be observed experimentally. The optimum parameters of the laser pulse are to be determined from the characteristics of a specific nanostructure or found by trial and error. Apparently, this effect can be used to implement operations with qubits in some models of quantum computers [16].

ACKNOWLEDGMENTS

REFERENCES

1. L. Jacak, P. Hawrylak, and A. Wójs, *Quantum Dots* (Springer, Berlin, 1998).

2. V. F. Elesin, Yu. V. Kopaev, L. A. Openov, and A. I. Podlivaev, Fiz. Tekh. Poluprovodn. (St. Petersburg) **28**, 1334 (1994) [Semiconductors **28**, 755 (1994)].

3. A. M. Bychkov, L. A. Openov, and I. A. Semenihin, Pis'ma Zh. Éksp. Teor. Fiz. **66**, 275 (1997) [JETP Lett. **66**, 298 (1997)].

4. O. P. Pchelyakov, Yu. B. Bolkhovityanov, A. V. Dvurechenskiĭ, *et al.*, Fiz. Tekh. Poluprovodn. (St. Petersburg) **34**, 1281 (2000) [Semiconductors **34**, 1229 (2000)].

5. L. A. Openov, Europhys. Lett. **55**, 539 (2001).

6. V. F. Elesin and A. V. Tsukanov, Fiz. Tekh. Poluprovodn. (St. Petersburg) **34**, 1404 (2000) [Semiconductors **34**, 1351 (2000)].

7. V. F. Elesin, I. Yu. Kateev, and A. I. Podlivaev, Fiz. Tekh. Poluprovodn. (St. Petersburg) **34**, 1373 (2000) [Semiconductors **34**, 1321 (2000)].

8. M. S. Sherwin, A. Imamoglu, and T. Montroy, Phys. Rev. A **60**, 3508 (1999).

9. F. Grossmann, T. Dittrich, P. Jung, and P. Hänggi, Phys. Rev. Lett. **67**, 516 (1991).

10. A. V. Krasheninnikov, S. N. Molotkov, S. S. Nazin, and L. A. Openov, Zh. Éksp. Teor. Fiz. **112**, 1257 (1997) [JETP **85**, 682 (1997)].

11. L. A. Openov, Phys. Rev. B **60**, 8798 (1999).

12. J. H. Oh, D. Ahn, and S. W. Hwang, Phys. Rev. A **62**, 052306 (2000).

13. A. I. Yakimov, A. V. Dvurechenskiĭ, A. I. Nikiforov, and O. P. Pchelyakov, Pis'ma Zh. Éksp. Teor. Fiz. **68**, 125 (1998) [JETP Lett. **68**, 135 (1998)].

14. V. M. Galitskiĭ, S. P. Goreslavskiĭ, and V. F. Elesin, Zh. Éksp. Teor. Fiz. **57**, 207 (1969) [Sov. Phys. JETP **30**, 117 (1969)].

15. K. Nomoto, R. Ugajin, T. Suzuki, and I. Hase, J. Appl. Phys. **79**, 291 (1996).

16. A. A. Larionov, L. E. Fedichkin, and K. A. Valiev, Nanotechnology **12**, 536 (2001).

Translated by M. Skorikov

<center>

LOW-DIMENSIONAL
SYSTEMS

</center>

Recombination Statistics and Kinetics in Semiconductor Nanostructures

A. V. Sachenko and Yu. V. Kryuchenko*

Institute of Semiconductor Physics, National Academy of Sciences of Ukraine, Kiev, 03028 Ukraine
*e-mail: div47@isp.kiev.ua
Submitted March 18, 2003; accepted for publication April 16, 2003

Abstract—A new approach to describing the observed features of recombination in semiconductor nanostructures is suggested. In addition to radiative exciton recombination, a nonradiative channel of exciton Auger recombination involving local interface states is taken into account. Recombination statistics and kinetics in semiconductor nanocrystals are considered both for low and high densities of local interface states. The case of a low excitation level, where a statistical approach to recombination in isolated nanocrystals is no longer valid, is analyzed. It is shown that the presence of nonradiative exciton Auger recombination accounts both for the linear dependence of photoluminescence intensity on the excitation level and for the low photoluminescence quantum efficiency. © 2004 MAIK "Nauka/Interperiodica".

1. INTRODUCTION

In numerous papers that have appeared in recent years (e.g., [1–8]), the photoluminescence (PL) of semiconductor nanostructures and nanocrystals was attributed to exciton radiative recombination. The exciton mechanism of PL became especially popular because the exciton binding energy and the oscillator strength for excitonic transitions increase sharply with decreasing nanocrystal size not only due to quantum confinement, but also due to the effect of "dielectric enhancement" [6–12]. The enhancement of Coulomb attraction between a hole and an electron in semiconductor nanocrystals surrounded by an insulator is produced by the redistribution of the electric field due to the smaller permittivity of the insulator compared to that of the semiconductor.

Calculations show that the exciton binding energy and oscillator strength for excitonic transitions increase with decreasing dimensionality, i.e., for the transition from quantum wells to quantum wires and quantum dots for a fixed nanocrystal thickness [10, 12].[1] It follows that, for one- and zero-dimensional nanocrystals, the exciton mechanism of PL can dominate over radiative interband recombination even at room temperature. Since PL in semiconductor nanocrystals is excited by band-gap light, theoretical description of excitonic PL in such structures must take into account that there are two coupled subsystems: an excitonic subsystem and an electron–hole subsystem. Such an approach was used in a number of publications [2, 4, 5, 12].

Until recently it was assumed that, for fairly low excitation levels, PL of semiconductor nanocrystals is related to excitonic radiative recombination, whereas nonradiative recombination involves free electron–hole pairs that recombine at defects at the nanocrystal interfaces. In this paper, we suggest a different recombination model. According to this model, nonradiative recombination is also excitonic, and its mechanism is exciton Auger dissociation at local centers at the interface. We analyze both exciton and free electron and hole recombination statistics and kinetics for the limiting cases of high and low densities of local states at the interfaces. We show that, compared to other models, a number of experimental facts find a simpler and more consistent explanation if our model is used.

We perform specific estimations and calculations using the parameters characteristic of silicon nanocrystals, although the results obtained have a more general significance and can be used in describing the properties of other semiconductor nanostructures and nanocrystals.

2. RECOMBINATION MODEL

In what follows, we explain the behavior of PL in silicon nanocrystals by including the mechanism of nonradiative exciton Auger recombination at deep local centers. For crystalline silicon, this mechanism was analyzed in [13–15], where it was shown that in some cases it controls the effective lifetime of free charge carriers. For this mechanism, the exciton nonradiatively dissociates at a bulk local center emitting a hot electron (or hole) into the corresponding band. As shown in [13, 14], the probability of an exciton Auger process in crystalline silicon is considerably higher than the probability of multiphonon recombination, since local car-

---

[1] Since for a quantum dot an exciton is not a mobile quasiparticle, one can use the term exciton only with certain reservations in this situation. However, it is important that the electron–hole spectrum remains strongly renormalized by Coulomb attraction.

rier density in an exciton is determined by its Bohr radius and is rather high (on the order of 3×10^{18} cm^{-3}). In nanocrystals, due to the effects of quantum confinement and dielectric enhancement, the characteristic exciton size is substantially smaller than the Bohr radius of the bulk exciton. Therefore, in nanocrystals we can expect a further increase in the probability of an exciton Auger process. In addition, if the nanocrystal size is decreased, not only bulk but also interface local centers become involved in the exciton Auger process (due to the increase in overlap of the wave functions of the exciton and these centers). Moreover, for quantum wires and especially for quantum dots of size smaller than 5 nm, the interface centers must play the major role, since, for structures of such a small size, the density of deep bulk centers can be vanishingly low.

Unfortunately, the microscopic theory of exciton Auger recombination in quantum wires and quantum dots is not yet well developed. Therefore, we assume that in the systems considered, just as in crystalline silicon, the above mechanism can result in small characteristic times of nonradiative recombination (smaller than the time of radiative exciton recombination). Moreover, for quantum dots, the time of exciton nonradiative recombination can be an oscillating function of the quantum dot diameter due to the discreteness of the energy spectrum; this circumstance provides more possibilities for explaining the experimental results.

Finally, we assume that the following hierarchy of relaxation processes is valid. The smallest times correspond to the cooling of electron–hole pairs generated by light and the formation of excitons. The times of nonradiative and radiative exciton recombination are longer, and the time of multiphonon recombination of electrons (and/or holes) is the longest.

Note that the phenomenological equations of continuity that describe the relation between the densities of electrons, holes, and excitons in nanocrystals can only be used if the statistical approach is justified, i.e., if N, $N_x \gg 1$, where N and N_x are the numbers of electrons and excitons in a nanocrystal.

However, for the excitation levels used in the experiment, the opposite condition is often satisfied, namely, N, $N_x \le 1$. For example, in the case of pulsed laser excitation (with excitation intensity $I = 10^{22}$ cm^{-2} s^{-1}, pulse duration on the order of 10^{-8} s, radiation focused on the area of 1 mm^2, light absorption coefficient $\alpha \approx 10^4$ cm^{-1}), only a single electron–hole pair is generated in a quantum dot of diameter 3 nm; subsequently, this pair forms an exciton. If there is at least one local level at the interface of the quantum dot considered, then the nonradiative exciton time of decay by the Auger process can be very short. If the number of local interface levels is increased, the nonradiative exciton lifetime becomes even shorter. Only those nanocrystals for which the exciton radiative time is shorter than the nonradiative time emit radiation. The greater the average number of local interface levels in nanocrystals, the smaller the

number of radiating quantum dots. Therefore, for nanostructures the PL intensity should decrease as the density of surface levels increases; the PL decay time should also decrease. This is precisely what is observed experimentally [4].

The presence of local interface levels (to be more exact, the relation between the number of free electrons and/or excitons and the number of interface centers) largely determines the recombination mechanism in nanocrystals also in the case where the inequalities N, $N_x \gg 1$ are satisfied. For example, in case I, where the number of the local centers N_t in a nanocrystal is much greater than N_x, we have the following scenario of recombination processes. At first, a hot electron–hole pair is thermalized, and then this pair forms an exciton. Then there is competition between the two processes: the process of excitonic radiative recombination and the process of nonradiative Auger dissociation of excitons at a local center with simultaneous emission of a hot electron or hole into the corresponding band. Then the hot carriers are thermalized and, finally, multiphonon recombination with a long characteristic time τ_n sets in. After switching the illumination on, at first the filling of local levels by electrons changes so that the electron and hole flows from the levels to the free bands and the backflows become practically equal. In this case, the exciton density is very low compared to the density of free electrons (or holes), and the excitonic PL intensity is extremely low. For short-pulse excitation, when the stationary state during the pulse is not established, the excitonic luminescence decays with a characteristic time τ_x equal to the total excitonic recombination time, and the density of free electrons (or holes) at first grows with the same τ_x and then decreases with a large characteristic time τ_n.

In case II, in which the inequalities N, $N_x \gg 1$ are satisfied but at the same time the inequality $N_t \ll N_x$ is valid, recombination in nanocrystals occurs in the following way. After binding thermalized electron–hole pairs into excitons, excitonic radiative recombination and nonradiative Auger recombination at deep centers occur simultaneously. In addition, electron–hole pairs that have not formed excitons recombine by the nonradiative multiphonon mechanism. In this case, excitonic nonradiative Auger recombination at local centers has the following specific features. At first, the filling of local centers is changed so that the probabilities of Auger processes with emission of hot holes and hot electrons become equal. The next stage of the recombination process corresponds to the simultaneous dissociation of two excitons at the same center with emission of a hot electron and a hot hole. This is actually the final stage of the process of nonradiative excitonic recombination at local centers. After thermalization, the pair can again form an exciton and take part in recombination.

In our case, the relation between the densities of excitons and free electron–hole pairs depends on the characteristic times τ_x and τ_n, excitation intensity I,

temperature T, and exciton binding energy E_x. Thus, the ratio of the exciton density to the density of electron–hole pairs increases with decreasing temperature T and with increasing exciton binding energy E_x; this is used as one of the proofs of the excitonic nature of luminescence in silicon nanostructures.

3. RECOMBINATION STATISTICS AND KINETICS

Now we calculate the stationary densities of excitons and free charge carriers, as well as the exciton and free carrier relaxation times for cases I and II for nanocrystals with specific parameters. We will show how to interpret some experimental results for silicon nanostructures within the framework of our recombination model.

First, we estimate the surface density of local levels at the interface; this density corresponds to the presence of at least a single local center in the quantum wire (quantum dot). In what follows, all estimations and numerical calculations are carried out for the case where the diameters of the quantum wire and quantum dot d are equal to 2.5 nm and the length of the quantum wire is $h = 10$ μm. To find the desired density, we use the condition $N_S S = 1$, where N_S is the surface density of the centers and S is the surface area equal to $\pi d h$ for a quantum wire and πd^2 for a quantum dot. Substitution of the parameters yields values on the order of 10^9 cm^{-2} for a quantum wire and 3×10^{12} cm^{-2} for a quantum dot. The corresponding "bulk" densities are 10^{16} cm^{-3} and 10^{20} cm^{-3}, respectively. The latter values are to be compared with the bulk densities of excitons and electrons in nanocrystals, i.e., with the numbers of electrons and excitons in a nanocrystal divided by its volume.

As stated above, for relatively low excitation intensities corresponding, for example, to excitation by a nitrogen laser, we cannot use the statistical approach to describe recombination in quantum dots, since in this case the conditions N, $N_x \leq 1$ are satisfied. The statistical approach can only be used for sufficiently high excitation levels; under these conditions, the role of higher-order Auger processes is greatly increased, resulting in a sublinear dependence of the PL intensity on the excitation level (e.g., see [4]).

For relatively low excitation intensities, the statistical approach can only be used for quantum wells and quantum wires. In the latter case, it is convenient to deal with densities per unit length [12]. Using such normalized densities, we write down the following system of equations describing recombination kinetics and statistics for quantum wires far from equilibrium:

$$\frac{dn_x}{dt} = \gamma_1 n p - \gamma_2 n_x - \tau_{xr}^{-1} n_x - G_n n_t n_x - G_p p_t n_x, \quad (1)$$

$$\frac{dn}{dt} = -\gamma_1 n p + \gamma_2 n_x + G_n n_t n_x - C_n n p_t + \alpha^* d^2 I, \quad (2)$$

$$\frac{dn_t}{dt} = -G_n n_t n_x + C_n n p_t + G_p p_t n_x - C_p n_t p, \quad (3)$$

$$n = p + p_t, \quad (4)$$

where n, n_x, p, and n_t are the densities of electrons in the conduction band, excitons, holes in the valence band, and electrons at the local centers, respectively; $p_t = N_t - n_t$; N_t is the density of the local centers; α^* is the effective absorption factor taking into account the multiple reflection of light; I is the illumination intensity; γ_1 and γ_2 are the probabilities of exciton formation and dissociation; τ_{xr} is the radiative exciton lifetime; G_n and G_p are the coefficients for Auger processes of exciton and dissociation at local centers with emission of a hot electron and a hot hole; and C_n and C_p are the coefficients of multiphonon capture of an electron and a hole by the local center. Obviously, γ_1, γ_2, τ_{xr}, G_n, G_p, C_n, and C_p are functions of the shape and size of nanocrystals, as well as temperature. Establishing the form of these functions is the aim of the microscopic theory.

Let us consider the steady-state case. Using Eq. (3), we can find the electron density on the local levels:

$$n_t = \frac{(G_p n_x + C_n n) N_t}{(G_n + G_p) n_x + C_n n + C_p p}. \quad (5)$$

Summing Eqs. (1), (2) and taking Eq. (5) into account, we derive the generation–recombination balance equation

$$\left(\frac{1}{\tau_{xr}} + \frac{G_p (G_n n_x + C_p p) N_t}{(G_n + G_p) n_x + C_n n + C_p p} \right) n_x$$
$$+ \frac{C_n (G_n n_x + C_p p) N_t n}{(G_n + G_p) n_x + C_n n + C_p p} = \alpha^* d^2 I. \quad (6)$$

Using Eqs. (1), (4), and (5) and the thermodynamic relation between γ_1 and γ_2 [12], we obtain the expression relating the exciton and free-electron densities:

$$n_x \approx n \left(n - \frac{(G_n n_x + C_p p) N_t}{(G_n + G_p) n_x + C_n n + C_p p} \right)$$
$$\times [n_0 \exp(-E_x / kT)]^{-1}, \quad (7)$$

where n_0 is the exciton statistical factor and E_x is the exciton binding energy. Solving system of Eqs. (6) and (7), we can find the densities of free electrons and excitons.

In case I, in which the exciton density is much smaller than the density of local levels, for silicon quantum wires we can use the fact that the probability of the Auger process with emission of a hot electron is higher than the probability of the Auger process with emission of a hot hole; i.e., $G_n > G_p$. Moreover, we assume that the following inequalities are valid:

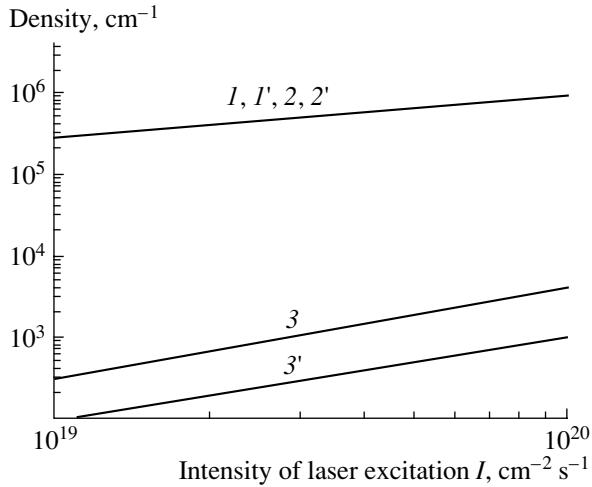$$C_n n \gg G_n n_x, \quad C_n n \gg C_p p, \quad G_n N_t \tau_{xr} \gg 1.$$

Density, cm^{-1}

Fig. 1. Illumination-intensity dependence of the densities of (*1, 1'*) free electrons, (*2, 2'*) holes trapped at local centers, and (*3, 3'*) excitons in silicon quantum wires at $T = 300$ K and for the exciton binding energy $E_x = 0.1$ eV. The densities of interface local centers N_t (cm^{-1}) are (*1–3*) 3×10^6 and (*1'–3'*) 10^7.

By using these inequalities, we can reduce the generation–recombination balance equation (6) to the form

$$G_n N_t n_x \approx \alpha^* d^2 I. \qquad (8)$$

Using Eq. (8), we obtain the following expression for n_x:

$$n_x \approx \alpha^* d^2 I / G_n N_t. \qquad (9)$$

In this case, the internal quantum efficiency of excitonic PL is

$$\eta \approx 1/\tau_{xr} G_n N_t, \qquad (10)$$

and the density of free electrons can be determined from the following condition:

$$p_t \approx \frac{G_n N_t n_x}{C_n n} \approx n, \qquad (11)$$

where $p_t = N_t - n_t$ is the density of holes trapped at local levels. Taking Eq. (9) into account and solving Eq. (11), we obtain

$$n \approx \sqrt{\alpha^* d^2 I / C_n}. \qquad (12)$$

Substituting the above expressions for n_x and n into the inequality $C_n n \gg G_n n_x$, we find the criterion of the validity of case I,

$$\frac{\sqrt{\alpha^* d^2 I C_n}}{G_n N_t} \ll 1. \qquad (13)$$

We can see from expressions (9) and (12) that in this case the exciton density linearly depends on illumination intensity, and the density of free electrons and holes trapped at local levels is proportional to $I^{1/2}$. Thus,

the internal quantum efficiency of excitonic PL is significantly smaller than unity and decreases with increasing density of local centers as $1/N_t$.

In Fig. 1, we plot the densities of holes trapped at local interface levels, free electrons, and excitons as functions of the excitation intensity. These densities were obtained by numerical solution of the system of Eqs. (5)–(7) for the following set of parameters:

$$n_0 = 10^6 \text{ cm}^{-1}, \quad \alpha^* = 2 \times 10^5 \text{ cm}^{-1}, \quad d = 2.5 \text{ nm},$$

$$T = 300 \text{ K}, \quad G_n = 10^2 \text{ cm/s}, \quad G_p = 10 \text{ cm/s},$$

$$C_n = 1 \text{ cm/s}, \quad C_p = 0.1 \text{ cm/s}, \quad \tau_{xr} = 10^{-5} \text{ s}.$$

It can be seen from Fig. 1 that, in the range of excitation intensities considered for the steady-state case, the exciton density is several orders of magnitude lower than the density of free electrons and holes trapped at the interface levels. The increase in the densities of free electrons and trapped holes with illumination intensity is sublinear, and the increase in the exciton density is almost linear. Finally, it can be seen from Fig. 1 that the densities of free electrons and trapped holes are practically equal.

Next we analyze the recombination kinetics for the case of short excitation pulses where the pulse duration t_i is much smaller than the above characteristic times, except for the thermalization times and the time of exciton formation from electron–hole pairs. In this case, during the pulse duration a quasi-equilibrium between electron–hole pairs and excitons is established, and the total density of excitons and electron–hole pairs is determined by the relation

$$n_x + n = \alpha^* d^2 I t_i, \qquad (14)$$

where

$$n_x \approx \frac{n^2}{n_0 \exp(-E_x/kT)}.$$

In what follows, we only consider the case in which the exciton binding energy E_x is sufficiently large, so that $n_x \gg n$. Thus, for example, for an illumination intensity of 10^{22} cm^{-2} s^{-1}, excitation pulse duration of 10^{-8} s, temperature of 300 K, and binding exciton energy $E_x = 0.3$ eV, the density of free electron–hole pairs is estimated to be only 1% of the exciton density.

At time t_i, which corresponds to switching the illumination pulse off, we have

$$n_x(t = t_i) \approx \alpha^* d^2 I t_i, \qquad (15)$$

and the densities of free electrons and holes are negligible. Then Eqs. (1) and (2) assume the following form:

$$\frac{dn_x}{dt} \approx -\frac{n_x}{\tau_x^{\text{eff}}}, \qquad (16)$$

$$\frac{dn}{dt} = G_n n_{t0} n_x - C_n p_{t0} n, \qquad (17)$$

where

$$\tau_x^{\text{eff}} = (\tau_{xr}^{-1} + G_n n_{t0})^{-1}, \quad p_{t0} = N_t - n_{t0},$$

and n_{t0} is the density of trapped electrons before the illumination is switched on. The function

$$n_x(t) \approx \alpha^* d^2 I t_i \exp(-t/\tau_x^{\text{eff}}) \tag{18}$$

is a solution of Eq. (16) with initial condition (15). With allowance for Eq. (18), the solution of Eq. (17) has the following form:

$$n(t) \approx \frac{\alpha^* d^2 I t_i G_n n_{t0} \tau_x^{\text{eff}}}{1 - \tau_x^{\text{eff}} C_n p_{t0}} \tag{19}$$

$$\times [\exp(-C_n p_{t0} t) - \exp(-t/\tau_x^{\text{eff}})].$$

Expression (19) is valid if $\tau_x^{\text{eff}} C_n p_{t0} < 1$.

In Fig. 2, we show the time dependence of excess densities and "instantaneous" characteristic relaxation times $\tau_i = -n_i/(dn_i/dt)$ for excitons and free electrons. The plots were obtained by numerical solution of a system of kinetic equations for excess densities for arbitrary deviations from equilibrium. The following values of the parameters were used in the calculations:

$$I = 10^{21} \text{ cm}^{-2} \text{ s}^{-1}, \quad E_x = 0.3 \text{ eV}, \quad \gamma_1 = 10^9 \text{ cm/s},$$

$$N_t = 10^6 \text{ cm}^{-1}, \quad n_{t0} = 0.9 N_t.$$

The numerical values of the other parameters are the same as in Fig. 1. The excitation illumination pulses were assumed to be rectangular, and their duration was $t_i = 10^{-8}$, 3×10^{-8}, and 6×10^{-8} s. We can see from Fig. 2a that, for such short pulses, the densities of excitons and electrons do not attain their steady-state values. We also see that, after switching the pulse off, for excitons the relaxation kinetics is monotonic, whereas for electrons it is nonmonotonic, in agreement with the above theoretical analysis. At the same time, in Fig. 2b we see that the pulses of specified duration are not sufficiently short for the instantaneous relaxation times to remain constant during the entire period of relaxation. For excitons, the instantaneous relaxation times first increase and then decrease, whereas for electrons they first decrease and then increase. The cause of this behavior is the variation in filling of interface levels by electrons during relaxation.

The above results allow us to explain why in the case of an unpassivated interface the PL intensity is extremely low. The reason is that excitons formed from electron–hole pairs very rapidly dissociate nonradiatively at local interface levels, and the dissociation time is the shorter, the greater the density of local levels.

In case II, the densities of free electrons and holes are equal. If the inequality
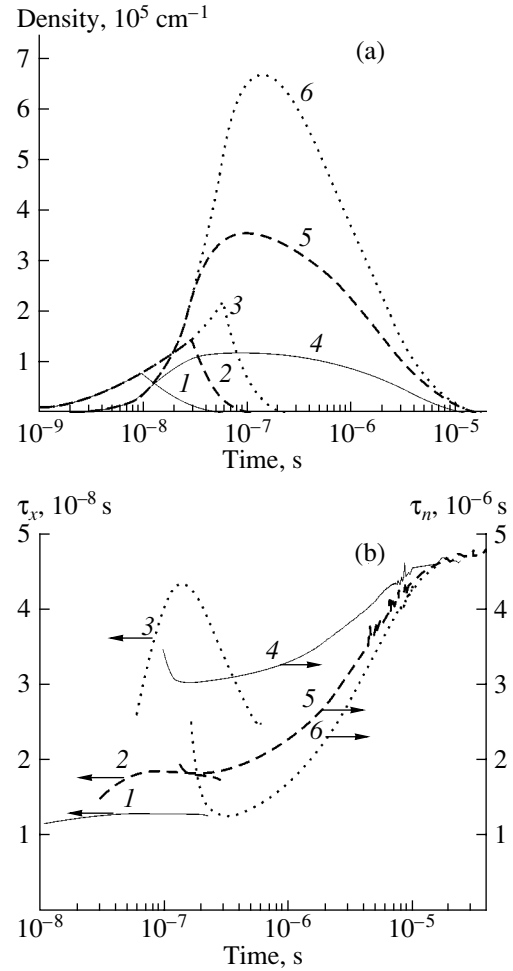
$$(G_n + G_p) n_x \gg (C_n + C_p) n$$

Fig. 2. (a) Time dependence of the excess densities of excitons and free electrons and (b) of the instantaneous relaxation times for silicon quantum wires; $T = 300$ K, $E_x = 0.3$ eV, $N_t = 10^6$ cm^{-1}, and $I = 10^{21}$ cm^{-2} s^{-1}. The curves correspond to (1–3) excitons and (4–6) free electrons. Excitation-pulse durations t_{imp} are (1, 4) 10^{-8}, (2, 5) 3×10^{-8}, and (3, 6) 6×10^{-8} s.

is taken into account, the equation of generation–recombination balance under steady-state conditions assumes the following form:

$$\frac{n_x}{\tau_x} + \frac{n}{\tau_n} = \alpha^* d^2 I, \tag{20}$$

where

$$\tau_x = \left(\frac{1}{\tau_{xr}} + \frac{G_n G_p N_t}{G_n + G_p}\right)^{-1}, \quad \tau_n = \frac{G_n + G_p}{G_n C_n N_t}.$$

Thus, the densities of excitons and electron–hole pairs are related by

$$n_x = \frac{n^2}{n_0 \exp(-E_x/kT) + 1/\gamma_1 \tau_x}. \tag{21}$$
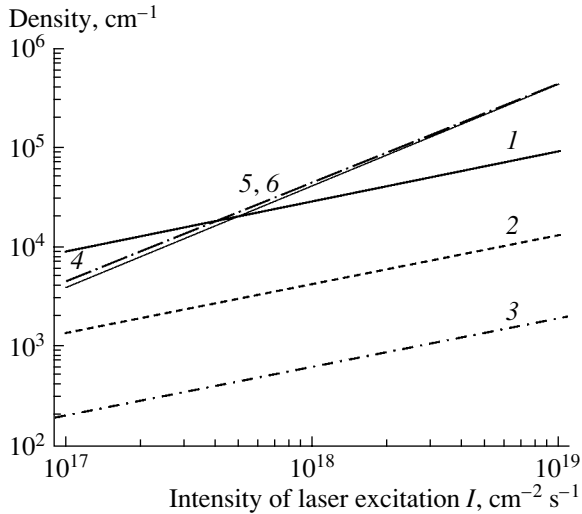
Density, cm^{-1}

Fig. 3. Illumination-intensity dependence of the densities of (1–3) electron–hole pairs and (4–6) excitons for silicon quantum wires; $T = 300$ K, $N_t = 10^4$ cm^{-1}. The exciton binding energies E_x are (1, 4) 0.1, (2, 5) 0.2, and (3, 6) 0.3 eV.
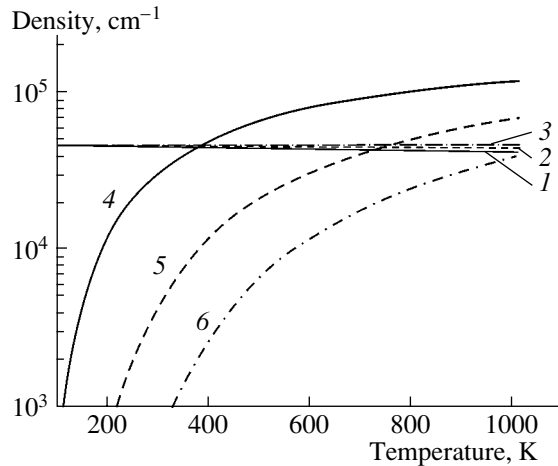
Density, cm^{-1}

Fig. 4. Temperature dependence of the density of (1–3) excitons and (4–6) electron–hole pairs in silicon quantum wires for the excitation intensity $I = 10^{18}$ cm^{-2} s^{-1}. The exciton binding energies E_x are (1, 4) 0.1, (2, 5) 0.2, and (3, 6) 0.3 eV.

We note that the term $1/\gamma_1\tau_x$ was earlier disregarded. The estimations using the values $\gamma_1 = 10^9$ cm/s and $\tau_x = 10^{-6}$ s show that this term can be important only for the case of large exciton binding energies and low temperatures, where $E_x/kT > 25$. Its inclusion affects only the density of electron–hole pairs, which in this case is significantly lower than the density of excitons.

As can be seen from expressions (20) and (21), the dependence of the densities of excitons and electron–hole pairs on illumination intensity and on other parameters in the equations can generally be found analytically. However, for silicon nanocrystals under typical conditions, the exciton recombination rate is consider-

ably higher than the rate of recombination of electron–hole pairs; i.e. $n_x/\tau_x \gg n/\tau_n$. In this case, we obtain

$$n_x \approx \alpha^* d^2 I\tau_{rx}, \tag{22}$$

$$n \approx \left\{\left[n_0\exp\left(-\frac{E_x}{kT}\right) + \frac{1}{\gamma_1\tau_x}\right]\alpha^* d^2 I\tau_x\right\}^{1/2}. \tag{23}$$

It follows that, just as for case I, the exciton density increases linearly with illumination intensity, whereas the density of electron–hole pairs grows as $I^{1/2}$.

The results of solving Eqs. (17) and (18) are shown in Fig. 3, where we plot the densities of excitons and electron–hole pairs as functions of the illumination intensity. In the calculations, we used the density of local interface centers $N_t = 10^4$ cm^{-1} and the same set of remaining parameters as for Fig. 1.

It can be seen from Fig. 3 that, first, the dependence of the exciton density on the illumination intensity is practically always linear, even for the case where the density of electron–hole pairs exceeds the exciton density. The slight superlinearity of curve 4 in the region of low excitation intensities is due to the fact that, in this case, the strong inequality $n_x/\tau_x \gg n/\tau_n$ is not satisfied. Second, although the density of electron–hole pairs decreases substantially with increasing exciton binding energy, the exciton density remains almost unchanged. Finally, we can see from Fig. 4, where the temperature dependence of the densities of excitons and electron–hole pairs is shown, that the temperature dependence of the exciton density is relatively weak. This fact shows that, for all the situations considered, the inequality $n_x/\tau_x > n/\tau_n$ is satisfied; i.e., the rate of exciton recombination exceeds the rate of recombination of electron–hole pairs.

In case II, for short excitation pulses, recombination kinetics calculated in the same approximations as for case I but with allowance for the relation $p = n$ and inequality $n_x/\tau_x \gg n/\tau_n$ is described by

$$n_x(t) \approx \alpha^* d^2 It_i\exp\left(-\frac{t}{\tau_x}\right), \tag{24}$$

$$n(t) \approx \sqrt{\alpha^* d^2 It_i n_0\exp\left(-\frac{E_x}{kT}\right)}\exp\left(-\frac{t}{2\tau_x}\right); \tag{25}$$

i.e., the characteristic electron-density decay time is $2\tau_x$.

4. DISCUSSION

Now let us compare the results for cases I and II. We can see from Figs. 1 and 3 that the density of free electrons in case I is comparable to the total density of excitons and electron–hole pairs in case II, although the density of the surface centers in case I is three orders of magnitude higher than in case II. To obtain similar results for nonradiative, purely multiphonon recombination, one has to assume that in addition to deep levels

there are fairly shallow levels (trapping levels for holes) with a high density and that the density of deep levels remains low for any degree of interface passivation. At the same time, in our approach, the accumulation of a large number of holes at local deep centers is naturally explained by the fast Auger process of exciton dissociation (with emission of hot electrons).

In the above approach, the size of the silicon nanocrystals and the effect of the environment (the density of the interface centers) were assumed to be unchanged. However, it is obvious that, in order to compare with experiment, it is necessary to perform averaging both over the nanocrystal size and over the parameters of the interface environment. Nevertheless, one can explain a number of experimental results obtained in [2, 3, 5, 16] for porous silicon by using our approach even disregarding the distribution of wire sizes but taking into account the fact that wires of the same size can have different surroundings. In particular, according to the results obtained for cases I and II, excitonic PL intensity $I_x^{PL} = n_x/\tau_{xr}$ increases with decreasing temperature because of the increase in exciton density and in the probability of radiative excitonic recombination $\tau_{xr}^{-1} \propto T^{-1/2}$ [12]. This increase in the PL intensity agrees with the experimental results in [2]. The larger increase in I_x^{PL} with decreasing temperature observed in [16] for as-prepared samples of porous silicon can be attributed to the decrease in exciton recombination rate in the crystalline substrate. The experimental temperature dependence of the free carrier density obtained for oxidized wires with a low density of interface levels [17] qualitatively agrees with the results in Fig. 4. The linear dependence of the excitonic PL intensity on the illumination intensity observed in porous silicon for rather low excitation levels [3, 5] also finds a natural explanation within the framework of our model. It is related to the fact that both radiative and nonradiative excitonic-recombination rates depend quadratically on the density of electron–hole pairs.

The above results account for the substantial change in the dependence of the PL internal quantum efficiency on the density of local interface centers. Thus, for low densities of local levels (Figs. 3, 4), the PL internal quantum efficiency for silicon nanocrystals is estimated to exceed 10%, whereas for high densities of local levels (Fig. 1) it is less than 0.01%. These examples show the important role played by the environment of individual nanocrystals; it can change the PL internal quantum efficiency for individual nanocrystals by orders of magnitude even if the other parameters (e.g., the nanocrystal size) are the same.

Note that the recombination model, which does not take into account nonradiative dissociation of excitons at local interface centers, cannot explain the small values of PL internal quantum efficiency in silicon nanostructures consisting of nanocrystals of approximately
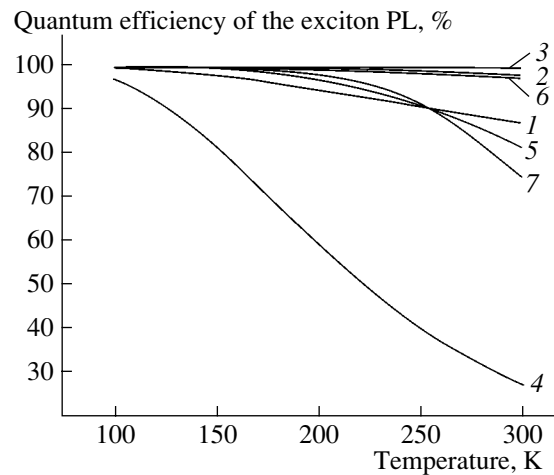

Fig. 5. Temperature dependence of the internal quantum efficiency of excitonic PL for silicon quantum wires for the excitation intensity $I = 10^{19}$ cm^{-2} s^{-1}. The following values of the parameters E_x (eV) and N_t (cm^{-1}) were used in the calculation: (1) 0.1 and 10^6, (2) 0.2 and 10^6, (3) 0.3 and 10^6, (4) 0.1 and 10^7, (5) 0.2 and 10^7, (6) 0.3 and 10^7, and (7) 0.3 and 10^8.

the same size with a large average density of local levels. This is illustrated in Fig. 5, where the temperature dependence of the internal quantum efficiency of excitonic PL is shown for the above set of parameters (except for the nonradiative exciton lifetime τ_{xn}, which was assumed to be infinite). The parameters for the various curves are the values of the exciton binding energy and the density of local interface centers. In Fig. 5 we can see that the quantum efficiency tends to 100% with increasing E_x and decreasing temperature even for very high densities of local interface centers.

In fact, the methods of self-organization that are widely used in the preparation of semiconductor nanostructures do not allow one to obtain nanocrystals of the same size, especially those with the same interfaces. The spread in nanocrystal size can itself substantially complicate the interpretation of experimental results. As an example, we can cite the results of [8]. In this paper, PL of individual silicon quantum dots was studied after the preparation of an ensemble of silicon nanocrystals of similar sizes. It appeared that only a small fraction of all these nanocrystals emits light. This may mean that either their sizes slightly differ, thus affecting the dependence of radiative exciton lifetime on the size of nanocrystals (see [12]), or that different quantum dots have different interfaces and only the interfaces of certain nanocrystals are properly passivated (the latter factor is more probable).

5. CONCLUSION

In this paper, we suggested a new model of recombination in semiconductor nanostructures including the

Auger mechanism of excitonic nonradiative recombination at deep interface local levels.

We have shown that, even for individual nanocrystals when a statistical approach may be used to describe recombination, recombination laws can appear to be completely different for structures with highly dissimilar densities of interface centers.

We established that our model can consistently explain a number of experimental results obtained for silicon nanostructures. In particular, by including only the nonradiative mechanism of excitonic recombination with the lifetime depending on the density of local interface levels, one can explain both the linearity of the PL intensity dependence on the excitation level and the low PL quantum efficiency for nanostructures with an unpassivated interface.

We also showed that, if the nonradiative channel of excitonic recombination is dominant, the density of free charge carriers in silicon nanostructures should increase as $I^{1/2}$ increases with illumination intensity I.

REFERENCES

1. A. G. Cullis, L. T. Canham, and P. D. J. Calcott, J. Appl. Phys. **82**, 909 (1997).

2. P. K. Kashkarov, B. V. Kamenev, E. A. Konstantinova, *et al.*, Usp. Fiz. Nauk **168**, 577 (1998) [Phys. Usp. **41**, 511 (1998)].

3. D. Kovalev, H. Heckler, G. Polissky, and F. Koch, Phys. Status Solidi B **215**, 871 (1999).

4. A. V. Sachenko, É. B. Kaganovich, É. G. Manoĭlov, and S. V. Svechnikov, Fiz. Tekh. Poluprovodn. (St. Petersburg) **35**, 1445 (2001) [Semiconductors **35**, 1383 (2001)].

5. M. G. Lisachenko, E. A. Konstantinova, V. Yu. Timoshenko, and P. K. Kashkarov, Fiz. Tekh. Poluprovodn. (St. Petersburg) **36**, 344 (2002) [Semiconductors **36**, 325 (2002)].

6. V. S. Dneprovskiĭ, E. A. Zhukov, O. A. Shalygina, *et al.*, Zh. Éksp. Teor. Fiz. **121**, 1362 (2002) [JETP **94**, 1169 (2002)].

7. V. S. Dneprovskiĭ, E. A. Zhukov, E. A. Mulyarov, and S. G. Tikhodeev, Zh. Éksp. Teor. Fiz. **114**, 700 (1998) [JETP **87**, 382 (1998)].

8. E. A. Mularov, E. Zhukov, V. S. Dneprovskii, and Y. Masumoto, Phys. Rev. B **62**, 7420 (2000).

9. V. S. Babichenko, L. V. Keldysh, and A. P. Silin, Fiz. Tverd. Tela (Leningrad) **22**, 1238 (1980) [Sov. Phys. Solid State **22**, 723 (1980)].

10. T. Takagahara, Phys. Rev. B **47**, 4569 (1993).

11. M. G. Lisachenko, E. A. Konstantinova, P. K. Kashkarov, and V. Ju. Timoshenko, Phys. Status Solidi A **182**, 297 (2000).

12. Yu. V. Kryuchenko and A. V. Sachenko, Physica E (Amsterdam) **14**, 299 (2002).

13. A. Hangleiter, Phys. Rev. B **35**, 9149 (1987).

14. A. Hangleiter, Phys. Rev. B **37**, 2594 (1988).

15. A. V. Sachenko, A. P. Gorban', and V. P. Kostylyov, Semicond. Phys. Quantum Electron. Optoelectron. **3**, 5 (2000).

16. A. M. Evstigneev, A. V. Sachenko, G. A. Sukach, *et al.*, Proc. SPIE **2648**, 396 (1995).

17. B. V. Kamenev and V. Yu. Timoshenko, Poverkhnost, No. 11, 91 (1998).

18. J. Valenta, R. Juhasz, and J. Linnros, J. Lumin. **98**, 15 (2002).

Translated by I. Zvyagin